

**Novel metallo-porphyrin based
colourimetric amine sensors and their
processing via plasma enhanced chemical
vapour deposition at atmospheric pressure
– synthesis, characterisation and
mechanistic studies**

Dissertation

zur Erlangung des Grades
„Doktor der Naturwissenschaften“
im Promotionsfach Chemie

am Fachbereich Chemie, Pharmazie und Geowissenschaften der
Johannes Gutenberg-Universität Mainz

Philip Christoph Heier
geboren in Oldenburg

Mainz, 2014

Die vorliegende Arbeit wurde unter der Betreuung von [REDACTED] in der Zeit vom Oktober 2010 bis Juli 2014 am Institut für Anorganische und Analytische Chemie der Johannes Gutenberg-Universität in Mainz, Deutschland und am Centre de Recherche Public – Gabriel Lippmann in Belvaux, Luxemburg angefertigt.

Mainz, Juli 2014

Dekan:

[REDACTED]

Erster Berichterstatter:

[REDACTED]

Zweiter Berichterstatter:

[REDACTED]

Tag der mündlichen Prüfung: 15. August 2014

D77

Abstract

Volatile amines are prominent indicators of food freshness, as they are produced during many microbiological food degradation processes. Monitoring and indicating the volatile amine concentration within the food package by intelligent packaging solutions might therefore be a simple yet powerful way to control food safety throughout the distribution chain.

In this context, this work aims to the formation of colourimetric amine sensing surfaces on different substrates, especially transparent PET packaging foil. The colour change of the deposited layers should ideally be discernible by the human eye to facilitate the determination by the end-user. The associated research topics addressed in this work can be summarised in three fields as shown in Figure 1.

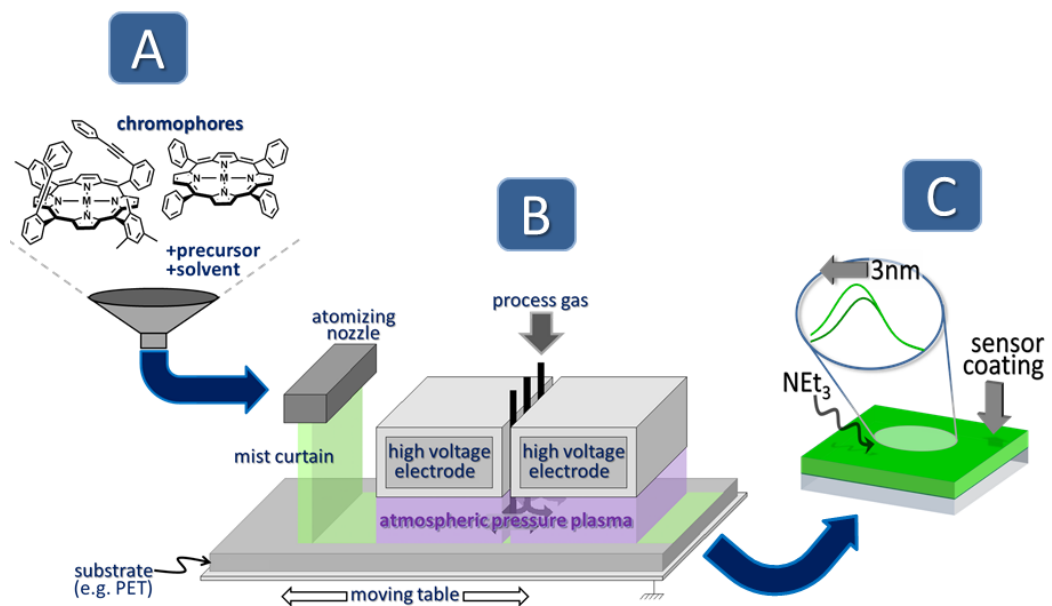


Figure 1 Graphical abstract of the research topics addressed in this work.

Different tailored zinc(II) and chromium(III) metalloporphyrins have been used as chromophores for the colourimetric detection of volatile amines (Figure 1, **A**). A new concept to increase the porphyrins absorbance change upon exposure to amines is introduced. Moreover, the novel porphyrins' processability during the deposition process is increased by their enhanced solubility in non-polar solvents.

The porphyrin chromophores have successfully been incorporated into polysiloxane matrices on different substrates via a dielectric barrier discharge enhanced chemical vapour deposition (**B**). This process allows the use of nitrogen as a cheap and abundant plasma gas, produces minor amounts of waste and by-products and can be easily introduced into (existing) roll-to-roll production lines. The formed hybrid sensing layers tightly incorporate the porphyrins and moreover form a porous structure to facilitate the amines diffusion to and interaction with the chromophores.

The work is completed with the thorough analysis of the porphyrins' amine sensing performance in solution as well as in the hybrid coatings (**C**). To reveal the underlying interaction mechanisms, the experimental results are supported by DFT calculations. The deposited layers could be used for the detection of NEt_3 concentrations below 10 ppm in the gas phase. Moreover, the coated foils have been tested in preliminary food storage experiments.

The mechanistic investigations on the interaction of amines with chromium(III) porphyrins revealed a novel pathway to the formation of chromium(IV) oxido porphyrins. This has been used for electrochemical epoxidation reactions with dioxygen as the formal terminal oxidant.

Contents

1. Introduction	1
1.1 Smart Food Packaging.....	2
1.1.1 Intelligent Packaging	3
1.1.2 Food Quality Indicators	5
1.2 Sensing of Amines	6
1.2.1 Biogenic and Volatile Amines.....	7
1.2.2 Optical Amine Sensing.....	9
1.3 (Metallo)Porphyrins.....	17
1.3.1 Synthesis of Artificial Porphyrins	18
1.3.2 Photophysical Properties of Porphyrins.....	19
1.3.3 Tuning of Porphyrin Absorption Spectra.....	21
1.4 Porphyrins in Sensing Applications	27
1.4.1 Porphyrin Based Gas Sensing Layers.....	29
1.5 Atmospheric Pressure Plasmas.....	34
1.5.1 Dielectric Barrier Discharge Plasmas.....	37
1.5.2 DBD Enhanced Chemical Vapour Deposition	39
1.6 Epoxidation of Olefins.....	43
1.7 Bibliography Introduction	46
2. Aim of the work.....	55
3. Results and Discussion.....	57
3.1 Plasma Polymer Membranes for Immobilising Metalloporphyrins.....	59
Introduction	61
Experimental Section	62
Results and Discussion	64
Discussion.....	71
Conclusion.....	72
References.....	73
3.2 Atmospheric pressure plasma polymerisation of metalloporphyrins containing mesoporous membranes for gas sensing applications	75
Introduction	77

Experimental	78
Results and discussion.....	79
Conclusions.....	85
References.....	86
3.3 Optical Sensing Responses of Cr^{III}Cl(TPP)(H₂O)-based Coatings Obtained by an Atmospheric Pressure Plasma Method – Application to the Detection of Volatile Amines	89
Introduction.....	91
Experimental	92
Results and Discussion	95
Conclusions.....	103
References.....	103
3.4 $\alpha\alpha$- and $\alpha\beta$-Zinc-meso-tetraarylporphyrins with large optical responses to triethylamine	107
Introduction.....	109
Results and discussion.....	110
Conclusions.....	125
Experimental section.....	126
Notes and references	129
3.5 New class of Zn^{II} and Cr^{III} porphyrins incorporated into mesoporous polymer matrixes via an atmospheric pressure plasma enhanced CVD to form gas sensing layers	133
Introduction.....	135
Experimental Section.....	136
Plasma Deposition of Sensor Coatings.....	139
Amine Sensing Experiments	146
Influence of Cr ^{III} Porphyrin Concentration on the Sensor Properties	150
Conclusions.....	152
Notes and References	153
3.6 Dual Application of (Aqua)(Chlorido)(Porphyrinato)Chromium(III) as Hypersensitive ON Switch Amine Detector and for Dioxygen Activation	155
Introduction.....	157
Results and Discussion.....	158
Conclusion.....	171

References.....	172
4. Summary	177
5. Outlook	179
6. Supporting Information	181
7. Acknowledgments	215
8. Curriculum Vitae.....	217
8.1 List of Publications.....	219
8.2 Conference contributions.....	220

Abbreviations

[O]	oxidant
δ	chemical shift (NMR) [ppm]
ΔG^\ddagger	activation energy
ε	extinction coefficient
λ	wavelength
λ_{em}	emission wavelength
λ_{ex}	excitation wavelength
λ_{Soret}	wavelength of the Soret band
ϕ	quantum yield
σ	standard deviation
ν	wavenumber
A	absorption
abs	absorption
AP-DBD	atmospheric pressure dielectric barrier discharge
aq	aqueous
Ar	aryl
ATR	attenuated total reflectance
a.u.	arbitrary units
Bn	benzyl
BODIPY	4-bora-3 <i>a</i> ,4 <i>a</i> -diazas-indacene
^t Bu	<i>tert</i> -butyl
Bu	butyl
CFC	Cephalotin-Sodium Fusidate-Centrime, growth medium on agar plates for the selective isolation of <i>Pseudomonas</i> species
cfg	colony forming units
COSY	correlated spectroscopy (NMR method)
Cp*	pentamethyl cyclopentadienyl
CTAB	cetyltrimethylammonium bromide
CVD	chemical vapour deposition
DBD	dielectric barrier discharge
DBU	1,8-diazabicyclo[5.4.0]undec-7-ene
DC	direct current

DCM	dichloromethane
DEA	diethyl amine
DEP	diethyl phthalate
DFT	density functional theory
dist	distal
DLD	delay-line detector
DMA	dimethyl amine
DMCPS	decamethylcyclopentasiloxane
DMF	dimethylformamide
D_{oop}	total out-of-plane distortion
E	potential
$E_{1/2}$	halfwave potential
EC	ethyl cellulose
EDTA	ethylenediaminetetraacetate
EDX	energy-dispersive X-ray spectroscopy
<i>e.g.</i>	<i>exempli gratia</i> (for example)
EPR	electronic paramagnetic resonance spectroscopy
em	emission
ESI	electron spray ionisation
Et	ethyl
Et ₂ O	diethyl ether
EtOH	ethanol
<i>et al.</i>	<i>et alii</i> (and others)
FcH	ferrocene
FcH ⁺	ferrocenium
FD	field desorption
FT-IR	fourier transform infrared spectroscopy
FWHM	full width at half maximum
GC	gas chromatography
GDS	glow-discharge-induced sublimation
GLC	gas-liquid chromatography
HMBC	heteronuclear multiple bond correlation (NMR method)
HMDSO	hexamethyldisiloxane
HMDSN	hexamethyldisilazane
HOD	hybrid orbital deformation

HOMO	highest occupied molecular orbital
HPLC	high-performance liquid chromatography
HR-MS	high resolution mass spectrometry
HSQC	heteronuclear single quantum coherence (NMR experiment)
<i>I</i>	intensity (of absorption)
IUPAC	International Union of Pure and Applied Chemistry
<i>K</i>	binding constant
LMCT	ligand-to-metal charge transfer
LTE	local thermodynamic equilibrium
LUMO	lowest occupied molecular orbital
<i>M</i>	molar mass or metal, depending on the context
MA	modified atmosphere
MCPBA	<i>meta</i> -chloroperoxybenzoic acid
Me	methyl
MeOH	methanol
MLCT	metal-to-ligand charge transfer
MS	mass spectrometry
<i>m/z</i>	mass to charge ratio
NC	nitro cellulose
NIR	near infra-red
NOE	nuclear Overhauser effect
NOESY	nuclear Overhauser-effect spectroscopy
NPOE	nitrophenyl octyl ether
NMR	nuclear magnetic resonance spectroscopy
NSD	normal-coordinate structural decomposition
OAc	acetate
OEP	octaethylporphyrinato
OMCTS	octamethylcyclotetrasiloxane
OPP	ooctaphenylporphyrinato
ox	oxidation
PDMS	polydimethyl siloxane
PET	polyethylene terephthalate
Ph	phenyl
pp-HMDSO	plasma polymerised hexamethyldisiloxane
pp-PDMS	plasma polymerised polydimethylsiloxane

pp-OMCTS	plasma polymerised octamethylcyclotetrasiloxane
ppb	parts per billion
ppm	parts per million
prox	proximal
PVC	poly(vinyl chloride)
PVD	physical vapour deposition
R	rest
red	reduction
RF	radio frequency
RH	relative humidity
RSF	relative sensitivity factor
salen	<i>N,N'</i> -ethylenebis (salicylimine)
SEM	scanning electron microscopy
SIMS	secondary ion mass spectrometry
SNR	signal-to-noise ratio
solv.	Solvent
<i>T</i>	temperature
<i>T_c</i>	coalescence temperature
<i>T_e</i>	electron temperature
<i>T_h</i>	heavy particle temperature
TBP	triphenyl phosphate
TCM	chloroform
TEA	triethylamine
TEP	triethyl phosphate
TEOS	tetraethoxy silane
THF	tetrahydrofuran
TLC	thin-layer chromatography
TMA	trimethyl amine
TMAO	trimethylamine- <i>N</i> -oxide
TMAO-ase	trimethylamine- <i>N</i> -oxide demethylase
TOF	time-of-flight
TNT	2,4,6-trinitrotoluene
TPP	<i>meso</i> -tetraphenylporphyrinato
TTI	Time-temperature indicator
TVB	total volatile bases

TVB-N	total volatile basic nitrogen
TVC	Total viable count: measure to quantify the number of microorganisms in a sample
UV	ultra violet
VA	volatile amines
VOC	volatile organic compounds
VTEOS	vinyltriethoxysilane
VTMOS	vinyltrimethoxysilane
vis	visible (light)
v/v	volume per volume (mixing ratio)
XF	cruciform fluorophores
XPS	X-ray photoelectron spectroscopy

1. Introduction

During the last decades there has been a growing demand for the development of sensitive, portable and cost-effective gas sensors. This trend arises from considerable public and industrial interests: novel health and environmental legislation demands the control of toxic gas concentrations in the environment, leakages in industrial processes needs to be indicated and the detection of trace amounts of explosives may help to ensure safety at airports and in conflict areas.

A further big market for cheap, reliable and easy-to-handle gas sensors is the food sector. Especially in the light of several food scandals during the last years, the control of food safety and freshness became a topic of crucial importance. A promising approach to address this subject is the development of food packages giving real-time information about the status of the packed good. Smart packaging foils may *e.g.* interact with the atmosphere inside the food container and give a readable output about its composition. This may lead to food packages indicating the freshness of the packed good by a discernable colour change – and thus an easy-to-handle but very powerful tool for producers, retailers, customers and controllers to monitor food safety throughout the value chain.

The following paragraphs will introduce the actual efforts to monitor food quality and freshness by intelligent packaging solutions and emphasize how the detection of volatile amines can be put into account.

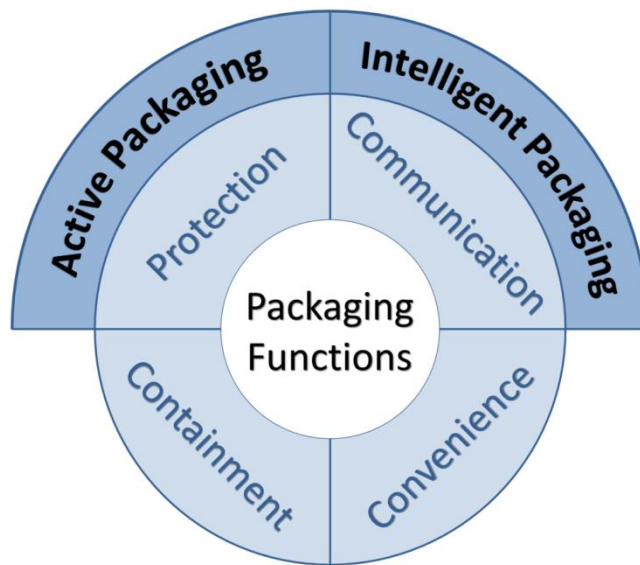
Different sensing approaches are discussed with special respect to colorimetric sensing systems. In this context, the use of porphyrin chromophores is accentuated not only with respect to amine sensing but to their successful application in colorimetric sensing in general. Concepts are shown to tune the porphyrins' selectivity and sensitivity and to optimise the observed colour changes.

The use of porphyrin-based sensor coatings, especially for the analysis of gaseous compounds, is shown and different techniques for their fabrication are discussed. In this context, special attention is paid on the use of plasma enhanced chemical vapour deposition at atmospheric pressure. Therefore, atmospheric pressure plasmas are briefly introduced in general and dielectric barrier discharges in more detail.

The introduction will end with a short digression concerning the epoxidation of olefins as new discoveries in this field will also be presented in this work.

1.1 Smart Food Packaging

The conventional basic features of food packages have been the reasonable *containment* of the respective good which facilitates *convenience* in handling and *protection* of the packed food against deteriorative effects from the environment. Additionally, information printed on the container has been used for *communication* with the customer (**Scheme 2.1**).^[1] During the past 3 decades these basic aspects have been supplemented by the concepts of *active* and *intelligent packaging*.



Scheme 2.1 Schematic representation of food packaging features.^[1]

The term *active packaging* comprises modified food packages providing “active” protection for the product and thus extending the shelf life of the packed goods.^[1,2] Examples for such technologies are the widely used modified atmosphere (MA) packaging^[3,4], oxygen and moisture scavengers, carbon dioxide and ethylene regulators or the use of antioxidant and antimicrobial materials.^[5–10]

A more recent development is a paradigm change of the *communication* aspect of the packages turning them into *intelligent packaging*.^[1,2] While the communication of classical food containers has been limited to information printed on the package prior

to its distribution, intelligent packaging solutions provide real time information about the containers history as well as the actual status of the packed goods.

1.1.1 Intelligent Packaging

According to current EU regulations, intelligent packaging materials are “materials and articles which monitor the condition of packaged food or the environment surrounding the food”.^[11,12] The intelligent packaging may *e.g.* indicate leakage of sealed packages or give information about the freshness of perishable food. The actual sensors’ response may be of manifold kind. But keeping future end-user applications in mind, it should ideally be visible by the human eye to facilitate easy and reliable use and thereby enhance food safety throughout the market.

Common to all intelligent packaging solutions is that they are non-invasive with respect to the integrity of the package. In contrast to most conventional techniques for the control of food safety like *e.g.* GC/MS, microbiological analysis protocols or portable headspace oxygen analysers, the package needs not to be opened or penetrated. There are two general types of intelligent packages with the indicator either placed *external* on the outside of the package or *internal* with direct contact to the packed food or the headspace within the container.

External sensors are represented by *time-temperature indicators* (TTI) placed onto the food package. These indicators give visible information about the full or partial temperature history of the food product by *e.g.* an irreversible temperature dependent colour change. This may either indicate a peak temperature above the recommended storage temperature or image the temperature profile along the whole supply chain. Time-temperature indicators have been extensively reviewed in the literature.^[13–15] Although some of these systems are already commercially available, there are some drawbacks in their use as food freshness indicators. The status of the packed food may only be estimated if temperature change is the only factor influencing its quality or degradation. Therefore, i) the precise starting quality of the packed good needs to be known, ii) changes in storing conditions besides temperature must not have any effect and iii) the exact degradations kinetics needs to be known.^[16]

Indicators placed inside the food packages with direct contact to the food or the headspace may be used to measure oxygen or carbon dioxide concentrations or monitor metabolites of microbiological activity.^[1,10]

In general, the optical *carbon dioxide sensors* used for intelligent packaging applications are based on pH responsive systems or their combination with pH independent fluorescent dyes.^[17] Carbon dioxide concentrations are thereby either indicated by changes in colour,^[18–22] luminescence intensity^[23–26], luminescence lifetime,^[23,27] or phase angle (in systems with two lumophores for ratiometric sensing).^[28–30] The main application of carbon dioxide monitoring in food containers is the leak detection in MA packages with a certain carbon dioxide concentration.^[31] But

as carbon dioxide may be produced during microbial growth, detection of higher carbon dioxide concentration has also been used to indicate microbial spoilage.^[22,32] Nevertheless, spoilage indicators based on carbon dioxide sensing are likely to give false-positive or false-negative responses due to carbon dioxide concentration changes caused by package leaks.

Oxygen sensors may be used to monitor the oxygen content in MA packages or to indicate leaks in MA packages with initial low-oxygen (0-2%) atmosphere.^[33] The detection of oxygen in intelligent packaging may either be lumophoric or colorimetric. Most optical oxygen sensors today are based on the quenching of the luminescence intensity or lifetime of excited lumophores with increasing partial pressure of oxygen.^[34-38] But as the lumophoric response is not visible to the human eye, additional (costly) instrumentation is required for read-out, which is a drawback regarding their adoption in the end-user market.^[33] In colorimetric systems, the detection of oxygen becomes visible by a colour change of the chromophore which may be initiated by either i) an oxygen-binding reaction,^[39-41] ii) a redox reaction^[42-44] or iii) a light-activated redox reaction.^[45-47] The latter approach is judged to be the most promising, as one may use inexpensive chromophores, which show a clearly discernable, irreversible colour change upon oxygen exposure and these systems tend to have a long ambient shelf-life.^[33]

An example of such a system published by Lawrie *et al.* is shown in **Figure 1.1**.^[47] The blue redox active dye methylene blue is inkjet-printed onto a polyester substrate (left). UVA light initiated TiO₂ catalysed reduction by a sacrificial reductant transforms the indicator into the active colourless leucomethylene blue (right). Exposure to air leads to a slow oxidation by oxygen and thereby a recovery of the initial blue colour within 12 h. The combination of oxygen sensitive dyes with oxygen absorbing components has further led to materials uniting the features of active and intelligent packaging.^[48]

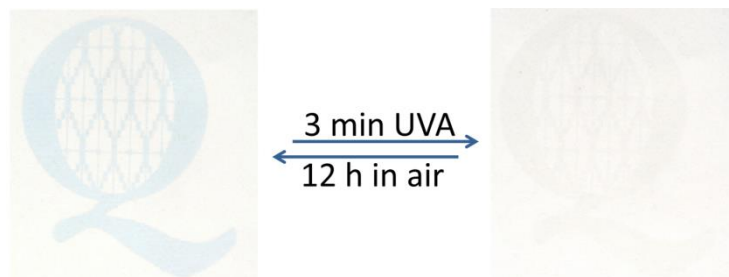


Figure 1.1 Photographs of the oxygen indicator MB/O₂-IJ published by Lawrie *et al.*^[47]; left: indicator as inkjet-printed onto a transparent polyester film, right: after activation under UVA light for 3 min; initial coloration is recovered by exposure to air for 12 h.

1.1.2 Food Quality Indicators

The sensors described above so far can monitor parameters in or on food packages which can give important information to estimate the condition and freshness of the packed good. Nonetheless, they are not directly connected to it. Temperature abuses may *e.g.* happen before packaging to TTI equipped containers and fresh leakages may very well lead to a detectable oxygen concentration in MA packages but may not imperatively lead to an immediate deterioration of the food. Even though oxidative stress can play a minor role in deterioration processes, spoilage of food is mostly associated with microbial activity. Therefore sensors monitoring proliferation of microbes or metabolites of microbial activity may give a more direct and reliable information about the food's condition. Such systems are called *freshness indicators*^[14] or *food quality indicators*^[13].

For the implementation of food quality indicators into intelligent packaging solutions characteristic metabolites of microbial activity needs to be identified. The associated changes in the headspace composition within the packages have to be further connected to the actual progress of spoilage. An ideal food quality indicator would therefore start changing its colour when a threshold concentration of a certain metabolite, which is associated with microbial spoilage and/or inferior quality of the packed food, is reached.

A successful connection is emphasized by the graph in **Figure 1.2.**^[49] It shows the response of a freshness indicator monitoring the bacterial spoilage of fresh cod kept at 20 °C over time. This system is based on the pH sensor bromocresol green. Its colour

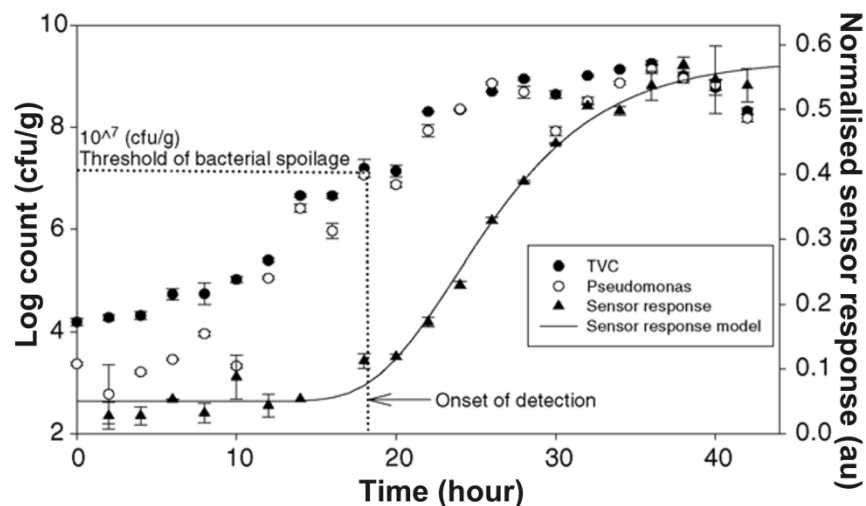


Figure 1.2 Correlation of bromocresol green based sensor response and changes in bacterial population of fresh cod kept at 20 °C over time. Bacterial data (TVC and Pseudomonas Log counts) are averages of two replicates while sensor data are average over 15 measurements. The error bars are standard error of the mean values.^[49]

change is induced by the acid-base reaction with basic volatile amines which represent one class of metabolites characteristic for microbial activity.

It can be seen that the sensor's onset of detection around 18 h correlates well with the threshold of bacterial spoilage connected to the end of shelf life. The numbers of bacteria on the fish samples associated with spoilage have been independently counted by classical microbiological plate count techniques at different time points. Solid dots represent the total viable count (TVC) on agar plates and open dots the *Pseudomonad* counts on CFC selective agar. The threshold of bacterial spoilage of 10^7 colony forming bacterial units per gram fish (cfu/g) has been defined in further studies.^[50,51]

The specific role of amines regarding the development of food quality indicators in general and with special respect to this work will be discussed in more detail in the following Section 1.2.

Another possible target metabolite is *hydrogen sulfide*. It is *e.g.* produced by *Pseudomonas* species on poultry^[52] or by *Enterobacteriaceae* on aerobically stored meats.^[53] In intelligent packaging, myoglobin based sensors maybe used for the optical detection of hydrogen sulfide. The initially brown sensors turn red under anaerobic or green under aerobic packaging conditions in the presence of hydrogen sulfide.^[54,55]

Lactic acid bacteria (*Lactobacillales*), which are often responsible for the spoilage of low oxygen MA packed food, produce *lactic acid* from carbohydrates.^[14,53,56] The associated changes in pH maybe detected by colorimetric pH indicators on or in the food package. Another metabolite of some Lactobacillales is *ethanol*^[53] whose concentrations could be connected to microbial activity on beef^[57] as well as chicken breasts and rainbow trouts.^[58] Optical detection of ethanol may be achieved by sensing membranes containing porphyrin chromophores^[59-61] or fluorescent dyes bearing trifluoroacetyl moieties^[62] to interact with the alcohol.

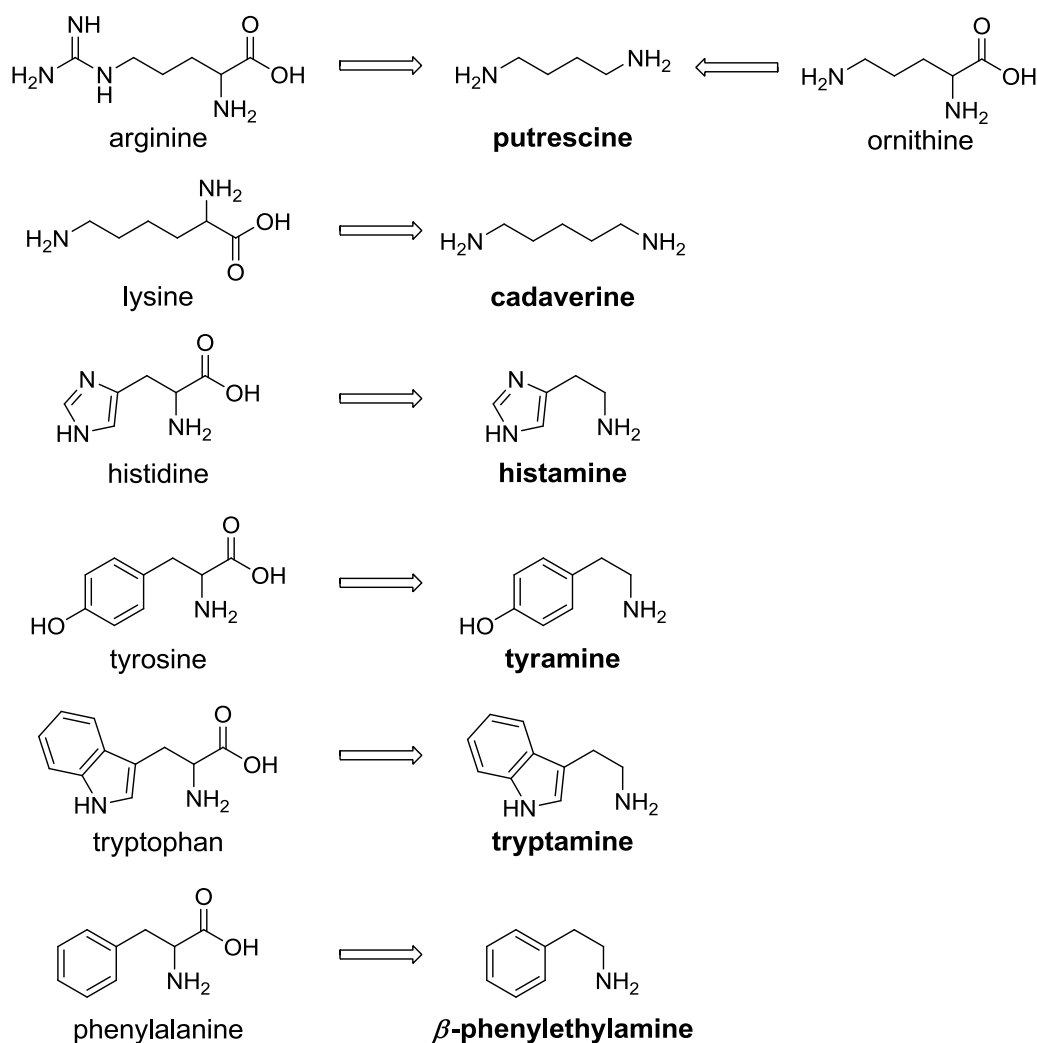
1.2 Sensing of Amines

Different kinds of amines are essential to numerous commercial applications. They are *e.g.* used as corrosion inhibitors, in fertilizers, as auxiliaries in dye manufacturing and for the production of cosmetics, pharmaceuticals and dyes.^[63] In this context, amine sensing can be of manifold interest: amine concentrations during the production process need to be monitored, residual amounts of amine in products may be controlled or undesired amine releases to the environment need to be detected.

Moreover, the qualitative and/or quantitative detection of amines can be of special interest for food safety applications. As different kinds of amines are formed by microbial activity or non-enzymatic decomposition processes, they can be used as indicators for spoilage and deterioration of foodstuff.

1.2.1 Biogenic and Volatile Amines

In the context of food safety, amines produced during microbial activity as a result of spoilage and aging are called *biogenic amines*. The most important biogenic amines occurring in foodstuff are histamine, putrescine, cadaverine, tyramine, tryptamine and β -phenylethylamine.^[64,65] These amines are produced by decarboxylation of the respective free amino acids as shown in **Scheme 1.1**. The responsible amino acid decarboxylases can be found in certain *Enterobacteriaceae*, *Clostridium*, *Lactobacillus*, *Streptococcus*, *Micrococcus* and *Pseudomonas* which are connected to food spoilage.^[65] The toxicological effects of biogenic amines after consumption, which includes headache, nausea and dizziness, have been extensively reviewed in the literature.^[65,66] The analysis of biogenic amines in food samples is so far a destructive process and requires their extraction from the food matrix. Moreover, as the amines need to be extracted from different matrices and different interfering compounds maybe present, there is no general approach.



Scheme 1.1 Biogenic amines connected to food safety issues and the respective amino acids they are built from by enzymatic decarboxylation.

In a first step the amines are extracted from the respective food matrix using trichloroacetic acid, hydrochloric acid and/or organic solvents. The contained amines are then identified and quantified by thin-layer chromatography (TLC), gas-liquid chromatography (GLC) or high-performance liquid chromatography (HPLC).^[65]

Monitoring biogenic amine concentrations have been successfully employed for the control of food freshness and safety, as they can be connected to microbial activity.^[67] Nonetheless, their analysis as described above is quite time-consuming and requires elaborated instrumentation and trained personal. Furthermore, as the biogenic amines are non-volatile compounds, they cannot be analysed by food quality indicators which are sensitive to changes of the headspace composition within the food packages.

Another class of amines connected to food safety are the so called *volatile amines* (VA) also referred to as total volatile basic nitrogen (TVB-N). These terms summarise volatile, low molecular weight amines such as *e.g.* trimethyl amine (TMA), dimethyl amine (DMA) and ammonia. The formation of volatile amines has been extensively studied for fishery products. For this group the VAs are formed by either enzymatic or non-enzymatic degradation of trimethylamine-*N*-oxide (TMAO; a main osmolyte in fish and crustaceans^[68,69]).

The non-enzymatic process is catalysed in the presence of iron(II),^[70-72] tin(II) or SO₂^[70] and leads to the formation of TMA and DMA from TMAO. The reaction rate is further enhanced in the presence of chelating ligands like cysteine or ethylenediaminetetraacetate (EDTA). This reaction can also be generally used for the artificial dealkylation of tertiary amines: in a first step tertiary amines are converted into the respective *N*-oxides by *m*-chloroperbenzoic acid which are subsequently dealkylated by treatment with iron(II) chloride yielding the secondary amine and an aldehyde.^[73]

However, in the context of food freshness control, volatile amines produced by enzyme activity are more significant. Different bacteria associated with fish spoilage can use TMAO as an alternative terminal electron acceptor in anaerobic respiration.^[74-77] Thereby the reduction of TMAO by TMAO reductases leads to the formation of TMA. The conversion of TMAO to DMA is enzymatically catalysed by TMAO demethylase (also called TMAO-ase). This enzyme can be found in fish flesh and may lead to the accumulation of elevated DMA concentrations after the fish's death.^[71,72,78] But in addition, TMAO demethylase is expressed by several bacteria and therefore the formation of DMA can also be connected to bacterial spoilage.^[79-81]

The formation of volatile amines associated with spoilage of poultry and meat is not understood as detailed as for fish products. However, some bacteria, like *e.g.* *S. putrefaciens*, are common to fish and meat spoilage and therefore similar pathways may hold.^[82]

For their use as target metabolites for food quality indicators, however, it is most important to connect changes in the volatile amine concentration to the actual progress of the food's spoilage. This has successfully been done in studies for fish^[49,83] and crab products^[84], but also for chicken^[85,86], beef and pork^[85,87] – regardless of the unclear mechanism of the VA's formation in the latter cases. Along with their volatile nature, which let them easily interact with quality indicators placed onto or within the food package, this makes volatile amines a versatile target metabolite for the freshness control of a broad scope of foodstuff.

1.2.2 Optical Amine Sensing

The European Commission has defined a standard method to determine the TVB-N levels in tissue samples for the control of food freshness and to compare it with quality indicating thresholds.^[88] It consists of extraction of the volatile bases from the tissue by perchloric acid solution followed by steam distillation of the extract. The distillate is collected in boric acid and titrated against standard HCl. This procedure clearly is a destructive, time consuming method which moreover requires trained personal and special instrumentation.

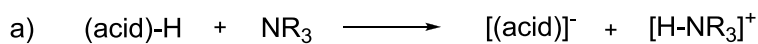
Intelligent packaging solutions exploiting volatile amines as indicating metabolites would in contrast lead to easy to use yet powerful tools for the control of food safety throughout the foodstuff's lifecycle. To reach this goal, there is a demand for amine sensing systems which provide an easily readable optical response – ideally even clearly discernable by the human eye.

This chapter should give a general overview over the different available approaches to optically detect amines. The examples given are not all necessarily connected to volatile amine sensing in the context of food safety, but should also show potential concepts applicable for future developments in this field. **Scheme 1.2** comprises different interaction modes between amines and the sensing molecules, which change colour or luminescence properties in case of amine detection. In the following, examples for the different concepts will be given.

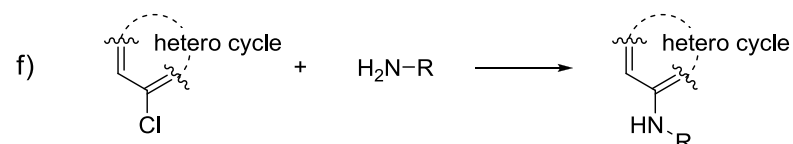
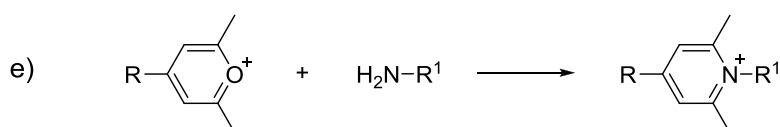
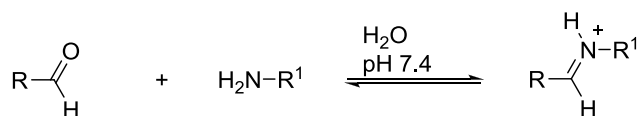
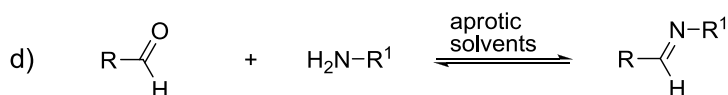
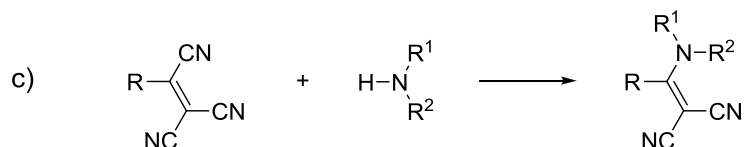
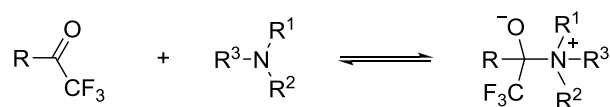
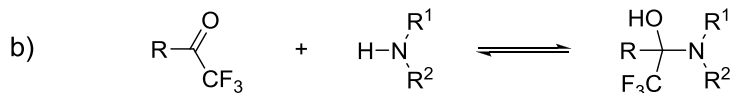
Acid-base chemistry

As manifold colorimetric pH sensitive dyes have been widely used for analytical purposes since decades, one obvious approach for the detection of amines is to exploit their basic nature. This has *e.g.* led to a patent in 1964 describing a method to determine amine concentrations in aqueous solutions by addition of sulfon phthalein based pH indicators and extraction of the formed coloured species by chloroform for further spectral analysis.^[89] But this approach is clearly not selective for amines and is prone to interferences by any other basic or acidic species present. However, some work has been published using Bromocresol green based systems for the detection of volatile amines in the gas phase. The pH indicator has been either immobilized onto mesoporous silica microspheres^[90] or in cellulose acetate layers.^[49] Both systems could

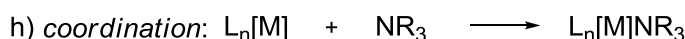
acid-base chemistry



covalent bond formation



coordination bond formation



Scheme 1.2 Different interaction modes between amines and sensors: a) deprotonation of acidic sensors, formation of b) hemi-aminals or zwitter-ions from trifluoroacetyl groups, c) 1-amino-2,2-dicyanovinyl derivatives from tricyanovinyl derivatives, d) imins or iminium-ions from aldehydes, e) pyridinium derivatives from pyrylium groups or f) nucleophilic substitution at sp^2 hybridised centres, g) exchange of ligands in complexes and h) coordination to metal complexes.

indicate volatile amines like DEA, TEA or ammonia by a colour change from orange to blue and with the help of spectral analysis these amines could be detected down to

ppm concentrations. The latter sensor system has furthermore been tested for the control of fish freshness. The absorption change induced by volatile amines released from the fish upon microbial degradation could successfully be connected to the actual bacterial spoilage of the food (see Figure 1.2 in section 1.1.2). Interferences with other basic compounds besides amines are unlikely in gas phase analysis, as amines can be considered to be the only basic volatile compounds in a common environment. Nevertheless, problems may arise upon interference with CO₂. Under humid conditions, CO₂ e.g. present in MA packages or formed during bacterial growth can form carbonic acid which in turn may (re-)protonate present pH indicators. This is further emphasized by the use of similar systems of immobilized pH indicators for the detection of CO₂ itself.^[19]

Covalent bond formation

To overcome problems arising from unspecific interferences in pH indicator-based amine sensors, further concepts have been developed during the last years providing a more selective interaction with amines in the gas-phase as well as in solution. One approach has been the formation of covalent bonds between the sensors and amines to be detected.

In this context, several amine sensors have been designed bearing at least one trifluoroacetyl moiety (Scheme 1.2b). This group can reversibly react with primary and secondary amines to form hemi-aminals or with tertiary amines to form zwitter-ionic species. Based on this concept, Mohr *et al.* developed a series of donor-acceptor substituted azobenzene and stilbene chromophores for amine sensing (**Figure 1.3**). In these systems, the trifluoroacetyl group acts as an electron acceptor and the alkyl amino group as an electron donor. When the trifluoroacetyl group reacts with an amine, its acceptor capacity is changed which leads to a remarkable hypsochromic shift

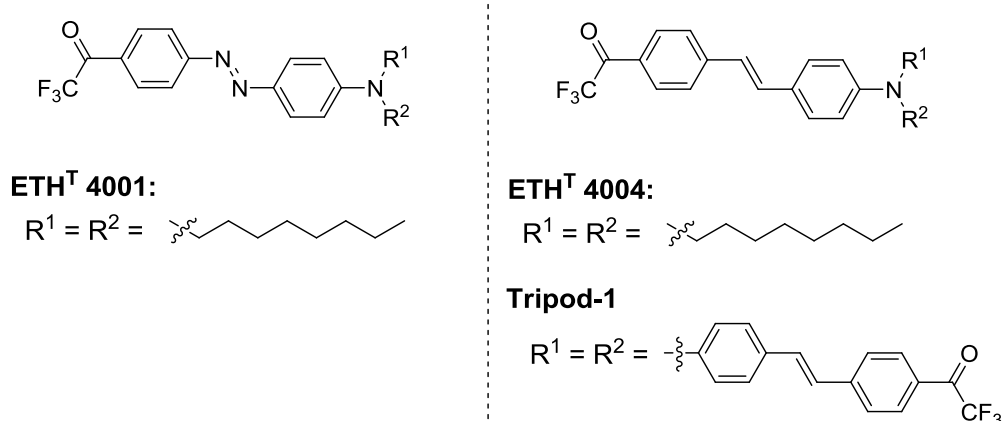


Figure 1.3 Amin sensors bearing trifluoroacetyl moieties by Mohr *et al.*; left: azobenzene-based: ETH^T 4001^[91–93]; right: stilbene-based: ETH^T 4004^[62,91] and Tripod-1.^[94]

in absorption and/or emission. ETH^T 4001 (see Figure 1.3) has been immobilised in different polymeric matrices, which is facilitated by the long alkyl chains at the terminal nitrogen atom.^[91–93] The exposure of these matrices to different aqueous amine solutions led to an absorption change of about 60 nm from $\lambda_{\text{max}} \approx 490$ to 430 nm. With the stilbene analogue ETH^T 4004 a decrease in emission around 490 nm is observed in similar experiments.^[62,91] The tripodal structure of Tripod-1 with three functionalized stilbene units attached to a central nitrogen led to an enhanced sensitivity and selectivity for diamines like 1,3-diaminopropane.^[94] Furthermore, by introduction of a nitro group in *meta* position to the trifluoroacetyl moiety of ETH^T 4001 the compound CR-546 (not shown) has been formed.^[95] The additional acceptor strength of the nitro group increased the reactivity, and thereby sensitivity, of the sensor. Moreover, the initial absorbance is bathochromically shifted by 40 nm enabling the use of cheaper light sources. These two chromophores, ETH^T 4001 and its nitro functionalized derivative CR-546, are commercially available at Sigma-Aldrich for the formation of amine sensing membranes.^[96,97]

Analogous di-azo dye sensors have been created by substitution of the trifluoroacetyl group of ETH^T 4001 with a tricyanovinyl group.^[98] The tricyanovinyl group readily reacts with nucleophiles like amines (Scheme 1.2c).^[99] It influences the performance of the colourimetric sensor by its larger acceptor strength compared to the trifluoroacetyl moiety. This leads to a red-shift in absorption of the formed push-pull system. The absorption maximum of the sensor in toluene solution can therefore be found at 590 nm and is shifted to 460 nm upon reaction with primary amines.^[98] This enables the use of cheaper light sources and detectors as *e.g.* compared to ETH^T 4001. When this sensor was immobilized in PVC plasticised with 2-nitrophenyloctyl ether, sensor layers could be formed to detect lipophilic amines in aqueous solutions by an absorption change from 640 to 470 nm.

The reactivity of aldehydes towards amines to form imines or hemi-aminals (Scheme 1.2d) has been exploited in several examples for amine sensing materials. Glass *et al.* developed a series of aldehyde functionalized coumarin (**A**) and quinolone (**B**) based sensors for primary amines in buffered aqueous solutions (see **Figure 1.4**). Sensor **A** gave especially good response towards different amino acids.^[100] Upon exposure the absorption maximum of **A** is bathochromically shifted from 445 to 480 nm. Furthermore, a remarkable fluorescence enhancement by *e.g.* 45 times with glutamate is observed ($\lambda_{\text{ex}} = 495$ nm, $\lambda_{\text{em}} = 510$ nm).

Quinolone based systems like **B** showed similar optical changes upon treatment with primary amines, even though the observed emission is bathochromically shifted compared to **A** ($\lambda_{\text{ex}} = 495$ nm, $\lambda_{\text{em}} = 530$ nm).^[101] Furthermore, when two quinolone moieties are connected by different bis-thiol bridges, sensors with high affinity towards diamines like 1,3-diaminopropane or ornithine are formed.^[101] In both systems **A** and **B** the formation of an iminium-ion is believed to be crucial for the observed sensor

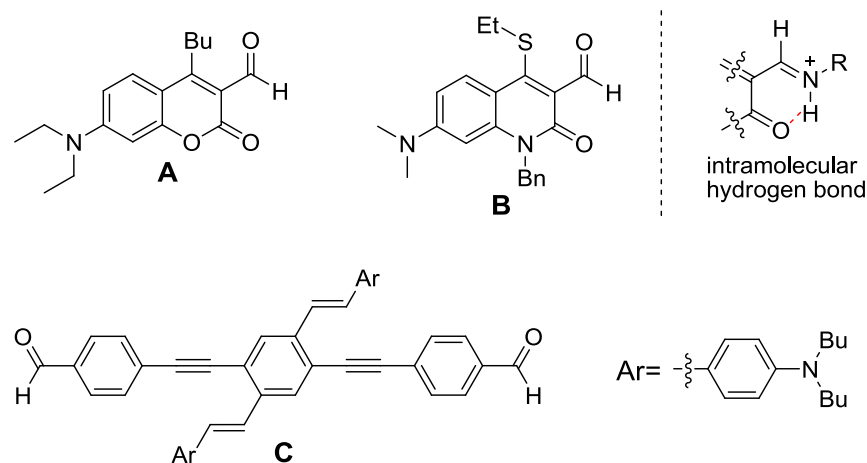


Figure 1.4 Different amine sensors bearing aldehyde functions as recognition moieties: coumarin (**A**) and quinolone (**B**) based systems and cruciform fluorophores (**C**); the formation of an intramolecular hydrogen bond after reaction of **A** and **B** with primary amines is indicated in the top right.

response. This should be the predominant species at pH 7.4 due to the high basicity of the intermediate imins. The observed optical changes are attributed to the formation of an intramolecular hydrogen bond to the carbonyl function as indicated in Figure 1.4. The formation of a neutral imine, lacking the possibility to form this hydrogen bond, does only induce minor changes of the electronic properties.

Another example of aldehyde functionalized amine sensors are so called cruciform fluorophores (XFs) like **C** published by Bunz *et al.* (Figure 1.4).^[102] In XFs the frontier molecular orbitals are spatially separated upon suitable donor-acceptor substitution of the peripheral aryl units.^[103] This is beneficial for the design of optical sensors, as the HOMO or the LUMO may be affected independently by the interaction with an analyte at a distinct site leading to pronounced changes of the photophysical properties. The sensor **C** can be used in different organic solvents to detect primary and secondary amines, which form imins or hemi-aminals, respectively.^[102] The reaction leads to a strong fluorescence turn-on by *e.g.* a factor of 700 with *n*-butylamine in dichloromethane. Aliphatic diamines like 1,3-diaminopropane form cyclic aminals upon reaction with **C** which induces a blue-shift of the emission to $\lambda_{em} = 507$ nm. Thereby they may be distinguished from amines forming imines or hemi-aminals, as these species show emission in the range of $\lambda_{em} = 540$ to 550 nm. Polymeric species created from aldehyde functionalized bis-stilbene building blocks similar to **C** have furthermore been immobilized on silica TLC plates and were used for amine detection in the gas phase.^[104]

A further functional group used in amine sensing compounds is the pyrylium moiety which reacts with primary amines to form a pyridinium function as shown in Scheme 1.2e. Wolfbeis *et al.* initially developed compound **D** (Figure 1.5) for staining proteins in gel electrophoresis.^[105,106] Amine groups of the proteins readily react

irreversibly with the dye which facilitates their identification on electrophoresis plates or their quantification in aqueous solutions. The formation of the pyrylium function upon reaction with amines results in a hypsochromic shift of the absorption maximum from 620 to 500 nm which becomes visible by a colour change from blue to red. Moreover, a strong fluorescence turn-on is observed with a 50-fold increase in emission. The applicability of this system to generally detect primary amines has already been addressed in the original publications. However, a further study especially dealt with the detection of biogenic amines. Therefore, **D** has been immobilized in a poly(acrylonitrile)-based hydrogel on paper strips along with the amine insensitive fluorescent dye fluorescein.^[107] Dipping of these strips into aqueous solutions of *e.g.* histamine, tyramine or putrescine lead to a visible colour change from green to red under UV irradiation. The immobilization in the hydrogel prevented interferences with *e.g.* proteins which cannot penetrate the matrix.

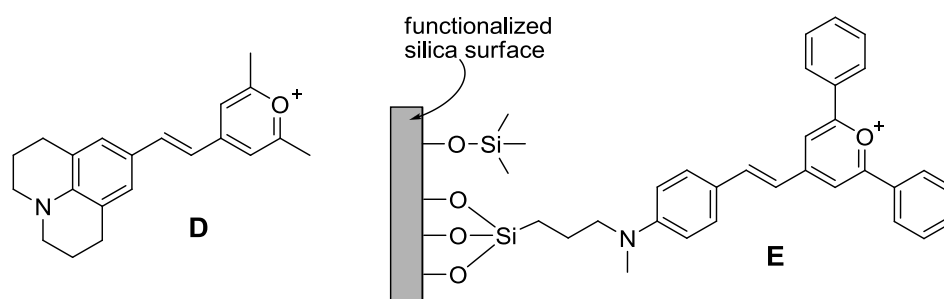


Figure 1.5 Pyrylium based amine sensors as published by Wolfbeis *et al.* (**D**) and Martínez-Máñez *et al.* (**E**).

A similar approach to generate certain selectivity in pyrylium-based amine sensors was followed by Martínez-Máñez *et al.*. They immobilized pyrylium-based chromogenic sensors in functionalized mesoporous silicas^[108] (**E**, Figure 1.5). By tuning the pore size as well as the hydrophobicity of the materials, they obtained a material which selectively changed colour from magenta to yellow with medium chain-length primary aliphatic amines, like *e.g.* *n*-heptylamine, but not with *e.g.* *n*-propyl or *n*-dodecylamine.^[109] A further chromophore doped silica material changed its colour from blue to magenta upon exposure to biogenic amines like histamine, putrescine or cadaverin but not the respective amino acids (see Scheme 1.1 for corresponding amino acids).^[110] Thereby, different concentrations of artificially added histamine could be detected in more complex media like aqueous extracts from fish samples without interferences from amino acids or proteins. In general, both materials referred to in this paragraph only worked as suspensions in a water/acetonitrile mixture.

In Scheme 1.2f the general possibility of amines reacting as nucleophiles in nucleophilic substitutions is emphasized. One example exploiting this reaction is based on the BODIPY (4-bora-3*a*,4*a*-diza-*s*-indacene) structure, which has been a versatile basis for numerous fluorescent dyes and sensors.^[111,112] The 3,5-dichloro-BODIPY derivative **F** shown in Figure 1.6 readily reacts with amines by a nucleophilic

substitution of one chloride in organic solvents at room temperature.^[113] In methanol for example, its initial absorption around 510 nm is hypsochromically shifted by 20 or 30 nm upon the reaction with aniline or piperidine, respectively. The reaction in both cases is further accompanied by a bathochromic shift of the sensor's emission from 520 to around 560 nm. The sensor **F** might therefore be used for the detection of less nucleophilic amines.

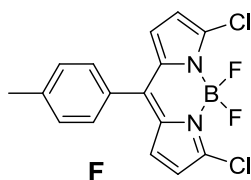


Figure 2.6 Chemical structure of the amine sensor **F**.

Coordination bond formation

The examples discussed in the former paragraphs are all based on molecular sensors forming covalent bonds with the amines to be detected. Another approach is to exploit the amines' ability to form coordinative bonds to metal centres. Generally two classes may be distinguished: as shown in Scheme 1.2g one or more ligands of the initial sensor complex may be exchanged by the amines or in another case an amine may coordinate to the complex expanding its coordination sphere (Scheme 1.2h).

One system representing the former class is shown in **Figure 1.7 (G)**. The heterobimetallic system is composed of two Ru^{II} centres, which are responsible for the signal transduction, and an Eu^{III} centre as the functional specific recognition site – connected to the Ru^{II} centres via cyanide bridges. This complex shows a strong MLCT absorption typical for Ru(bipyridine) moieties at 417 nm. However, their characteristic ³MLCT emission is dramatically quenched due to the coordination to Eu^{III}. Upon exposure to amines in ethanol solution, a stable Eu^{III}-complex is formed and the [Ru(^tBu-bipyridine)(CN)₄]²⁻ (**H**) complexes are released as exemplarily shown in Figure 1.7 for histamine. This is accompanied by a strong emission turn-on upon excitation of **H** at 354 nm which becomes visible by a deep red color ($\lambda_{em} = 654$ nm). By this method different biogenic amines like putrescine, histamine, spermidine and dissolved ammonia could be detected down to ppb levels. No response could be observed for aromatic amines like aniline or other volatiles like H₂S or CO. This sensor has also been used to evaluate fish freshness. Therefore, gaseous samples have been taken from the headspace above spoiled fish and were transferred to solutions of the sensor in ethanol. The sensor's emission changed due to the interaction with the TVB-N which had been released to the headspace by microbial degradation of the fish. The headspace TVB-N levels were independently checked by GC-MS measurements and could successfully be correlated to the sensor's response.

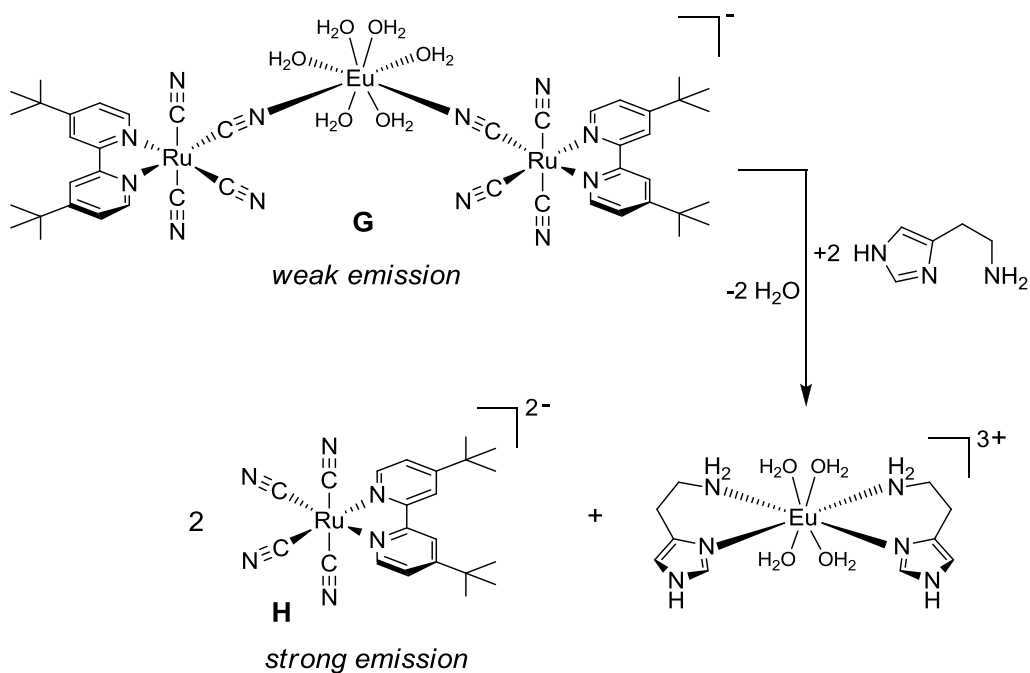


Figure 1.7 Structure of the heterobimetallic sensor **G** and its representative reaction with histamine illustrating the release of the strongly emitting complex **H**.

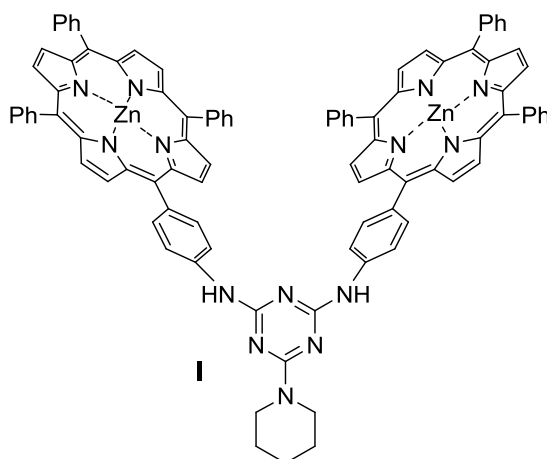


Figure 1.8 Molecular structure of the metalloporphyrin based sensor **I**.

An example for a molecular amine sensor in which a vacant coordination site is occupied by amines present in solution is shown in **Figure 1.8 (I)**.^[114] The tweezers-like structure of **I** with the two zinc porphyrin moieties facing each other makes this sensor especially sensitive for the detection of aliphatic diamines. Upon exposure of **I** to diamines of the general structure $\text{H}_2\text{N}-(\text{CH}_2)_n-\text{NH}_2$ (with $n = 4-8$) in CH_2Cl_2 the colour of the solution changed from purple to blue. The amines are coordinated between the two zinc centres leading to high affinity constants varying from $K = 4.2 \times 10^6$ to $3.4 \times 10^7 \text{ M}^{-1}$. In contrast, the affinity for the aliphatic mono-amine *n*-butylamine is significantly lower with $K = 3.2 \times 10^4 \text{ M}^{-1}$.

Metalloporphyrins generally show some beneficial properties suggesting their use for colorimetric amines sensing: i) they bear a potential coordination site at the metal centre for amine recognition, ii) they exhibit intense absorption of UV and especially visible light which is affected by amine coordination and iii) different approaches for their functionalization are established to regulate their selectivity and/or affinity towards amines. Therefore, and as metalloporphyrins are one main aspect of the research presented in this work, they will be discussed more detailed in the following section with respect to their general chemical and physical properties as well as their use in sensing applications.

1.3 (Metallo)Porphyrins

The core structure common to all porphyrins is the porphin, which is shown in **Figure 1.9a** along with the general IUPAC nomenclature to describe substituent patterns of porphyrins.^[115] The four pyrrole units are connected via methine bridges leading to a macrocycle with 22 conjugated π electrons. The porphyrin's aromatic system is commonly described by 18 delocalized π electrons as shown in **Figure 1.9b**.^[116,117] They therefore fulfil the $(4n+2)$ -Hückel rule for aromatic systems and may be seen as diaza[18]annulenes.^[118,119]

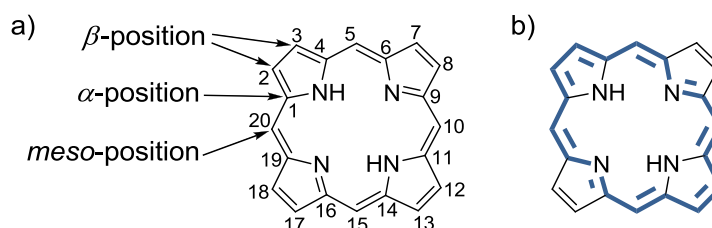


Figure 1.9 a) Porphin with the general IUPAC nomenclature for porphyrins; b) illustration of the aromatic diaza[18]annulene structure (blue) in porphyrins.

Porphyrins are amphoteric compounds. In their neutral form, the two inner protons are highly mobile between the four nitrogen atom sites.^[120] At room temperature, their exchange is fast compared to the NMR time-scale leading to only one ^1H resonance around $\delta = -1.4$ to -4.4 ppm.^[121] The characteristic up-field shift is caused by the strong ring currents of the porphyrin macrocycle. Under acidic conditions, the porphyrin can be protonated to a stable di-cationic form.^[122] Deprotonation to the mono-anionic form is possible by strong organic bases.^[123] However, the acidic nature of the porphyrin is most obvious by the formation of the deprotonated di-anion upon complexation of metal ions within the porphyrin cavity. The rich coordination chemistry of porphyrins is emphasized by the table in **Figure 1.10** which summarizes all elements for which porphyrin complexes are currently known.^[124] Elements in shadowed boxes are known in more than one oxidation state within porphyrins.

	1	2	3	4	5	6	7	8	9	10	11	12	13	14	15
	Li												B	C	
	Na	Mg											Al	Si	P
	K	Ca	Sc	Ti	V	Cr	Mn	Fe	Co	Ni	Cu	Zn	Ga	Ge	As
	Rb	Sr	Y	Zr	Nb	Mo	Tc	Ru	Rh	Pd	Ag	Cd	In	Sn	Sb
	Cs	Ba	Ln	Hf	Ta	W	Rs	Os	Ir	Pt	Au	Hg	Ti	Pb	Bi
			Ac												

Figure 1.10 Periodic table showing the elements that are known to form porphyrin complexes. Those shown in shaded boxes are known in more than one oxidation state within porphyrin complexes.^[124]

1.3.1 Synthesis of Artificial Porphyrins

Depending on the substitution pattern, three main types of porphyrins may be distinguished: *meso*-substituted, β -substituted and *dodeca*-substituted porphyrins (see **Figure 1.11**).

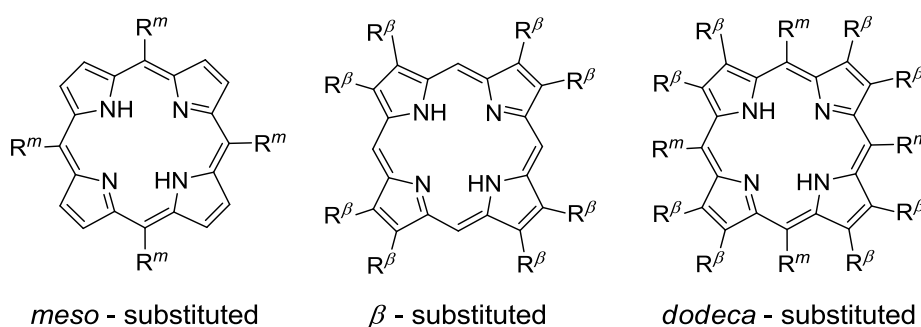


Figure 2.11 Different substitution patterns of porphyrins.

Literally all synthetic routes to porphyrins are based on the condensation of pyrrole derivatives with aldehydes – whether in a single- or multi-step procedure. Therefore β -substituents need to be introduced via the respective pyrrole derivatives, which may not be easily accessible.^[125] Functionalization in the *meso*-position can be achieved by use of different aldehydes whose chemistry is much more established.

The first synthetic route to *meso*-substituted A_4 -porphyrins (see **Figure 1.12a**) published by Rothmund is based on the condensation of pyrrole with different aldehydes at elevated temperatures.^[126,127] The procedure has been further optimized by Brønsted or Lewis acid catalysis in organic solvents leading to yields up to 30%.^[128,129] Unsymmetrically substituted porphyrins of all kinds may be synthesised by statistical methods using pyrroles or dipyrromethanes with a mixture of different aldehydes. However, yields of the desired porphyrin may be low and the separation from other porphyrins formed is challenging. Therefore rational synthetic routes have been developed for the different types of *meso*-substituted porphyrins. The different approaches are summarised in two papers by Lindsey *et al.*^[130,131] Possible rational routes to A_2B_2 - and AB_2C -porphyrins are exemplarily shown in **Figure 1.12 b)** and **c)**,

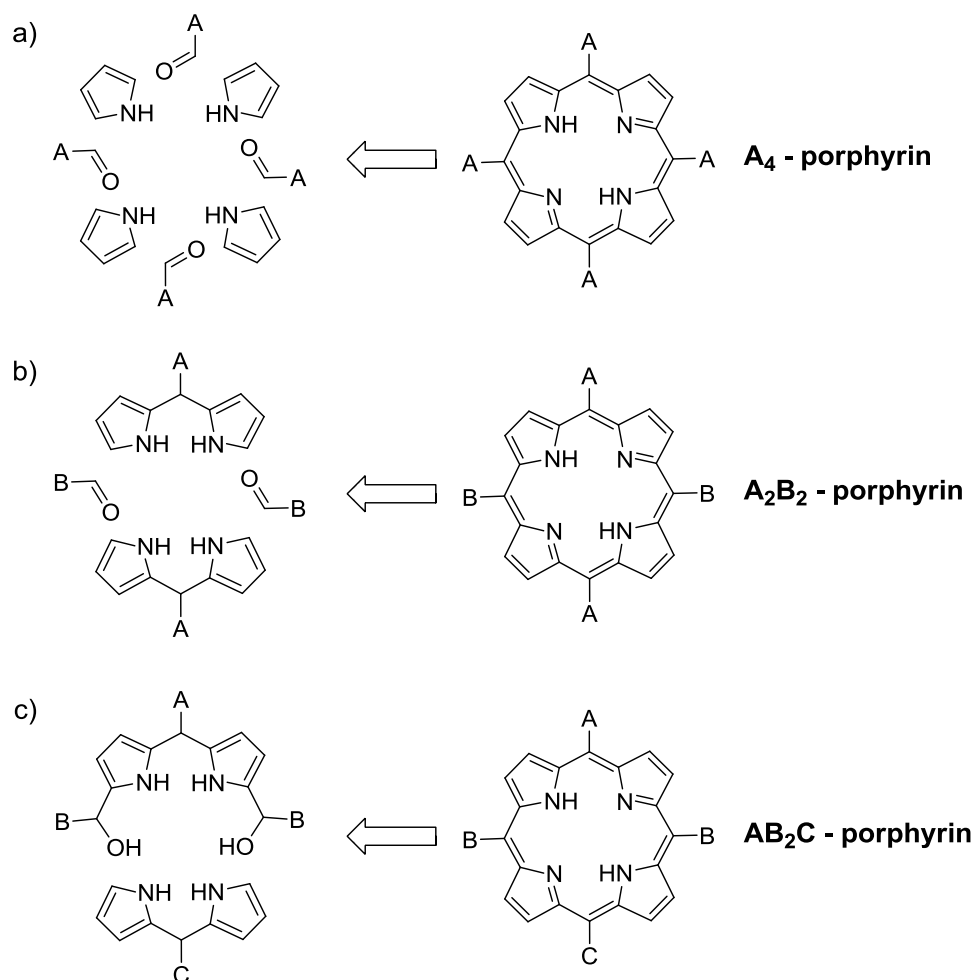


Figure 1.12 Exemplary retro-synthetic cuts for the synthesis of a) A_4 -, b) A_2B_2 - and c) AB_2C - porphyrins.

respectively. Synthesis of *trans*- A_2B_2 porphyrins involve the selective preparation of dipyrromethanes bearing one of the *meso*-substituents which are in a second step linked with aldehydes bearing the other.^[130,132] Lowering the symmetry to AB_2C -porphyrins requires further steps for rational synthesis. The cyclisation step involves a dipyrromethane bearing the C-substituent and a BAB-substituted dipyrromethane-dicarbino, which has to be synthesized in multiple steps beforehand.^[130,131,133]

1.3.2 Photophysical Properties of Porphyrins

Porphyrins are intensively coloured compounds which show a characteristic absorption pattern: The very intense Soret-band (or B-band) can be found in the near UV region and the less intense Q-bands in the visible part of the spectrum. **Figure 1.13** exemplarily shows the UV/vis absorption spectra of a) the *meso*-tetraphenylporphyrin (H_2TPP) and b) the *meso*-tetraphenylporphyrinato zinc(II) ($Zn(TPP)$) complex in chloroform.

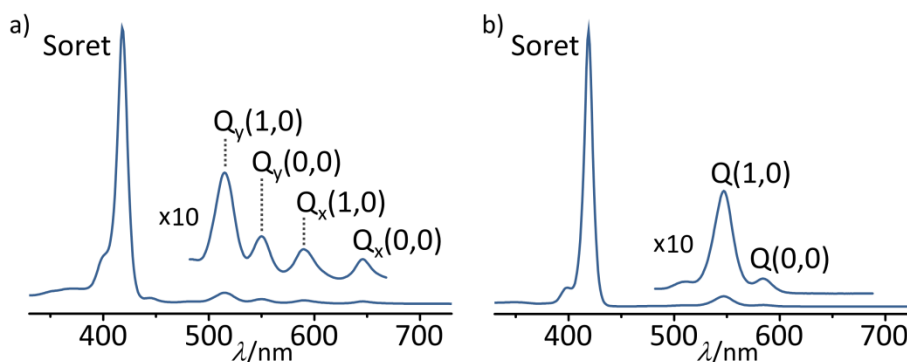


Figure 1.13 UV/vis absorption spectra of a) *meso*-tetraphenylporphyrin and b) *meso*-tetraphenylporphyrinato zinc(II) in chloroform.

The unique shape of the (metallo-) porphyrins' absorption spectra can be explained by the Four Orbital Model developed by Gouterman.^[134–137] In this model, the observed absorptions are attributed to π, π^* transitions between the porphyrins two highest occupied molecular orbitals (HOMO and HOMO-1) and the two lowest unoccupied molecular orbitals (LUMO and LUMO+1). The shape of the respective molecular orbitals is illustrated in **Figure 1.14a**. In a D_{4h} local point symmetry, like for metalloporphyrins, the HOMOs can be labelled as a_{2u} and a_{1u} symmetric while the LUMOs are labelled $e_{g,x}$ and $e_{g,y}$ to distinguish their orientation. Nevertheless, Gouterman introduced the more general notation b_1/b_2 for the HOMOs and c_1/c_2 for the LUMOs, as the aforementioned symmetry labels may not hold in systems with lower symmetry.

For metalloporphyrins with an effective local D_{4h} symmetry the two LUMOs are degenerate by symmetry whereas the two HOMOs are considered to be similar in energy coincidentally as illustrated in **Figure 1.14b**. Two of the possible one-electron excited states, $^1(a_{1u}, e_{g,y})$ and $^1(a_{2u}, e_{g,x})$, have x-polarisation while the other two, $^1(a_{1u}, e_{g,x})$ and $^1(a_{2u}, e_{g,y})$, show y-polarisation. Due to their similar energy and symmetry the x- and y-polarised excited states mix among each other resulting in i) two degenerate high-energy transitions with parallel transition dipoles leading to a high intensity (the Soret band or rather B_x and B_y absorption) and ii) two degenerate low-energy transitions for which the nearly cancellation of the anti-parallel transition dipoles leads to lower intensity (the Q_x and Q_y absorption) as shown in **Figure 1.14c**. Vibronic progression of the Q-band transition often increases the number of the Q-bands observed (see Figure 1.13). The respective oscillation modes are specified by the numbers in parentheses. The first number indicates the vibronic mode of the excited electronic state and the second one of the respective electronic ground state.

Absorption spectra of free-base porphyrins can be explained within the same model if their lower D_{2h} symmetry, compared to the D_{4h} symmetry of the metalloporphyrins, is considered. The two protons in free-base porphyrins are by definition connected to the two nitrogen atoms along the x-axis. This breaks the

degeneracy of c_1 and c_2 , as c_2 is stabilized with respect to c_1 (Figure 1.14d, the absolute as well as relative effect on b_1 and b_2 depends on the respective substituent pattern of the very porphyrin). This leads to a splitting of the Q_x and Q_y as well as the B_x and B_y absorptions. Along with the vibronic progression, this leads to the four Q-bands as seen in Figure 1.13b for H_2TPP . The predicted energetic difference of B_x and B_y is normally not resolved. However, there is an example for porphin in which the splitting could be observed at very low temperatures.^[138]

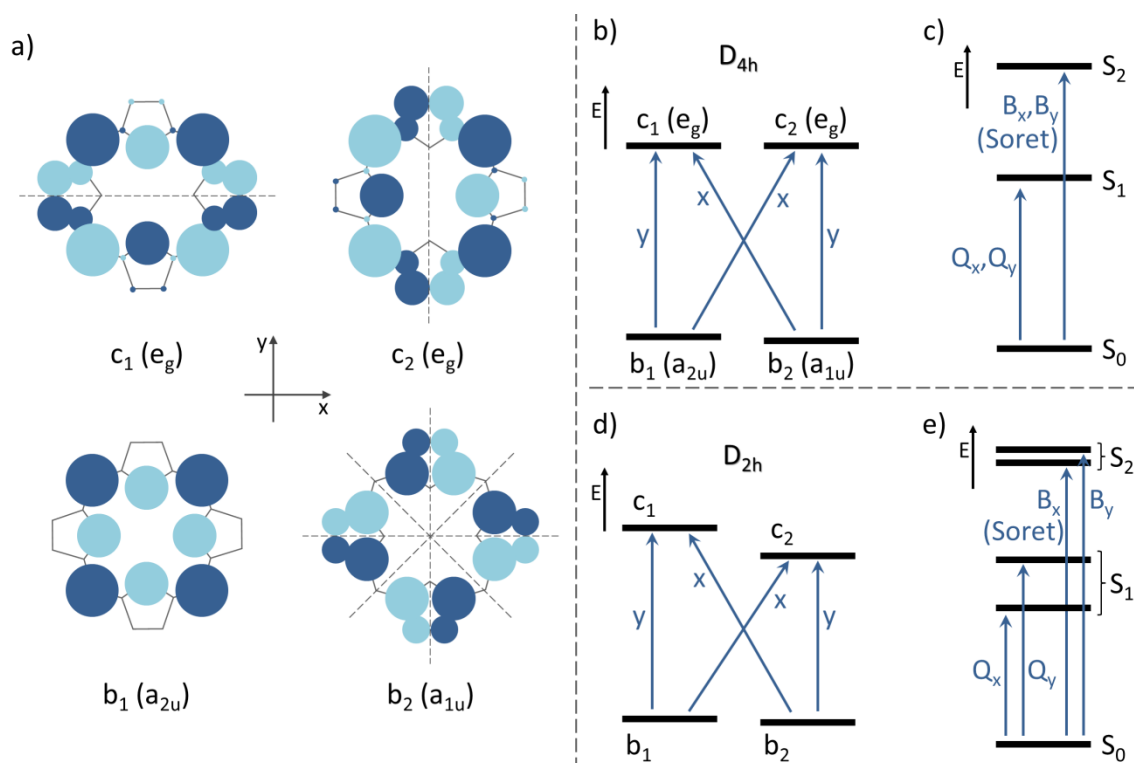


Figure 1.14 a) Schematic representation of the molecular frontier orbitals of porphin; top: LUMO and LUMO+1; bottom: HOMO and HOMO-1; b) to d) Simplified Gouterman's four orbital model: b) relative orbital energies and c) possible electronic transitions in metalloporphyrins; d) relative orbital energies and e) possible electronic transitions in free-base porphyrins.

1.3.3 Tuning of Porphyrin Absorption Spectra

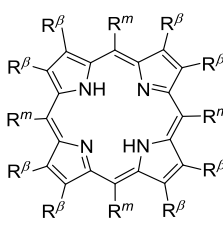
Substituents in β - and *meso*-Positions

The introduction of *meso*-substituents to the porphyrin structure leads to bathochromic shifts of the Q as well as Soret band absorptions. Similar shifts are observed for aliphatic or aromatic substituents.

For instance, the Soret band absorption of porphin ($\lambda_{\text{Soret}} = 394$ nm) is shifted to 420 nm in *meso*-tetramethylporphyrin and to 419 nm in *meso*-tetraphenylporphyrin (H_2TPP). The bathochromic shifts of the Q-bands range from 34 to 48 nm and from 26 to 35 nm in the case of methyl or phenyl groups, respectively (see Table 1.1). Electron

donating groups at the *meso*-arylsubstituents enhance the bathochromic shift while electron withdrawing groups diminish it. However, the general effect on the absorptions is quite small. For instance, *meso*-tetra(*p*-methoxyphenyl)porphyrin shows a Soret band absorption at 423 nm in contrast to *meso*-tetra(*p*-pentafluorophenyl)porphyrin with its Soret band at 417 nm (see **Table 1.1** for Q-bands). The influence of several *meso* aryl substituents with different electron donating power has been studied in more detail by Heinze *et al.*^[139,140] The generally small effects can be explained by the fact that the *meso*-arylsubstituents are orientated perpendicular to the macrocycle of planar porphyrins and electronic communication is reduced thereby. An extension of the porphyrins' aromatic system to the *meso*-arylsystems is not observed which may also account for the aforementioned similar effect of methyl and phenyl substitution.

Table 1.1 Electronic absorption data for different porphyrins in chloroform.

	Substituents		Absorption Bands ^a [nm]				
	R ^m	R ^β	Soret	Q _y (1,0)	Q _y (0,0)	Q _x (1,0)	Q _x (0,0)
	H	H	394	490	515	562	615
	Me	H	420	524	560	610	664
	Ph	H	419	516	550	590	648
	<i>p</i> -Ph(OMe)	H	423	520	557	595	651
	F ₅ Ph	H	414	507	538	583	657
	H	Me	400	500	535	568	620
	Ph	Me	454	553	sh ^b	602	694
	<i>tert</i> -butyl	H	446 ^c	552 ^c	596 ^c	628 ^c	692 ^c

[a] if not stated otherwise all data from reference [121]; [b] shoulder; [c] data taken from reference[141].

Introduction of methyl groups to the β -positions of the porphyrin has a minor effect compared to *meso*-substitution. The Soret band in β -octamethylporphyrin is *e.g.* only shifted bathochromically to 400 nm compared to porphyrin while the shift of the Q-bands range between 5 and 20 nm (**Table 1.1**). This difference to *meso*-substitution can be ascribed to the overall smaller orbital coefficients at the β -positions of the HOMOs and LUMOs as compared to the *meso*-positions (see Figure 1.14). However, if β -substitution is combined with *meso*-substitution, bathochromic shifts are observed which exceed the ones observed for single β -substitution or *meso*-substitution by far. In β -octamethyl-*meso*-tetraphenylporphyrin the Soret band is shifted to 454 nm and the Q-bands between 40 and 79 nm compared to porphyrin (Table 1.1). But these remarkable shifts are rather connected steric effects rather than electronic effects and will be discussed in detail in the next paragraph.

Distortion Effects

Due to the delocalisation of the π -electrons, the porphyrin macrocycle shows a planar structure. The planarity of the porphyrin core is also preserved for common

substitution patterns like *meso*-substitution (see **Figure 1.15a**). However, strong distortions can occur under certain circumstances. The most convenient way to describe out-of-plane distortions of the porphyrin macrocycle is the normal-coordinate structural decomposition (NSD) method established by Shelnutt *et al.*^[142,143] In a NSD analysis, the observed deformation of a porphyrin is described by a linear combination of the macrocycle's lowest frequency vibrational deformations as shown in **Figure 1.16**.

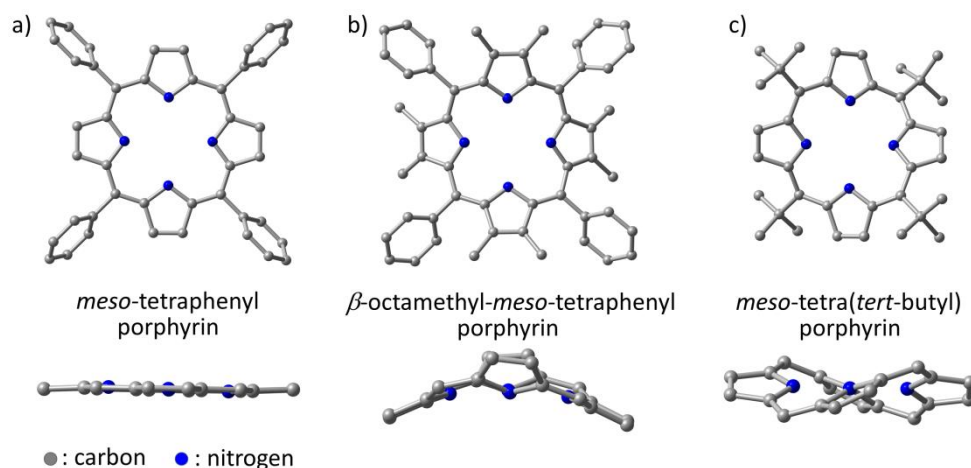


Figure 1.15 Illustrations of the porphyrin macrocycles' distortion of a) *meso*-tetraphenylporphyrin, b) β -octamethyl-*meso*-tetraphenylporphyrin and c) *meso*-tetra(*tert*-butyl)porphyrin; top shows the view along the z-axis (hydrogen atoms have been omitted for clarity); bottom shows the 24 atoms macrocycle (view along the x-axis); all coordinates have been derived from DFT calculations (b3lyp/LANL2DZ, iefpcm for CH_2Cl_2).

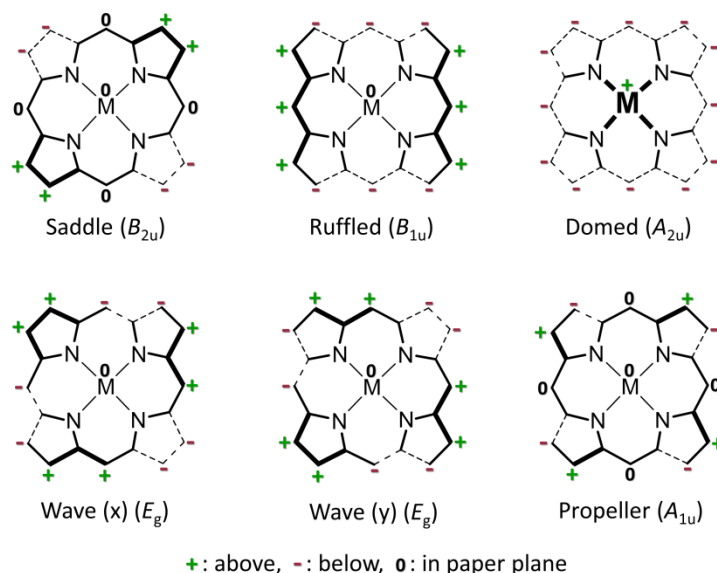


Figure 1.16 Illustration of the normal-coordinate decomposition modes used to describe the actual distortions of porphyrins' macrocycles; they are named by their trivial names as well as their respective symmetry; bold bonds above, dashed bonds below the paper plane.

A computational analysis of crystallographic or calculated structural data is possible by a special free NSD software.^[144]

The absorption spectra of porphyrins are commonly shifted bathochromically by the distortion of the macrocycle. This is attributed to the hybrid orbital deformation (HOD) effect, which minimises the energy gap between the occupied b_1/b_2 (HOMO) and the unoccupied c_1/c_2 (LUMO) orbitals.^[145–147] However, the magnitude of the redshift is not linearly correlated to the degree of distortion as measured by NSD analysis.^[146,148] Non-planar deformations in the B_{1u} symmetric ruffling mode or the B_{2u} symmetric saddling mode showed the strongest impact on the absorption spectra.^[146,149]

There are different ways to effect the distortion of the porphyrin macrocycle. One approach is the covalent *ring fusion* of the porphyrin's β -position with the *meso*-substituent, e.g. by a carbonyl bridge as in **J** (see **Figure 1.17**).^[150] Accordingly, distortion of the macrocycle may also be induced by the covalent connection of two adjacent or opposite *meso*-substituents by "short" bridges as exemplarily shown in the porphyrin **K** (Figure 1.17). The resulting stress in these *strapped porphyrins* is reduced by the distortion of the porphyrin ring.^[145,149]

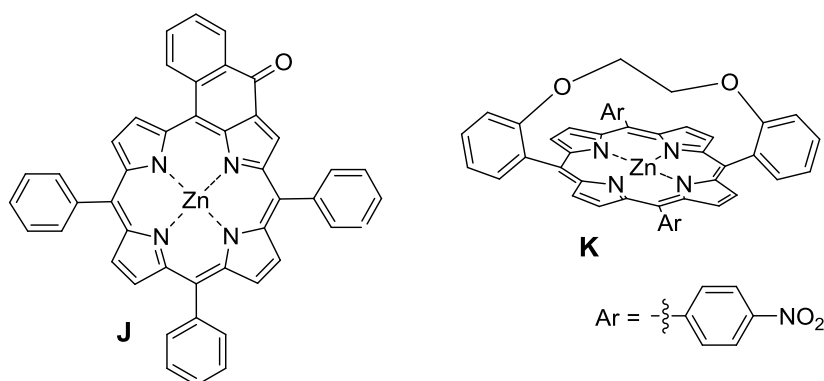


Figure 2.17 Examples for covalent ring fusion (**J**)^[150] and strapped porphyrins (**K**).^[145]

Another approach to induce distortions of the porphyrins' macrocycle is the so-called *over-crowding*. This term describes the introduction of moderately bulky groups at the β - and *meso*-position of the porphyrin or very bulky substituents in either the β - or *meso*-position. Their steric repulsion with the macrocycle or among each other consequently leads to the observed non-planar deformations. One example is the β -octamethyl-*meso*-tetraphenylporphyrin as described above. **Figure 1.15b** illustrates the deformation of its porphyrin core compared to the planar structure of tetraphenylporphyrin (Figure 1.15a). A similar distortion can be observed for porphyrins bearing very bulky groups only in the *meso*-positions. This is exemplified by the distortions of *meso*-tetra(*tert*-butyl)porphyrin as shown in **Figure 1.15c**. In this porphyrin the Soret band is shifted bathochromically to 446 nm and the Q-bands by 62 to 81 nm compared to porphyrin (see. **Table 1.1**).

Porphyrin distortion can also be induced by ligand coordination to the metal centre of metalloporphyrins. In complexes with zinc(II) porphyrins, for example, the zinc ion is displaced out of the porphyrin plane by around 0.3 Å towards the fifth ligand which is accompanied by a domed distortion of the porphyrin core.^[124] Besides the electronic effects determined by the Lewis-acidity of the ligand, this also contributes to the generally observed red shift of the zinc(II) porphyrins' UV/vis absorption upon coordination of neutral or anionic ligands.^[151–153] This ligand-induced distortion effect has further been studied on chromium(III) octaphenylporphyrins of the general formula $[\text{Cr}^{\text{III}}(\text{OPP})\text{L}_2]^+$.^[154] Upon changing the axial ligands from piperidine to pyridine, a bathochromic shift of the Soret band from 469 to 483 nm is observed. This could be attributed to the more pronounced non-planar deformation of the porphyrin core in $[\text{Cr}^{\text{III}}(\text{OPP})(\text{pyridine})_2]^+$ as compared to $[\text{Cr}^{\text{III}}(\text{OPP})(\text{piperidine})_2]^+$ (**Figure 2.18**). The different electronic effects of the two ligands do have only minor effects in this system.

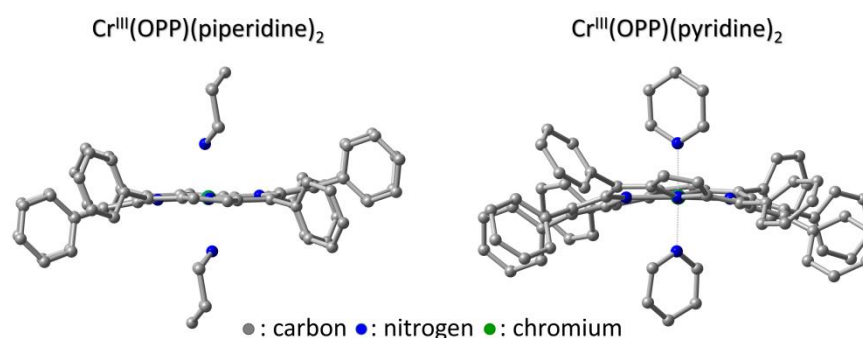


Figure 2.18 Solid state structures^[154] of $[\text{Cr}^{\text{III}}(\text{OPP})(\text{piperidine})_2]^+$ and $[\text{Cr}^{\text{III}}(\text{OPP})(\text{pyridine})_2]^+$; hydrogen atoms as well as co-crystallised counter ions and solvent molecules have been omitted for clarity.

The correlation between porphyrin distortion and bathochromic absorption shifts as described above can be exploited for the development of colorimetric (amine-) sensors. A purposive steric interaction of the analyte with the porphyrin sensor may lead to an increased distortion of the porphyrin core and consequently an enhanced colour shift which may become easily visible by the human eye. Based on this concept novel amine sensors which will be described in Section 3.4 have been developed.

Effects of Metal Complexation

The formation of metalloporphyrins from their free-base equivalents most obviously leads to an increase of the local point symmetry of the porphyrin macrocycle from D_{2h} to D_{4h} . The resulting effect on the absorption spectra with the decrease of the number of Q-bands for *e.g.* ZnTPP compared to H_2TPP has been discussed in Section 1.3.2.. However, there are further effects depending on the population and relative energy of the d-orbitals of the respective metal within the macrocycle.

Metalloporphyrins with metals having d^0 or d^{10} configuration show so called *normal* UV/vis spectra. In these cases there is only a slight interaction of the metals'

empty (d^0) or filled (d^{10}) orbitals with the porphyrins' a_{2u} and e_g orbitals. There is no interaction with the a_{1u} orbital as it has nodes at the coordinating nitrogen atoms (see Figure 1.14). The absorptions of such metalloporphyrins is dominated by the π, π^* transitions within the macrocycle as described by Gouterman's Four Orbital Model (Section 1.3.2). They show the intense Soret band in the range of 320 to 450 nm and Q-bands within 570 to 700 nm.^[155]

The so called *hypso* spectra look similar to the *normal* spectra, but show Q-bands with $\lambda < 570$ nm.^[155,156] These spectra are observed for metals with d^6 to d^9 configuration and are prominent for Rh^{II} , Ni^{II} , Pd^{II} or Pt^{II} porphyrins. The hypsochromic shift of the Q-bands is attributed to an interaction of the filled $e_g(d_{xz}, d_{yz})$ metal orbitals with the e_g LUMOs of the porphyrin macrocycle. This interaction, which may be described as a metal-to-ligand π -back-bonding, raises the energy of the porphyrin LUMOs and thereby the energy of the π, π^* transitions.

In addition to the π, π^* transitions described by the Four Orbital Model, porphyrins of the *hyper* type show prominent charge transfer absorptions in the near UV/vis region. In p-type *hyper* porphyrins additional absorption bands arise from metal-to-ligand charge transfer transitions (MLCT) from a metal centred $a_{2u}(p_z)$ orbital to the e_g LUMOs of the porphyrin.^[155-157] These transitions are commonly observed for complexes with main group elements in low oxidation states like Sn^{II} , Pb^{II} , As^{III} or Sb^{III} . D-type *hyper* porphyrins are found with d^1 to d^6 transition metals with vacancies in the metal centred $e_g(d_{xz}, d_{yz})$ orbitals and low reduction potentials like *e.g.* Fe^{III} , Mn^{III} or Cr^{III} . Here a ligand-to-metal charge transfer transition (LMCT) can be observed from the a_{1u} and a_{2u} HOMOs of the porphyrin to the $e_g(d_{xz}, d_{yz})$ of the respective metal. **Figure 1.19** exemplarily shows the UV/vis absorption spectrum of $Cr^{III}(TPP)(Cl)(H_2O)$ in dichloromethane along with the respective band assignment and a schematic energy diagram of the orbitals involved.^[155,158]

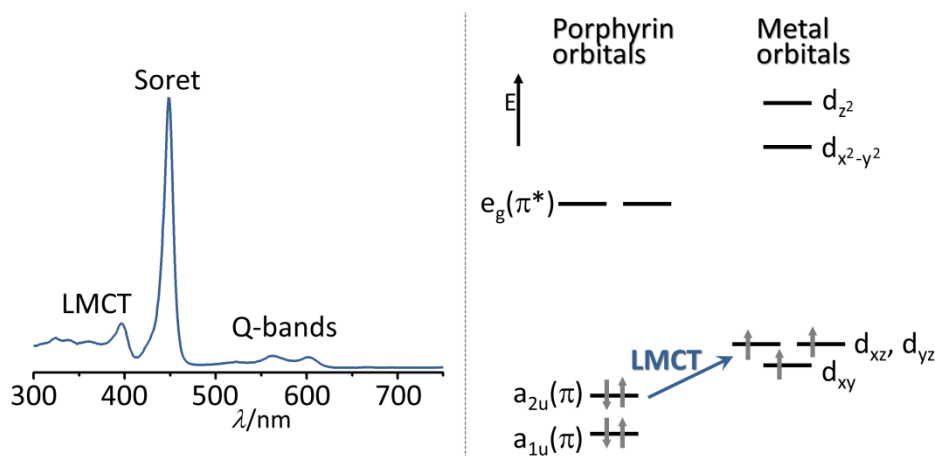


Figure 1.19 Left: UV/vis absorption spectra of $Cr^{III}(TPP)(Cl)(H_2O)$ in CH_2Cl_2 with the respective band assignments; right: LMCT transition illustrated in a schematic energy diagram showing the HOMO/LUMO orbitals of TPP^{2-} and Cr^{III} .

Effects of Ligand Coordination or Substitution

The UV/vis spectra of metalloporphyrins are also affected by the coordination or substitution of axial ligands. Zinc porphyrins generally show a bathochromic shift upon the coordination of a fifth ligand. This is on the one hand attributed to the induced doming distortion as described above. On the other hand the degree of the red shift depends on the Lewis acidity of the fifth ligand. The more electron density is transferred to the zinc centre, the more the porphyrin HOMOs are in turn lifted energetically relative to the LUMOs – and the more pronounced becomes the induced bathochromic shift.^[151,152] A similar trend can *e.g.* be observed for chromium(III) porphyrins.^[158–160] It should be noted here that axial ligand exchange in chromium(III) porphyrins is generally up to 10^4 times faster as compared to other chromium(III) complexes.^[161,162] In case there are no sterical restrictions, the trend for the affinity of the Cr^{III}(porphyrin)(Cl) fragment towards different donor atoms follows the order $N \gg P > O \approx S$.^[124,159]

1.4 Porphyrins in Sensing Applications

As described in the previous section, metalloporphyrins have several properties which enable their use for the development of specific optical sensing systems. First of all, porphyrins show strong absorptions in the UV/vis region which are changed by the coordination of the analyte and thereby indicate their detection. Different metal centres may be used, which brings selectivity for particular functional groups in terms of the Pearson acid base concept. Furthermore, the porphyrins' periphery may be designed to improve the selectivity for special functional groups and moreover to create shape-selective sensors.

Two porphyrin-based sensor arrays developed by Suslick *et al.* emphasise the power and versatility of adjustable porphyrins for optical sensing. In a first trial, the sensor array has been composed of ten different metallo tetraphenylporphyrins along with the free-base tetraphenylporphyrin (see **Figure 1.20a**).^[163] Spots of the respective porphyrins were immobilised on reversed-phase silica plates and then exposed to different gaseous analytes. Images of the sensor array have been taken by a flatbed scanner before and after the exposure. The obtained colour change profiles for ethanol, tri-*n*-butylphosphine ($P(C_4H_9)_3$), *n*-hexylamine and dichloromethane (CH_2Cl_2) are exemplarily shown in **Figure 1.20b**. The different analytes can be readily distinguished by their unique difference colour patterns which results from their specific interactions with the different metalloporphyrins.

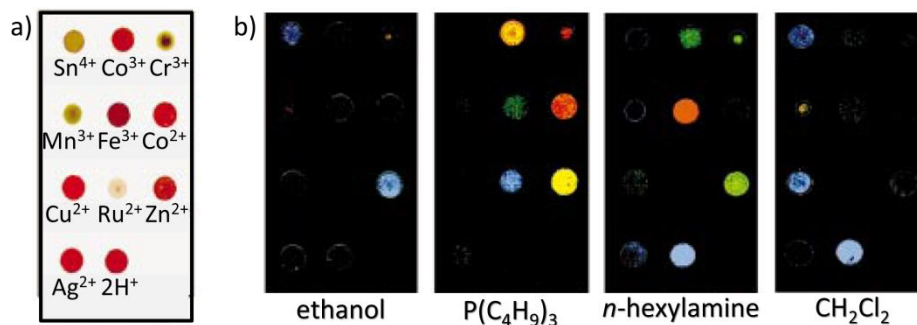


Figure 1.20 a) Sensor array from different metallo tetraphenylporphyrins immobilised on reversed-phase silica plate; b) difference color images of the sensor array before and after exposure to the respective gaseous analytes.^[163]

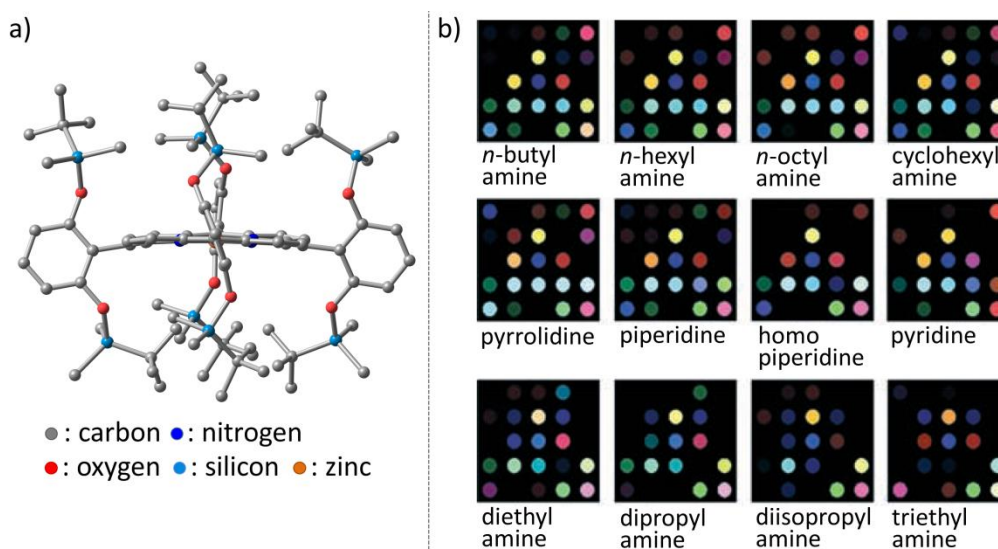


Figure 1.21 a) Solid state structure^[166] of the bis-pocket porphyrin 5,10,15,20-tetrakis(2,6-bis(dimethyl(*tert*-butyl)siloxy)phenyl)porphyrinato zinc(II), hydrogen atoms are omitted for clarity; b) colour difference maps of the sensor array form reference [165] for a family of 12 amines; maps are generated from the absolute values of the differences of the red, green and blue values before and after exposure to the respective amine.

An improved sensor array has been created by immobilisation of different metalloporphyrins on reversed-phase silica along with solvatochromic dyes and pH indicators.^[164,165] Further selectivity was achieved by the additional use of so-called bis-pocket porphyrins as for example the 5,10,15,20-tetrakis(2,6-bis(dimethyl(*tert*-butyl)siloxy)phenyl)porphyrinato zinc(II) as shown in **Figure 1.21a**.^[166] The steric interaction with the bis-pocket porphyrins' substituents helps to further differentiate the analytes by shape and size. **Figure 1.21b** shows the digitalised colour-difference maps of this sensor array upon exposure to 12 different amines. It can be seen that through the interplay of the 24 sensors used even similar analytes from one compound class (here: amines) can be distinguished.^[165]

1.4.1 Porphyrin Based Gas Sensing Layers

The formation of porphyrin based and porphyrin containing layers has been extensively studied with respect to manifold applications like dye-sensitized solar cells^[167–173] or photonic and electronic devices.^[174–180] Moreover, they are widely used for the formation of gas-sensing layers for a broad range of analytes: explosives,^[181,182] NO₂,^[183–185] Cl₂,^[186] volatile organic compounds (VOC) in general^[163,187–190] or alcohol vapours^[59,60,191] and volatile amines in particular.^[165,192–195]

Different deposition techniques to create porphyrin based or containing layers on supporting substrates have been employed for sensing applications. In the following they will be introduced with the help of selected examples.

Porphyrin based layers

The principle of the *Langmuir-Blodgett deposition* technique is illustrated in **Figure 1.22a**. In a first step, a solution of a hydrophobic chromophore in an appropriate organic solvent is carefully dripped onto a water surface. After evaporation of the organic solvent, a mono-layer of the chromophore is formed on the water surface. When a lipophilic substrate is moved perpendicular through this layer, the chromophore molecules settle on its surface. The moveable barriers of the set-up make sure that the internal pressure within the layer on the water stays constant as material is removed by the substrate. By repeating the dipping process, layer-by-layer architectures can be built on the substrate.^[196] Richardson *et al.* used the Langmuir-Blodgett technique to deposit layers of the free-base porphyrin **L**, which is functionalized with lipophilic alkyl chains (**Figure 1.22b**), onto hydrophobically treated glass slides.^[197] After three dipping cycles nominally 6 mono-layers of the porphyrin have formed on the glass slide. As the glass slides were analysed by UV/vis spectrometry, the Soret band absorption of the porphyrin could be detected at 432 nm. Exposure of the porphyrin-coated substrates to NO₂ vapours resulted in a decrease of the Soret band absorption and an increase of the absorption at 465 nm. This could be used to colorimetrically detect NO₂ concentrations down to 0.88 ppm in the gas phase.

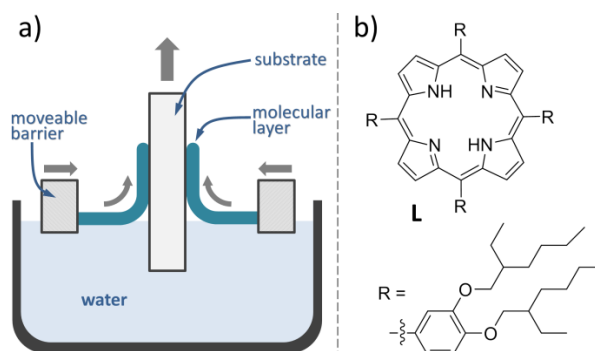


Figure 1.22 a) Schematic illustration of the Langmuir-Blodgett deposition technique; b) molecular structure of **L**.

For the preparation of thin films via the *spin-coating* technique a small amount of dissolved coating material is applied on the centre of the substrate which is subsequently rotated at high speed. Due to the centrifugal force a thin liquid film is formed on the substrate whereby the thickness is determined by the solutions' viscosity and the time and speed of the rotation. Evaporation of the solvent, which may be supported by heating of the substrate, leads to the hardening of the thin film. Spadavecchia *et al.* used this technique to form thin ZnTPP layers on quartz glass.^[194] Therefore, a solution of ZnTPP in chloroform was applied to the substrate turned at 2000 rounds per minute for 30s. Evaporation of the solvent resulted in 100 nm thick coloured films which showed broadened and slightly red-shifted UV/vis spectra as compared to the ZnTPP's absorption in solution. Absorbance changes of the film upon exposure to 4-aminophenol vapours could be used for quantitative detection between 5 and 40 ppb.

The schematic setup for the *vacuum evaporation* deposition technique is shown in **Figure 1.23a**. The solid material to be deposited is placed into a heatable melting crucible within a vacuum chamber. The substrate to be coated is placed opposite to the aperture of the crucible. After the chamber has been evacuated, the source material is heated until it evaporates to the chamber. Due to the relatively low temperature of the substrate, the vaporised material condenses onto its surface forming thin layers. By this technique very pure layers can be obtained as pure source material may be used without any solvent. Tonezzer *et al.* used this technique to coat quartz glass with thin H₂TPP, CoTPP or FeTPP(Cl) layers.^[60] Therefore the melting crucible containing the respective porphyrin has been heated to 300 °C and the pressure within the chamber was set to 10⁻⁴ Pa.

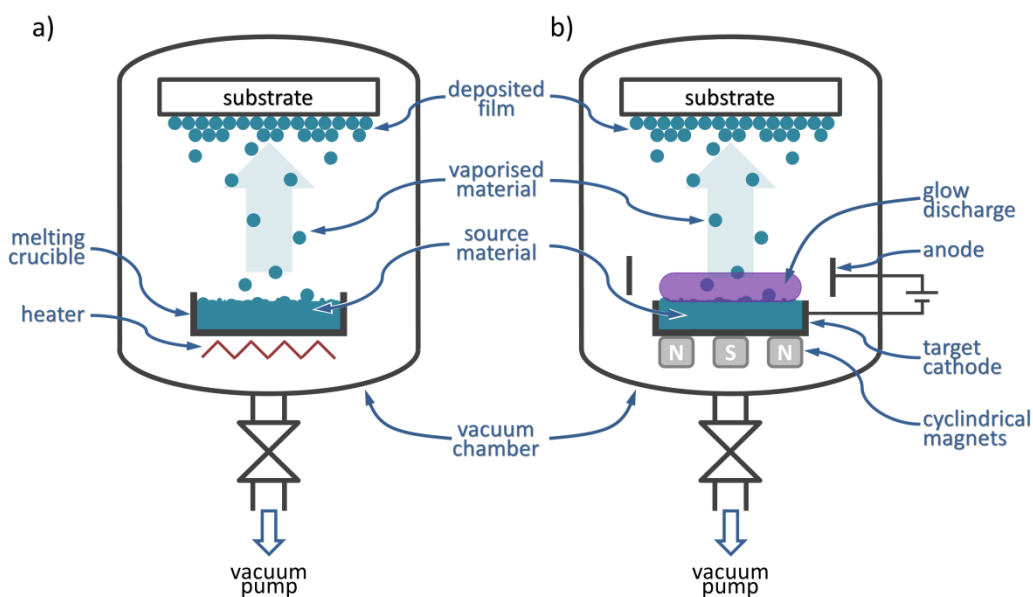


Figure 1.23 Schematic illustrations of the setup for the a) *vacuum evaporation* and b) *glow discharge induced sublimation* deposition techniques.

The coated substrates showed the characteristic absorption spectra of the respective porphyrins. However, the absorption bands are significantly broadened due to aggregation of the porphyrins. The H₂TPP based layer *e.g.* showed the Soret band at 434 nm and the Q-bands in the range of 522 to 653 nm. The layers' absorption changes upon exposure to alcohol vapours could be used to monitor the concentrations of methanol, ethanol and *iso*-propanol in the range from 500 to 8000 ppm.

A similar technique to the aforementioned vacuum evaporation is the *glow-discharge-induced sublimation* (GDS) technique. In GDS the layers are also deposited onto the substrate from solid source materials vaporised into a vacuum chamber. In contrast to the vacuum evaporation technique, the source material is not thermally heated but treated with a low energy glow discharge using helium as the feed gas. Interaction of the weakly ionized helium gas with the solid source material facilitates its sublimation. The schematic setup of the process, which is based on conventional radio frequency magnetron sputtering equipment,^[198] is shown in **Figure 1.23b**. The successful application of GDS for the deposition of CoTPP coatings onto quartz glass substrates has been shown by Tonezzer *et al.*^[183] The formed layers show the characteristic Soret band absorption at 447 nm and the integrity of the CoTPP molecules after the deposition has been further proven by mass spectrometry. The layers have successfully been used for the colorimetric detection of NO₂ vapours down to 0.81 ppm. The improvement of the sensitivity towards NO₂ compared to CoTPP based sensing layers deposited by spin coating (42 ppm) or vacuum evaporation (7.2 ppm) has been attributed to the increased roughness and porosity of the coatings formed via GDS.^[183]

Both processes, vacuum evaporation and GDS, belong to the class of Physical Vapour Deposition (PVD) techniques. Common to all PVDs is the deposition of films (or particles) from atomic or molecular gases without any chemical reaction taking place before, during or after the evaporation of the source material.

Porphyrin containing layers

The porphyrin *based* sensing layers described above are all solely based on the chromophores and built up by non-covalent interactions of the respective porphyrins with the substrate and among each other. However, to increase the thermal and mechanical stability of the devices it is convenient to incorporate the porphyrins into a proper matrix. The matrix should be adherent to the substrate and tightly incorporate the sensing chromophores. Moreover, to increase the sensitivity of the device, the matrix may prevent the chromophores from aggregation and facilitate the interaction with the analyte molecules by a porous structure.^[181,187]

One approach to form porphyrin containing membranes is their co-deposition with *polymers and plasticisers*.^[187,195,199] Therefore a solution of the porphyrin chromophore, the polymer and a plasticiser in an appropriate solvent is cast onto the

substrate and the matrix is hardened by subsequent evaporation of the solvent at room or elevated temperature. For example, Baron *et al.* tested different polymers (polydimethyl siloxane (PDMS), poly(vinyl chloride) (PVC), ethyl cellulose (EC) and nitro cellulose (NC)) along with several plasticisers (diethyl phthalate (DEP), tributyl phosphate (TBP), triethyl phosphate (TEP) and nitrophenyl octyl ether (NPOE)) to form ZnTPP containing membranes for the optical detection of NH₃.^[195] In their studies the best results were obtained using a solution of 25 mg PVC and 50 mg DEP in 375 mL THF containing 1.0×10^{-5} mol L⁻¹ ZnTPP. This mixture has been cast onto acid-washed glass slides and spread manually using micro-pipetter tips. After evaporation of the solvent at room temperature 20 to 30 µm thick layers had been formed which showed pink colour and the porphyrins' Soret band absorption at 426 nm. The absorbance changes observed upon exposure to NH₃ vapours could be exploited to reversibly detect NH₃ in the range between 45 and 975 ppm in air.

The beneficial influence of the plasticiser on the sensors' performance is made clear by comparison of the response times of ZnTPP containing membranes formed with and without DEP. Generally, the response time indicates the time between the exposure of the sensor to the analyte and the first measurable response given. Pure PVC based coatings showed a response time of 6 min which is reduced to 6 sec using PVC along with DEP as described above.^[195] The better performance is attributed to the formation of a more porous structure with the plasticiser which facilitates the analytes diffusion to the chromophores.

Another approach to incorporate porphyrin chromophores into a suitable matrix is the *sol-gel* technique as briefly illustrated in **Figure 1.24**. It starts with the dissolution of a matrix precursor, *e.g.* of the widely used alkoxy silane class, in an appropriate organic solvent with a controlled amount of water. The acid catalysed hydrolysis and subsequent condensation reaction of the precursor leads to the formation of a polymeric Si-O-Si network (see **Figure 1.24** grey box). Initially, this results in the formation of small polymer particles about 1 to 100 nm in size. The dispersion of these particles is the so-called *sol*. As the polymerisation proceeds, the particles aggregate or even link to each other via new Si-O-Si bonds. This increases the viscosity of the reaction mixture by time and the so-called *gel* is formed. The gel may be transferred onto a substrate by simple casting, dip-coating or spin-coating as described above. This leads to the formation of a thin gel film which hardens upon further polymerisation over time. This curing process may be supported by elevated temperatures or UV light. After evaporation of the solvent at room or elevated temperature a solid polymeric matrix on the substrate is obtained.

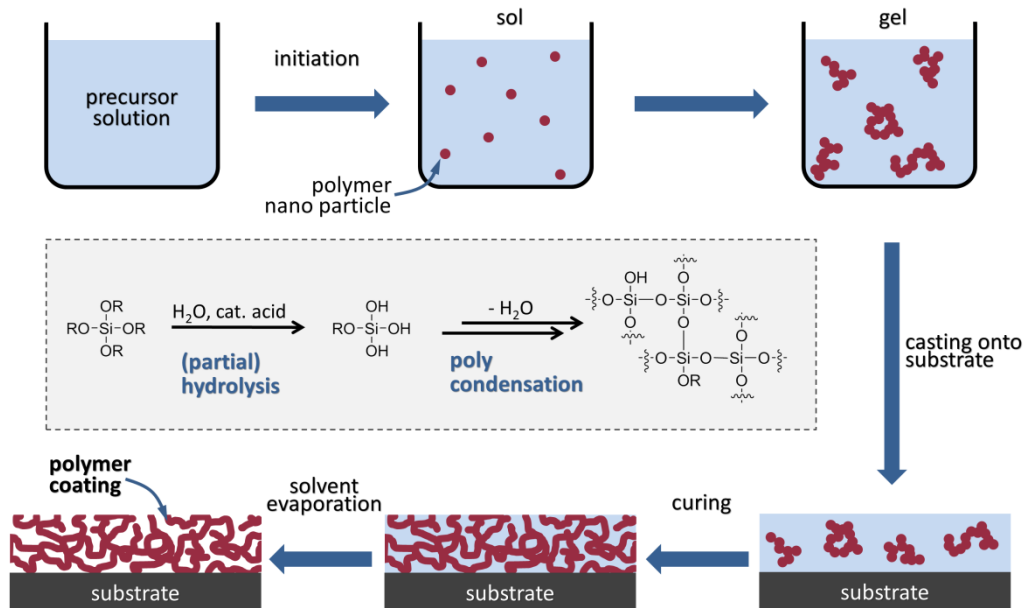


Figure 1.24 Scheme of the subsequent steps to form polymer coatings via the sol-gel process; the central grey box illustrates the reaction steps involved to form the polymeric Si-O-Si network from the widely used alkoxy silanes.

The *sol-gel* approach has been used by Li *et al.* to form meso-porous membranes for the fluorimetric detection of trinitrotoluene (TNT).^[182] The sol was formed from the widely used tetraethoxy silane (TEOS) and the trialkoxy silane functionalised porphyrin **M** (see **Figure 1.25**) in a mixture of ethanol and water under HCl catalysis. The functionalization of the porphyrin leads to a co-condensation with the precursor and therefore a tight covalent incorporation into the formed silica matrix. The gel was transferred onto glass substrates via spin-coating and the formed films have been cured for 6 days at room temperature and further 24 h at 100 °C. Exposure of these 300 nm thick films to 100 ppb of TNT in the gas phase lead to a slight fluorescence quenching of about 10 % after several hours. However, the performance of the sensor layers could be dramatically enhanced by the addition of the surfactant cetyltrimethylammonium bromide (CTAB, **Figure 1.25**) to the solution during the sol-gel process. After curing of the films deposited along with CTAB, the surfactant could be removed by refluxing the silica films with HCl in ethanol. This gives rise to films showing a 3D meso-porous structure in contrast to the amorphous films formed without the CTAB template. Therefore the chromophores within the film are reached more easily by diffusion of the analytes leading to strongly improved sensitivity and response times. The porphyrin-doped nanocomposite layer produced from TEOS and the porphyrin **M** along with the surfactant CTAB showed a fluorescence quenching of 33 % after 10 s and even 90 % after 20 min of exposure to 100 ppb TNT.

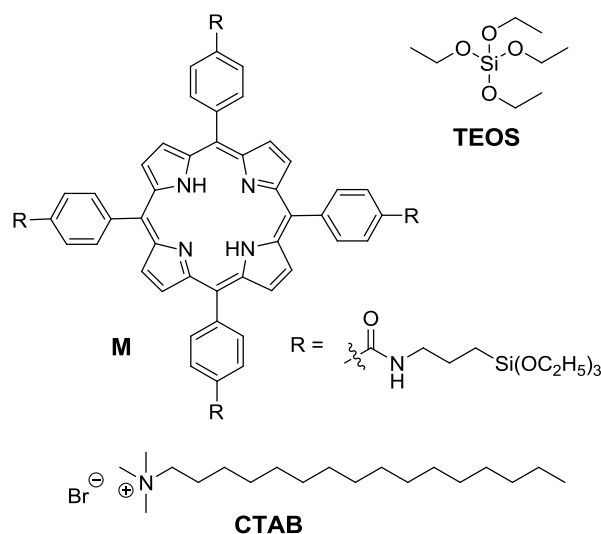


Figure 1.25 Molecular structures of the silica matrix precursor tetraethyl orthosilicate (TEOS), the porphyrin **M** and the surfactant cetyltrimethylammonium bromide (CTAB).

It has to be noted that the successful formation of porphyrin containing polymer films via the sol-gel technique has also been reported with porphyrins lacking trialkoxy silane moieties.^[185,187] The functionalization as described by Li *et al.* is not a prerequisite for this technique.

A new arising technology for the deposition of hybrid polymer layers is the plasma enhanced chemical vapour deposition at atmospheric pressure. This technique is of growing interest due to its versatility, the low environmental impact and the possibilities to integrate it into (existing) mass production lines. The next paragraphs will therefore start with the introduction of atmospheric plasmas in general and show some of their actual applications. With special respect to this work, the main focus will be on dielectric barrier discharges and their use for the deposition of (hybrid) polymer layers.

1.5 Atmospheric Pressure Plasmas

Plasma is called the fourth state of matter which constitutes more than 99% of the universe. Generally, plasmas are composed of a mixture of ions, electrons and neutral species in their fundamental as well as excited states. The plasma in its entity is neutral, but contains highly mobile charge carriers and is thus electrically conductive.

Electrons and ions are formed from the so-called feed or process gas (neutral atoms or molecules) by collision with photons, electrons or other particles with sufficient energy to induce the ionisation. As comprised in **Figure 1.26**, there are different ways to generate plasmas from neutral gases and supply the necessary energy.^[200] Thermal energy, for example, can be produced by exothermal chemical reactions like in flames. Adiabatic compression of gases may also lead to temperatures

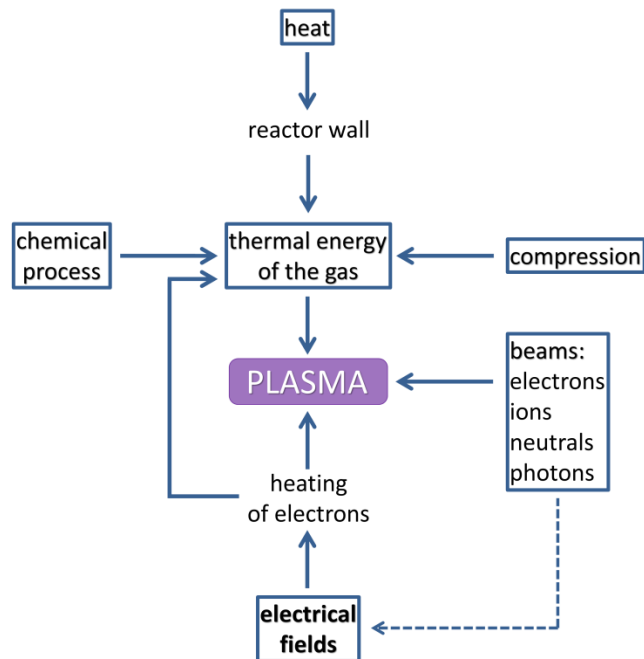


Figure 1.26 Illustration of the different ways to ignite and maintain a plasma.^[200]

sufficient to ignite a plasma. The treatment of a gas with high energy beams of electrons, ions, neutral species or photons from external sources may also lead to plasma generation. The most common way, however, is the use of an external electric field to ignite and maintain the plasma.

The established setups for the formation of plasmas by electrical energy at atmospheric pressure are well summarised in a review article by Tendero *et al.*^[201] The different systems can be classified according to their mode of ignition: i) direct current (DC) or low frequency discharges,^[202–206] ii) radio frequency (RF) discharges^[207–211] and iii) microwave induced plasmas.^[212–215] The microwave systems work electrode-less. In these setups the microwaves are rather guided along the system in a special way to transmit their energy to the plasma gas electrons which in turn induce the ionisation when they reach a sufficient energy level. In the former two classes, the given frequency refers to the alternating voltage between two electrodes in between which the process gas is ionised.

Applications of Atmospheric Plasmas

Generally, atmospheric plasma sources can be tailored for a broad scope of applications by tuning the device structure, the power supply, the process gas, the plasma temperature or the working mode (constant or pulsed). For instance, microwave induced plasmas have been successfully used for gas cleaning applications: a broad range of pollutants like *e.g.* carbon monoxide, chlorofluorocarbons or nitrogen oxides could be decomposed by collisions with energetic plasma species and the subsequent radical reactions.^[216–218] On the other hand, plasmas can also be used for

the systematic synthesis of gases like methanol^[219] or ozone,^[220,221] the latter process being widely used in industry for ozone mass production. A further application of plasmas is the use of arc discharges with DC power supply for welding^[222] or even cutting of metals and alloys.^[223,224] These processes make use of the high and localized temperatures which may be obtained with plasmas. In contrast, pulsed radio frequency plasmas are used for the sterilization and deodorization of heat sensitive PET bottles.^[209]

LTE vs. non-LTE Plasmas

One main factor facilitating the versatile applications of atmospheric plasmas is the possibility to control their gas-temperature from more than 10000 K to less than 300 K by choosing the right setup. Therefore, the different forms of plasmas can be divided into *thermal plasmas* and *cold plasmas* – or LTE and non-LTE plasmas, respectively. LTE means Local Thermodynamic Equilibrium which indicates the physical background for the different observed temperatures.^[201]

In *LTE plasmas* all collisions are balanced by their inverse like excitation with deexcitation and ionisation with recombination. All transitions and chemical reactions need to be governed by collisions and not by radiative processes.^[225] The diffusion time of the particles is similar or higher than the time the particles need to reach the equilibrium. This leads to low local gradients of the plasmas' properties (temperature, density, thermal conductivity). For LTE plasmas high electron densities are needed ($n_e = 10^{21} - 10^{26} \text{ m}^{-3}$). Inelastic collision between the electrons and the heavy gas particles create the plasmas' reactive species (ions, radicals, excited species). Numerous elastic collisions heat the heavy particles and lead to a similar temperature of the two particle classes (electron temperature = $T_e = T_h$ = heavy particle temperature). This can lead to gas temperatures up to 14000 K.^[201]

In *non-LTE plasmas* the electron density is lower than 10^{19} m^{-3} . This results in less elastic collisions with heavy particles and consequently to a lower temperature of the heavy particles ($T_h = 300 - 4000 \text{ K}$). As the electrons do not dissipate all their energy to the heavy particles, their temperature remains high ($T_e = 10000 - 100000 \text{ K}$). Due to the huge mass difference between electrons and the heavy particles, the plasma temperature is determined by T_h . Therefore non-LTE plasmas show plasma temperatures between 300 and 4000 K.^[201] Moreover, radiative deexcitation processes, especially for low-lying excited states, become significant in non-LTE plasmas in contrast to the solely collision mediated processes in LTE plasmas.

One example of low-temperature non-LTE plasmas are dielectric barrier discharges (DBD) which can therefore be used for the treatment of heat-sensitive materials like polymers. As such applications are envisaged in this work, DBD plasmas are introduced in more detail during the next section.

1.5.1 Dielectric Barrier Discharge Plasmas

The basic configurations for dielectric barrier discharges (DBD) are illustrated in **Figure 1.27**. The dielectric may either be connected to one or both flat parallel high voltage electrodes or placed in between them. There are also applications for which annular discharge gaps between cylindrical electrodes are used. Depending on the dielectric material and the plasma gas the discharge gap may vary from 0.1 mm to a few cm. The dielectric material may generally be glass, ceramic or polymer layers. As a consequence of the dielectrics' insulating properties, DC currents cannot pass the setup. Therefore alternating voltages with frequencies in the range of 50 Hz to 10 MHz are used to ignite DBD plasmas.^[226]

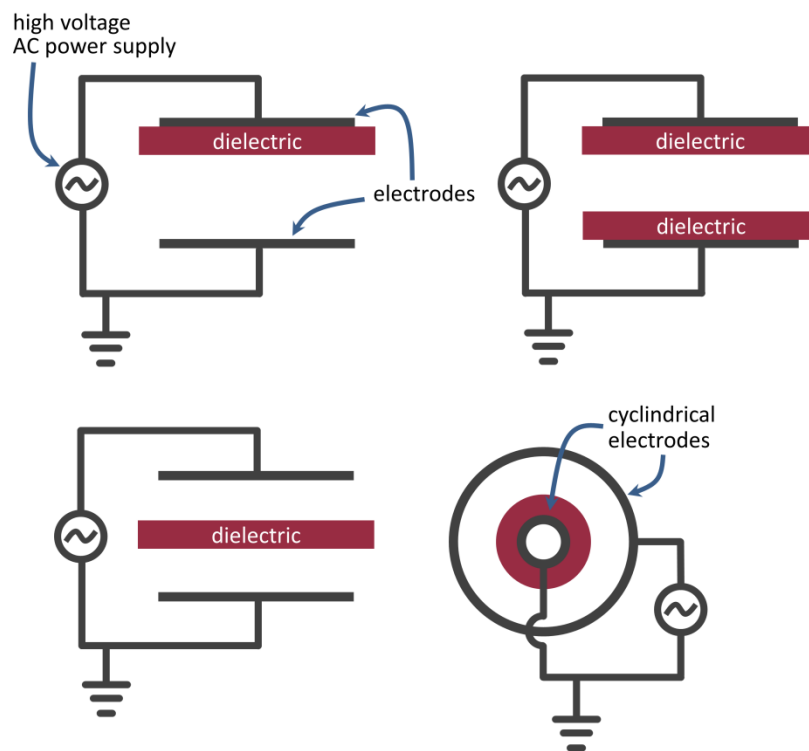


Figure 1.27 Illustration of the basic setups for dielectric barrier discharges.

When the electric field in the discharge gap becomes larger than the breakdown field, numerous small microdischarges are ignited between the electrodes, as illustrated by the sketch in **Figure 1.28a**. The voltage needed for ignition range from a few hundred V to several kV depending on the discharge gap, the plasma gas and the dielectric used. When charges accumulate at the electrodes as a result of an external voltage, initially local surface discharges are ignited from which cylindrical plasma channels are formed.^[227–229] As these conductive microdischarges connect the anode and cathode, charge migration reduces the local field below the breakdown field and the respective microdischarge is choked.^[226] Therefore the life-times of the filaments are in the dimension of a few nanoseconds.^[227] As long as the external voltage keeps rising, subsequent microdischarges will form, because the local field is only reduced in the

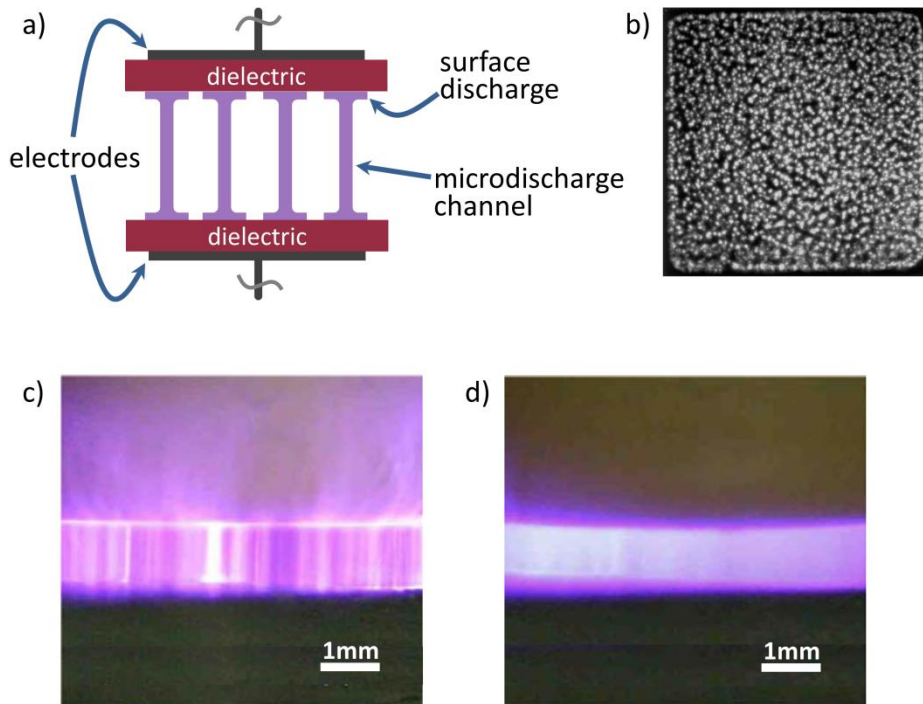


Figure 1.28 a) Illustration of the microdischarge channels formed in DBDs; b) top view photograph of a DBD through a transparent electrode with 20 ms exposure time,^[226] side view photograph of c) μ s and d) ns pulsed DBDs in air.^[231]

very area of the filaments' surface discharges. A typical value is about 10^6 microdischarges per cm^2 per second.^[230] In average, this results in an even lateral distribution of the filaments across the electrodes' surface. The photograph in **Figure 2.18b** shows the top view through a transparent DBD electrode in which the light spots represent the individual discharges.

The photograph in **Figure 1.28c** shows the side view of a DBD fed with air.^[231] The microdischarge filaments can be observed as light stripes in the violet plasma zone. A similar setup is used for the DBD shown in **Figure 1.28d**, but single filaments can hardly be identified in this plasma. The only difference between the two experiments is the pulse duration of the voltage.^[231] In the example in Figure 1.28c the voltage is pulsed in the μ s range while the pulses are shortened to ns for the example in Figure 1.28d. This exemplifies how the use of a chopped energy supply can be used to obtain diffuse and smooth discharges.

The homogeneity of DBD discharges is also influenced by the type of the process gas used. The radius of the propagating streamers depends on the gas density and the ionisation properties of the gas and is typically roughly around $100 \mu\text{m}$ at atmospheric pressure. The radii of the streamer channels follow the following order: oxygen < carbon dioxide < air < nitrogen < xenon < helium. Diffuse discharges can be obtained when there is sufficient overlap of simultaneously propagating filaments. This condition is met most easily in helium with its relatively wide streamer channels.

In contrast to many low pressure plasmas, the chemistry in atmospheric pressure DBDs is not controlled by charged species. In the majority of DBD applications these species recombine before any chemical reaction can take place. The chemistry in DBD discharges is rather described as free-radical chemistry initiated by excited species, atoms or molecular fragments.^[226] The initial dissociation of the plasma gas has *e.g.* been studied for O₂,^[232–235] N₂^[235–237] and CO₂.^[238,239] For O₂ a high efficiency for the dissociation upon collisions with electrons up to 85% has been observed. With CO₂ the dissociation efficiency is reduced to 40%. When N₂ is used, even less energy of the electrons can be utilized for the dissociation, as most energy is absorbed by the excitation of vibrational levels. However, radical reactions may also be initiated by the collision of molecular monomers with such excited plasma gas species. It has to be noted that the composition of the reactive species within the plasma is controlled by the choice of the plasma gas, the size and shape of the discharge gap, the nature of the dielectric and the pulse mode of the energy source. Scaling up the electrode area or increasing the power density, however, just leads to more microdischarges per unit of time or per unit of electrode area, respectively. But each microdischarge filament has to be treated as an individual plasma reactor.

The rich radical chemistry of DBDs can be used to induce radical polymerisations within the discharge. This may be used to deposit polymer coatings on a variety of substrates when they are brought into the plasma zone along with proper monomers. This plasma enhanced chemical vapour deposition will be discussed more detailed in the next section.

1.5.2 DBD Enhanced Chemical Vapour Deposition

In contrast to PVD processes described in Section 1.4.1, Chemical Vapour Deposition (CVD) involves the dissociation and/or chemical reaction of gaseous reactants in an activated (heat, light, plasma) environment with subsequent formation of a solid product. The deposition involves homogenous reactions in the gas phase and/or heterogeneous reactions on or near the target surface. Different CVD techniques and applications are comprised in a review by Choy.^[240]

DBD enhanced CVD can be used for thin film deposition from a variety of matrix precursors and on manifold substrates.^[201,241] Substrates ranging from aluminium^[242] and borosilicate glass^[243] to heat sensitive compounds like polyethylene terephthalate^[244] and polypropylene.^[245] A widely investigated class of coatings are organosilicon polymer films deposited by DBD enhanced CVD. Some of the precursors used for their deposition are *e.g.* vinyltriethoxysilane (VTEOS), tetraethoxysilane (TEOS), octamethylcyclotetrasiloxane (OMCTS), decamethylcyclopentasiloxane (DMCPS), hexamethyldisiloxane (HMDSO) or hexamethyldisilazane (HMDSN) as summarized in **Figure 1.29a**. The most convenient way to introduce the matrix precursor into the plasma zone is to enrich the plasma gas with such volatile monomers via a bubbling system as illustrated in **Figure 1.29b**.

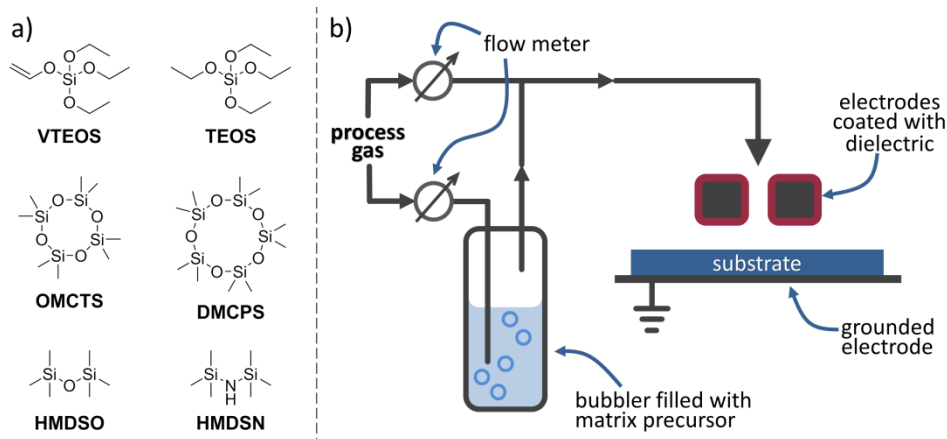


Figure 1.29 a) Chemical structure of precursors for the formation of organosilicon polymers via DBD enhanced CVD; b) convenient setup to introduce volatile matrix precursors into the plasma zone via enrichment of the process gas using a bubbler system.

In contrast to conventional polymers, the plasma polymers formed during DBD enhanced CVD do not consist of chains with regular repetitive units. They rather form irregular three-dimensional cross-linked networks whose composition may vary from “organic” polydimethylsiloxane-like to quasi-inorganic silica films. The (surface) structure and the composition of the deposited film depend on the process gas, the precursor, the substrate temperature as well as the power and frequency of the used voltage.^[242,246–248]

The influence of the sinusoidal voltage frequency on the coatings’ properties is exemplified by an example from Boscher *et al.*^[249] They used HMDSO as the precursor for the deposition of plasma polymerised polydimethylsiloxane (pp-PDMS) on aluminium foils. The goal was to obtain surfaces which show high water contact angles and also large water slipping angles – this means that water forms droplets on the surface, but still sticks to it due to a high adhesive force. This effect is called “Wenzel-Cassie’s state” and can be *e.g.* observed on rose petals.^[250] **Figure 1.30a** shows photographs of a water droplet on the pp-PDMS coated aluminium surface coated with a power frequency of 10 kHz. The contact angle is 106° and the droplet still sticks to the surface at vertical orientation of the aluminium foil. If the power frequency, however, is increased to 22.5 kHz, the contact angle is increased to 155° while the sticky character of the surface is preserved (**Figure 1.30b**). This can be attributed to the different nano structuring of the two surfaces which can be seen by the scanning electron micrographs in **Figure 1.30c** and **d**, respectively. Wettability and the water contact angle are a result of the high retention of hydrophobic methyl groups in the polymer along with the distinct surface’s nano structure as obtained by the different plasma conditions.

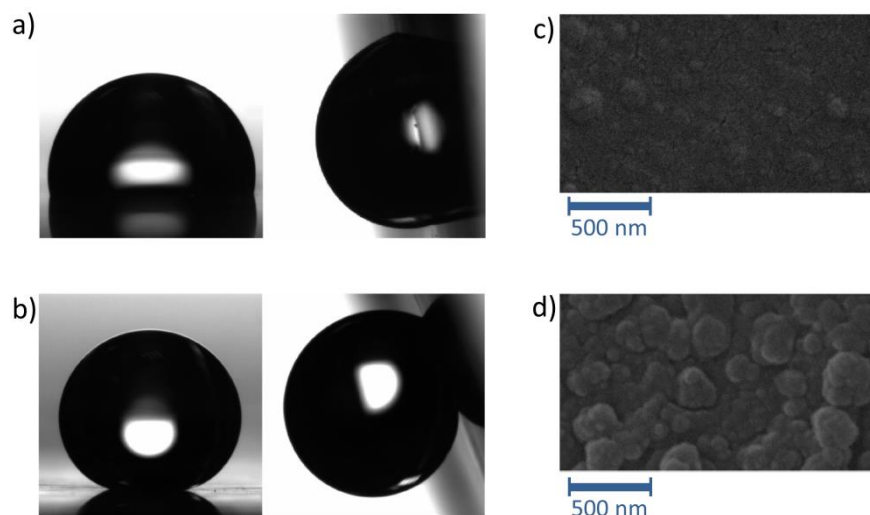


Figure 2.30 Water droplets (3 μL) on pp-HMDSO coated aluminium foils for different plasma frequencies a) 10000 Hz, b) 22500 Hz (left: substrate tilted 0° , right: substrate tilted 90° , respectively); scanning electron micrographs of the substrate coated at c) 10000 Hz, d) 22500 Hz.^[249]

The impact of the plasma gas' mixture on the structure of the polysiloxane network is illustrated by **Table 1.2**. The shown values have been taken from a work dealing with polysiloxane based anti-corrosion layers on aluminium. The table comprises the percentages of the different siloxy units bearing three (*M*), two (*D*), one (*T*) or none (*Q*) methyl group within the polymer matrix (see illustration in **Table 1.2**). Both coatings investigated have been deposited under the same conditions using OMCTS as matrix precursor – the only difference being the composition of the plasma gas. The use of pure nitrogen results in the preservation of several methyl groups within the plasma polymer. This is reflected by the high percentage of *D* and *T* fragments in the polymer. Enrichment of the plasma gas with 20% O_2 induces stronger fragmentation of the OMCTS in the discharge and consequently a more “inorganic” polymer with a higher percentage of SiO_4 (*Q*) fragments.^[251]

Table 1.2 Relative percentages of different siloxy units in pp-OMCTS depending on the plasma gas composition.

gas composition [%]		relative percentage ^a			
N_2	O_2	<i>M</i>	<i>D</i>	<i>T</i>	<i>Q</i>
100	0	0	26	53	21
80	20	0	2	85	80

[a] values taken from reference [251].

Hybrid layers from DBD enhanced CVD

DBD enhanced CVD has also been used to deposit hybrid polymer coatings. For example, Bardon *et al.* deposited pp-PDMS matrices containing cerium-based nano particles for anti-corrosion purposes.^[252] During the deposition process, the AlCeO_3 particles have been sprayed into the plasma zone along with the matrix precursor HMDSO by an atomizer system. The nano particles form small agglomerates within the 300 nm thick polysiloxane layers on galvanized steel. The anti-corrosion performance of the cerium containing hybrid layers is enhanced compared to similar pure pp-PDMS coatings. Furthermore, they show self-healing properties after scratch damaging.

Boscher *et al.* showed the successful incorporation of lanthanide-based luminescent particles into polysiloxane matrices via a nitrogen fed DBD enhanced CVD.^[253] The particles were composed of a coordination polymer of the general formula $[\text{Eu}_{x-2}\text{Tb}_x(1,4\text{-benzene-dicarboxylate})_3(\text{H}_2\text{O})_4]_n$.^[254] They have been sprayed into the plasma zone by an atomizing system from a suspension in the matrix precursor HMDSO. The films formed on aluminium or polypropylene substrates have been 500 nm thick, transparent and colourless. However, upon excitation with UV light the coated substrates showed green colour arising from the embedded nano-particles' luminescence.

The deposition of plasma polymerised coatings containing enzymes has been shown by Paulussen *et al.*^[255] Different enzymes like glucose oxidase, lipase or alkaline phosphatase have been immobilised into matrices formed from acetylene or pyrrole in a helium fed DBD. The enzymes have been transferred into the discharge zone by the use of an atomizing system and the respective aqueous solutions. The formation of a protective water shell around the enzymes in the spray is supposed to protect them from the reactive conditions within the plasma. The incorporation of the enzymes into the matrices on glass slides or PET foils enhanced their thermal stability as well as their tolerance against organic solvents. The preservation of the enzymes' structure and functionality has been shown by catalysis experiments after the plasma deposition process.

In this work, DBD enhanced CVD at atmospheric pressure has been further developed to incorporate tailored porphyrins into porous pp-PDMS matrices. These results will be discussed in the sections 3.1, 3.2, 3.3 and 3.5 along with the coatings performances' in colorimetric amine sensing experiments.

1.6 Epoxidation of Olefins

Mechanistic studies in this work regarding amine sensing with chromium porphyrins revealed a novel path for oxygen activation which may be used in epoxidation reactions. Therefore a brief introduction to the epoxidation of olefins will be given in this section.

Epoxides are valuable building blocks in organic chemistry. Therefore, numerous routes were established for the epoxidation of olefins in the laboratory but also in industrial scale. The vast majority of processes use oxidants like hydroperoxides, peracids, hypochlorite or iodosylbenzol.^[256] The epoxidation with these compounds, however, needs to be catalysed by metal complexes. Epoxidation reactions have been realised with the help of oxido- or peroxidometal complexes.

The schematic reaction pathway for the molybdenum catalysed formation of propylene oxide from propene and alkylhydroperoxides is *e.g.* shown in **Figure 1.31**. The catalytic cycle starts from the alkylperoxido complex **N**. The α -oxygen, which is activated by the coordination to the electron poor Mo^{VI} centre, is attacked by the olefin in a nucleophilic manner (**O**) which results in the subsequent formation of the epoxide and an alkoxido complex (**P**). The catalytic cycle is closed by protolytic cleavage with an alkylhydroperoxide. The metals' oxidation state remains unchanged during the whole process.^[257] No carbon-metal bonds are formed during the process – the olefins are not activated by complexation. Other metals with low oxidation potential and high Lewis acidity in their highest oxidation state like tungsten, vanadium and titanium may also be used in such epoxidation reactions.^[258]

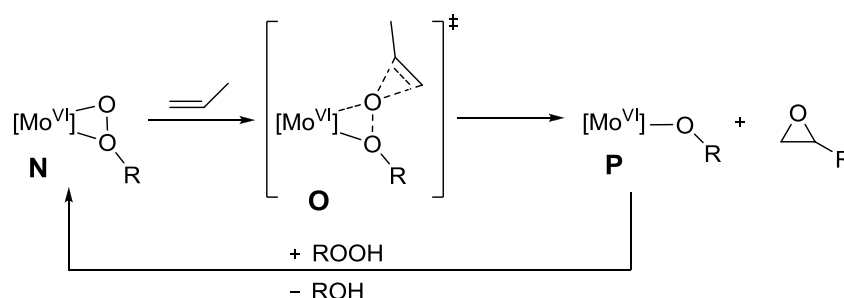


Figure 1.31 Epoxidation of propylene by alkylhydroperoxides via molybdenum catalysis.

An example for an oxidometal complex utilised for epoxidation reactions is the so-called manganese salen complex shown in **Figure 1.32** (salen = *N,N'*-ethylenebis(salicylimine)). The initial Mn^{III} complex **Q** is oxidised to the Mn^{V} -oxido complex **R** upon reaction with hypochlorite, iodosylbenzol or pyridine-*N*-oxide. This complex can oxidize olefins to epoxides by oxygen transfer and reacts back to the Mn^{III} complex **Q**.^[258] The use of chiral salen derivatives in such reactions allow for the enantioselective epoxidation of pro-chiral compounds.^[259,260]

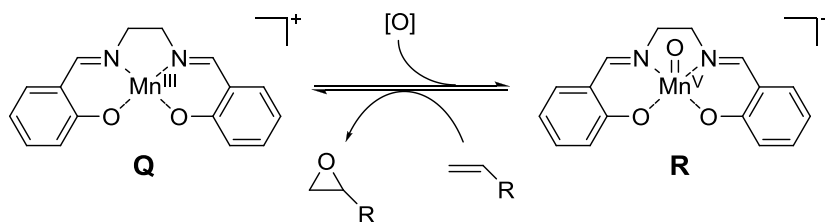


Figure 1.32 Epoxidation of alkenes by the manganese salen complex **P**; re-oxidation by the oxidant [O] = hypochlorite, iodosylbenzol or pyridine-*N*-oxide.

In a similar manner, epoxidations can also be catalysed by manganese as well as iron and chromium porphyrins.^[261,262] These reactions start with the metal centre in its three-valent oxidation state. Upon exposure to hypochlorite, iodosylbenzol or alkylhydroperoxides, the oxidometal porphyrinato complexes are formed. In these complexes the metal has the formal oxidation state +5 – but due to the non-innocent character of the porphyrins, this may in some cases rather be described as the metal in the +4 state along with the porphyrin as a radical cation. Depending on the substrate and the Lewis acidity of the metal centre such reactions may either be concerted or proceed via a radical intermediate.^[263]

Examples for the use of dioxygen as oxidant in epoxidation reactions are rare. On industrial scale, only the epoxidation of ethylene to ethyleneoxide with dioxygen is realised. This heterogenic process is based on contact catalysis at 200 to 300 °C and 1 to 3 bar on silver immobilised on Al₂O₃.^[264] There are only a few catalysts using dioxygen without the use of sacrificial co-factors in homogeneous epoxidation reactions.^[265-270] For instance, the Ru^{II} complex **S** (**Figure 1.33**) activates dioxygen in solution to the complex Ru^{IV} **T**.^[267] In this 4e⁻ reaction the ruthenium centre as well as two of the seleno moieties are formally oxidised. The complex **T** can epoxidise nucleophilic alkenes like 2,3-dimethyl-2-butene. In this reaction both oxygen atoms are subsequently transferred onto two substrates with concomitant re-formation of **S**.

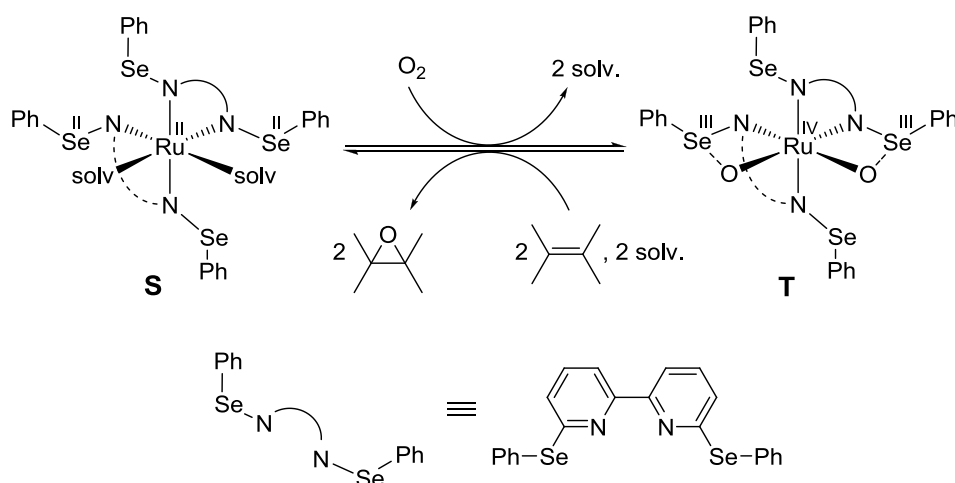


Figure 1.33 Oxygen activation by complex **S** and subsequent epoxidation of 2,3-dimethyl-2-buten with the formed complex **T**.

Epoxidation with ruthenium(II) porphyrins has first been reported by Groves *et al.*^[265] The Ru^{VI}(O)₂ porphyrin **U** can transfer one oxygen atom to different alkene substrates. (**Figure 1.34**) Two of the formed Ru^{IV}(O) porphyrins **V** can disproportionate to the Ru^{VI} porphyrin **U** and the Ru^{II} porphyrin **W**, which in turn can be re-oxidised to **V** by dioxygen. The use of chiral ruthenium porphyrins has further led to the enantioselective epoxidation of pro-chiral olefins.^[266]

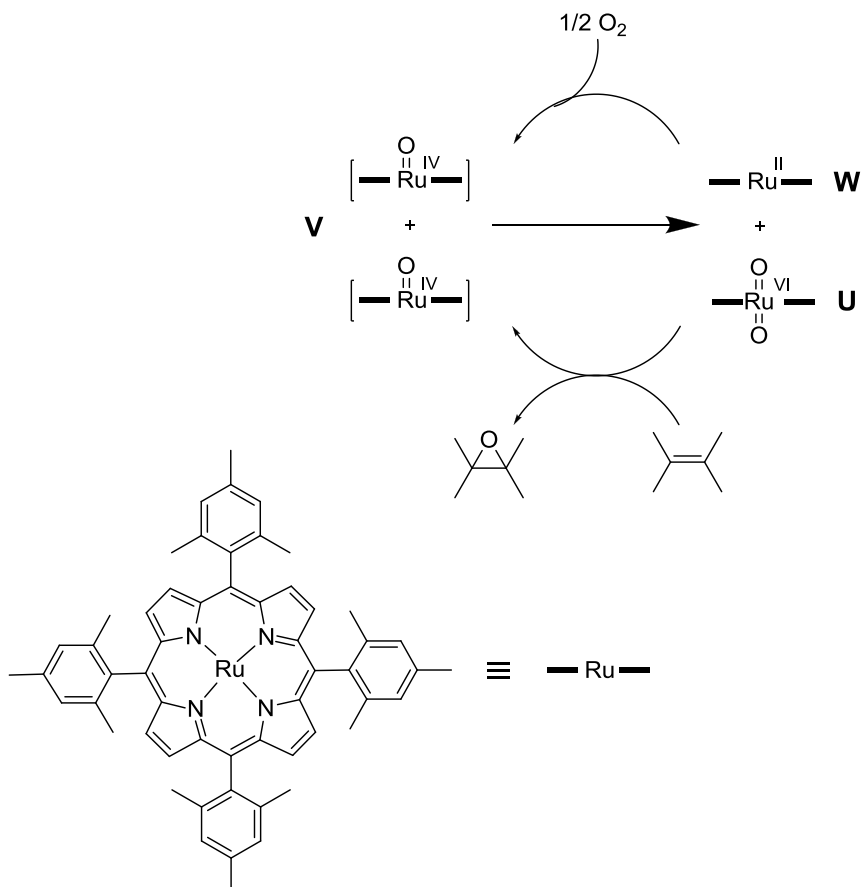


Figure 1.34 Epoxidation of olefins by the ruthenium porphyrin **U**.

The results from this work regarding the formal activation of dioxygen from air with the help of chromium(III) porphyrins and their use for epoxidation reactions will be presented in section 3.6.

1.7 Bibliography *Introduction*

- [1] K. L. Yam, P. T. Takhistov, J. Miltz, *J. Food Sci.* **2005**, *70*, R1–R10.
- [2] D. Restuccia, U. G. Spizzirri, O. I. Parisi, G. Cirillo, M. Curcio, F. Iemma, F. Puoci, G. Vinci, N. Picci, *Food Control* **2010**, *21*, 1425–1435.
- [3] C. A. Phillips, *Int. J. Food Sci. Technol.* **1996**, *31*, 463–479.
- [4] M. Sivertsvik, W. K. Jeksrud, J. T. Rosnes, *Int. J. Food Sci. Technol.* **2002**, *37*, 107–127.
- [5] L. Vermeiren, F. Devlieghere, M. van Beest, N. de Kruijf, J. Debevere, *Trends Food Sci. Technol.* **1999**, *10*, 77–86.
- [6] C. Wessling, T. Nielsen, J. R. Giacini, *J. Sci. Food Agric.* **2001**, *81*, 194–201.
- [7] P. Appendini, J. H. Hotchkiss, *Innov. Food Sci. Emerg. Technol.* **2002**, *3*, 113–126.
- [8] P. Suppakul, J. Miltz, K. Sonnewald, S. W. Bigger, *J. Agric. Food Chem.* **2003**, *51*, 3197–3207.
- [9] P. Suppakul, J. Miltz, K. Sonnewald, S. W. Bigger, *J. Food Sci.* **2003**, *68*, 408–420.
- [10] J. P. Kerry, M. N. O'Grady, S. A. Hogan, *Meat Sci.* **2006**, *74*, 113–130.
- [11] *Regulation (EC) 1935/2004 L338 p.4*, **2004**.
- [12] *Regulation (EC) 450/2009 L135 p.3*, **2009**.
- [13] A. Pacquit, K. Crowley, D. Diamond, in *Smart Packag. Technol. Fast Mov. Consum. Goods* (Eds.: J. Kerry, P. Butler), John Wiley & Sons Ltd., **2008**, pp. 75–98.
- [14] S. A. Hogan, J. P. Kerry, in *Smart Packag. Technol. Fast Mov. Consum. Goods* (Eds.: J. Kerry, P. Butler), John Wiley & Sons Ltd., **2008**, pp. 33–59.
- [15] M. Smolander, H.-L. Alakomi, T. Ritvanen, J. Vainionpää, R. Ahvenainen, *Food Control* **2004**, *15*, 217–229.
- [16] P. S. Taoukis, T. P. Labuza, *J. Food Sci.* **1989**, *54*, 783–788.
- [17] P. Puligundla, J. Jung, S. Ko, *Food Control* **2012**, *25*, 328–333.
- [18] A. Mills, N. McMurray, *PCT Int. Pat. Appl.* **1991**, WO 91/05252.
- [19] A. Mills, Q. Chang, N. McMurray, *Anal. Chem.* **1992**, *64*, 1383–1389.
- [20] S. N. Balderson, R. . Whitwood, *US Pat.* **1995**, 5439648.
- [21] A. Mills, A. Lepre, L. Wild, *Sens. Act. B Chem.* **1997**, *39*, 419–425.
- [22] A. Nopwinyuwong, S. Trevanich, P. Suppakul, *Talanta* **2010**, *81*, 1126–32.
- [23] N. B. Borchert, J. P. Kerry, D. B. Papkovsky, *Sens. Act. B Chem.* **2013**, *176*, 157–165.
- [24] D. Wencel, J. P. Moore, N. Stevenson, C. McDonagh, *Anal. Bioanal. Chem.* **2010**, *398*, 1899–907.
- [25] I. M. Pérez de Vargas-Sansalvador, M. a Carvajal, O. M. Roldán-Muñoz, J. Banqueri, M. D. Fernández-Ramos, L. F. Capitán-Vallvey, *Anal. Chim. Acta* **2009**, *655*, 66–74.
- [26] A. Mills, Q. Chang, M. Keynes, *Analyst* **1993**, *118*, 839–843.
- [27] G. Neurauter, I. Klimant, O. S. Wolfbeis, *Anal. Chim. Acta* **1999**, *382*, 67–75.
- [28] C. S. Burke, A. Markey, R. I. Nooney, P. Byrne, C. McDonagh, *Sens. Act. B Chem.* **2006**, *119*, 288–294.
- [29] C. von Bültzingslöwen, A. K. McEvoy, C. McDonagh, B. D. MacCraith, *Anal. Chim. Acta* **2003**, *480*, 275–283.
- [30] C. von Bültzingslöwen, A. K. McEvoy, C. McDonagh, B. D. MacCraith, I. Klimant, C. Krause, O. S. Wolfbeis, *Analyst* **2002**, *127*, 1478–1483.
- [31] M. Smolander, E. Hurme, R. Ahvenainen, *Trends Food Sci. Technol.* **1997**, *8*, 101–106.
- [32] B. Holte, *PCT Int. Pat. Appl.* **1993**, WO 93/15402.

- [33] A. Mills, *Chem. Soc. Rev.* **2005**, *34*, 1003–1011.
- [34] D. B. Papkovsky, N. Papkovskaia, A. Smyth, J. Kerry, V. I. Ogurtsov, *Anal. Lett.* **2000**, *33*, 1755–1777.
- [35] A. Mills, *Sens. Act. B Chem.* **1998**, *51*, 60–68.
- [36] B. A. Mills, *Platin. Met. Rev.* **1997**, 115–127.
- [37] P. Hartmann, M. J. P. Leiner, M. E. Lippitsch, *Anal. Chem.* **1995**, *67*, 88–93.
- [38] S. Draxler, M. E. Lippitsch, *J. Phys. Chem.* **1995**, *4*, 3162–3167.
- [39] K. E. Chung, E. H. Lan, M. S. Davidrron, B. S. Dunn, J. S. Valentine, J. I. Zinkt, *Anal. Chem.* **1995**, *67*, 1505–1509.
- [40] A. Del Bianco, F. Baldini, M. Bacci, I. Klimant, O. S. Wolfbeis, *Sens. Act. B Chem.* **1993**, *11*, 347–350.
- [41] Z. Zhujun, W. R. Seitz, *Anal. Chem.* **1986**, *222*, 220–222.
- [42] A. Mills, K. Lawrie, J. Bardin, A. Apedaile, G. a Skinner, C. O'Rourke, *Analyst* **2012**, *137*, 106–112.
- [43] K. Eaton, *Sens. Act. B Chem.* **2002**, *85*, 42–51.
- [44] R. Ahvenainen, M. Eilamo, E. Hurme, *Food Control* **1997**, *8*, 177–184.
- [45] S.-K. Lee, A. Mills, A. Lepre, *Chem. Commun.* **2004**, *44*, 1912–3.
- [46] S.-K. Lee, M. Sheridan, A. Mills, *Chem. Mater.* **2005**, *17*, 2744–2751.
- [47] K. Lawrie, A. Mills, D. Hazafy, *Sens. Act. B Chem.* **2013**, *176*, 1154–1159.
- [48] T. Mattila-Sandholm, R. Ahvenainen, E. Hurme, I. T. Järvi-Kääriäinen, *Eur. Pat.* **1998**, EP 0 666 977 B1.
- [49] A. Pacquit, K. T. Lau, H. McLaughlin, J. Frisby, B. Quilty, D. Diamond, *Talanta* **2006**, *69*, 515–520.
- [50] E. Martinsdbttir, J. Oehlenschbger, P. Dalgaard, B. Jensen, I. Undeland, I. M. Mackie, G. Henehan, J. Nielsen, H. Nilsen, *Trends Food Sci. Technol.* **1997**, *8*, 258–265.
- [51] K. Koutsoumanis, *Appl. Environ. Microbiol.* **2001**, *67*, 1821–1829.
- [52] L. R. Freeman, G. J. Silverman, P. Angelini, C. M. Jr, W. B. Esselen, *Appl. Environ. Microbiol.* **1976**, *32*, 222–231.
- [53] R. H. Dainty, *Int. J. Food Microbiol.* **1996**, 19–33.
- [54] R. Ahvenainen, T. Pullinen, E. Hurme, M. Smolander, M. Siika-Aho, *Int. Pat.* **1998**, WO 98/21120.
- [55] M. Smolander, E. Hurme, K. Latva-Kala, T. Luoma, H.-L. Alakomi, R. Ahvenainen, *Innov. Food Sci. Emerg. Technol.* **2002**, *3*, 279–288.
- [56] H. Shu, H. Hdkanson, B. Mattiasson, *Anal. Chim. Acta* **1993**, *283*, 727–737.
- [57] E. Borch, H. Agerhem, *Int. J. Food Microbiol.* **1992**, *15*, 99–108.
- [58] K. Randell, R. Ahvenainen, K. Latva-Kala, E. Hurme, T. Matilla-Sandholm, L. Hyvönen, *J. Food Sci.* **1995**, *210*, 667–672.
- [59] S. Kladsomboon, T. Kerdcharoen, *Anal. Chim. Acta* **2012**, *757*, 75–82.
- [60] M. Tonezzer, A. Quaranta, G. Maggioni, S. Carturan, G. Della Mea, *Sensors Actuators B Chem.* **2007**, *122*, 620–626.
- [61] A. C. Paske, L. D. Earl, J. L. O'Donnell, *Sensors Actuators B Chem.* **2011**, *155*, 687–691.
- [62] G. J. Mohr, U. E. Spichiger-keller, *Anal. Chim. Acta* **1997**, *351*, 189–196.
- [63] S. A. Lawrence, *Amines - Synthesis, Properties and Applications*, Cambridge University Press, Cambridge, **2004**.
- [64] A. Naila, S. Flint, G. Fletcher, P. Bremer, G. Meerdink, *J. Food Sci.* **2010**, *75*, R139–50.
- [65] A. R. Shalaby, *Food Res. Int.* **1997**, *29*, 675–690.
- [66] I. Al Bulushi, S. Poole, H. C. Deeth, D. A. Dykes, *Crit. Rev. Food Sci.* **2009**, *49*, 369–377.
- [67] L. V Jørgensen, P. Dalgaard, H. H. Huss, *J. Agric. Food Chem.* **2000**, *48*, 2448–53.

- [68] B. A. Seibel, P. J. Walsh, *J. Exp. Biol.* **2002**, *306*, 297–306.
- [69] P. H. Yancey, M. E. Clark, S. C. Hand, R. D. Bowlus, G. N. Somero, *Science* **1982**, *217*, 1214–1222.
- [70] J. Spinelli, B. Koury, *J. Agric. Food Chem.* **1979**, *27*, 1104–1108.
- [71] M. Kimura, I. Kimura, N. Seki, *Fish. Sci.* **2003**, *69*, 414–420.
- [72] R. C. Lundstrom, F. F. Correia, K. a. Wilhelm, *J. Food Sci.* **1982**, *47*, 1305–1310.
- [73] I. Monkovic, H. Wong, C. Bachand, *Synthesis* **1985**, 770–773.
- [74] L. Gram, P. Dalgaard, *Curr. Opin. Biotechnol.* **2002**, *13*, 262–266.
- [75] S. Gon, M. T. Giudici-Ortoni, V. Méjean, C. Iobbi-Nivol, *J. Biol. Chem.* **2001**, *276*, 11545–11551.
- [76] E. L. Barrett, *Ann. Rev. Microbiol.* **1985**, *39*, 131–149.
- [77] a R. Strøm, J. a Olafsen, H. Larsen, *J. Gen. Microbiol.* **1979**, *112*, 315–320.
- [78] K. L. Parkin, H. O. Hultin, *J. Biochem.* **1986**, *100*, 77–86.
- [79] I. Lidbury, J. C. Murrell, Y. Chen, *Proc. Natl. Acad. Sci. U. S. A.* **2014**, *111*, 2710–2715.
- [80] J. Colby, L. J. Zatman, *Biochem. J.* **1973**, *132*, 101–12.
- [81] P. J. Large, *FEBS Lett.* **1971**, *18*, 297–300.
- [82] J. J. Joffraud, F. Leroi, C. Roy, J. L. Berdagué, *Int. J. Food Microbiol.* **2001**, *66*, 175–184.
- [83] M. T. Veciana-Nogués, A. Mariné-Font, M. C. Vidal-Carou, *J. Agric. Food Chem.* **1997**, *45*, 2036–2041.
- [84] Y. Xu, W. Xia, J. M. Kim, *Int. J. Food Sci. Technol.* **2009**, *44*, 1547–1552.
- [85] J. S. Min, S. O. Lee, A. Jang, C. Jo, C. S. Park, M. Lee, *Asian-Aust. J. Anim. Sci.* **2007**, *20*, 1278–1284.
- [86] C. Balamatsia, A. Patsias, M. Kontominas, I. Savvaidis, *Food Chem.* **2007**, *104*, 1622–1628.
- [87] J. S. Byun, J. S. Min, I. S. Kim, J. W. Kim, M. S. Chung, M. Lee, *J. Food Prot.* **2003**, *66*, 1733–1737.
- [88] *EU Regulation (95/149/EC) p.84, 1995.*
- [89] A. S. Pearce, E. L. Streatfield, *Ger. Pat.* **1965**, DE 1190229.
- [90] K. I. Oberg, R. Hodyss, J. L. Beauchamp, *Sens. Act. B Chem.* **2006**, *115*, 79–85.
- [91] G. J. Mohr, C. Demuth, U. E. Spichiger-Keller, *Anal. Chem.* **1998**, *70*, 3868–3873.
- [92] G. J. Mohr, T. Nezel, U. E. Spichiger-keller, *Anal. Chim. Acta* **2000**, *414*, 181–187.
- [93] S. M. Korent, A. Lobnik, G. J. Mohr, *Anal. Bioanal. Chem.* **2007**, *387*, 2863–2870.
- [94] S. Körsten, G. J. Mohr, *Chem. Eur. J.* **2011**, *17*, 969–975.
- [95] G. J. Mohr, *Anal. Chim. Acta* **2004**, *508*, 233–237.
- [96] SigmaAldrich, “Sensory Applications / Ionophores,” can be found under <http://www.sigmaaldrich.com/analytical-chromatography/analytical-reagents/sensory-applications.html>, date accessed: 26.06. 2014.
- [97] SigmaAldrich, “Amine Sensing Materials,” can be found under http://www.sigmaaldrich.com/content/dam/sigma-aldrich/docs/Sigma-Aldrich/Bulletin/n_amine.pdf, date accessed: 26.06. 2014.
- [98] G. J. Mohr, *Dye. Pigment.* **2004**, *62*, 77–81.
- [99] G. N. Sausen, V. A. Engelhardt, W. J. Middleton, *J. Am. Chem. Soc.* **1958**, *80*, 2815–2822.
- [100] E. K. Feuster, T. E. Glass, *J. Am. Chem. Soc.* **2003**, *125*, 16174–16175.
- [101] K. Secor, J. Plante, C. Avetta, T. Glass, *J. Mater. Chem.* **2005**, *15*, 4073.
- [102] C. Patze, K. Broedner, F. Rominger, O. Trapp, U. H. Bunz, *Chem. Eur. J.* **2011**, *17*, 13720–13725.
- [103] A. J. Zuccherro, P. L. McGrier, U. H. F. Bunz, *Acc. Chem. Res.* **2010**, *43*, 397–408.
- [104] J. Kumpf, J. Freudenberg, S. T. Schwaebel, U. H. F. Bunz, *Macromolecules* **2014**, *47*, 2569–2573.

- [105] B. K. Wetzl, S. M. Yarmoluk, D. B. Craig, O. S. Wolfbeis, *Angew. Chem. Int. Ed.* **2004**, *43*, 5400-5402; *Angew. Chemie* **2004**, *116*, 5515–5517.
- [106] B. K. Hoefelschweiger, A. Duerkop, O. S. Wolfbeis, *Anal. Biochem.* **2005**, *344*, 122–129.
- [107] M. Steiner, R. J. Meier, A. Duerkop, O. S. Wolfbeis, *Anal. Chem.* **2010**, *82*, 8402–8405.
- [108] J. el Haskouri, D. Ortiz de Zárate, C. Guillem, J. Latorre, M. Caldés, A. Beltrán, D. Beltrán, A. B. Descalzo, G. Rodríguez-López, R. Martínez-Mañez, M. D. Marcos, P. Amorós, *Chem. Commun.* **2002**, 330–331.
- [109] M. Comes, M. D. Marcos, R. Martínez-Manez, F. Sancenon, J. Soto, L. a. Villaescusa, P. Amorós, D. Beltrán, *Adv. Mater.* **2004**, *16*, 1783–1786.
- [110] B. García-Acosta, M. Comes, J. L. Bricks, M. a. Kudinova, V. V. Kurdyukov, A. I. Tolmachev, A. B. Descalzo, M. D. Marcos, R. Martínez-Mañez, A. Moreno, F. Sancenón, J. Soto, L. a. Villaescusa, K. Rurack, J. M. Barat, I. Escriche, P. Amorós, *Chem. Commun.* **2006**, 2239–2241.
- [111] G. Ulrich, R. Ziessel, A. Harriman, *Angew. Chem. Int. Ed. Engl.* **2008**, *47*, 1184–1201; *Angew. Chem.* **2008**, *120*, 1202–1219.
- [112] N. Boens, V. Leen, W. Dehaen, *Chem. Soc. Rev.* **2012**, *41*, 1130–1172.
- [113] T. Rohand, M. Baruah, W. Qin, N. Boens, W. Dehaen, *Chem. Commun.* **2006**, 266–268.
- [114] T. Carofiglio, E. Lubian, I. Menegazzo, G. Saielli, A. Varotto, *J. Org. Chem.* **2009**, *74*, 9034–9043.
- [115] G. P. Moss, *Pure Appl Chem* **1987**, *59*, 779–832.
- [116] M. K. Cyranski, T. M. Krygowski, M. Wisiorowsky, N. J. R. van Eikema Hommes, P. von Rague Schleyer, *Angew. Chem. Int. Ed.* **1998**, 177–180.
- [117] L. E. Webb, E. B. Fleischer, *J. Am. Chem. Soc.* **1964**, 667–669.
- [118] M. Bröring, *Angew. Chem. Int. Ed. Engl.* **2011**, *50*, 2436–2438; *Angew. Chem.* **2011**, *123*, 2484–2486.
- [119] E. Vogel, *Pure Appl Chem* **1993**, *65*, 143–152.
- [120] C. B. Storm, Y. Teklu, *J. Am. Chem. Soc.* **1972**, 1745–1747.
- [121] N. Z. Mamardashvili, O. a. Golubchikov, *Russ. Chem. Rev.* **2001**, *70*, 577–606.
- [122] A. Stone, E. B. Fleischer, *J. Am. Chem. Soc.* **1968**, *90*, 2735–2748.
- [123] J. Braun, C. Hasenfratz, R. Schwesinger, H.-H. Limbach, *Angew Chem Int Ed Engl* **1994**, 2215–2217, *Angew. Chem.* **1994**, *106*, 2302–2304.
- [124] J. K. M. Sanders, N. Bampos, Z. Clyde-Watson, S. L. Darling, J. C. Hawley, H.-J. Kim, C. C. Mak, S. J. Webb, in *Porphy. Handb.* (Eds.: M. Kadish, K.M. Smith, R. Guillard), Academic Press, New York, **2000**, pp. 1–48.
- [125] B. C. Milgram, K. Eskildsen, S. M. Richter, W. R. Scheidt, K. A. Scheidt, *J. Org. Chem.* **2007**, 3941–3944.
- [126] P. Rothmund, *J. Am. Chem. Soc.* **1936**, 625–627.
- [127] P. Rothmund, A. R. Menotti, *J. Am. Chem. Soc.* **1941**, *63*, 267–270.
- [128] A. D. Adler, F. R. Longo, J. D. Finarelli, *J. Org. Chem.* **1967**, 476.
- [129] J. S. Lindsey, K. A. Maccrum, J. S. Tyhonas, Y. Chuang, *J. Org. Chem.* **1994**, 579–587.
- [130] J. S. Lindsey, *Acc. Chem. Res.* **2010**, *43*, 300–311.
- [131] P. D. Rao, S. Dhanalekshmi, B. J. Littler, J. S. Lindsey, *J. Org. Chem.* **2000**, *65*, 7323–7344.
- [132] C.-H. Lee, J. S. Lindsey, *Tetrahedron* **1994**, *50*, 11427–11440.
- [133] K. Heinze, A. Reinhart, *Dalton Trans.* **2008**, 469–480.
- [134] M. Gouterman, *J. Chem. Phys.* **1959**, *30*, 1139–1161.
- [135] M. Gouterman, G. H. Wagnière, L. C. Snyder, *J. Mol. Spectrosc.* **1963**, *11*, 108–127.
- [136] M. Gouterman, *J. Mol. Spectrosc.* **1961**, *6*, 138–163.

- [137] C. Weiss, H. Kobayashi, M. Gouterman, *J. Mol. Spectrosc.* **1965**, *16*, 415–450.
- [138] C. Rimington, S. F. Mason, O. Kennard, *Spectrochim. Acta* **1958**, *12*, 65–77.
- [139] J. Melomedov, J. R. Ochsmann, M. Meister, F. Laquai, K. Heinze, *Eur. J. Inorg. Chem.* **2014**, *2014*, 1984–2001.
- [140] J. Melomedov, A. Wünsche von Leupoldt, M. Meister, F. Laquai, K. Heinze, *Dalton Trans.* **2013**, *42*, 9727–39.
- [141] T. Ema, M. Senge, N. Y. Nelson, H. Ogoshi, K. M. Smith, *Angew. Chem. Int. Ed.* **1994**, *33*, 1879–1881.
- [142] W. Jentzen, S. Xing-Zhi, J. A. Shelnut, *J. Phys. Chem. B* **1997**, *101*, 1684–1699.
- [143] W. Jentzen, J. G. Ma, J. A. Shelnut, *Biophys. J.* **1998**, *74*, 753–763.
- [144] *NSD Software 3.0*, can be found under <http://jasheln.unm.edu/jasheln>, date accessed: 26.06. 2014.
- [145] Z. Zhou, C. Cao, Q. Liu, R. Jiang, *Org. Lett.* **2010**, *12*, 1780–1783.
- [146] J. A. Shelnut, X.-Z. Song, J.-G. Ma, S.-L. Jia, W. Jentzen, C. J. Medforth, *Chem. Soc. Rev.* **1998**, *27*, 31–42.
- [147] K. M. Barkigia, L. Chantranupong, K. M. Smith, J. Fajer, *J. Am. Chem. Soc.* **1988**, 7566–7567.
- [148] W. Jentzen, M. C. Simpson, J. D. Hobbs, X. Song, T. Ema, N. Y. Nelson, C. J. Medforth, K. M. Smith, M. Veyrat, M. Mazzanti, R. Ramasseul, J.-C. Marchon, T. Takeuchi, W. A. Goddard III, J. A. Shelnut, *J. Am. Chem. Soc.* **1995**, *117*, 11085–11097.
- [149] R. E. Haddad, S. Gazeau, J. Pécaut, J.-C. Marchon, C. J. Medforth, J. A. Shelnut, *J. Am. Chem. Soc.* **2003**, *125*, 1253–1268.
- [150] D. M. Cleland, K. C. Gordon, D. L. Officer, P. Wagner, P. J. Walsh, *Spectrochim. Acta. A. Mol. Biomol. Spectrosc.* **2009**, *74*, 931–935.
- [151] M. Nappa, J. S. Valentine, *J. Am. Chem. Soc.* **1978**, *100*, 5075–5080.
- [152] O. Kolling, *Inorg. Chem.* **1979**, *18*, 1175–1176.
- [153] T. Kojima, T. Nakanishi, T. Honda, R. Harada, M. Shiro, S. Fukuzumi, *Eur. J. Inorg. Chem.* **2009**, *2009*, 727–734.
- [154] R. Harada, Y. Matsuda, H. Ōkawa, R. Miyamoto, S. Yamauchi, T. Kojima, *Inorganica Chim. Acta* **2005**, *358*, 2489–2500.
- [155] K. S. Suslick, R. A. Watson, *New J. Chem.* **1992**, *16*, 633–642.
- [156] A. Antipas, J. W. Buchler, M. Gouterman, P. D. Smith, *J. Am. Chem. Soc.* **1978**, *100*, 3015–3024.
- [157] L. K. Hanson, W. A. Eaton, S. G. Sligar, S. G. S. Gunsalus, M. Gouterman, C. R. Connell, *J. Am. Chem. Soc.* **1976**, *2135*, 2672–2674.
- [158] M. Gouterman, L. K. Hanson, G.-E. Khalil, W. R. Leenstra, J. W. Buchler, *J. Chem. Phys.* **1975**, *62*, 2343.
- [159] D. A. Summerville, R. D. Jones, B. M. Hoffmann, F. Basolo, *J. Am. Chem. Soc.* **1977**, *99*, 8195–8202.
- [160] T. Ozawa, A. Hanaki, *Inorganica Chim. Acta* **1985**, *102*, 169–171.
- [161] E. B. Fleischer, M. Krishnamaurthy, *J. Am. Chem. Soc.* **1971**, *93*, 3784–3786.
- [162] P. O'Brien, D. A. Sweigart, *Inorg. Chem.* **1982**, *21*, 2094–2095.
- [163] N. A. Rakow, K. S. Suslick, *Nature* **2000**, *406*, 710–713.
- [164] K. S. Suslick, N. A. Rakow, A. Sen, *Tetrahedron* **2004**, *60*, 11133–11138.
- [165] N. A. Rakow, A. Sen, M. C. Janzen, J. B. Ponder, K. S. Suslick, *Angew. Chemie Int. Ed.* **2005**, *44*, 4528–4532; *Angew. Chem.* **2005**, *117*, 4604–4608.
- [166] A. Sen, K. S. Suslick, *J. Am. Chem. Soc.* **2000**, *122*, 11565–11566.
- [167] A. S. Hart, C. B. Kc, H. B. Gobeze, L. R. Sequeira, F. D'Souza, *Appl. Mater. Interfaces* **2013**, *5*, 5314–5323.
- [168] L.-L. Li, E. W.-G. Diau, *Chem. Soc. Rev.* **2013**, *42*, 291–304.

- [169] C.-L. Wang, W.-B. Zhang, R. M. Van Horn, Y. Tu, X. Gong, S. Z. D. Cheng, Y. Sun, M. Tong, J. Seo, B. B. Y. Hsu, A. J. Heeger, *Adv. Mater.* **2011**, *23*, 2951–2956.
- [170] H. Imahori, S. Kang, H. Hayashi, M. Haruta, H. Kurata, S. Isoda, S. E. Canton, Y. Infahsaeng, A. Kathiravan, T. Pascher, P. Chábera, A. P. Yartsev, V. Sundström, *J. Phys. Chem. A* **2011**, *115*, 3679–90.
- [171] A. Yella, H.-W. Lee, H. N. Tsao, C. Yi, A. K. Chandiran, M. K. Nazeeruddin, E. W.-G. Diao, C.-Y. Yeh, S. M. Zakeeruddin, M. Grätzel, *Science* **2011**, *334*, 629–34.
- [172] A. Huijser, T. J. Savenije, A. Kotlewski, S. J. Picken, L. D. A. Siebbeles, *Adv. Mater.* **2006**, *18*, 2234–2239.
- [173] Q. Wang, W. M. Campbell, E. E. Bonfantani, K. W. Jolley, D. L. Officer, P. J. Walsh, K. Gordon, R. Humphry-Baker, M. K. Nazeeruddin, M. Grätzel, *J. Phys. Chem. B* **2005**, *109*, 15397–15409.
- [174] M. H. Hoang, Y. Kim, M. Kim, K. H. Kim, T. W. Lee, D. N. Nguyen, S.-J. Kim, K. Lee, S. J. Lee, D. H. Choi, *Adv. Mater.* **2012**, *24*, 5363–5367.
- [175] S.-J. Choi, Y.-C. Lee, M.-L. Seol, J.-H. Ahn, S. Kim, D.-I. Moon, J.-W. Han, S. Mann, J.-W. Yang, Y.-K. Choi, *Adv. Mater.* **2011**, *23*, 3979–3983.
- [176] A. Huijser, T. J. Savenije, S. C. J. Meskers, M. J. W. Vermeulen, L. D. a Siebbeles, *J. Am. Chem. Soc.* **2008**, *130*, 12496–12500.
- [177] A. Huijser, B. M. J. M. Suijkerbuijk, R. J. M. Klein Gebbink, T. J. Savenije, L. D. A. Siebbeles, *J. Am. Chem. Soc.* **2008**, *130*, 2485–92.
- [178] M. O. Senge, M. Fazekas, E. G. a. Notaras, W. J. Blau, M. Zawadzka, O. B. Locos, E. M. Ni Mhuircheartaigh, *Adv. Mater.* **2007**, *19*, 2737–2774.
- [179] Y.-Y. Noh, J.-J. Kim, K. Yase, S. Nagamatsu, *Appl. Phys. Lett.* **2003**, *83*, 1243.
- [180] Z. Liu, A. a Yasseri, J. S. Lindsey, D. F. Bocian, *Science* **2003**, *302*, 1543–5.
- [181] B. Johnson-White, M. Zeinali, K. M. Shaffer, C. H. Patterson Jr, P. T. Charles, M. A. Markowitz, *Biosens. Bioelectron.* **2007**, *22*, 1154–1162.
- [182] S. Tao, G. Li, H. Zhu, *J. Mater. Chem.* **2006**, *16*, 4521–4528.
- [183] M. Toneyzer, G. Maggioni, E. Dalcanale, *J. Mater. Chem.* **2012**, *22*, 5647–5655.
- [184] T. H. Richardson, R. A. Brook, F. Davis, C. A. Hunter, *Colloids Surfaces A Physicochem. Eng. Asp.* **2006**, *284-285*, 320–325.
- [185] O. Worsfold, C. M. Dooling, T. H. Richardson, M. O. Vysotsky, R. Tregonning, C. A. Hunter, C. Malins, *Colloids Surfaces A Physicochem. Eng. Asp.* **2002**, *200*, 859–867.
- [186] V. C. Smith, T. Richardson, H. L. Anderson, *Supramol. Sci.* **1997**, *4*, 503–508.
- [187] S. H. Lim, L. Feng, J. W. Kemling, C. J. Musto, K. S. Suslick, *Nat. Chem.* **2009**, *1*, 562–567.
- [188] C. Di Natale, R. Paollesse, A. Macagnano, A. Mantini, A. D’Amico, A. Legin, L. Lvova, A. Rudnitskaya, Y. Vlasov, *Sens. Act. B Chem.* **2000**, *64*, 15–21.
- [189] S. a. Brittle, T. H. Richardson, A. D. F. Dunbar, S. M. Turega, C. a. Hunter, *J. Mater. Chem.* **2011**, *21*, 4882.
- [190] A. D. F. Dunbar, S. Brittle, T. H. Richardson, J. Hutchinson, C. A. Hunter, D. Building, B. Hill, S. Sheffield, *J. Phys. Chem. B* **2010**, 11697–11702.
- [191] M. Toneyzer, G. Maggioni, A. Quaranta, S. Carturan, G. Della Mea, *Sensors Actuators B Chem.* **2009**, *136*, 290–296.
- [192] D. Delmarre, C. Bied-Charreton, *Sens. Act. B Chem.* **2000**, *62*, 136–142.
- [193] W. Qin, P. Parzuchowski, W. Zhang, M. E. Meyerhoff, *Anal. Chem.* **2003**, *75*, 332–340.
- [194] J. Spadavecchia, R. Rella, P. Siciliano, M. G. Manera, A. Alimelli, *Sens. Act. B Chem.* **2006**, *115*, 12–16.
- [195] F. A. Nwachukwu, M. G. Baron, *Sens. Act. B Chem.* **2003**, *90*, 276–285.
- [196] G. Giancane, L. Valli, *Adv. Colloid Interface Sci.* **2012**, *171-172*, 17–35.

- [197] C. M. Dooling, O. Worsfold, T. H. Richardson, R. Tregonning, M. O. Vysotsky, C. A. Hunter, K. Kato, K. Shinbo, F. Kaneko, *J. Mater. Chem.* **2001**, *11*, 392–398.
- [198] P. . Kelly, R. . Arnell, *Vacuum* **2000**, *56*, 159–172.
- [199] A. A. Vaughan, M. G. Baronb, R. Narayanaswamy, *Anal. Commun.* **1996**, *33*, 393–396.
- [200] H. Conrads, M. Schmidt, *Plasma Sources Sci. Technol.* **2000**, *9*, 441–454.
- [201] C. Tendero, C. Tixier, P. Tristant, J. Desmaison, P. Leprince, *Spectrochim. Acta B At. Spectrosc.* **2006**, *61*, 2–30.
- [202] D. S. Antao, D. a Staack, A. Fridman, B. Farouk, *Plasma Sources Sci. Technol.* **2009**, *18*, 035016.
- [203] P. Fauchais, A. Vardelle, B. Dussoubs, *J. Therm. Spray Technol.* **2001**, *10*, 44–66.
- [204] Z. Machala, E. Marode, C. O. Laux, C. H. Kruger, *J. Adv. Oxid. Technol.* **2004**, *7*, 133–137.
- [205] W. Zhu, J. L. Lopez, *Plasma Sources Sci. Technol.* **2012**, *21*, 034018.
- [206] a Fridman, a Chirokov, a Gutsol, *J. Phys. D. Appl. Phys.* **2005**, *38*, R1–R24.
- [207] M. Moravej, S. E. Babayan, G. R. Nowling, X. Yang, R. F. Hicks, *Plasma Sources Sci. Technol.* **2004**, *13*, 8–14.
- [208] J. Park, I. Henins, H. W. Herrmann, G. S. Selwyn, J. Y. Jeong, R. F. Hicks, D. Shim, C. S. Chang, *Appl. Phys. Lett.* **2000**, *76*, 288.
- [209] P. Koulik, S. Begounov, S. Goloviatinskii, *Plasma Chem. Plasma Process.* **1999**, *19*, 311–327.
- [210] M. I. Boulos, *J. Therm. Spray Technol.* **1992**, *1*, 33–40.
- [211] H. Koinuma, H. Ohkubo, T. Hashimoto, K. Inomata, T. Shiraishi, A. Miyanaga, S. Hayashi, *Appl. Phys. Lett.* **1992**, *60*, 816.
- [212] Y. Kabouzi, M. D. Calzada, M. Moisan, K. C. Tran, C. Trassy, *J. Appl. Phys.* **2002**, *91*, 1008.
- [213] H. Matusiewicz, *Spectrochim. Acta B At. Spectrosc.* **1992**, *47*, 1221–1227.
- [214] Q. Jin, C. H. U. Zhu, M. W. Borer, G. M. Hieftje, *Spectrochim. Acta Part B At. Spectrosc.* **1991**, *46*, 417–430.
- [215] C. I. M. Beenakker, *Spectrochim. Acta B At. Spectrosc.* **1976**, *31*, 483–486.
- [216] M. Jasi ski, J. Mizeraczyk, Z. Zakrzewski, T. Ohkubo, J.-S. Chang, *J. Phys. D. Appl. Phys.* **2002**, *35*, 2274–2280.
- [217] M. Baeva, H. Gier, A. Pott, J. Uhlenbusch, J. Höschle, J. Steinwandel, *Plasma Chem. Plasma Process.* **2001**, *21*, 225–247.
- [218] M. Baeva, H. Gier, A. Pott, J. Uhlenbusch, J. Höschele, J. Steinwandel, *Plasma Sources Sci. Technol.* **2002**, *11*, 1–9.
- [219] M. Okumoto, A. Mizuno, *Catal. Today* **2001**, *71*, 211–217.
- [220] J. Chen, J. H. Davidson, *Plasma Chem. Plasma Process.* **2002**, *22*, 495–522.
- [221] M. Kogoma, S. Okazakit, *J. Phys. D. Appl. Phys.* **1985**, *27*, 1985–1987.
- [222] A. C. H. J. Liefkens, W. G. Essers, *US Pat.* **1971**, 3 612 807.
- [223] V. a Nemchinsky, W. S. Severance, *J. Phys. D. Appl. Phys.* **2006**, *39*, R423–R438.
- [224] S. Ramakrishnan, M. W. Rogozinski, *J. Phys. D. Appl. Phys.* **1997**, *30*, 636–644.
- [225] M. D. Calzada, M. Moisan, A. Gamero, A. Sola, *J. Appl. Phys.* **1996**, *80*, 46.
- [226] U. Kogelschatz, *Plasma Chem. Plasma Process.* **2003**, *23*, 1–46.
- [227] B. Eliasson, M. Hirth, U. Kogelschatz, *J. Phys. D. Appl. Phys.* **1987**, *20*, 1421–1437.
- [228] D. Braun, U. Kuchler, G. Pietsch, *J. Phys. D. Appl. Phys.* **1991**, *24*, 564–572.
- [229] G. Steinle, D. Neundorf, W. Hiller, M. Pietralla, *J. Phys. D. Appl. Phys.* **1999**, *32*, 1350–1356.
- [230] J. J. Coogan, A. D. Sappey, *IEEE Trans Plasma Sci* **1996**, *24*, 91–92.

- [231] J. Hirschberg, T. Omairi, N. Mertens, A. Helmke, S. Emmert, W. Viöl, *J. Phys. D. Appl. Phys.* **2013**, *46*, 165201.
- [232] H. Search, C. Journals, A. Contact, M. Iopscience, I. P. Address, *J. Phys. B At. Mol. Opt. Phys.* **1986**, *19*, 1241–1247.
- [233] S. Kajita, S. Ushiroda, Y. Kondo, *J. Appl. Phys.* **1990**, *67*, 4015–4023.
- [234] P. C. Cosby, *J. Chem. Phys.* **1993**, *98*, 9560–9569.
- [235] B. Eliasson, U. Kogelschatz, P. Baessler, *J. Phys. B At. Mol. Opt. Phys.* **1984**, *17*, L797–L801.
- [236] A. V Phelps, L. C. Pitchford, *Phys. Rev. A* **1985**, *31*, 2932–2949.
- [237] P. C. Cosby, *J. Chem. Phys.* **1993**, *98*, 9544–9554.
- [238] M. Braglia, R. Winkler, J. Wilhelm, *Contrib. to Plasma Phys.* **1991**, *31*, 463–481.
- [239] H. N. Küçükarpaci, J. Lucas, *J. Phys. D. Appl. Phys.* **1979**, *12*, 2123–2138.
- [240] K. Choy, *Prog. Mater. Sci.* **2003**, *48*, 57–170.
- [241] P. Heyse, R. Dams, S. Paulussen, K. Houthoofd, K. Janssen, P. a. Jacobs, B. F. Sels, *Plasma Process. Polym.* **2007**, *4*, 145–157.
- [242] N. D. Boscher, P. Choquet, D. Duday, S. Verdier, *Plasma Process. Polym.* **2010**, *7*, 163–171.
- [243] M. Bashir, J. M. Rees, W. B. Zimmerman, *Surf. Coatings Technol.* **2013**, *234*, 82–91.
- [244] B. Twomey, D. Dowling, G. Byrne, L. O'Neill, L.-A. O'Hare, *Plasma Process. Polym.* **2007**, *4*, S450–S454.
- [245] L. O'Neill, L. -a. O'Hare, S. R. Leadley, a. J. Goodwin, *Chem. Vap. Depos.* **2005**, *11*, 477–479.
- [246] N. D. Boscher, P. Choquet, D. Duday, S. Verdier, *Surf. Coat. Technol.* **2010**, *205*, 2438–2448.
- [247] F. Fanelli, S. Lovascio, R. D'Agostino, F. Arefi-Khonsari, F. Fracassi, *Plasma Process. Polym.* **2010**, *7*, 535–543.
- [248] R. Morent, N. De Geyter, S. Van Vlierberghe, P. Dubruel, C. Leys, E. Schacht, *Surf. Coatings Technol.* **2009**, *203*, 1366–1372.
- [249] N. D. Boscher, D. Duday, S. Verdier, P. Choquet, *ACS Appl. Mater. Interfaces* **2013**, *5*, 1053–1060.
- [250] R. N. Wenzel, *Ind. Eng. Chem.* **1936**, 988–994.
- [251] N. D. Boscher, P. Choquet, D. Duday, S. Verdier, *Surf. Coatings Technol.* **2011**, *205*, 5350–5357.
- [252] J. Bardon, J. Bour, D. Del Frari, C. Arnoult, D. Ruch, *Plasma Process. Polym.* **2009**, *6*, S655–S659.
- [253] N. D. Boscher, P. Choquet, D. Duday, N. Kerbellec, J.-C. Lambrechts, R. R. Maurau, *J. Mater. Chem.* **2011**, *21*, 18959.
- [254] N. Kerbellec, D. Kustaryono, V. Haquin, M. Etienne, C. Daiguebonne, O. Guillou, *Inorg. Chem.* **2009**, *48*, 2837–43.
- [255] P. Heyse, A. Van Hoeck, M. B. J. Roeyfaers, J.-P. Raffin, A. Steinbüchel, T. Stöveken, J. Lammertyn, P. Verboven, P. A. Jacobs, J. Hofkens, S. Paulussen, B. F. Sels, *Plasma Process. Polym.* **2011**, *8*, 965–974.
- [256] S. T. Oyama, *Mechanism of Homogeneous and Heterogeneous Epoxidation Catalysis*, Elsevier B.V, Amsterdam, **2008**.
- [257] D. V Deubel, G. Frenking, P. Gisdakis, W. a Herrmann, N. Rösch, J. Sundermeyer, *Acc. Chem. Res.* **2004**, *37*, 645–52.
- [258] D. Steinborn, in *Grundlagen der metallorganischen. Komplexkatalyse*, Vieweg + Teubner, Wiesbaden, **2010**, p. 283.
- [259] E. N. Jacobsen, W. Zhang, A. R. Muci, J. R. Ecker, L. Deng, *J. Am. Chem. Soc.* **1991**, *113*, 7063–7064.
- [260] W. Zhang, J. L. Loebach, S. R. Wilson, E. N. Jacobsen, *J. Am. Chem. Soc.* **1990**, *112*, 2801–2803.
- [261] B. Meunier, *Chem. Rev.* **1992**, *92*, 1411–1456.
- [262] T. G. Traylor, A. R. Miksztal, *J. Am. Chem. Soc.* **1989**, *111*, 7443–7448.

- [263] D. Ostovic, T. C. Bruice, *Acc. Chem. Res.* **1992**, *25*, 314–320.
- [264] P. A. Kilty, W. M. H. Sachtler, *Catal. Rev. - Sci. Eng.* **1974**, *10*, 1–16.
- [265] J. T. Groves, R. Quinn, *J. Am. Chem. Soc.* **1985**, *107*, 5790–5792.
- [266] T. Lai, R. Zhang, K. Cheung, H. Kwong, C. Che, *Chem. Commun.* **1998**, 1583–1584.
- [267] A. Laskavy, L. J. W. Shimon, L. Konstantinovski, M. a Iron, R. Neumann, *J. Am. Chem. Soc.* **2010**, *132*, 517–523.
- [268] S. Koya, Y. Nishioka, H. Mizoguchi, T. Uchida, T. Katsuki, *Angew. Chem, Int. Ed.* **2012**, *51*, 8243–8246; *Angew. Chem.* **2012**, *124*, 8368-8371.
- [269] C. Sun, B. Hu, Z. Liu, *Chem. Eng. J.* **2013**, *232*, 96–103.
- [270] A. Bhunia, M. a Gotthardt, M. Yadav, M. T. Gamer, A. Eichhöfer, W. Kleist, P. W. Roesky, *Chem. - A Eur. J.* **2013**, *19*, 1986–1995.

2. Aim of the work

The objective of this work is the development of colorimetric gas sensing layers for the detection of volatile amines. Their integration into food containers would lead to intelligent packaging solutions for easy and reliable control of food freshness and safety.

The deposition of the coatings should be based on an atmospheric pressure plasma assisted chemical vapour deposition, as such processes are environmental friendly, cost-effective and may be introduced into existing mass production lines.

The work to achieve this goal can be categorised into three main fields.

One deals with the development, synthesis and analysis of chromophores for colourimetric amine detection. Metalloporphyrins have been chosen because of their strong absorptions in the visible part of the spectrum, their known interactions with amines and their thermal and chemical stability, which should enable their deposition in a plasma assisted process. The porphyrins should be tailored to give an easily discernible colour change upon exposure to amines and to facilitate their further processing.

The second objective is the development of the actual deposition process. The sensor layers should be deposited on different substrates like aluminium or PET-foils by a dielectric barrier discharge enhanced chemical vapour deposition at atmospheric pressure. The process parameters will be optimised to ensure that the final coatings meet the crucial requirements for their future application in intelligent packaging solutions. The coating needs to be coloured, stable and adherent to the substrate. The formed matrix should tightly incorporate the chromophores and prevent them from agglomeration. Moreover, the formed layers need to be porous to facilitate the analytes' diffusion to and interaction with the metalloporphyrins within.

The work is completed with the comprehensive analysis of the novel porphyrin chromophores as well as the formed sensing layers. The mechanisms leading to the colour changes of the metalloporphyrins upon exposure to amines should be investigated and spectroscopic results rationalised by assisting DFT calculations. The performance of deposited sensing coatings should be tested with different gaseous amines and in first food-storage experiments.

3. Results and Discussion

The outcome of this work will be presented here as a collection of the articles which resulted from it. They have been published in peer-reviewed journals and are re-printed here with the permission of the respective publishers.

The article in section 3.1 (pp. 59 – 74) shows the successful incorporation of ZnTPP into polysiloxane matrices deposited from hexamethyldisiloxane (HMDSO) in a dielectric barrier discharge enhanced chemical vapour deposition. Furthermore, the influences of different deposition parameters on the adherence, morphology and porosity of the formed coatings are investigated.

The deposition of Cr(TPP)(Cl)(H₂O) containing coatings employing the optimised deposition parameters is reported in section 3.2 (pp. 75 – 88). The performance of the formed sensing layers in colourimetric amine detection is tested upon exposure to NEt₃ as a prototypical volatile amine.

The article in section 3.3 (pp. 89 – 106) describes Cr(TPP)(Cl)(H₂O) containing coatings deposited from vinyltrimethoxysilane (VTMOS) solutions instead of HMDSO-based ones. The higher solubility of Cr(TPP)(Cl)(H₂O) in VTMOS enables the use of more concentrated precursor solutions and therefore highly coloured coatings could be obtained. The deposition parameters of the DBD enhanced CVD are optimised in the light of the distinct precursor composition. The importance of a proper matrix surrounding the chromophores for the sensors' performance is emphasized by the different responses towards the exposure to NEt₃ of foils deposited under different conditions. The best performing foils have also been tested for the detection of further amines and in food storage experiments with fish samples.

In section 3.4 (pp. 107 – 132) the development of novel zinc(II) porphyrins with increased absorption changes upon exposure to NEt₃ is reported. The origin of the pronounced colour changes as compared to ZnTPP is investigated by NMR

experiments, DFT calculations as well as NSD analyses. Furthermore, the porphyrins' solubility in non-polar solvents, which is of special interest for their further processing, is analysed in the light of the distinct intermolecular interactions indicated by the respective solid state structures.

The incorporation of the novel zinc(II) porphyrins and their chromium(III) equivalents in plasma polymerised polysiloxane matrices is shown in section 3.5 (pp. 133 – 154). The integrity of the more complex structures after the DBD enhanced CVD is checked by UV/vis spectroscopy and mass spectrometry on the deposited coatings. The foils' optical responses upon exposure to NEt_3 vapours are tested and compared to tetraphenyl porphyrin based ones. Furthermore, the influence of different porphyrin loadings on the growth and hence the performance of the deposited coatings is investigated.

The unexpected interaction mechanism of $\text{Cr(TPP)(Cl)(H}_2\text{O)}$ with NEt_3 and other amines is revealed in section 3.6 (pp. 155 – 176). A novel green pathway for the formation of Cr(TPP)(O) is disclosed and its use in electrochemical epoxidation reactions is presented.

3.1

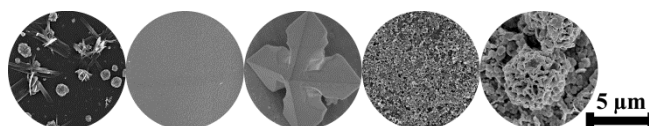
Plasma Polymer Membranes for Immobilizing Metalloporphyrins

N. Boscher, D. Duday, P. Heier, K. Heinze, F. Hilt, P. Choquet

Plasma Processes and Polymers **2013**, *10*, 336 – 344.

Abstract

Atmospheric pressure dielectric barrier discharge formation of organosilicon thin films loaded with zinc 5,10,15,20-tetraphenylporphyrin (Zn(TPP)) was investigated for different deposition conditions. UV–visible spectroscopy and scanning electron microscopy revealed the effects of the metalloporphyrins injection parameters and the plasma polymerisation conditions can affect the dispersion of the metalloporphyrins and the morphology of the coatings. The stability of the embedded Zn(TPP) molecules was investigated by orbitrap mass spectrometry.



Introduction

Porphyrin and metalloporphyrin-based coatings have attracted a growing interest over the past decade due to their unique optical and electronic properties and have notably found applications as dye-sensitized solar cells,^{1,2,3} photonic devices⁴ or chemical sensors.^{5,6} Porphyrin-sensitized solar cells are usually prepared by soaking semiconducting films in a porphyrin solution, absorbing the porphyrins onto the surface.^{2,7} Stacking and aggregation of the porphyrins, which has been reported to reduce the solar cell efficiency, was prevented by the control of the solution composition and sensitization time.^{3,7} The preparation of porphyrin gas sensing layers has already been achieved by Langmuir-Blodgett techniques,^{8,9} spin-coating,¹⁰ vacuum evaporation¹⁰ and glow-discharge-induced sublimation.¹¹ However, to reduce the problems associated with aggregation, to improve the detection sensitivity and to increase the thermal and mechanical stability of the films, it is more desirable to trap the porphyrins into a suitable matrix.^{12,13} The formed composite films are able to keep the sensing porphyrin molecules in the matrix while allowing the diffusion of small volatile organic compounds (VOCs) to be detected through their pores.¹² Up to date, the synthesis of porphyrin-containing hybrid layers has mainly involved the immobilisation in polymers and plasticizers^{14,15} or sol-gel deposited silica films.¹⁶

Among the wide range of techniques used to grow smart composite films, atmospheric pressure dielectric barrier discharge (AP-DBD) is a new arising technology.¹⁷⁻¹⁹ AP-DBD, which generates low-temperature plasmas, offers the opportunity to work with heat-sensitive particles or substrates.²⁰ In contrast with the limitations in industrial developments of low-pressure plasmas or sol-gel coatings, AP-DBD can be easily adapted on a coil-to-coil production line and is already used for industrial purposes such as thin films deposition, surface cleaning, sterilising or decontaminating, wettability or adhesion enhancement.²¹ Moreover, neither large amounts of unwanted by-products nor waste are produced during the process and inexpensive plasma gases such as nitrogen²² or air²³ can be used. Recently, enzymes have been trapped in a polymer network grown by AP-DBD fed with helium.¹⁷ A water shell surrounding the enzymes, which has likely been formed during the atomizing injection process, was proposed to protect them from the harsh plasma conditions. Whereas, luminescent coatings have been obtained by embedding organic lanthanide-containing coordination polymer particles in a SiO_x matrix polymerised by AP-DBD¹⁸ and hybrid anticorrosion layers have been achieved by dispersing inorganic AlCeO₃ particles in an organosilicon matrix.¹⁹ However, in both cases the chemical composition and size of the particles (*ca.* 100 nm) strongly differs from the one of single porphyrin molecules (*ca.* 1 nm), which are likely to be chemically altered or undergo full cleavage of the macrocycle when exposed to inappropriate plasma conditions.^{24,25} Moreover, in previous AP-DBD studies, the aggregation of the particles was not a critical issue. However, in applications such as gas sensing, stacking of the porphyrins within the matrix would likely disturb the formation of a complex between the porphyrin and the

analyte.²⁶ Most importantly, the porosity of the plasma grown layer has to be carefully controlled such as in classical wet methods, in order to allow the analyte to reach the coordination site of the metalloporphyrins.²⁷

In this paper, we report the formation of composite zinc 5,10,15,20-tetraphenylporphyrin (Zn(TPP)) and polydimethylsiloxane (PDMS) coatings by AP-DBD. Ultraviolet-visible spectroscopy (UV-vis) and scanning electron microscopy (SEM) are used to show how the injection and plasma process parameters influence the dispersion and aggregation of the porphyrin molecules immobilised in the films. Orbitrap mass spectrometry (MS) is employed to study the stability of the Zn(TPP) molecules embedded using optimised preparation conditions. While the loading density and dispersion of the metalloporphyrins in the matrix are determined by X-ray photoelectron spectroscopy (XPS) and secondary ion mass spectrometry (SIMS), respectively.

Experimental Section

Chemicals and Solution Preparation

The zinc 5,10,15,20-tetraphenylporphyrin (Zn(TPP)) molecules to be embedded in the plasma-polymerised layers described in this paper were obtained from Sigma-Aldrich and used without further purification. 50 mg of Zn(TPP) were added to a 25 mL mixture composed of hexamethyldisiloxane (HMDSO) (98.5 %) as matrix precursor and/or solvent, ethanol (99.8 %) or chloroform (TCM) (99.5 %), all obtained from Sigma-Aldrich. To ensure the formation of stable solutions and prevent aggregation, the metalloporphyrins were first dissolved in pure solvent prior to the addition of the matrix precursor.

Plasma Deposition of Composite Coatings

The Zn(TPP)-based layers were deposited on two different substrates: 50 μm thick polyethylene terephthalate (PET) (Goodfellow) for the ultraviolet-visible absorption measurements and 525 μm thick (100) silicon wafers (Siltronix). In a first strategy, liquid layers of the prepared porphyrin solutions were spin-coated onto the substrate at 3000 rpm for 30 seconds and exposed to the plasma after a 60 s delay. In a second approach, the prepared solutions were sprayed onto the substrates, within the plasma reactor chamber, thanks to a 48 kHz ultrasonic atomising nozzle (Sono-Tek Corporation) operating at 2 Watts and fed by a syringe driver delivering $0.2 \text{ mL}\cdot\text{min}^{-1}$. The mean diameter of the produced particles was 50 micrometres. In both cases, the deposited liquid layers were polymerised with an atmospheric pressure dielectric barrier discharge (AP-DBD) device (**Figure 1**), which is made of two flat parallel high voltage electrodes ($1.5 \times 30 \text{ cm}^2$ each) covered with alumina and a moving stage as grounded electrode.

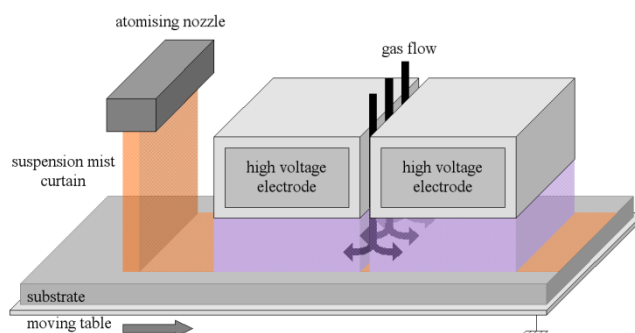


Figure 1 Schematic illustration of the gas-sensing coating deposition from an atomising nozzle and an AP-DBD.

The moving stage speed was varied between 1 and 100 mm·s⁻¹ and the number of passes from 100 to 1, in order to maintain the effective plasma polymerisation time at 30 seconds. The discharge gap between the high voltage electrodes and the substrate placed on the grounded electrode was kept to 1 mm. Plasma was ignited by means of a 1667 Hz modulated 10 kHz sinusoidal signal and the average power dissipated in the discharge was varied from 0.1 to 5 W·cm⁻². The overall plasma process gas flow, composed of argon (99.999 %) or nitrogen (99.999 %) and up to 4 L·min⁻¹ of oxygen (99.999 %), all obtained from Air Liquide, was maintained at 20 L·min⁻¹ for all experiments. Additional HMDSO vapours (500 ppm in the overall gas flow) were injected into the reactor using a classic bubbler system and a constant 0.5 L·min⁻¹ argon or nitrogen carrier flow. A summary of the different parameters investigated for the two strategy investigated can be found in **Table 1**.

Table 1 Solution compositions and plasma polymerization conditions investigated for the two injection strategies explored.

Injection strategy	Spin coater	Ultrasonic atomizer
Starting solution composition	ZnTPP (2 g L ⁻¹) HMDSO/EtOH (100:0 – 0:100 v/v)	ZnTPP (2 g L ⁻¹) HMDSO/EtOH or TCM (100:0 – 0:100 v/v)
Delay prior to exposure to plasma	60 s	1 – 100 s
Plasma power density	0 – 5 W cm ⁻²	0 – 5 W cm ⁻²
Plasma gas composition	N ₂ HMDSO (500ppm)	N ₂ or Ar or N ₂ :O ₂ (100:0 – 80:20) HMDSO (500ppm)
Plasma exposure time	30 s	30 s

Characterisation of the Plasma Layers

UV-visible absorption spectra were obtained with a PerkinElmer Lambda 950 UV-vis-NIR (InGaAs) spectrophotometer equipped with an integrating sphere. Adhesion of the coatings was rated by rubbing firmly their surface with a dry or an ethanol impregnated wipe. The coating removed during the dry wipe test were rated as non-adhesive, while the adhesion of the ones removed by the ethanol wipe test was rated as weak. The

adhesion of coatings which undergo no or very little modifications during the ethanol wipe test were rated as strong and fair, respectively. SEM was performed on a Hitachi SU-70 FE-SEM. Prior to SEM observations, the non-conductive sample was sputter coated with 5 nm of platinum to prevent charging and distortion. FT-IR analysis was performed on a Bruker Hyperion 2000 spectrometer equipped with a Ge-ATR-crystal. XPS analyses were realised with a Kratos Axis-Ultra DLD instrument using a monochromatic Al K α X-ray source ($h\nu = 1486.6$ eV) at pass energy of 20 eV. SIMS measurement was performed with a Cameca NanoSIMS 50. Cs⁺ was used as the primary ion and accelerated at 8 kV towards the sample surface (-8 kV). The primary ion beam was focalised to a spot size of about 100 nm, which corresponds to a 1.5 pA beam current. The fragments studied simultaneously in multicollection mode were ¹⁶O, ¹²C¹⁴N, ²⁸Si, ³⁵Cl, ⁶⁴Zn¹⁶O. Images, with a size of 20 × 20 μm^2 , were recorded as a matrix of 256 × 256 points. Mass resolution (M/ Δ M) was 3000. High resolution mass spectra of the extracted metalloporphyrins were recorded with a Thermo Fisher Scientific LTQ-orbitrap XL mass spectrometer equipped with an electrospray ionisation source (ESI). Extraction of the metalloporphyrins from the plasma coatings was conducted by rinsing the substrate with 10 mL of ethanol. The operation was repeated 40 times and the collected solution concentrated by evaporation. The sample was re-dissolved in 3 mL of ethanol prior to analysis.

Results and Discussion

Optimisation of the Deposition Conditions

Preliminary work to this study has focused on a metalloporphyrins injection method compatible with the atmospheric pressure plasma growth of gas sensing composite coatings. As the lack of volatility of metalloporphyrins prevents the use of classical injection methods,¹¹ a two-step approach was investigated. The first step involved the deposition of a metalloporphyrins-containing liquid layer, followed by a plasma-polymerisation step meant to immobilise the macrocycles in an adherent and cohesive coating. Mixtures composed of zinc 5,10,15,20-tetraphenylporphyrin (Zn(TPP)), hexamethyldisiloxane (HMDSO) or/and ethanol were spin-coated onto transparent PET substrates that were further exposed to an atmospheric pressure dielectric barrier discharge fed with nitrogen. The low solubility of Zn(TPP) in pure HMDSO induced the formation of large porphyrin aggregates and a poor coloration of the formed Zn(TPP) suspension. Due to agglomeration, stacking or crystallisation, the films deposited using pure HMDSO were weakly coloured and UV-vis spectroscopy showed that the absorption properties of the porphyrins were severely modified, as compared to the monomeric porphyrin optical properties in solution (**Figure 2a**). The use of pure solvents to introduce Zn(TPP), coupled to a separate injection of the matrix precursor, was also proved to be inefficient, as the fast evaporation of the solvent led to a prompt agglomeration of the porphyrins prior to their immobilisation in the siloxane matrix cured by AP-DBD.

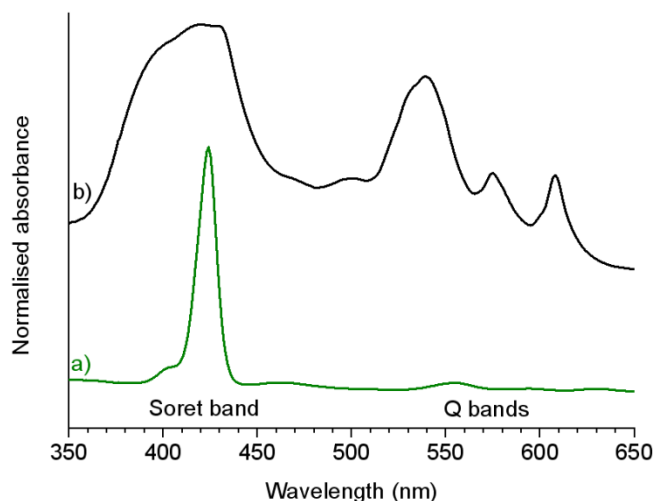


Figure 2 Normalised UV-vis absorption spectra of (a) Zn(TPP) in a HMDSO:EtOH 80:20 (v/v) solution and (b) plasma cured ZnTPP-based PDMS coating deposited by spin-coating from the same solution.

The plasma-polymerised layers obtained from a HMDSO:EtOH 80:20 (v/v) mixture exhibited a purple colouration and the characteristic UV-vis spectrum of porphyrins (Figure 2b), indicating the structure retention of a large portion of porphyrin macrocycles. However, irrespective of the starting solution's composition or the thickness deposited, the ratio between the Soret band and the Q bands of the plasma cured coatings differ strongly from the porphyrin's reference spectrum in solution (Figure 2b). Moreover, the full width at half maximum (FWHM) of the main absorption band, called Soret band, was much larger (75 nm) than the one observed on the reference spectrum of the starting solution (12 nm). This broadening is typical of metalloporphyrin aggregates, as observed for other spin-coated metalloporphyrin films.²⁸ In addition, it should also be noted that the layers had a rather low adherence to the substrate.

For several applications, such as gas sensing, aggregation phenomena have to be avoided to keep the molecular properties or to prevent the hindrance of the coordination site.²⁹ Following the initial observations made, an ultrasonic atomising nozzle was employed to allow the in-line deposition of thinner liquid layers and to drastically reduce the delay before polymerisation (Figure 1). The interval prior to the exposure to plasma, reciprocally proportional to the treatment speed, was shown to strongly affect the absorption properties of the layers (**Table 2**). Indeed, the UV-vis spectrum obtained for the film deposited from a HMDSO:EtOH 80:20 (v/v) mixture with the highest deposition speed ($100 \text{ mm}\cdot\text{s}^{-1}$) and exposed to an $0.1 \text{ W}\cdot\text{cm}^{-2}$ nitrogen fed plasma (**Figure 3b**) was very similar to the one obtained for the reference solution (Figure 2a) with a small FWHM of the Soret band (16 nm). Scanning electron microscopy (SEM) revealed a smooth surface where no second phase or large aggregates were observed (**Figure 4b**). However, the increase of the polymerisation delay from less than 1 second ($100 \text{ mm}\cdot\text{s}^{-1}$) to 90 seconds ($1 \text{ mm}\cdot\text{s}^{-1}$)

Table 2 Soret band characteristics and adhesion rating of the Zn(TPP)-loaded PDMS films deposited from a HMDSO:EtOH 80:20 (v/v) solution for different plasma discharge gas, power density and treatment speed.

Plasma parameters			Soret Band			Adhesion
Plasma gas	Power [W cm ⁻²]	Speed [mm s ⁻¹]	Position [nm]	FWHM [nm]	Area [a.u.]	
n.a.	0.0	100	443	67	11	No adhesion
N ₂	0.1	1	429	44	10	Weak
N ₂	0.1	10	429	31	8	Fair
N ₂	0.1	100	429	16	7	Strong
N ₂	1.0	100	430	15	5	Strong
N ₂	5.0	100	430	12	3	Weak
Ar	0.1	100	427	21	5	Weak
N ₂ :O ₂	0.1	100	436	47	2	Strong
Synthetic air	0.1	100	428	36	1	Strong

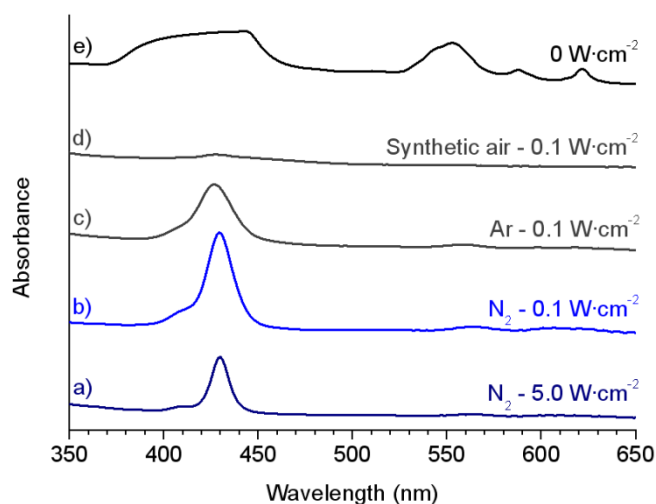


Figure 3 UV-vis absorption spectra of the Zn(TPP)-loaded PDMS films deposited from a HMDSO:EtOH 80:20 (v/v) solution for different plasma discharge gas and power density: (a) Nitrogen as plasma gas and 5 W cm⁻² power density, (b) N₂ and 0.1 W cm⁻², (c) Ar and 0.1 W cm⁻², (d) synthetic air and 0.1 W cm⁻² and (e) non-exposed to plasma.

resulted in the broadening of the Soret band from 16 to 44 nm (Table 2), indicating an agglomeration of metalloporphyrins.²⁸ The UV-vis spectrum of the sample non-exposed to plasma (Figure 3e), corresponding to an infinite polymerisation delay, did show an even broader Soret band with a 67 nm FWHM close to the one observed for the layers prepared by spin-coating (Figure 2b). Moreover, the coating did not show any adhesion to the substrate after evaporation of the solvent and matrix precursor. SEM showed the formation of two different morphological phases (Figure 4a), 1 to 5 μm plate-like crystallites orientated parallel to the substrate and

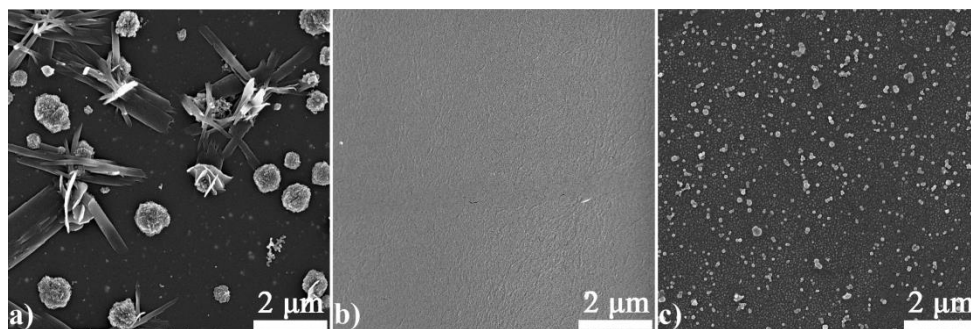


Figure 4 Scanning electron micrographs of the coatings deposited from a HMDSO:EtOH 80:20 (v/v) mixture (a) not exposed to plasma, (b) polymerised by a 0.1 W cm^{-2} plasma fed with nitrogen and (c) polymerised by a 0.1 W cm^{-2} plasma fed with synthetic air.

0.2 to $1 \mu\text{m}$ cauliflower-like particles, which were both identified as ZnTPP aggregates by Energy-Dispersive X-ray spectroscopy (EDX).

The nature of the plasma gas was also found to have a strong influence on the metalloporphyrins integrity. Notably the presence of oxygen in the discharge, which could be useful to control the matrix structure and chemistry, was shown to readily lead to a full disruption of the metalloporphyrins cycles. An oxygen concentration as low as 1 % already induced a drop of intensity of the Soret band by a factor two. As shown in Figure 3d, an almost complete disappearance of the Zn(TPP) was even observed for the film deposited from synthetic air. SEM revealed the presence of numerous particles, with a size distribution varying from 50 to 200 nm, all over the surface of the films produced from synthetic air (Figure 4c). In contrast, the plasma power density was not observed to have a significant influence on the porphyrins integrity. Despite a slight decrease of the absorption bands areas likely to be due to a destruction of a fraction of the porphyrins exposed to a $5 \text{ W}\cdot\text{cm}^{-2}$ plasma, the FWHM of the Soret band was as narrow (12 nm) as the one measured for the reference solution (Figure 3a). Even though the use of higher power densities is expected to induce a more efficient plasma polymerisation of the siloxane monomer, which leads to a faster immobilisation of the metalloporphyrins, adhesion of the layer deposited at the highest power density ($5 \text{ W}\cdot\text{cm}^{-2}$) was poor due to the formation of a non-cohesive powdery layer.

To investigate the influence of the precursor solution's composition, solutions with different amounts of either polar, coordinating EtOH or less polar, weakly coordinating TCM were prepared and used with the optimised plasma deposition conditions described before. Such as observed during the spin-coating approach, the film grown from Zn(TPP) dispersed in pure HMDSO has a weak Soret band intensity (**Figure 5a**) with a broad FWHM (47 nm) suggesting the agglomeration of the Zn(TPP) molecules. Indeed, SEM observations coupled to EDX analysis revealed the presence of large Zn(TPP) crystals at the surface of the coatings (**Figure 6a**).

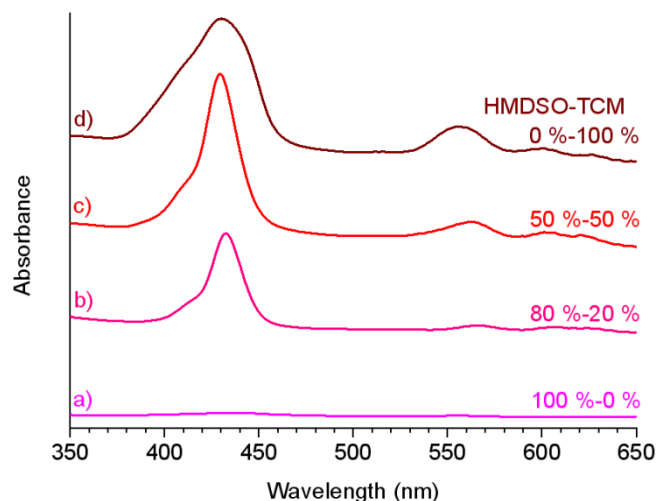


Figure 5 UV-vis absorption spectra of the Zn(TPP)-loaded PDMS films obtained at a speed of 100 mm s^{-1} from a $0.1 \text{ W}\cdot\text{cm}^{-2}$ AP-DBD fed with N_2 and different HMDSO:TCM compositions: (a) 100:0 (v/v), (b) 80:20 (v/v), (c) 50:50 (v/v) and (d) 0:100 (v/v).

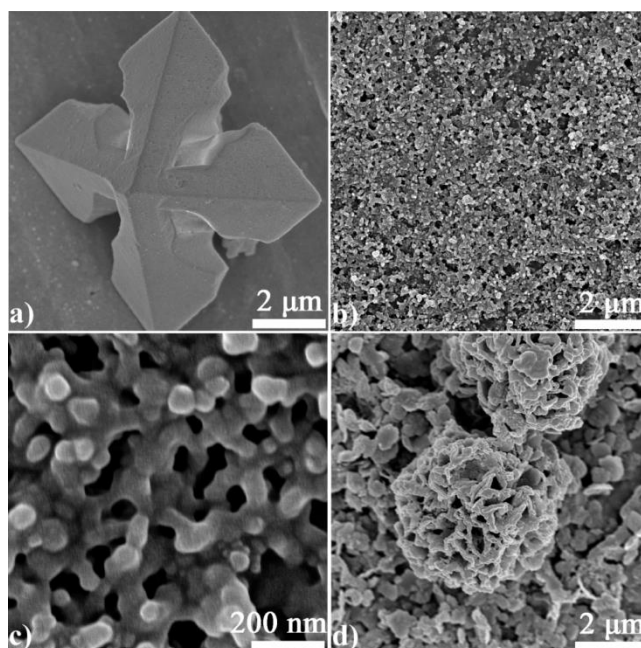


Figure 6 Scanning electron micrographs of the Zn(TPP)-loaded PDMS films obtained from a 0.1 W cm^{-2} AP-DBD fed with N_2 and different HMDSO:TCM compositions: (a) 100:0 (v/v), (b & c) 80:20 (v/v), (d) 50:50 (v/v).

Small admixture of solvent to the starting solution readily led to a narrowing and intensity increase of the Soret band. As shown in **Table 3**, the films obtained from a mixture containing 10 % to 20 % of ethanol or TCM exhibited a FWHM of the Soret band narrower than 20 nm and were adherent to the substrate. SEM did not reveal the formation of a second phase or large aggregates (Figure 4b & Figure 6b). However, the nature of the solvent was found to strongly influence the morphology

Table 3 Soret band characteristics and adhesion rating of the Zn(TPP)-loaded PDMS films deposited from a $0.1 \text{ W}\cdot\text{cm}^{-2}$ AP-DBD fed with N_2 for different starting solution compositions.

Starting solution composition		Soret Band			Adhesion
		Position [nm]	FWHM [nm]	Area [a.u.]	
HMDSO	100:0 v/v	434	47	<1	Strong
HMDSO/EtOH	90:10 v/v	432	15	1	Strong
	80:20 v/v	429	16	7	Strong
	50:50 v/v	432	25	12	Fair
	0:100 v/v	429	49	30	No adhesion
HMDSO/TCM	90:10 v/v	429	14	<1	Strong
	80:20 v/v	432	19	10	Fair
	50:50 v/v	430	21	20	Weak
	0:100 v/v	430	45	27	No adhesion

of the layers. While rather smooth surfaces were obtained from ethanol-based starting solutions (Figure 4b), numerous pores, with sizes ranging from 10 to 200 nm, were observed at the surface of the layers using TCM (Figure 6b & c). These porosities were assumed to be induced by solvent evaporation occurring during the thin film plasma polymerisation. Such as in classical polymer membrane formation, the concentration and evaporation rate have to be carefully controlled. Indeed, the use of higher solvent concentrations increases the nucleation and the pore growth rates, which transform the polymeric membrane into “popcorn” with large flakes and porosities (Figure 6d). The layers, obtained from a HMDSO:solvent 50:50 (v/v) mixture, presented a broader Soret band indicating an increase of the interactions between the metalloporphyrins induced by the decrease of the polymer concentration. It can be noted that no chlorine was detected by EDX or XPS in the later cases, confirming the total evaporation of TCM during the process. For the layers grown from Zn(TPP) dispersed in pure solvent, and therefore in the absence of polymeric membrane, the Soret band was remarkably broad with values ranging from 45 to 49 nm. SEM did show the formation of small features, with a 100 nm mean size, that were identified as Zn(TPP) aggregates.

The FT-IR spectra of the Zn(TPP)-loaded PDMS films obtained using a $0.1 \text{ W}\cdot\text{cm}^{-2}$ AP-DBD fed with N_2 from either a HMDSO:EtOH (80:20, v/v) or a HMDSO:TCM (80:20, v/v) solution (**Figure 7**), confirms the reticulation of the siloxane precursor into plasma-polymerised PDMS. The strong and broad band observed at 1051 cm^{-1} is assigned to a Si-O-Si network vibration, while the peaks at 2960 and 2904 cm^{-1} ($\nu(\text{CH}_3)$), 1410 cm^{-1} ($\nu^a(\text{CH}_3)$), 1255 cm^{-1} ($\delta^s(\text{Si-CH}_3)$), 847 cm^{-1} ($\rho(\text{CH}_3)$ and $\nu(\text{Si-C})$), 806 cm^{-1} and 758 cm^{-1} ($\nu(\text{Si-CH}_3)$) indicate the high retention of methyl groups from the siloxane monomer.³⁰ The peaks observed at 1555 cm^{-1} ,

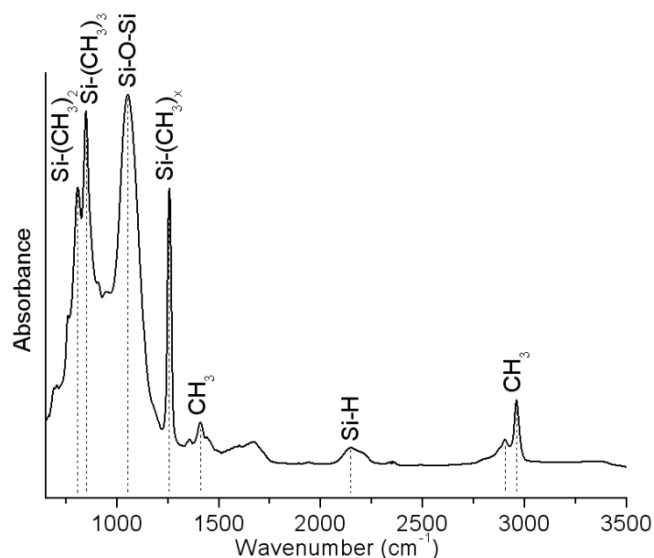


Figure 7 FT-IR spectrum of the metalloporphyrins-containing PDMS AP-DBD coating obtained using a 0.1 W cm^{-2} AP-DBD fed with N_2 from either a HMDSO:EtOH 80:20 (v/v).

1655 cm^{-1} and 2150 cm^{-1} , commonly observed for plasma-polymerised PDMS coatings, are attributed to C=N and Si-H, respectively.²² Due to a possible overlapping of the strong bands related to the siloxane network with the metalloporphyrin bands, expected around $700\text{--}800 \text{ cm}^{-1}$ ($\delta(\beta\text{-H}$ on the pyrrole rings)), 1000 cm^{-1} ($\nu(\text{C-C})$ and $\nu(\text{C-N})$) and 1070 cm^{-1} ($\delta(\text{C-H})$),³¹ no clear-cut evidence of Zn(TPP) in the PDMS layer could be detected by FT-IR.

Investigation of the Zn(TPP) Loading and Integrity of the Porphyrin Macrocycle

Two coatings elaborated from the most successful conditions previously identified were further characterised by X-ray photoelectron spectroscopy (XPS), secondary ion mass spectrometry (SIMS) and Orbitrap mass spectrometry (MS) to investigate the loading density, dispersion and integrity of the ZnTPP molecules, respectively. The two films were deposited using a $0.1 \text{ W}\cdot\text{cm}^{-2}$ AP-DBD fed with N_2 from either a HMDSO:EtOH (80:20, v/v) or a HMDSO:TCM (80:20, v/v) solution.

Despite that no evidence of Zn(TPP) in the PDMS layer could be detected by FT-IR, the presence of ZnTPP was confirmed by UV-vis and the presence of zinc in the layer was both detected by X-ray photoelectron spectroscopy (XPS) and nano secondary ion mass spectrometry (SIMS). The zinc content in the embedded metalloporphyrin, $\text{C}_{44}\text{H}_{28}\text{N}_4\text{Zn}$, being rather low (ca. 2 %), only traces of the zinc element (ca. $0.3 \% \pm 0.1 \%$) were detected in the layers, which were mainly composed of silicon (16 %), oxygen (20 %), carbon (59 %) and nitrogen (5 %). This suggests a relatively high loading of the metalloporphyrins, which represent $14 \% (\pm 6 \%)$ of the composite layer if unaltered. Secondary ion mass spectrometry revealed the presence of zinc all over the surface of the coatings, suggesting a rather homogeneous loading of the Zn(TPP)

metalloporphyrins. Furthermore, orbitrap mass spectrometry (MS) of ethanol extracts of the porous plasma deposited layer from a HMDSO:TCM 80:20 (v/v) solution, did confirm the integrity of the Zn(TPP) molecules embedded. The experimental isotopic pattern of the molecular ion peak, presented in **Figure 8**, matches the expected pattern of Zn(TPP).

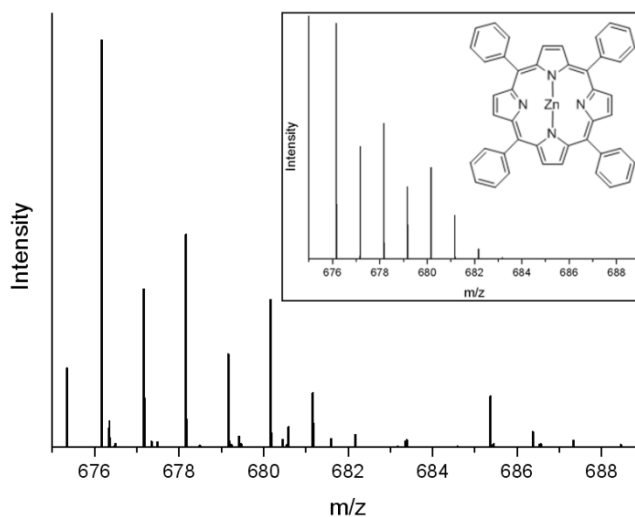


Figure 8 Experimental mass spectrum of ethanol extracts of the plasma layers acquired in the LTQ-orbitrap mass spectrometer and (inset) calculated isotopic pattern of the molecular ion peak of Zn(TPP).

Discussion

The AP-DBD method described herein successfully allows the non-covalent immobilisation of metalloporphyrins in a polymer matrix thanks to their simultaneous injection with the matrix precursor and a suitable solvent. The addition of solvent prevents the porphyrin agglomeration or stacking in the starting solution, ensuring a good dispersion of the porphyrins in the resulting layers. The UV-vis spectra of the coatings obtained for the optimised deposition conditions, similar in shape and FWHM of the Soret-band (15-19 nm) to the one of the metalloporphyrins dissolved in a HMDSO:EtOH 80:20 (v/v) solution, suggest the existence of ZnTPP in a monomeric, non-aggregated form within the polymer matrix. The plasma deposition of such composite layers, in which the single molecule properties rather than the bulk ones are thus enhanced, might be of great interest in the preparation of porphyrin-sensitized solar cells,^{2,32} photon up-conversion layers,³³ photonic devices⁴ or chemical sensors¹⁴ where porphyrins stacking and aggregation have been reported to reduce the overall efficiency.

SEM did reveal the formation of mesoporous structures, which might be of particular interest for numerous applications, including gas sensing,³⁴ catalysis,³⁵ drug release³⁶ or anchoring of different active guests,³⁷ where accessible pore sizes and high surface areas are desired. The presence of a suitable solvent, such as in classical polymer membrane creation, favours the formation of porosity while evaporating

during the thin film plasma polymerisation. The solution concentration and solvent evaporation rate have to be carefully controlled to reach the targeted morphology. Therefore, the method described in the present work offers an efficient and industrially compatible alternative to the wet methods reported to date to grow such a mesoporous assembly.^{14,15,16}

The Zn(TPP)-loaded siloxane layers described in this work could be employed as colorimetric gas sensors. In contrast with reported ZnTPP-loaded silicone elastomers or thermoplastics gas sensors,¹⁴ no changes of the UV-vis spectra were observed after a one year storage in the laboratory atmosphere. The plasma-polymerised siloxane scaffold immobilises the metalloporphyrins and ensures mechanical and water stability of the sensor device. The material, which can be stored under ambient conditions, could therefore be of great interest in the food packaging industry.¹¹ However, ZnTPP is not particularly selective for a given analyte and does not undergo a large colour shift upon analyte binding. Therefore, experiments involving a new class of *trans*-A₂B₂-porphyrins that exhibit stronger colour shifts upon exposure to triethylamine and a higher selectivity are currently in progress.³⁸ Moreover, further detailed analyses are underway in order to investigate the metalloporphyrin arrangements in the coatings and interactions within the plasma films.

Conclusion

In conclusion, the plasma deposition method described in this paper is an effective route towards the immobilisation of non-aggregated metalloporphyrins in a mesoporous structure and a useful alternative to classical wet methods employed to prepare such coatings. UV-vis, orbitrap MS and SEM showed the influence of the starting solution composition and the plasma polymerisation parameters on the dispersion and integrity of the metalloporphyrins and the morphology of the layers. Composite coatings grown from a HMDSO:EtOH (80:20, v/v) or a HMDSO:TCM (80:20, v/v) solution and a 0.1 W·cm⁻² AP-DBD polymerisation fed with N₂, exhibited a narrow Soret band indicating a good dispersion of the metalloporphyrin molecules. MS of ethanol extracts of the deposited layer revealed the expected mass spectrum of Zn(TPP) further corroborating its integrity.

Acknowledgements: The Luxembourgish “Fonds National de la Recherche” (FNR) is thanked for financial support through the SurfAmine project. Dr. J.-N. Audinot, Dr. J. Guillot and Dr. G. Frache from the CRP-Gabriel Lippmann are hereby gratefully acknowledged for their skilful characterisations and valuable discussions.

Received: September 21, 2012; Revised: November 5, 2012; Accepted: December 12, 2012; DOI: 10.1002/ppap.201200132

Keywords: dielectric barrier discharges (DBD); composites; hexamethyldisiloxane (HMDSO); immobilization of molecules; UV-vis spectroscopy

References

- 1 A. Yella, H.-W. Lee, H. N. Tsao, C. Yi, A. K. Chandiran, M. K. Nazeeruddin, E. W.-G. Diao, C.-Y. Yeh, S. M. Zakeeruddin, M. Grätzel, *Science* **2011**, *334*, 629.
- 2 H. Imahori, S. Kang, H. Hayashi, M. Haruta, H. Kurata, S. Isoda, S. E. Canton, Y. Infahsaeng, A. Kathiravan, T. Pascher, P. Chabera, A. P. Yartsev, V. Sundstrom, *J. Phys. Chem. A* **2011**, *115*, 3679.
- 3 M. G. Walter, A. B. Rudine, C. C. Wamser, *J. Porphyrins Phthalocyanines* **2010**, *14*, 759.
- 4 Z. M. Liu, A. A. Yasseri, J. S. Lindsey, D. F. Bocian, *Science* **2003**, *302*, 1543.
- 5 N. A. Rakow, K. S. Suslick, *Nature* **2000**, *406*, 710.
- 6 N. A. Rakow, A. Sen, M. C. Janzen, J. B. Ponder, K. S. Suslick, *Angew. Chem. Int. Ed.* **2005**, *44*, 4528.
- 7 M. Planells, A. Forneli, E. Martínez-Ferrero, A. Sánchez-Díaz, M. A. Sarmentero, P. Ballester, E. Palomares, B. C. O'Regan, *Appl. Phys. Lett.* **2008**, *92*, 153506.
- 8 T. H. Richardson, C. M. Dooling, L. T. Jones, R. A. Brook, *Adv. Colloid Interface* **2005**, *116*, 81.
- 9 C. M. Dooling, O. Worsfold, T. H. Richardson, R. Tregonning, M. O. Vysotsky, C. A. Hunter, K. Kato, K. Shinbo, F. Kaneko, *J. Mater. Chem.*, **2001**, *11*, 392.
- 10 M. Tonezzer, A. Quaranta, G. Maggioni, S. Carturan, G. D. Mea, *Sens. Actuators B* **2007**, *122*, 620.
- 11 M. Tonezzer, G. Maggioni, E. Dalcanale, *J. Mater. Chem.* **2012**, *22*, 5647.
- 12 B. Johnson-White, M. Zeinali, K. M. Shaffer, C. H. Patterson, P. T. Charles, M. A. Markowitz, *Biosens. Bioelectron.* **2007**, *22*, 1154.
- 13 S. H. Lim, L. Feng, J. W. Kemling, C. J. Musto, K. S. Suslick, *Nat. Chem.* **2009**, *1*, 562.
- 14 F. A. Nwachukwu, M. G. Baron, *Sens. Actuators B* **2003**, *90*, 276.
- 15 A. A. Vaughan, M. G. Baron, R. Narayanaswamy, *Anal. Commun.* **1996**, *33*, 393.
- 16 S. Tao, G. Li, H. Zhu, *J. Mater. Chem.* **2006**, *16*, 4521.
- 17 P. Heyse, A. Van Hoeck, M. B. J. Roeffaers, J.-P. Raffin, A. Steinbüchel, T. Stöveken, J. Lammertyn, P. Verboven, P. A. Jacobs, J. Hofkens, S. Paulussen, B. F. Sels, *Plasma Process. Polym.* **2011**, *8*, 965.
- 18 N. D. Boscher, P. Choquet, D. Duday, N. Kerbellec, J.-C. Lambrechts, R. Maurau, *J. Mater. Chem.* **2011**, *21*, 18959.
- 19 D. Del Frari, J. Bour, J. Bardou, O. Buchheit, C. Arnoult, D. Ruch, *J. Nanosci. Nanotechnol.* **2009**, *9*, 1.
- 20 C. Tendero, C. Tixier, P. Tristant, J. Desmaison, P. Leprince, *Spectrochim. Acta B* **2006**, *61*, 2.
- 21 U. Kogelschatz, *Plasma Chem. Plasma P.* **2003**, *23*, 1.
- 22 N. D. Boscher, P. Choquet, D. Duday, S. Verdier, *Plasma Process. Polym.* **2010**, *7*, 163.
- 23 N. D. Boscher, P. Choquet, D. Duday, S. Verdier, *Surf. Coat. Tech.* **2011**, *205*, 5350.
- 24 M. Tonezzer, G. Maggioni, A. Quaranta, S. Carturan, G. Della Mea, *Sens. Actuators B* **2009**, *136*, 290.
- 25 K. Nakamura, M. Watanabe, M. Zhou, M. Fujishima, M. Tsuchiya, T. Handa, S. Ishii, H. Noguchi, K. Kashiwagi, Y. Yoshida, *Thin Solid Films* **1999**, *345*, 99.
- 26 G. Giancane, L. Valli, *Adv. Colloid Interfac.* **2012**, *171*, 17.
- 27 R. S. Dudhe, J. Sinha, A. Kumar, V. R. Rao, *Sens. Actuators B* **2010**, *148*, 158.
- 28 B. Wang, Z. Chen, X. Zuo, Y. Wu, C. He, X. Wang, Z. Li, *Sens. Actuators B* **2011**, *160*, 1.
- 29 A. Gulino, P. Mineo, I. Fragalà, *Inorg. Chim. Acta* **2008**, *361*, 3877.
- 30 N. D. Boscher, P. Choquet, D. Duday, S. Verdier, *Surf. Coat. Technol.* **2010**, *205*, 2438.
- 31 Y.-H. Zhang, W.-J. Ruan, Z.-Y. Li, Y. Wu, J.-Y. Zheng, *Chem. Phys.* **2005**, *315*, 201.

- 32 M. K. Nazeeruddin, R. Humphry-Baker, D. L. Officer, W. M. Campbell, A. K. Burrell, M. Grätzel, *Langmuir* **2004**, *20*, 6514.
- 33 J. S. Lissau, J. M. Gardner, A. Morandeira, *J. Phys. Chem. C* **2011**, *115*, 23226.
- 34 A. Palaniappan, S. Moochhala, F. E. H. Tay, X. Su, N. C. L. Phua, *Sens. Actuators B* **2008**, *129*, 184.
- 35 A. Taguchi, F. Schüth, *Micropor. Mesopor. Mater.* **2005**, *77*, 1.
- 36 N. Ehlert, M. Badar, A. Christel, S. J. Lohmeier, T. Luessenhop, M. Stieve, T. Lenarz, P. P. Mueller, P. Behrens, *J. Mater. Chem.* **2011**, *21*, 752.
- 37 D. F. Rohlfiing, J. Rathousky, Y. Rohlfiing, O. Bartels, M. Wark, *Langmuir* **2005**, *21*, 11320.
- 38 P. Heier, C. Förster, D. Schollmeyer, N. Boscher, P. Choquet, K. Heinze, *Dalton Trans.*, DOI: 10.1039/c2dt31943h.

3.2

Atmospheric Pressure Plasma Polymerisation of Metallo-porphyrins Containing Mesoporous Membranes for Gas-sensing Applications

N. Boscher, D. Duday, P. Heier, K. Heinze,
F. Hilt, P. Choquet

Surface and Coatings Technology **2013**, 243,
48 – 52.

Abstract

Metalloporphyrins are embedded in an organosilicon matrix by an easily up-scalable atmospheric pressure dielectric barrier discharge method. The integrity of the metalloporphyrins, followed by UV–visible spectroscopy, is successfully preserved and their aggregation prevented. The single molecule properties, rather than the bulk ones, are thus enhanced. Exposure to triethylamine, which reaches the metalloporphyrins through the pores of the organosilicon membrane, led to a shift in the absorption spectrum and confirms the gas sensing potential of such coatings.

Introduction

Porphyrin and metalloporphyrin-based colorimetric gas sensors have gained growing interest over the past decade [1,2]. Through changes in their optical absorption spectra, the sensors allow the rapid detection of a wide range of gases including 2,4,6-trinitrotoluene (TNT) [3], NO₂ [4], 4-aminophenol [5], NH₃ and triethylamine [6]. Porphyrin gas sensing layers have been deposited by Langmuir-Blodgett [4], vacuum evaporation [7,8], spin-coating [7,8], and low-pressure plasma techniques [8]. However, to reduce the problems associated with aggregation and to increase the detection sensitivity as well as the thermal and mechanical stability of the films, it is highly desirable to embed the porphyrins into a suitable matrix [9,10]. The composite films formed must be able to keep the sensing porphyrin molecules within the matrix while allowing the diffusion of volatile organic compounds to be detected through their pores. Up to date, the synthesis of porphyrin-containing hybrid layers has mainly involved immobilisation in polymers and plasticizers [6,11] or sol-gel deposition [3].

Among the wide range of techniques used to grow smart composite films, atmospheric pressure dielectric barrier discharge (AP-DBD) is a new arising technology. AP-DBD, which generates low-temperature plasmas, offers the opportunity to work with heat-sensitive particles or substrates. In contrast with the limitations in industrial developments of low-pressure plasmas or sol-gel coatings, AP-DBD can be easily adapted on a coil-to-coil production line and is already used for industrial purposes such as thin film deposition, surface cleaning, wettability or adhesion enhancement [12]. In recent years, the formation of composite layers by AP-DBD has been explored. Hybrid anticorrosion layers have been achieved by dispersing inorganic AlCeO₃ particles in an organosilicon matrix [13]. Whereas luminescent coatings have been obtained by embedding organic lanthanide-containing coordination polymer particles in a SiO_x matrix polymerised by AP-DBD [14]. However, in both cases the size of the particles (ca. 100 nm) strongly differs from the one of single porphyrin molecules (ca. 1 nm), which are likely to be altered or undergo full disruption of their macrocycle when exposed to inappropriate plasma conditions [15,16]. Moreover, in previous works, aggregation of the particles was not a critical point. However, stacking of the porphyrins within the matrix would possibly hinder the formation of a complex between the coordination site and the analyte [17]. Most importantly, the porosity of the plasma grown layer has to be carefully controlled in order to allow the analyte to reach the coordination site of the metalloporphyrins [18].

In this work, we report, for the first time, the embedment of aqua(chloro)(5,10,15,20-tetraphenylporphyrinato) chromium(III) (Cr^{III}Cl(TPP)(H₂O)) in a mesoporous plasma-polymerised polydimethylsiloxane (PDMS) matrix. The integrity of the metalloporphyrins was assessed by UV-visible (UV-vis) spectroscopy, while their dispersion and loading density were determined by secondary ion mass spectrometry (SIMS) and X-ray photoelectron spectroscopy (XPS), respectively. The morphology of

the layer was characterised by scanning electron microscopy (SEM) and the reticulation of the plasma-polymer membrane was evaluated by Fourier-transform infrared spectroscopy (FT-IR). The optical sensing capabilities of the layer towards triethylamine were demonstrated.

Experimental

Materials and deposition procedure

The Cr^{III}Cl(TPP)(H₂O) metalloporphyrins embedded in the plasma polymerised coating described in this paper were synthesised according to reported literature procedure [19]. 7.5 mg of the Cr^{III}Cl(TPP)(H₂O) metalloporphyrins were dissolved in a solution composed of 5 mL of dichloromethane (DCM) (99.8%) and 20 mL of hexamethyldisiloxane (HMDSO) (98.5%), both obtained from Sigma-Aldrich and used without further purification. The prepared solution was sprayed by an ultrasonic atomising nozzle (Sono-Tek Corporation) operating at 48 kHz and fed by a syringe driver delivering 0.2 mL min⁻¹ onto 50 μm thick transparent polyethylene terephthalate foils (Goodfellow) placed on the moving stage of an AP-DBD reactor [14]. The moving stage speed, set-up to 6 m min⁻¹, allowed to promptly expose the deposited liquid layer to the plasma discharge in order to polymerise the siloxane precursor. Delay between the liquid layer deposition and plasma treatment was one second. The AP-DBD reactor consists of two flat parallel high voltage electrodes (1.5 × 30 cm²) covered with alumina and the moving stage as grounded electrode [20]. The discharge gap between the high voltage electrode and the substrate placed on the grounded electrode was maintained to 1 mm. The AP-DBD reactor was fed by a 20 L min⁻¹ N₂ flow (Air Liquide, 99.999 %) containing 500 ppm of HMDSO. The plasma discharge was ignited by means of a 10 kHz sinusoidal signal, chopped by a 1667 Hz rectangular signal [20]. The operating discharge power density was maintained to 0.1 W cm⁻². 100 passes, corresponding to a 30 seconds effective deposition times, were performed.

Thin film characterisations

SEM was performed on a Hitachi SU-70 FE-SEM. Prior to SEM observations, the non-conductive sample was sputter coated with 5 nm of platinum to prevent charging and distortion. FT-IR analysis was performed on a Bruker Hyperion 2000 spectrometer equipped with a Ge-ATR-crystal. XPS analyses were realised with a Kratos Axis-Ultra DLD instrument using a monochromatic Al K α X-ray source ($h\nu = 1486.6$ eV) at pass energy of 20 eV. SIMS measurement was performed with a Cameca NanoSIMS 50. Cs⁺ was used as the primary ion and accelerated at 8 kV towards the sample surface (-8 kV). The primary ion beam was focalised to a spot size of about 100 nm, which corresponds to a 1.5 pA beam current. The fragments studied simultaneously in multicollection mode were ¹⁶O, ¹²C¹⁴N, ²⁸Si, ³⁵Cl, ⁵²Cr¹⁴N and ⁵²Cr¹⁶O. Images, with a size of 20 × 20 μm², were recorded as a matrix of 256 × 256 points. Mass resolution (M/ΔM) was 3000. UV-visible absorption spectra were obtained with a PerkinElmer Lambda 950

UV-vis-NIR (InGaAs) spectrophotometer equipped with an integrating sphere. The optical sensing capabilities of the plasma polymerised $\text{Cr}^{\text{III}}\text{Cl}(\text{TPP})(\text{H}_2\text{O})$ -based coating, followed by UV-vis, were investigated by exposing the sample to triethylamine. Before any triethylamine exposure, an optical absorption spectrum of the film was acquired in air over the visible range (350-700 nm). Then, the sample was exposed to saturated triethylamine vapours in a closed cuvette and a second optical absorption spectrum was acquired. The cuvette was further flushed with air for 1 h to recover the sample. In order to highlight the absorption changes, absorbance difference spectra were calculated as the subtraction of the pre-exposure spectrum to the post-exposure spectrum. For comparison, the absorption spectrum of $\text{Cr}^{\text{III}}\text{Cl}(\text{TPP})(\text{H}_2\text{O})$ in dichloromethane was normalised prior the calculation to the film spectrum.

Results and discussion

The composite coating described in this paper exhibits a uniform pale green colour and was adherent to the substrate. Neither visually noticeable cracks nor particles were observed at the surface of the sample. Furthermore, the sample is shown to be stable in water. Scanning electron microscopy (SEM) revealed spherical features assembled in a porous structure (Fig. 1a). Both grains and pores were shown to have a mean grain size lower than 50 nm (Fig. 1b). At highest magnification, the pattern observed at the surface of the particles is attributed to the sputtered platinum grains. In contrast to previous hybrid coatings obtained by AP-DBD [14,15], no second phase was observed by SEM. This is consistent with the initial size of the metalloporphyrins and suggests that they do not form large aggregates. The thickness, measured by cross-section SEM, was 1 μm .

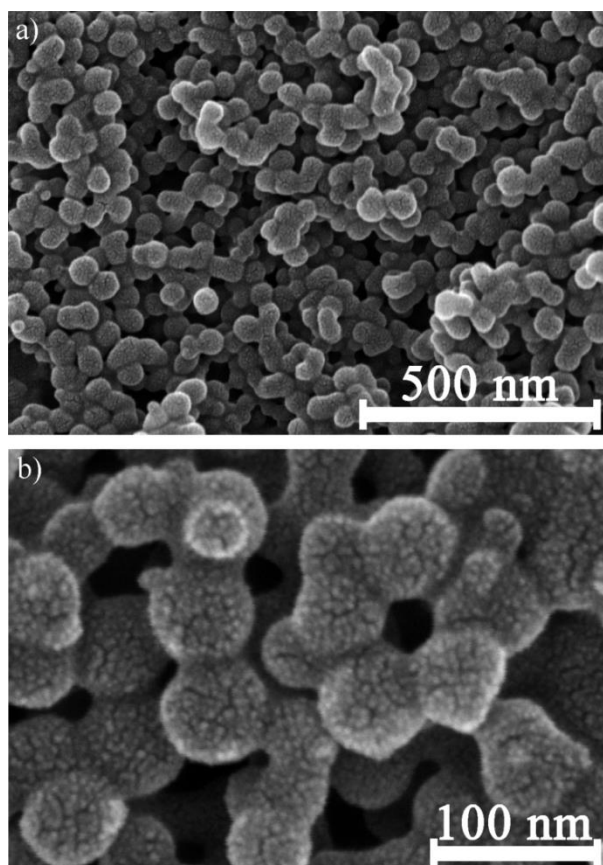


Figure 1 Scanning electron micrograph of the plasma polymerised $\text{Cr}^{\text{III}}(\text{TPP})(\text{Cl})(\text{H}_2\text{O})$ -based coating at (a) intermediate magnification ($\times 100,000$) and (b) high magnification ($\times 350,000$).

Fourier-transform infrared spectroscopy (FT-IR), shown in Fig. 2, confirms the formation of a PDMS-like coating. The strong and broad band observed at 1051 cm^{-1} is assigned to a Si-O-Si network vibration, while the peaks at 2960 and 2904 cm^{-1} ($\nu(\text{CH}_3)$), 1410 cm^{-1} ($\nu_{\text{a}}(\text{CH}_3)$), 1255 cm^{-1} ($\delta_{\text{s}}(\text{Si-CH}_3)$), 847 cm^{-1} ($\rho(\text{CH}_3)$ and $\nu(\text{Si-C})$), 806 cm^{-1} and 758 cm^{-1} ($\nu(\text{Si-CH}_3)$) indicate the high retention of methyl groups from the siloxane monomer [20]. Due to a possible overlapping of the strong bands related to the siloxane network with the metalloporphyrin bands, expected around $700\text{-}800\text{ cm}^{-1}$ ($\nu(\text{C-H})$), 1000 cm^{-1} ($\nu(\text{C-C})$ and $\nu(\text{C-N})$) and 1070 cm^{-1} ($\delta(\text{C-H})$) [21], no evidence of $\text{Cr}^{\text{III}}\text{Cl}(\text{TPP})(\text{H}_2\text{O})$ in the plasma polymerised coating could be detected by FT-IR.

Nevertheless, the presence of chromium in the plasma polymerised coating was both detected by X-ray photoelectron spectroscopy (XPS) and nano secondary ion mass spectrometry (SIMS). The chromium content in the embedded metalloporphyrin, $\text{C}_{44}\text{H}_{28}\text{N}_4\text{Cr}$, being rather low (ca. 1.4 %), only traces of the Cr element (ca. 0.3%) were detected in the plasma polymerised $\text{Cr}^{\text{III}}\text{Cl}(\text{TPP})(\text{H}_2\text{O})$ -based coating, which was mainly composed of silicon (18%), oxygen (21%), carbon (57%) and nitrogen (4%). This suggests a relatively high loading of the metalloporphyrins, which could thus represent up to 20% of the composite layer if unaltered. In order to perform comparative

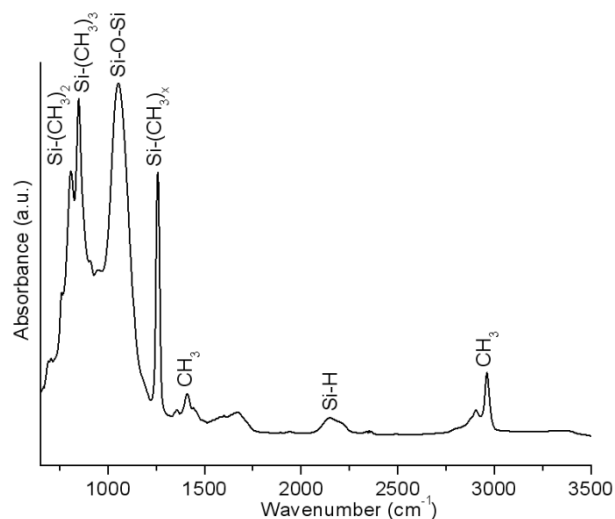


Figure 2 FT-IR spectrum of the plasma polymerised $\text{Cr}^{\text{III}}\text{Cl}(\text{TPP})(\text{H}_2\text{O})$ -based coating.

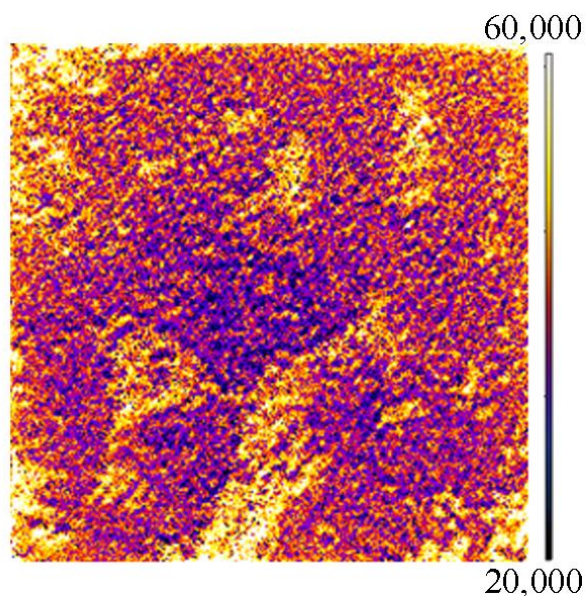


Figure 3 $20 \times 20 \mu\text{m}^2$ secondary ion mass spectrometry image of the $^{52}\text{Cr}^{14}\text{N}/^{28}\text{Si}$ ratio derived from $(^{52}\text{Cr}^{14}\text{N})$ and (^{28}Si) .

analyses of the surface, it is essential to normalize the SIMS signal intensity of the element ($^{52}\text{Cr}^{14}\text{N}$) with the ion intensity of the major element (^{28}Si) [22]. This method allows to reduce the topography and matrix effect. The SIMS image of the $^{52}\text{Cr}^{14}\text{N}/^{28}\text{Si}$ ratio derived from $(^{52}\text{Cr}^{14}\text{N})$ and (^{28}Si) presented in Fig. 3, revealed the dispersion of the chromium element within the siloxane matrix. The ratio intensity, varying from less than a factor of three between the different areas observed, suggested a rather homogeneous loading of the $\text{Cr}^{\text{III}}\text{Cl}(\text{TPP})(\text{H}_2\text{O})$ metalloporphyrins in the porous layer. The light heterogeneities observed are assumed to be linked to the injection method generating a mist of fine droplets, which randomly deposited at the surface of the substrate.

UV–visible absorption spectroscopy of the plasma polymerised $\text{Cr}^{\text{III}}\text{Cl}(\text{TPP})(\text{H}_2\text{O})$ -based coating showed the typical absorption spectrum of integer porphyrins (Fig. 4b) with an intense Soret absorption band observed at 450 nm. The weaker Q bands were observed at 569 and 610 nm. These positions were shown to be slightly red-shifted in comparison to the ones observed on the UV-vis spectrum obtained for $\text{Cr}^{\text{III}}\text{Cl}(\text{TPP})(\text{H}_2\text{O})$ dissolved in dichloromethane. The $\pi(a_{2u}, a_{1u}) \rightarrow d(e_g)$ charge-transfer absorption band was observed at 399 nm indicating the presence of the central metal ion [23]. A slight broadening of the Soret band, with a full-width at half-maximum (FWHM) varying from 12 nm for the solution spectrum to 19 nm for the plasma polymerised $\text{Cr}^{\text{III}}\text{Cl}(\text{TPP})(\text{H}_2\text{O})$ -based coating, was also observed. This red-shift and weak broadening of the absorption bands are attributed to porphyrin-porphyrin and/or porphyrin-matrix interactions in the solid state [3]. Nevertheless, the good match between the plasma polymerised $\text{Cr}^{\text{III}}\text{Cl}(\text{TPP})(\text{H}_2\text{O})$ -based coating spectrum and the solution spectrum, reported as a reference on Fig. 4a, indicates that the chromium metalloporphyrin was preserved during the plasma process. This result contrasts with previous plasma deposited porphyrin-based coatings that have shown a large broadening (FWHM = 45–80 nm) and loss of intensity [15,16] or even disappearance of the Soret band [16].

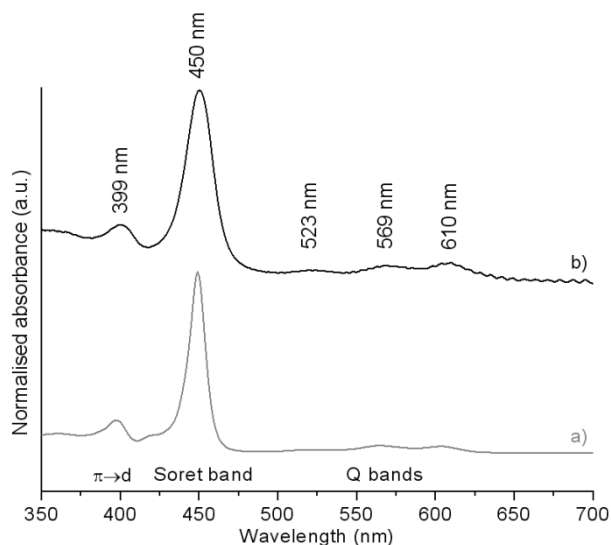


Figure 4 UV-vis absorption spectra of (a) $\text{Cr}^{\text{III}}\text{Cl}(\text{TPP})(\text{H}_2\text{O})$ dissolved in dichloromethane and (b) of the plasma polymerised $\text{Cr}^{\text{III}}\text{Cl}(\text{TPP})(\text{H}_2\text{O})$ -based coating. The interferences observed between 600 and 700 nm are associated to the polyethylene foil substrate.

The optical sensing capability of the plasma polymerised $\text{Cr}^{\text{III}}\text{Cl}(\text{TPP})(\text{H}_2\text{O})$ -based coating was investigated by exposing the sample to a triethylamine saturated gas atmosphere. The spectrum, acquired over the visible range, did show a blue-shift of the Soret and Q bands. The hypsochromic 5 nm shift of the Soret band indicates the successful permeation of triethylamine through the siloxane matrix and the formation of complexes between the metalloporphyrins embedded in the coating and the triethylamine analyte (Fig. 5). The observed shift was smaller compared to the spectral

changes in solution (ca. 12 nm), suggesting that triethylamine did not coordinate to all the porphyrins present in the layer. Moreover, the slight broadening of the Soret band, from 19 nm to 21 nm FWHM, suggests that the porphyrin environment was more diverse after exposure to triethylamine, namely, with the presence of both $\text{Cr}^{\text{III}}\text{Cl}(\text{TPP})(\text{H}_2\text{O})$ and triethylamine-coordinated $\text{Cr}^{\text{III}}\text{Cl}(\text{TPP})(\text{NEt}_3)$.

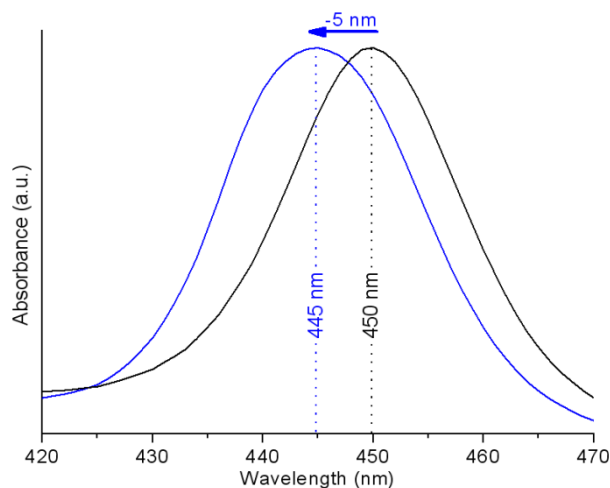


Figure 5 UV-vis absorption spectra of the as-deposited polymerised $\text{Cr}^{\text{III}}\text{Cl}(\text{TPP})(\text{H}_2\text{O})$ -based coating (right) and plasma polymerised $\text{Cr}^{\text{III}}\text{Cl}(\text{TPP})(\text{H}_2\text{O})$ -based coating exposed to a saturated triethylamine atmosphere (left).

Changes in the metalloporphyrin spectrum are highlighted by the absorbance difference spectrum of the film upon exposure to saturated NEt_3 vapours and prior exposure (Fig. 6). The separation between the peak and the trough positions ($\Delta\lambda = 16$ nm) measured for the plasma polymerised $\text{Cr}^{\text{III}}\text{Cl}(\text{TPP})(\text{H}_2\text{O})$ -based coating is similar to the one obtained for the $\text{Cr}^{\text{III}}\text{Cl}(\text{TPP})(\text{H}_2\text{O})$ solution ($\Delta\lambda = 15$ nm), confirming the formation of $\text{Cr}^{\text{III}}\text{Cl}(\text{TPP})(\text{NEt}_3)$ complexes in the layer. However, a difference in the total change intensities (ΔI), providing indication on the sensitivity of the sensor, was observed. The total intensity change obtained for the plasma polymerised $\text{Cr}^{\text{III}}\text{Cl}(\text{TPP})(\text{H}_2\text{O})$ -based coating (Fig. 6b) represents 38% of the one measured for the $\text{Cr}^{\text{III}}\text{Cl}(\text{TPP})(\text{H}_2\text{O})$ solution (Fig. 6a). This observation confirms that not all the $\text{Cr}^{\text{III}}\text{Cl}(\text{TPP})(\text{H}_2\text{O})$ metalloporphyrins presented in the layer coordinate to triethylamine.

Fig. 7 depicts the Soret band position of the plasma polymerised $\text{Cr}^{\text{III}}\text{Cl}(\text{TPP})(\text{H}_2\text{O})$ -based coating over a cycle of exposure to triethylamine and recovery. The position of the Soret band, illustrated by the inner UV-vis figures, is shown to be driven by the presence of triethylamine in the gas phase. Following a one minute exposure to triethylamine, which led to a 5 nm hypsochromic shift of the initial Soret band position (Fig. 5 & 7), a 4 nm bathochromic shift was observed after a one hour purge of the sample with dinitrogen suggesting nearly quantitative reversibility.

The non-volatile character of metalloporphyrins required a simultaneous injection with the matrix precursor when elaborating such composite layers from an

atmospheric pressure plasma method. In present case, the addition of solvent prevents their agglomeration or stacking in the starting solution, ensuring a good dispersion of the porphyrins in the layers. The single molecule properties rather than the bulk ones are thus enhanced. Such deposition method could be useful in the preparation of porphyrins-sensitized solar cells [24,25] or photonic devices [26] in which porphyrins stacking and aggregation have been reported to reduce the overall efficiency.

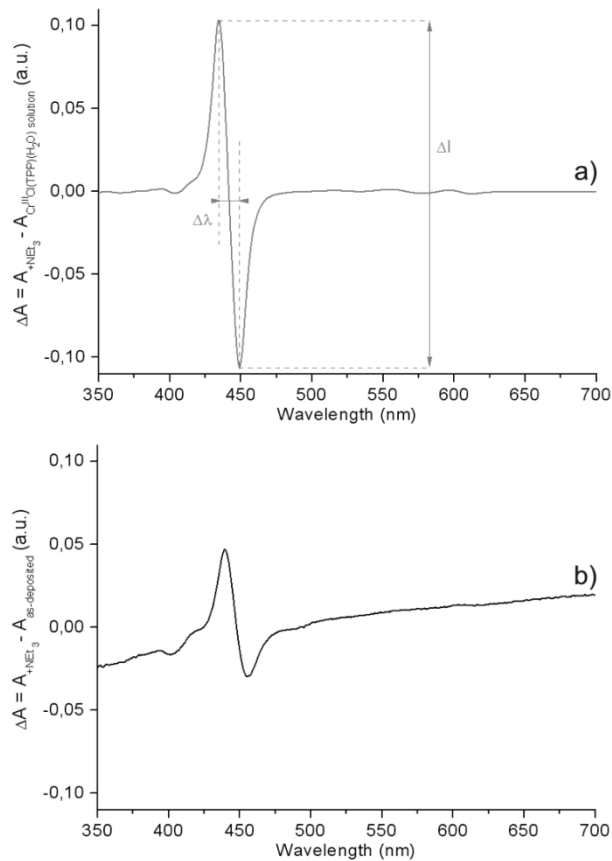


Figure 6 Absorbance difference spectra of (a) $Cr^{III}Cl(TPP)(H_2O)$ dissolved in dichloromethane and of (b) $Cr^{III}Cl(TPP)(H_2O)$ -based coating after exposure to a saturated NEt_3 environment and prior exposure.

In the preparation of porphyrin-embedded materials for gas sensing applications, where accessible pore sizes and high surface areas are desired, the presence of solvent is favouring the formation of porosity while evaporating during the thin film plasma polymerisation. Such as in classical polymer membrane formation, the solution concentration and evaporation rate of the solvent have to be carefully controlled to reach the targeted morphology. Fast evaporation of the solvent, occurring when heating the substrate or applying a plasma, reduces the nucleation and the pore growth rate with a rapid increase of the polymer concentration. In addition, fast evaporation of the solvent induces agglomeration of the porphyrins. Therefore, such layers would be more likely deposited via atmospheric pressure or high-pressure plasma techniques. Low-pressure techniques, which induce a faster evaporation of

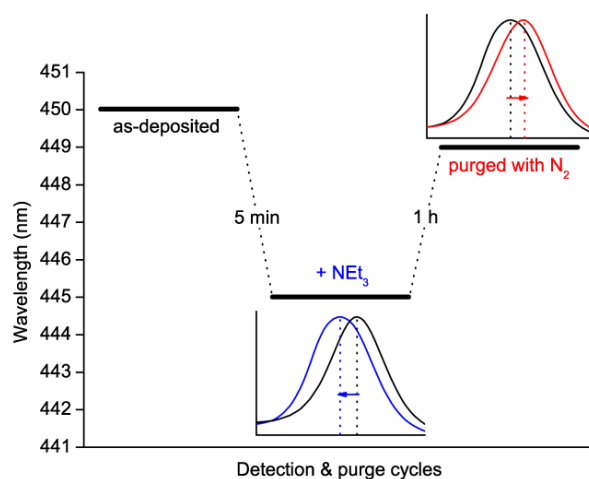


Figure 7 Position of the Soret band of the plasma polymerised $\text{Cr}^{\text{III}}\text{Cl}(\text{TPP})(\text{H}_2\text{O})$ -based coating repeatedly exposed to a dinitrogen atmosphere and triethyl-amine vapours.

both the solvent and the matrix precursor, would presumably result in a partial loss of the gas-sensing properties of the porphyrins due to agglomeration.

The method described in the present work offers an efficient and industrially compatible alternative to the wet methods reported to date to grow such a mesoporous assembly [3,6,11]. The plasma-polymerised siloxane scaffold immobilises the metalloporphyrins and ensures mechanical and water stability of the sensor device. The material, which can be stored under ambient conditions, could therefore be of great interest in the food packaging industry [8]. It should be noted that $\text{Cr}^{\text{III}}\text{Cl}(\text{TPP})(\text{H}_2\text{O})$ is not specific for triethylamine and could be used for the detection of other volatile amines. However, due to some steric, chemical or physical hinderance, the colour shift of the film obtained in the presence of triethylamine is rather low and could not yet be observed by human eyes. Therefore, experiments involving a new class of $\text{trans-A}_2\text{B}_2$ -porphyrins that exhibits stronger colour shifts upon exposure to triethylamine and a higher selectivity are currently in progress [27].

Conclusions

In conclusion, the plasma deposition method described in this paper has shown to be an effective route toward the formation of colorimetric gas sensing surfaces. $\text{Cr}^{\text{III}}\text{Cl}(\text{TPP})(\text{H}_2\text{O})$ metalloporphyrins were successfully immobilised in a mesoporous PDMS membrane by AP-DBD. As shown by UV-vis, their integrity was preserved while preventing their aggregation. A good permeation kinetic of the analyte through the bulk of the film and the complexation of the analyte to the central metallic ion of the porphyrin was confirmed by gas detection experiments. Nevertheless, the colour shift obtained in the presence of triethylamine was rather low and could not yet be observed by human eyes. More experiments to investigate the detection limits and kinetics towards triethylamine and other volatile amines are currently in progress.

Moreover, further analyses are underway in order to investigate the metalloporphyrin arrangements in the coatings and interactions within the plasma films.

Acknowledgements The Luxembourgish "Fonds National de la Recherche" (FNR) is thanked for financial support through the SurfAmine project. Dr. J.-N. Audinot from CRP-Gabriel Lippmann is hereby gratefully acknowledged for his skilful characterisations and valuable discussions.

References

- [1] N.A. Rakow, K.S. Suslick, *Nature* 406 (2000) 710-713.
- [2] N.A. Rakow, A. Sen, M.C. Janzen, J.B. Ponder, K.S. Suslick, *Angew. Chem. Int. Ed.* 44 (2005) 4528-4532.
- [3] S. Tao, G. Li, H. Zhub, *J. Mater. Chem.* 16 (2006) 4521-4528.
- [4] T. H. Richardson, C. M. Dooling, L. T. Jones, R. A. Brook, *Adv. Colloid Interfac.* 116 (2005) 81-96.
- [5] J. Spadavecchia, R. Rella, P. Siciliano, M. G. Manera, A. Alimelli, R. Paolesse, C. Di Natale, A. D'Amico, *Sensor. Actuat. B* 115 (2006) 12-16.
- [6] A. A. Vaughan, M. G. Baron and R. Narayanaswamy, *Anal. Commun.* 33 (1996) 393-396.
- [7] M. Tonezzer, A. Quaranta, G. Maggioni, S. Carturan, G. Della Mea, *Sensor. Actuat. B* 122 (2007) 620-626.
- [8] M. Tonezzer, G. Maggioni, E. Dalcanale, *J. Mater. Chem.* 22 (2012) 5647-5655.
- [9] B. Johnson-White, M. Zeinali, K. M. Shaffer, C. H. Patterson Jr, P. T. Charles, M. A. Markowitz, *Biosens. Bioelectron.* 22 (2007) 1154-1162.
- [10] S. H. Lim, L. Feng, J. W. Kemling, C. J. Musto, K. S. Suslick, *Nat. Chem.* 1 (2009) 562-567.
- [11] F. A. Nwachukwu, M. G. Baron, *Sensor. Actuat. B* 90 (2003) 276-285.
- [12] C. Tendero, C. Tixier, P. Tristant, J. Desmaison, P. Leprince, *Acta B* 61 (2006) 2-30.
- [13] D. Del Frari, J. Bour, J. Bardou, O. Buchheit, C. Arnoult, D. Ruch, *J. Nanosci. Nanotechnol.* 9 (2009) 1-9.
- [14] N. D. Boscher, P. Choquet, D. Duday, N. Kerbellec, J.-C. Lambrechts, R. Maurau, *J. Mater. Chem.* 21 (2011) 18959-18961.
- [15] M. Tonezzer, G. Maggioni, A. Quaranta, S. Carturan, G. Della Mea, *Sensor. Actuator. B* 136 (2009) 290-296.
- [16] K. Nakamura, M. Watanabe, M. Zhou, M. Fujishima, M. Tsuchiya, T. Handa, S. Ishii, H. Noguchi, K. Kashiwagi, Y. Yoshida, *Thin Solid Films* 345 (1999) 99-103.
- [17] G. Giancane, L. Valli, *Adv. Colloid Interfac.* 171 (2012) 17-35.
- [18] R. S. Dudhe, J. Sinha, A. Kumar, V. R. Rao, *Sensor. Actuat. B* 148 (2010) 158-165.
- [19] D. A. Summerville, R. D. Jones, B. M. Hoffman, F. Basolo, *J. Am. Chem. Soc.* 99 (1977) 8195-8202.
- [20] N. D. Boscher, P. Choquet, D. Duday, S. Verdier, *Plasma Process. Polym.* 7 (2010) 163-171.
- [21] Y.-H. Zhang, W.-J. Ruan, Z.-Y. Li, Y. Wu, J.-Y. Zheng, *Chem. Phys.* 315 (2005) 201-213.
- [22] J. L. S. Lee, I. S. Gilmore, M. P. Seah, A. P. Levick, A. G. Shard, *Surf. Interface Anal.* 44 (2012) 238-245.
- [23] M. Gouterman, L. K. Hanson, G. Khalil, W. R. Leenstra, J. W. Buchler, *J. Chem. Phys.* 62 (1975) 2343-2353.
- [24] M. K. Nazeeruddin, R. Humphry-Baker, D. L. Officer, W. M. Campbell, A. K. Burrell, M. Grätzel, *Langmuir* 20 (2004) 6514-6517.

- [25] H. Imahori, S. Kang, H. Hayashi, M. Haruta, H. Kurata, S. Isoda, S. E. Canton, Y. Infahsaeng, A. Kathiravan, T. Pascher, P. Chabera, A. P. Yartsev, V. Sundstrom, *J. Phys. Chem. A* 115 (2011) 3679-3690.
- [26] Z. M. Liu, A. A. Yasseri, J. S. Lindsey, D. F. Bocian, *Science* 302 (2003) 1543-1545.
- [27] P. Heier, C. Förster, D. Schollmeyer, N. Boscher, P. Choquet, K. Heinze, *Dalton Trans.* (2012) DOI: 10.1039/c2dt31943h.

3.3

Optical Sensing Responses of $\text{Cr}^{\text{III}}\text{Cl}(\text{TPP})(\text{H}_2\text{O})$ -based Coatings Obtained by an Atmospheric Pressure Plasma Method – Application to the Detection of Volatile Amines

N. Boscher, T. Bohn, P. Heier, F. Moisy,
B. Untereiner, K. Heinze, P. Choquet

Sensors and Actuators B **2014**, 191, 553-560.

Abstract

Food spoilage processes are a considerable concern for both the food industry and the consumer, due to financial, food quality and food safety aspects. A primary issue is the prevention/monitoring of the formation of biogenic and volatile amines, such as occurring in fish and in other microbiologically unstable food items rich in proteins, produced by e.g. oxidative decarboxylation of amino acids. One strategy for their monitoring is the development of films with colorimetric sensing properties that are able to indicate food spoilage. The aim of this investigation was the development of a novel metalloporphyrin-based coating allowing the sensitive detection of typical volatile amines, such as trimethylamine (TMA), triethylamine (TEA) and dimethylamine (DMA), which were tested under static and dynamic flow conditions. (Aqua)(chloro)(5,10,15,20-tetraphenyl-porphyrinato)chromium(III) in solution at 0.75 mg mL^{-1} was deposited by means of an atmospheric pressure dielectric barrier discharge deposition method onto $50 \mu\text{m}$ thick transparent polyethylene terephthalate foils. Produced foils were able to detect volatile amines, as indicated via a hypsochromic shift of the Soret band of 5 nm and differential absorption at 442 nm, at 10 ppm, while detectable static concentrations were higher (ca. 150 ppm). Sensitivity was significantly higher for TMA, TEA and DMA than for NH_3 ($P < 0.001$), and sufficient humidity was a pre-requisite for sensitive detection. Results were confirmed by experiments with spoiled fish (mackerel, trout). Further investigations of metalloporphyrins that could act as selective food spoilage indicators amenable to naked-eye detection are warranted.

Reproduced by permission of Elsevier B.V.

Introduction

Food freshness indicators incorporated within food packages have become a topic of great interest for the food industry in the past years, including several applications such as detection of CO₂ by chitosan-based detectors [1], pH sensing detectors [2], or oxygen detection by fluorescent dyes [3]. One important area is the development of gas sensing surfaces that result in colorimetric changes which can be easily monitored, even by the consumer without expensive equipment, and such simple yet powerful devices for the inspection and control of food freshness are especially needed. One area where intelligent foils have been employed includes the detection of volatile amines, which are e.g. formed during fish spoilage, albeit also other protein rich foods such as chicken meat are potential applications [4]. Fish is especially prone to spoilage due to the protein rich matrix, soft tissue, and the microbiota associated with fish skin such as *Pseudomonas* or *Acinetobacter* [5], resulting in the production of a variety of biogenic amines such as cadaverine or histamine, which may cause toxic effects upon consumption such as headache, nausea, and dizziness [6]. Along with the formation of these biogenic amines, volatile amines such as trimethylamine (TMA), dimethylamine (DMA) and others are produced from trimethylamine-oxide (TMAO, e.g. via TMAO-ase or TMAO demethylase), that are, as they appear to correlate with the formation of biogenic amines, also used as spoilage indicators, termed total volatile bases (TVB). One existing example on the market is the Fresh-Tag developed by the food packaging company COX technologies (Belmont, NC) [3], employing a proprietary dye changing colour with increased concentrations of volatile amines.

A potential candidate for the colorimetric detection of amines are metalloporphyrin-based coatings, as these have been reported to possess a high affinity toward these functional groups [7,8]. In addition to the choice of indicator, appropriate coating techniques are crucial in order to assure optimal functionality, such as optimal access of the sensed molecules. The preparation of metalloporphyrin-based gas sensing layers has notably been achieved by spin coating [9,10], vacuum evaporation [10] and glow-discharge induced sublimation [11]. However, such methods are hardly compatible with typical industrial requirements. Moreover, to reduce the problems associated with aggregation, to improve the detection sensitivity and to increase the thermal and mechanical stability of the films, it is more desirable to trap the porphyrins into a suitable matrix [12,13]. The formed composite films are able to keep the sensing metalloporphyrin molecules in the matrix while allowing the diffusion of small volatile organic compounds (VOCs) to be detected through their pores. The synthesis of metalloporphyrin-containing hybrid layers has notably involved the sol-gel deposition of silica films [14] or other wet methods [13,15]. A promising arising technology for the preparation of colorimetric gas sensing surfaces is the atmospheric pressure dielectric barrier discharge (AP-DBD) deposition of metalloporphyrin-based coatings [16]. AP-DBD, which can be readily adapted on a roll-to-roll production line, has been successfully used to immobilise aqua(chloro)(5,10,15,20-tetraphenyl

porphyrinato)chromium(III) ($\text{Cr}^{\text{III}}\text{Cl}(\text{TPP})(\text{H}_2\text{O})$) [16] and (5,10,15,20-tetraphenyl porphyrinato)zinc(II) ($\text{Zn}^{\text{II}}(\text{TPP})$) in porous plasma-polymerised polydimethylsiloxane (pp-PDMS) layers [17]. The pp-PDMS scaffold, which ensured the mechanical and water stability of the layer, allowed the analyte permeation to the sensing molecule. Upon exposure to a saturated triethylamine atmosphere, the Soret and Q bands of the embedded $\text{Cr}^{\text{III}}\text{Cl}(\text{TPP})(\text{H}_2\text{O})$ metalloporphyrin did undergo a characteristic hypsochromic shift, confirming the interaction of the amine and the dye [16].

In this pursuit, we report the optical sensing capabilities of plasma deposited $\text{Cr}^{\text{III}}\text{Cl}(\text{TPP})(\text{H}_2\text{O})$ -based coatings. UV-visible (UV-vis) spectroscopy was used to investigate the integrity of the embedded metalloporphyrins and the optical gas sensing properties of the films. The response magnitude of the samples exposed to triethylamine fluxes at different concentration was related to the layer composition determined by Fourier-transform infrared spectroscopy (FT-IR) and X-ray photoelectron spectroscopy (XPS). Finally, the developed coated films were tested during fish (Atlantic mackerel and trout) spoilage experiments.

Experimental

Materials and deposition procedure

Unless stated otherwise, all chemicals were obtained from Sigma-Aldrich (St. Louis, MO) and were of HPLC reagent quality or higher, and only 18 M Ω water (Millipore, Billerica, MA) was used. The $\text{Cr}^{\text{III}}\text{Cl}(\text{TPP})(\text{H}_2\text{O})$ metalloporphyrin (Figure 1) embedded in the plasma polymerised coatings described in this paper were synthesised according to a reported literature procedure [18]. Around 7.5 mg of the $\text{Cr}^{\text{III}}\text{Cl}(\text{TPP})(\text{H}_2\text{O})$ metalloporphyrin with a purity of ca. 98% were dissolved in a solution composed of 8 mL of vinyltrimethoxysilane (VTMOS) (98%) and 2 mL of dichloromethane (DCM)

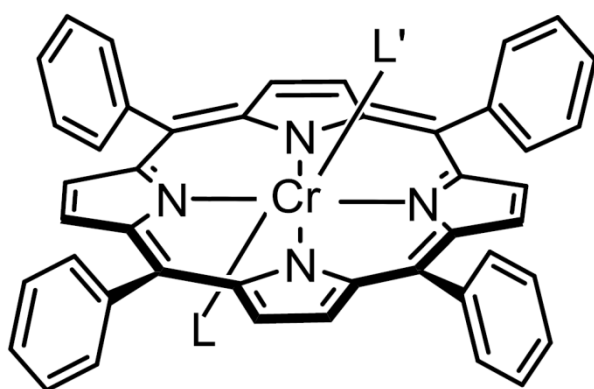


Figure 1 Molecular structure of (aqua)(chloro)(5,10,15,20-tetraphenylporphyrinato)chromium(III) employed as the sensing molecule in the plasma deposited films.

(99.8%). The prepared solution was sprayed by an ultrasonic atomising nozzle (Sono-Tek Corporation, Milton, NY) operating at 48 kHz and fed by a syringe driver delivering 0.25 mL min^{-1} onto $50 \text{ }\mu\text{m}$ thick transparent biaxially oriented polyethylene terephthalate foils (DuPont, Wilmington, DE) or $200 \text{ }\mu\text{m}$ thick 8011 series cold-rolled aluminium foils (Eurofoil, Belvaux, Luxembourg) placed on the moving stage of an AP-DBD reactor [19]. The moving stage speed, set to 6 m min^{-1} , allowed to promptly expose the deposited liquid layer to the plasma discharge in order to polymerise the siloxane precursor. Delay time between the liquid layer deposition and plasma treatment was one second. The AP-DBD reactor consisted of two flat parallel high voltage electrodes ($0.7 \times 13 \text{ cm}^2$) covered with alumina and the moving stage as grounded electrode. The discharge gap between the high voltage electrode and the substrate placed on the grounded electrode was maintained at 1 mm . The AP-DBD reactor was fed by a 20 L min^{-1} nitrogen flow (Air Liquide, Pétange, Luxembourg, 99.999%) containing up to 500 ppm of hexamethyldisiloxane (HMDSO) vapours. The additional siloxane precursor, HMDSO, was injected into the reactor using a bubbler system made of a cylinder and a frit. Three flow rates of nitrogen through the HMDSO bubbler were investigated, 0.0 (for **1**), 0.2 (for **2**) and 0.5 L min^{-1} (for **3**). The plasma discharge was ignited by means of a 10 kHz sinusoidal signal, chopped by a 1667 Hz rectangular signal. The operating discharge power density was maintained at 0.5 W cm^{-2} . One hundred passes, corresponding to 14 s effective deposition times, were performed. The deposited film was stored in dry plastic containers at room temperature under light exclusion.

Thin film characterization

Scanning electron microscopy (SEM) was performed on a Hitachi SU-70 FE-SEM (Hitachi, Tokyo, Japan). Prior to SEM observations, the non-conductive sample was sputter-coated with 5 nm of platinum to prevent charging and distortion. FT-IR analysis was performed on a Bruker Hyperion 2000 (Bruker, Ettlingen, Germany) spectrometer equipped with a Ge-ATR-crystal. XPS analyses were realised with a Kratos Axis-Ultra DLD instrument (Kratos, Manchester, UK) using a monochromatic Al $K\alpha$ X-ray source ($h\nu = 1486.6 \text{ eV}$) at a pass energy of 20 eV . UV/visible absorption spectra of the film exposed to volatile amines were obtained with a DU800 Beckman Coulter UV/Vis spectrophotometer (Beckman Coulter, Krefeld, Germany), employing 10 mm quartz type cuvettes (Starna Scientific, Hainault, UK).

Optical gas sensing experiments

The gas sensing properties of the $\text{Cr}^{\text{III}}\text{Cl}(\text{TPP})(\text{H}_2\text{O})$ -based coatings towards triethylamine (TEA) vapours were investigated by a homebuilt gas flow setup and a DU800 Beckman Coulter UV/Vis spectrophotometer (Figure 2). All gas-flow sensing measurements were performed at 20°C in a temperature controlled room. Nitrogen (99.999 %), used as a reference and carrier gas, was continuously fed into the

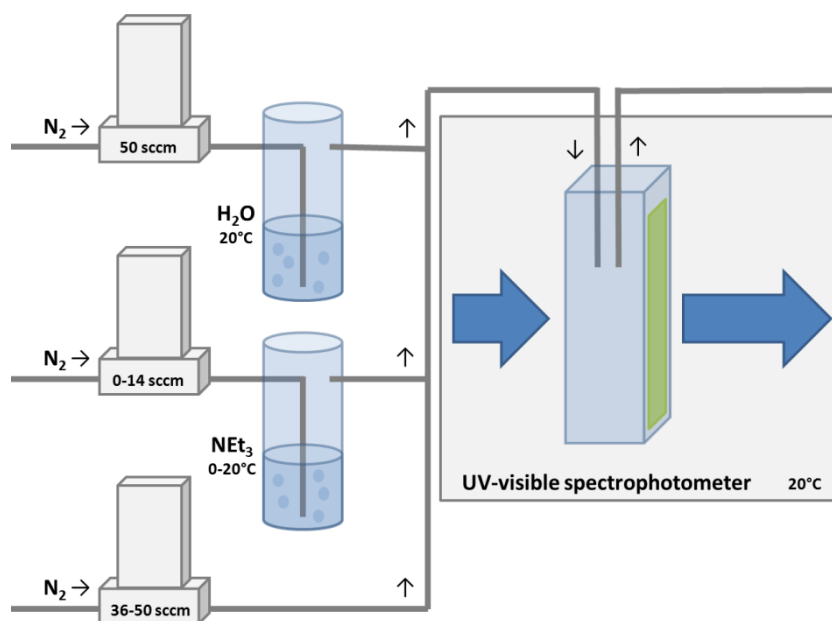


Figure 2 Scheme of the experimental setup used for the volatile amine sensing test during the dynamic detection measurements.

measurement chamber at a total flow of 100 mL min^{-1} . Three mass flow controllers (MKS instruments, Andover, MA) were used to control the triethylamine vapor concentration and the relative humidity (RH) of the overall nitrogen gas stream. The triethylamine gas concentration was ensured by passing a clean dry nitrogen flow into a bubbler containing the analyte to be detected. Control of the bubbler temperature, immersed into an isothermal bath at 0 or 20°C , and of the nitrogen flow through the bubbler, from 0 to 14 mL min^{-1} further diluted in the overall 100 mL min^{-1} gas stream, allows to investigate triethylamine concentrations of 10 ppm, 100 ppm, 1000 ppm and 10000 ppm. The relative humidity, maintained at 50% for all measurements, was ensured by the use of a de-ionised water bubbler, immersed into an isothermal bath at 20°C , in which 50 mL min^{-1} of clean dry nitrogen were passed and further diluted in the overall 100 mL min^{-1} gas stream. The measurement cells were 3 mL septum cap quartz cuvettes in which the plasma coated polyethylene terephthalate foils were placed. When gas sensing layers were exposed to triethylamine vapours, the Soret band underwent a hypsochromic shift with a maximum intensity change around 442 nm. Therefore, the response of the different $\text{Cr}^{\text{III}}\text{Cl}(\text{TPP})(\text{H}_2\text{O})$ -based coatings was measured from the absorbance changes at 442 nm for various triethylamine gas phase concentrations. The reference wavelength was measured at 500 nm. Prior to any triethylamine exposure, the wavelength of each sample was monitored under a nitrogen flux for 10 minutes (50% relative humidity, RH); then the samples were exposed to a triethylamine-containing nitrogen flux (50% RH) at different concentration for 2 h. The sample system was finally regenerated under a nitrogen flux (50% RH).

In addition, the absorption spectra time-evolution of the $\text{Cr}^{\text{III}}\text{Cl}(\text{TPP})(\text{H}_2\text{O})$ -based coatings was also investigated by static measurements after adding 2 μL of either pure analyte containing solutions or equivalent, together with 1 μL of water at the bottom of the cuvette containing glass beads (for surface enhancement) which was then rapidly sealed. The procedure, performed at room temperature, was repeated for different concentrations of triethylamine (TEA, 100%), trimethylamine (TMA, as hydrochloride), dimethylamine (DMA, as hydrochloride) and ammonia (solution of 25% in water) diluted in a non-coordinating solvent, dichloromethane (DCM). For release of the pure volatile amine from the corresponding hydrochloride, the respective aqueous solutions were exposed to small volumes of NaOH (25% in water). In order to highlight the absorption changes, the maximum absorbance difference was calculated as the subtraction of the pre-exposure spectrum to the post-exposure spectrum, at the wavelengths of highest sensitivity, at approximately 442 nm. For comparison across foils of different batches, the absorption spectra of the $\text{Cr}^{\text{III}}\text{Cl}(\text{TPP})(\text{H}_2\text{O})$ -based coatings were normalized to the Soret band intensity prior to exposition to amine.

Fish storage experiments

Atlantic mackerel (*Scomber scombrus*) and rainbow trout (*Oncorhynchus mykiss*) were purchased in fresh but frozen from local markets. Filets of fish including the skin were then minced by a mixer (mini chopper DO-9018MC, DOMO, Herentals, Belgium), and small aliquots (ca. 100 mg) were placed into 1 cm quartz cuvettes containing the sensing film and sealed with parafilm. In addition, fish was stored at room temperature in a heating oven (Memmert, UF model, Eagle, WI) for several days and small volumes of the resulting liquefied tissues (2 μL) were likewise placed into quartz cuvettes containing the film and sealed. Absorption spectra were monitored for up to 30 days following exposure.

Results and Discussion

Characterization of the $\text{Cr}^{\text{III}}\text{Cl}(\text{TPP})(\text{H}_2\text{O})$ -based coatings

The $\text{Cr}^{\text{III}}\text{Cl}(\text{TPP})(\text{H}_2\text{O})$ -based coatings described in this paper exhibited a uniform green colour and were optically indistinguishable from each other. Neither visually noticeable cracks nor particles were observed on the surface of the sample. Furthermore, all the plasma deposited $\text{Cr}^{\text{III}}\text{Cl}(\text{TPP})(\text{H}_2\text{O})$ -based coatings were adherent to both of the substrates investigated and stable in water. Low magnification SEM confirmed that all the composite films deposited covered the whole substrate and were pinhole-free and smooth with very little particle formation. In contrast to previous hybrid coatings obtained by AP-DBD [19,20], no second phase was observed by SEM. This is consistent with the initial nanometre size of the metalloporphyrins and suggested that they do not form large aggregates. The coating growth rates were determined by cross-section SEM (Table 1). Expectedly, the maximum thickness (ca. 110 nm) was obtained for the film grown with the highest HMDSO concentration in the plasma gas (500 ppm).

Coatings as thin as 20 nm were deposited in the absence of HMDSO injection in the plasma gas.

Table 1 Deposition conditions, thickness and Soret band characteristics before and after exposure to a saturated triethylamine atmosphere for three batches of Cr^{III}Cl(TPP)(H₂O)-based coatings obtained with varying HMDSO fluxes.

Batch	1	2	3
HMDSO flux (L min ⁻¹)	0	0.2	0.5
Thickness (nm)	20	90	110
Elemental composition			
Si (%)	8	21	20
Cr(%)	0.9	0.3	0.2
Cr ^{III} Cl(TPP)(H ₂ O) loading (%)	45	14	10
Soret Band			
Position (nm)	455	453	452
FWHM (nm) ^a	25	27	25
Intensity (a.u.) ^b	0.2	0.3	0.3

^a Peak width: full-width at half-maximum.

^b Absorption units

The FT-IR spectra of the Cr^{III}Cl(TPP)(H₂O)-based coatings were shown to be greatly influenced by the presence of HMDSO in the plasma gas (Figure 3). The Cr^{III}Cl(TPP)(H₂O)-based coatings obtained using 0.2 and 0.5 L min⁻¹ HMDSO fluxes confirmed the formation of a PDMS-like matrix with a strong and broad band assigned to a Si-O-Si network vibration (1051 cm⁻¹). The peaks at 2962 and 2906 cm⁻¹ (ν (CH₃)), 1410 cm⁻¹ (ν_a (CH₃)), 1259 cm⁻¹ (δ_s (Si-CH₃)), 845 cm⁻¹ (ρ (CH₃) and ν (Si-C)), 806 cm⁻¹ and 758 cm⁻¹ (ν (Si-CH₃)) indicated the high retention of methyl groups from the siloxane monomer [21]. In contrast, only little evidence of siloxane bonds, with small humps or

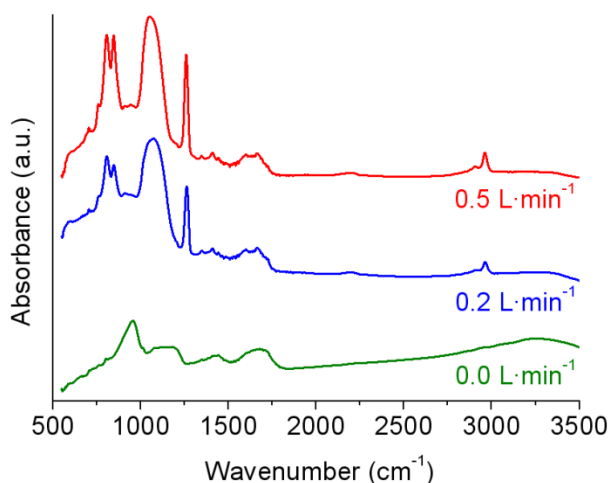


Figure 3 FT-IR spectra of Cr^{III}Cl(TPP)(H₂O)-based coatings obtained using an atmospheric pressure dielectric barrier discharge fed with varying HMDSO fluxes.

peaks at 760 and 802 cm^{-1} ($\nu(\text{Si-CH}_3)$), 1012 cm^{-1} ($\nu(\text{Si-O-Si})$) and 2964 cm^{-1} ($\nu(\text{CH}_3)$), could be identified for the coating grown in the absence of HMDSO. The major absorption band observed at 955 cm^{-1} was attributed to Al-O-Al asymmetric stretching originating from the aluminium substrate. The absorption bands at 1120 and 3250 cm^{-1} were attributed to $\delta(\text{Al-O})$ or $\delta(\text{AlO-H})$ and $\nu(\text{OH})$, respectively. The peak at 1442 cm^{-1} could possibly be attributed to C-H deformation from pyrrole, however no clear evidence of $\text{Cr}^{\text{III}}\text{Cl}(\text{TPP})(\text{H}_2\text{O})$ in the plasma polymerised coating could be detected by FT-IR.

Nevertheless, the presence of chromium in the plasma polymerised coating was detected by X-ray photoelectron spectroscopy (XPS). However, as the chromium content in the embedded metalloporphyrin, $\text{C}_{44}\text{H}_{28}\text{N}_4\text{Cr}$ was rather low (ca. 1.4 %), only traces of the Cr element were detected in the plasma polymerised $\text{Cr}^{\text{III}}\text{Cl}(\text{TPP})(\text{H}_2\text{O})$ -based coatings deposited from the three conditions investigated. XPS showed that all the films also contained silicon, oxygen, nitrogen and carbon at concentrations that depended on the plasma gas composition. In pure nitrogen plasma gas (**1**), the produced film contained 8 % of silicon and 0.9 % of chromium, suggesting a rather high loading of the metalloporphyrins, which could thus represent up to 45 % of the composite layer if unaltered. Addition of HMDSO vapours to the plasma process resulted in a decrease of the chromium-to-silicon ratio in the films (Table 1). The maximum $\text{Cr}^{\text{III}}\text{Cl}(\text{TPP})(\text{H}_2\text{O})$ concentrations, diluted in thicker siloxane matrices, were reduced to 14 and 10 % for coatings obtained using a (**2**) 0.2 and (**3**) 0.5 L min^{-1} flow through the HMDSO bubbler, respectively.

UV-visible absorption spectroscopy of the plasma polymerised $\text{Cr}^{\text{III}}\text{Cl}(\text{TPP})(\text{H}_2\text{O})$ -based coatings showed the typical absorption spectra of integer metalloporphyrins with an intense Soret absorption band and weaker Q bands. The $\pi(a_{2u}, a_{1u}) \rightarrow d(e_g)$ charge-transfer absorption band was observed at 399 nm, confirming the presence of the central metal ion [22]. The Soret band position of the plasma polymerised $\text{Cr}^{\text{III}}\text{Cl}(\text{TPP})(\text{H}_2\text{O})$ -based coatings was shown to be slightly red-shifted in comparison to the one observed in the UV-vis spectrum obtained for $\text{Cr}^{\text{III}}\text{Cl}(\text{TPP})(\text{H}_2\text{O})$ dissolved in dichloromethane (449 nm). Interestingly, the Soret band position of the $\text{Cr}^{\text{III}}\text{Cl}(\text{TPP})(\text{H}_2\text{O})$ -based coating deposited in a pure nitrogen atmosphere was more red-shifted (455 nm) than the one of the coatings grown with additional HMDSO vapours (452-453 nm) (Figure 4). A slight broadening of the Soret band, with a full-width at half-maximum (FWHM) varying from 13 nm for the spectrum in solution (DCM) to 25-27 nm for the plasma polymerised $\text{Cr}^{\text{III}}\text{Cl}(\text{TPP})(\text{H}_2\text{O})$ -based coatings, was also observed. This red-shift and weak broadening of the absorption bands were attributed to porphyrin-porphyrin and/or porphyrin-matrix interactions in the solid matrix [16]. Another noticeable difference was the maximum Soret band intensity, ranging from 0.2 for the film grown in pure nitrogen atmosphere to 0.3 for films grown with additional HMDSO vapours. As the injection conditions and notably the sprayed $\text{Cr}^{\text{III}}\text{Cl}(\text{TPP})(\text{H}_2\text{O})$ quantity were identical for the three studied conditions and the FWHM of the Soret band were

also similar, it can be assumed that some metalloporphyrins were altered by exposition to plasma for condition **1** (0 L min^{-1}). Indeed, $\text{Cr}^{\text{III}}\text{Cl}(\text{TPP})(\text{H}_2\text{O})$ molecules directly exposed to plasma are likely to undergo a full disruption of their macrocycle. Nevertheless, the good match between the plasma polymerised $\text{Cr}^{\text{III}}\text{Cl}(\text{TPP})(\text{H}_2\text{O})$ -based coating spectra and the solution spectrum, reported as a reference in Figure 4, indicated that for any of the three studied conditions, most of the $\text{Cr}^{\text{III}}\text{Cl}(\text{TPP})(\text{H}_2\text{O})$ metalloporphyrins were preserved during the plasma process. This result contrasts with previous plasma deposited porphyrin-based coatings that have shown a large broadening (FWHM = 45-80 nm) and loss of intensity [23,24] or even disappearance of the Soret band [24].

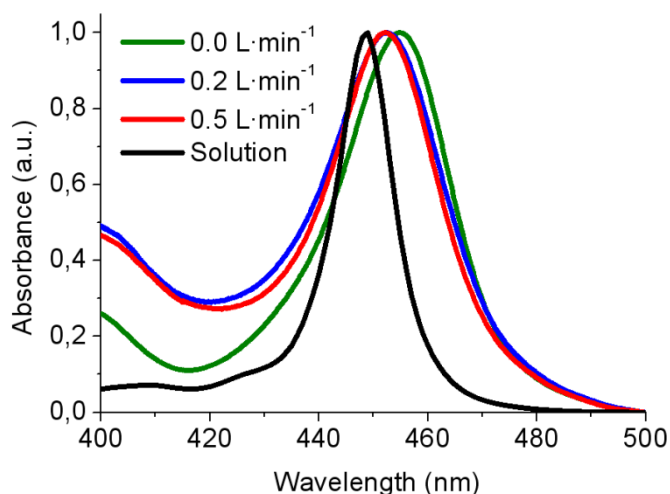


Figure 4 Normalized UV-vis absorption spectra of the $\text{Cr}^{\text{III}}\text{Cl}(\text{TPP})(\text{H}_2\text{O})$ starting VTMOs/DCM solution and of $\text{Cr}^{\text{III}}\text{Cl}(\text{TPP})(\text{H}_2\text{O})$ -based coatings obtained using an atmospheric pressure dielectric barrier discharge fed with varying HMDSO fluxes.

Optical sensing responses towards amines – dynamic non-equilibrium conditions

The optical sensing capabilities of the $\text{Cr}^{\text{III}}\text{Cl}(\text{TPP})(\text{H}_2\text{O})$ -based coatings were investigated toward TEA as a representative of the volatile amines using the gas flow setup presented in Figure 2. TEA was preferred for testing due to its liquid state at room temperature and ease of handling. For any of the deposition conditions investigated the absorption spectra, acquired over the visible range (400-800 nm), did show a blue-shift of the Soret and Q bands. This hypsochromic shift of the Soret band indicated the successful permeation of TEA into the coating of the film and the interaction between the embedded metalloporphyrins and TEA. As an example, Figure 5 is presenting the Soret band absorption of coating **2** (0.2 mL min^{-1} HMDSO) before and after exposure to a nitrogen flux containing 1000 ppm of TEA vapour. The observed shift (3 nm) was smaller compared to the spectral changes in solution (12 nm) [16], suggesting that TEA did not access to all the porphyrins present in the layer. Moreover, the slight broadening of the Soret band, from 27 nm to 31 nm FWHM,

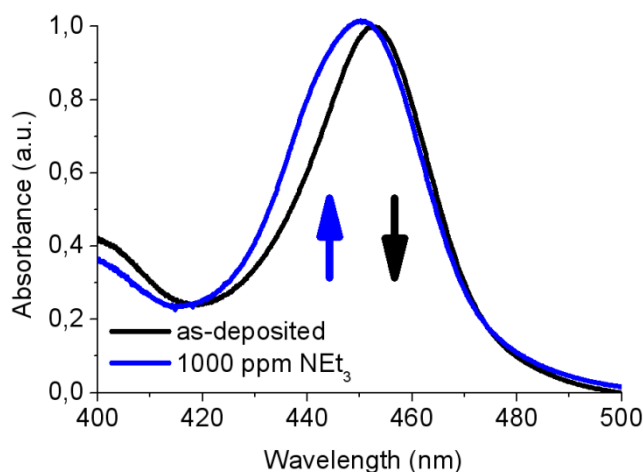


Figure 5 UV-vis absorption spectra of the deposited plasma polymerized $\text{Cr}^{\text{III}}\text{Cl}(\text{TPP})(\text{H}_2\text{O})$ -based coatings obtained using an atmospheric pressure dielectric barrier discharge fed with 0.2 L min^{-1} HMDSO flux (right) and after exposure to a 1000 ppm triethylamine vapour-containing nitrogen flux (left).

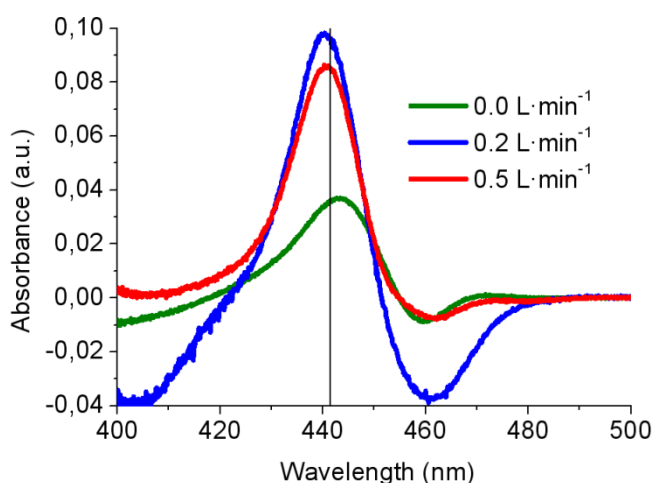


Figure 6 Absorbance difference spectra of $\text{Cr}^{\text{III}}\text{Cl}(\text{TPP})(\text{H}_2\text{O})$ -based coatings obtained using an atmospheric pressure dielectric barrier discharge fed with varying HMDSO flux after exposure to 1000 ppm triethylamine in the gas phase and prior to exposure.

suggested that the porphyrin environment was more diverse after exposure to TEA, i.e. with the presence of both $\text{Cr}^{\text{III}}\text{Cl}(\text{TPP})(\text{H}_2\text{O})$ and TEA-modified porphyrin.

Changes in the metalloporphyrin spectrum were highlighted by the differential absorbance spectra of the films upon exposure to TEA vapours and prior to exposure (Figure 6). For comparisons across various film batches, the absorption spectra of the $\text{Cr}^{\text{III}}\text{Cl}(\text{TPP})(\text{H}_2\text{O})$ -based coatings were normalized by the Soret band intensity prior to exposition to amine. For the three deposition conditions investigated, a maximum intensity change, due to the formation of $\text{Cr}^{\text{III}}\text{Cl}(\text{TPP})(\text{NEt}_3)$ complexes in the layer, was observed around 442 nm. The changed intensities, which provided an indication of the sensitivity of the sensors, were observed to be strongly dependent on the deposition

conditions and analyte concentration. However, the sensor was not completely reversible within the observed time period following flushing with nitrogen (Figure 7), indicating that the interaction between the sensor and the amine is partly irreversible, which would not pose a disadvantage for its potential usage in food packages.

The response of the three different $\text{Cr}^{\text{III}}\text{Cl}(\text{TPP})(\text{H}_2\text{O})$ -based coatings as a function of the TEA gas concentration (10, 100, 1000 and 10000 ppm), indicating the range of concentration over which the coatings were sensitive, is shown in Figure 7. Irrespective of the deposition condition, the magnitude of the optical absorbance change at 442 nm was shown to increase with increasing TEA gas concentration. However, the response magnitude strongly depended on the deposition conditions and five time higher response magnitude was observed for the coating deposited from conditions **2** and **3**. The lower limit of detection was inferior to 10 ppm for all the samples investigated, and is expected to be far lower than 10 ppm for the foils obtained from condition **2** and **3**, as the response magnitude observed is well above the noise level.

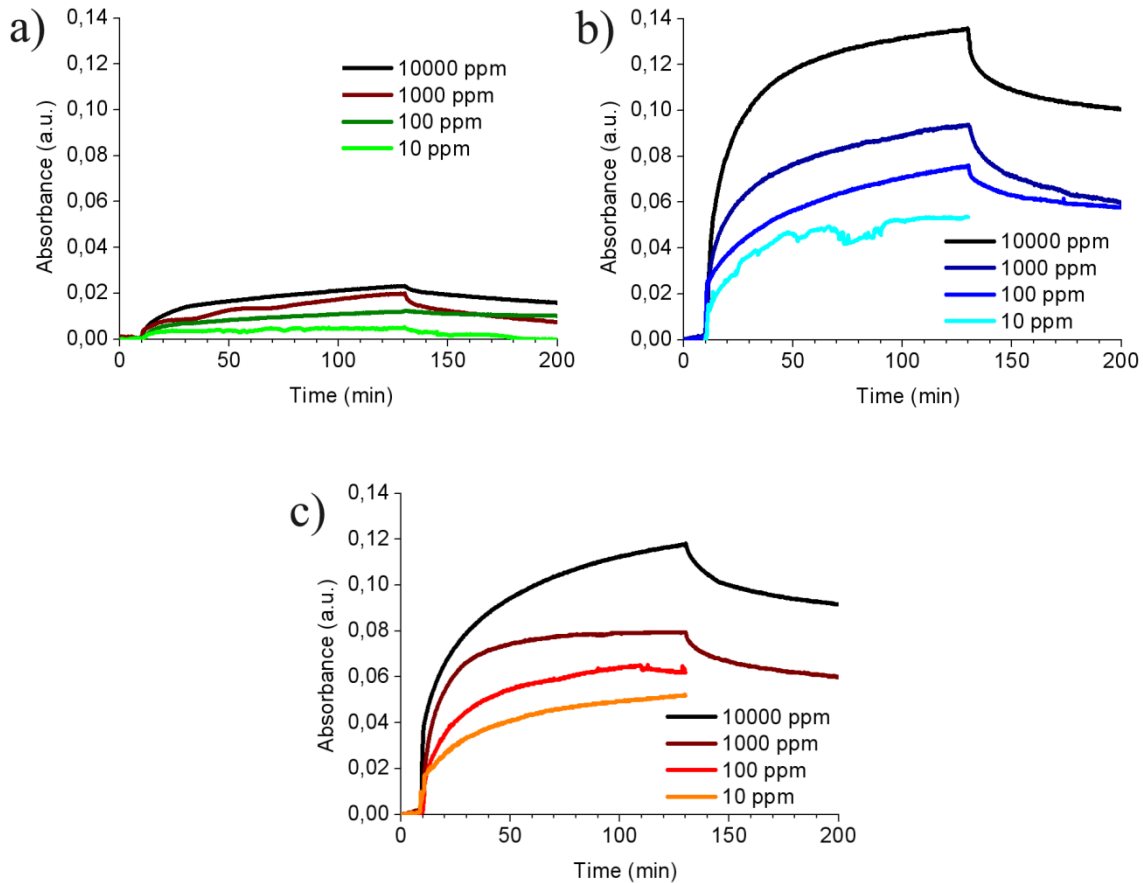


Figure 7 Dynamic responses monitored at 442 nm upon exposure to different triethylamine gas concentrations at 20 °C for the $\text{Cr}^{\text{III}}\text{Cl}(\text{TPP})(\text{H}_2\text{O})$ -based coatings obtained using an atmospheric pressure dielectric barrier discharge fed with three different HMDSO fluxes: a) 0.0 L min^{-1} , b) 0.2 L min^{-1} , c) 0.5 L min^{-1} .

Optical sensing responses toward amines – static equilibrium conditions

$\text{Cr}^{\text{III}}\text{Cl}(\text{TPP})(\text{H}_2\text{O})$ however was not only specific toward TEA. The $\text{Cr}^{\text{III}}\text{Cl}(\text{TPP})(\text{H}_2\text{O})$ -based coatings obtained from deposition condition 2, chosen for its largest response magnitude, was investigated for the detection of other volatile amines, namely TMA, DMA, and ammonia. As can be seen in Figure 8, sensitivity followed the order $\text{DMA} > \text{TMA} > \text{TEA} > \text{NH}_3$ with small differences between TEA, TMA and DMA, while sensitivity was considerably lower for ammonia ($P < 0.001$). We are not sure about the underlying reasons for this observation and the influence of the amines' aliphatic groups is currently under detailed analysis. Despite this being a limitation, it could also serve as an advantage for detection of food spoilage, as ammonia alone has been criticized as a marker of especially early spoilage, despite its production from amino acids by the adherent microbiota [25, 26]. When calculating sensitivity of the coated film toward the amine, assuming full evaporation of the added amount, it was estimated that ca. 150 ppm were readily detected by the sensor. Thus, the amounts detected

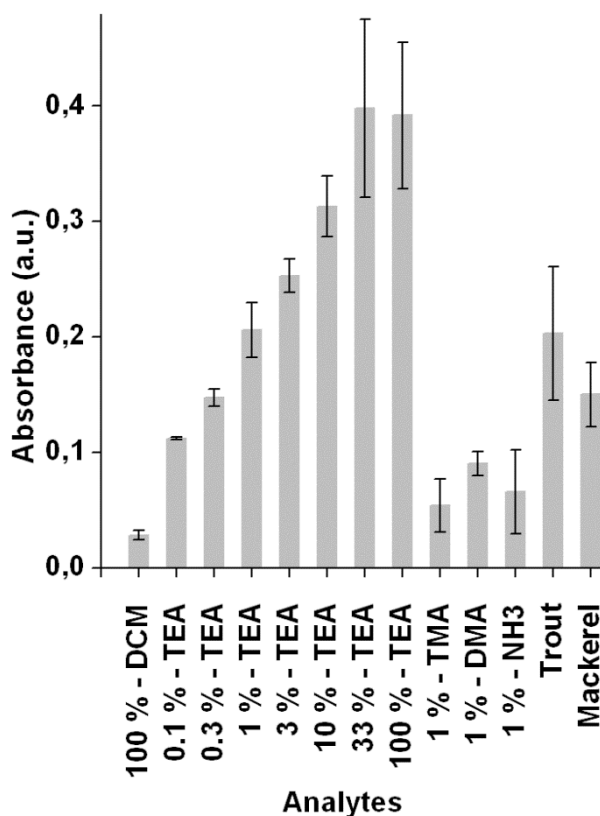


Figure 8 Comparison histogram of the absorption change of the foil at 442 nm upon static exposure to different liquid analytes and spoilt fishes, at 20°C for the $\text{Cr}^{\text{III}}\text{Cl}(\text{TPP})(\text{H}_2\text{O})$ -based coating obtained using an atmospheric pressure dielectric barrier discharge fed with a 0.2 L min^{-1} HMDSO flux. For experiments, either 2 μL of pure compound (triethylamine, TEA) together with 1 μL of water, or equivalent amounts of hydrochloric salts (trimethylamine, TMA; dimethylamine, DMA) or NH_3 (25% aqueous solution) were added, i.e. 20 μg (1% TMA, TEA, DMA), up to 2000 μg (NH_3).

appeared to be somewhat higher than those in the dynamic system, possibly due to accumulative effects of continuous exposure during the dynamic trial. It also has to be noted that our film also cross-reacted with ethanol, at higher concentrations comparable to the sensitivity toward ammonia. Ethanol formation could occur as a product formed from fermentation, and therefore also constitute an additional spoilage indicator by e.g. lactic acid bacteria, such as occurring in anaerobically packed chicken [27].

A few detection methods for volatile amines in the gas phase have been reported in the literature. The use of a fibre-optic fluorescence sensor using 2-naphthol bonded to polyethylene oxide with a sensitivity of 24 ppm has been reported [28], whereas another approach, employing octaethylporphyrin indium(III) in an optical sensor was reported with a sensitivity of 0.1 ppm [29]. However, in both cases, high relative humidity was reported to drastically impact the sensitivity of the layers. In terms of visual indicators, a novel optical sensing system employing a microsphere sensor containing bromocresol green was shown to allow the detection of very low concentrations of amines, down to sub-ppm levels [30]. Nevertheless, such method involved heating of the substrate to 80°C, making it unsuitable for food packaging. Other approaches include the use of Reichardt's dye [31], albeit detection limits for TMA have not been reported, and the use of calyx(4)arene containing nitrophenylazophenol, with a reported sensitivity of around 20 ppb [32]. Such levels may even be too sensitive, detecting trace amounts in unspoiled food-items. In addition, heating at temperatures greater than 300°C was required during the sample preparation. In contrast with the previously cited works, the atmospheric pressure plasma deposition method described herein can be readily implemented on a mass production line.

Fish storage experiments

During fish spoilage, bacterial formation of ammonia from deamination of amino acids, TMA from microbial reduction of TMAO, and also other volatile amines such as DMA in some fish such as gadoids containing TMAO-ase or TMAO-demethylase may occur, and typically, total volatile amines expressed as total volatile bases (TVB), mostly expressed in terms of nitrogen content (TVB-N) correlate well with TMA production [33]. Responses observed in the present investigation were stable over the observed time period of 30 days, and did not increase any more after 10 days (data not shown). Differences between trout and mackerel appeared to be small and insignificant, possibly due to various contents of TMAO and varying microflora, even though saltwater fish typically have higher concentrations of the protein stabilizer TMAO than fresh water fishes [34]. Concentrations of TVB-N in spoiled fish and seafood samples between ca. 10 and 100 mg/100 g have been reported [33,35], and around 0.1-45 mg/100 g for TMA-N. Concentrations of 30-35 mg/100 g for TVB-N and around 10 mg/100 g have been reported to be related to initial decomposition [36]. In the

present study, around 2 µg volatile amine could be detected in our static mode (equal to ca. 0.5 µg nitrogen). Thus, around 1-2 mg fish matrix for TVB-N and 5 mg for TMA-N would appear sufficient to have caused a colour change even in our static system. However, further studies are needed to correlate the sensitivity of the novel developed film with present biogenic amines in the food matrix to obtain a clearer picture for its potential usage. It also has to be stated that in all experiments conducted, due to some steric, chemical or physical hindrance, the colour shift of the films obtained in the presence of TEA was rather low and would hardly be observable by the human eye alone. Therefore, experiments involving a new class of trans-A₂B₂-porphyrins that exhibit stronger colour shifts upon exposure to TEA and a higher selectivity, but coatable by using the same techniques, are currently in progress [37].

Conclusions

Concentrations as low as 10 ppm of TEA were detectable by the Cr^{III}Cl(TPP)(H₂O)-based coating covered foil under the dynamic conditions chosen, albeit with higher detection limits in the static models, as both verified by differential absorption spectra and also optical shifts of the Soret band, suggesting that the chosen deposition method, namely atmospheric pressure dielectric barrier discharge and the metalloporphyrin is a promising approach toward the development of freshness indicators for food packages. The importance of the surrounding matrix was highlighted by dynamic gas flow measurements, with a factor five increase of the response magnitude when injecting additional siloxane monomer vapours in the plasma gas phase.

Acknowledgements The Luxembourgish “Fonds National de la Recherche” is thanked for financial support through the SurfAmine project. Dr. D. Duday, J. Didierjean and Dr. J. Guillot from CRP-Gabriel Lippmann are hereby gratefully acknowledged for their skillful characterizations and valuable discussions.

References

- [1] J. Jung, P. Puligundla, S. Ko, Proof-of-concept study of chitosan-based carbon dioxide indicator for food packaging applications, *Food Chem.* 135 (2012) 2170-2174.
- [2] A. Nopwinyuwong, S. Trevanich, P. Suppakul, Development of a novel colorimetric indicator label for monitoring freshness of intermediate-moisture dessert spoilage, *Talanta* 81 (2010) 1126-1132.
- [3] J. P. Kerry, M. N. O'Grady, S. A. Hogan, Past, current and potential utilisation of active and intelligent packaging systems for meat and muscle-based products: A review, *Meat Sci.* 74 (2006) 113-130.
- [4] C. C. Balamatsia, A. Patsias, M. G. Kontominas, I. N. Savvaidis, Possible role of volatile amines as quality-indicating metabolites in modified atmosphere-packaged chicken fillets: Correlation with microbiological and sensory attributes, *Food Chem.* 104 (2007) 1622-1628.
- [5] B. Austin, The bacterial microflora of fish, *ScientificWorldJournal* 2 (2002) 558-572.
- [6] I. Al Bulushi, S. Poole, H. C. Deeth, G. A. Dykes, Biogenic amines in fish: roles in intoxication, spoilage, and nitrosamine formation--a review, *Crit. Rev. Food Sci.* 49 (2009) 369-377.
- [7] X. Huang, K. Nakanishi, N. Berova, Porphyrins and Metalloporphyrins: Versatile Circular Dichroic Reporter Groups for Structural Studies, *Chirality* 12 (2000) 237-255.

- [8] B. R. Takulapalli, G. M. Laws, P. A. Liddell, J. Andréasson, Z. Erno, D. Gust, T. J. Thornton, Electrical detection of amine ligation to a metalloporphyrin via a hybrid SOI-MOSFET, *J. Am. Chem. Soc.* 130 (2008) 2226-2233.
- [9] B. Wang, Z. Chen, X. Zuo, Y. Wu, C. He, X. Wang, Z. Li, Comparative NH₃-sensing in palladium, nickel and cobalt tetra-(tert-butyl)-5,10,15,20-tetraazaporphyrin spin-coating films, *Sens. Actuators B* 160 (2011) 1-6.
- [10] M. Tonezzer, A. Quaranta, G. Maggioni, S. Carturan, G.D. Mea, Optical sensing responses of tetraphenyl porphyrins toward alcohol vapours: A comparison between vacuum evaporated and spin-coated thin films, *Sens. Actuators B* 122 (2007) 620-626.
- [11] M. Tonezzer, G. Maggioni, E. Dalcanale, Production of novel microporous porphyrin materials with superior sensing capabilities, *J. Mater. Chem.* 22 (2012) 5647-5655.
- [12] S.A. Trammell, M. Zeinali, B.J. Melde, P.T. Charles, F.L. Velez, M.A. Dinderman, A. Kusterbeck, M.A. Markowitz, Nanoporous organosilicas as preconcentration materials for the electrochemical detection of trinitrotoluene, *Anal. Chem.* 80 (2008) 4627-4633.
- [13] S.A. Trammell, B.J. Melde, D. Zabetakis, J.R. Deschamps, M.A. Dinderman, B.J. Johnson, A.W. Kusterbeck, Electrochemical detection of TNT with in-line pre-concentration using imprinted diethylbenzene-bridged periodic mesoporous organosilicas, *Sens. Actuators B* 155 (2011) 737-744.
- [14] S. Tao, G. Li, H. Zhu, Metalloporphyrins as sensing elements for the rapid detection of trace TNT vapour, *J. Mater. Chem.* 16 (2006) 4521-4528.
- [15] F.A. Nwachukwu, M.G. Baron, Polymeric matrices for immobilising zinc tetraphenylporphyrin in absorbance based gas sensors, *Sens. Actuators B* 90 (2003) 276-285.
- [16] N.D. Boscher, D. Duday, P. Heier, K. Heinze, F. Hilt, P. Choquet Atmospheric pressure plasma polymerisation of metalloporphyrins containing mesoporous membranes for gas sensing applications, *Surf. Coat. Tech.* (2013) DOI: 10.1016/j.surfcoat.2012.12.034.
- [17] N.D. Boscher, D. Duday, P. Heier, K. Heinze, F. Hilt, P. Choquet, Plasma polymer membranes for immobilising metalloporphyrins, *Plasma Process. Polym.* 10 (2013) 336-344.
- [18] D.A. Summerville, R.D. Jones, B.M. Hoffman, F. Basolo, Chromium(III) porphyrins. Chemical and spectroscopic properties of chloro-meso-tetraphenylporphinatochromium(III) in nonaqueous solutions, *J. Am. Chem. Soc.* 99 (1977) 8195-8202.
- [19] N.D. Boscher, P. Choquet, D. Duday, N. Kerbellec, J.-C. Lambrechts, R. Maurau, Luminescent lanthanide-based hybrid coatings deposited by atmospheric pressure plasma assisted chemical vapour deposition, *J. Mater. Chem.* 21 (2011) 18959-18961.
- [20] D. Del Frari, J. Bour, J. Bardon, O. Buchheit, C. Arnoult, D. Ruch, Hybrid layers deposited by an atmospheric pressure plasma process for corrosion protection of galvanized steel, *J. Nanosci. Nanotechnol.* 9 (2009) 1-9.
- [21] N.D. Boscher, D. Duday, S. Verdier, P. Choquet, Single-step process for the deposition of high water contact angle and high water sliding angle surfaces by atmospheric pressure dielectric barrier discharge, *ACS Appl. Mater. Interfaces* 5 (2013) 1053-1060.
- [22] M. Gouterman, L.K. Hanson, G. Khalil, W.R. Leenstra, J.W. Buchler, Porphyrins. XXXII. Absorptions and luminescence of Cr(III) complexes, *J. Chem. Phys.* 62 (1975) 2343-2353.
- [23] M. Tonezzer, G. Maggioni, A. Quaranta, S. Carturan, G. Della Mea, Optical properties of free-base tetraphenylporphyrin embedded in fluorinated polyimides and their ethanol and water vapours sensing capabilities, *Sens. Actuators B* 136 (2009) 290-296.
- [24] K. Nakamura, M. Watanabe, M. Zhou, M. Fujishima, M. Tsuchiya, T. Handa, S. Ishii, H. Noguchi, K. Kashiwagi, Y. Yoshida, Plasma polymerization of cobalt tetraphenylporphyrin and the functionalities of the thin films produced, *Thin Solid Films* 345 (1999) 99-103.
- [25] H.H. Huss, Quality and quality changes in fresh fish, Food and Agricultural Organization of the United Nations, Roma, 1995.
- [26] M. Etienne, Volatile amines as criteria for chemical quality assessment, *Seafoodplus Traceability*, 2005.

- [27] K. Randell, R. Ahvenainen, K. Latva-Kala, E. Hurme, T. Mattila-Sandholm, L. Hyvönen, Modified atmosphere-packed marinated chicken breast and rainbow trout quality as affected by package leakage, *J. Food Sci.* 60 (1995) 667-672.
- [28] J.M. Charlesworth, C.A. McDonald, A fibre-optic fluorescing sensor for amine vapours, *Sens. Actuators B* 8 (1992) 137-142.
- [29] W. Qin, P. Parzuchowski, W. Zhang, M.E. Meyerhoff, Optical sensor for amine vapors based on dimmer-monomer equilibrium of indium (III) octaethylporphyrin in a polymeric film, *Anal. Chem.* 75 (2003) 332-340.
- [30] K.I. Oberg, R. Hodyss, J.L. Beauchamp, Simple optical sensor for amine vapors based on dyed silica microspheres, *Sens. Actuators B* 115 (2006) 79-85.
- [31] B. Onida, S. Fiorilli, G. Borello, G. Viscardi, D. Macquarries, E. J. Garrone, Mechanism of the optical response of mesoporous silica impregnated with Reichardt's dye to NH₃ and other gases, *J. Phys. Chem. B* 108 (2004) 166617-16620.
- [32] M. McCarrick, S.J. Harris, D.J. Diamond, Assessment of a chromogenic calyx(4)arene for the rapid colorimetric detection of trimethylamine, *J. Mater. Chem.* 4 (1994) 217-221.
- [33] Y. Xu, X. Wenshui, J.M. Kim, Biogenic and volatile amines in Chinese mitten crab (*Eriocheir sinensis*) stored at different room temperatures, *Int. J. Food Sci. Tech.* 44 (2009) 1547-1552.
- [34] B.K. Larsen, D. Schlenk, Effect of urea and low temperature on the expression and activity of flavin-containing monooxygenase in the liver and gill of rainbow trout (*Oncorhynchus mykiss*), *Fish Physiol. Biochem.* 25 (2002) 19-29.
- [35] R.J. Shakila, K. Vijayalakshmi, G. Jeyasekaran, Changes in histamine and volatile amines in six commercially important species of fish of the Thoothukkudi coast of Tamil Nadu, India stored at ambient temperature, *Food Chem.* 82 (2003) 347-352.
- [36] J.J. Connell, *Control of fish quality*, fourth ed., Wiley-Blackwell, England: 1995.
- [37] P. Heier, C. Förster, D. Schollmeyer, N. Boscher, P. Choquet, K. Heinze, $\alpha\alpha$ - and $\alpha\beta$ -Zinc-meso-A₂B₂-tetraarylporphyrins with large optical responses to triethylamine, *Dalton T.* 42 (2013) 906-917.

3.4

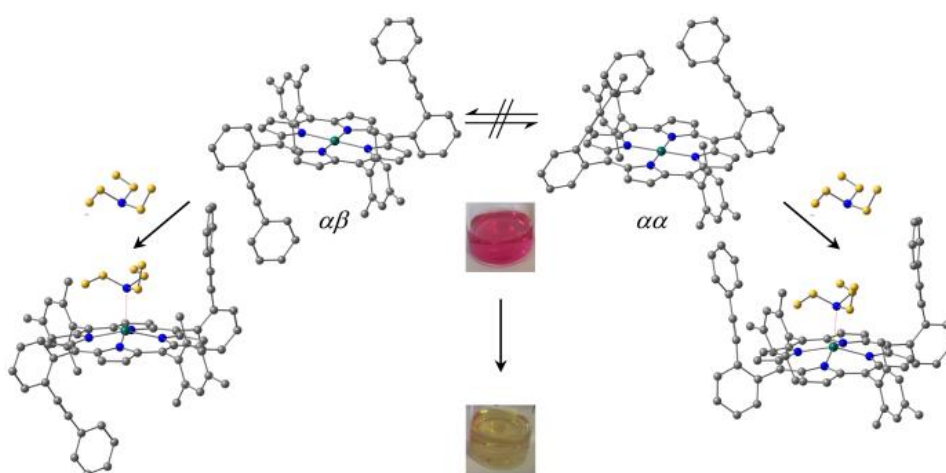
$\alpha\alpha$ - and $\alpha\beta$ -Zinc-*meso*-A₂B₂-Tetraarylporphyrins with Large Optical Response to Volatile Amines

P. Heier, C. Förster, D. Schollmeyer, N. Boscher, P. Choquet, K. Heinze


Dalton Transactions **2013**, 42, 906 – 917.

Abstract

Synthesis and separation of $\alpha\alpha$ - and $\alpha\beta$ -*meso*-A₂B₂-zinc(II) tetraarylporphyrin atropisomers with A = mesityl and B = *ortho*-phenylethynyl-phenyl are reported. Both isomers exhibit large optical responses upon axial NEt₃ coordination which are visible to the human eye and could therefore be beneficial for the design of smart amine sensing materials. The larger spectral changes as compared to Zn(TPP) are attributed to pronounced distortions of the porphyrin π -system due to steric interactions of the coordinating amine with the porphyrin periphery. This effect as well as the coordination site of NEt₃ at the $\alpha\alpha$ -isomer have been studied by NMR experiments and were rationalized by DFT calculations and NSD analyses. The solubility in non-polar solvents is greatly enhanced as compared to Zn(TPP), especially of the $\alpha\alpha$ -isomer. This is explained by analysis of the solid state structures as derived from partial single crystal X-ray diffraction studies.



Reproduced by permission of The Royal Society of Chemistry



Supplementary Information can be found at pp. 183 – 198
(without the cartesian coordinates of the DFT optimised structures)

The full supplementary information are available online;
see DOI: [10.1039/c2dt31943h](https://doi.org/10.1039/c2dt31943h)

Introduction

Sensing of aliphatic as well as aromatic amines down to low concentrations is of great interest in manifold applications. In an industrial context, aliphatic amines and diamines are used *e.g.* as fertilizers, auxiliaries in dye manufacturing or in pharmaceutical synthesis. Furthermore, biogenic amines, which are products of the enzymatic decarboxylation of α -amino acids, are indicators for food freshness and their detection might lead to simple but powerful devices for the control of food quality.¹

During the past decades, several approaches have been developed to control amine concentrations in different environments, ranging from chromatographic² to enzyme-based methods³, immobilized pH-indicators^{1,4}, molecularly imprinted⁵ or functionalized polymers⁶ as well as a broad range of molecular sensors.⁷ For instance, aldehyde cruciforms show a fluorescence turn-on when exposed to primary and secondary amines due to covalent binding of the analytes⁸ and could detect 1,3-diaminopropane down to 100 ppm concentrations in THF.

Based on trifluoroacetyl groups as receptor moieties, Mohr *et al.* developed star-shaped tripodal chemosensors to monitor concentrations of aliphatic mono- and diamines by changes in the absorption spectrum as well as by fluorescence turn-on.⁹ In addition to covalent binding to the described sensors, amines can also be detected via coordination to appropriate metal centers. Metalloporphyrins are especially suitable, as they are either bearing a vacant coordination site at the metal center or axial ligand exchange is often facilitated thanks to strong in-plane metal-porphyrin interactions compared to other metal-ligand interactions. As a broad range of different metal centers can be introduced and as there are well-established approaches to functionalize the porphyrin core itself, the coordination site can be tailored in manifold ways to enhance the sensitivity and selectivity of the sensor.

Based on these possibilities several metalloporphyrin-based sensor systems have been developed. A triad of zinc(II) tetraarylporphyrins has been used for the detection of primary, secondary, cyclic tertiary as well as aromatic amines in THF solutions with a bathochromic shift of the Soret absorption ranging from 3 to 6 nm.¹⁰ Using the same porphyrin triad as manganese(III) acetate salt gives rise to hypsochromic shifts up to 35 nm of the Soret-band in THF solutions upon exposure to primary and secondary amines, but neither with tertiary nor aromatic ones.¹⁰ Melamine-bridged bis(zinc(II)porphyrin) receptors with a tweezers-like structure have been utilized as molecular sensors¹¹ or attached to polymer beads¹² for the detection of linear aliphatic α,ω -diamines with chain lengths between four and eight carbon atoms. The affinity towards α,ω -diamines in these systems is much higher as compared to monoamines like *n*-butylamine and the bathochromic shift of the Soret-absorption ranges between 5 nm for butane 1,4-diamine and 9 nm for octane 1,8-diamine. The combination of different bis-pocket zinc(II) porphyrins with a series of various metalated tetraphenylporphyrins in one colorimetric array led to a sensor device which could not

only detect but discriminate 12 different primary, secondary, tertiary as well as aromatic amines.^{13,14}

To gain access to robust, cheap and easy to handle amine sensing devices for a broad group of users, *e.g.* with respect to control food freshness, a promising approach is the development of optical sensors featuring responses towards amines which might not only be investigated by sophisticated and expensive spectrometers in detail but also show characteristic changes visible by the human eye.^{1,15} A new approach for the large scale synthesis of such colorimetric sensor devices is the atmospheric pressure dielectric barrier discharge technique, for which stable sensor molecules like porphyrins are most suitable.^{16,17}

Typically, the Soret- as well as the Q-bands of zinc(II) porphyrins undergo a bathochromic shift upon coordination of a neutral or an anionic ligand to the metal center.^{18,19} Based on UV/vis experiments Valentine *et al.* assume, that the extent of the bathochromic shift for a given zinc(II) porphyrin is mainly attributed to the amount of charge transfer from the monodentate ligand via the zinc(II) ion to the porphyrin ring.¹⁹ However, bathochromical absorption shifts in intrinsically distorted porphyrins has been connected to different degrees of nonplanar deformations of the porphyrin macrocycle.²⁰⁻²² And furthermore, it has been shown on chromium(III) porphyrins that the distortion of the porphyrin core due to ligand-porphyrin interactions also contributes to the extent of the spectral shifts after axial ligand coordination.²³ Therefore, to enhance the spectral shift upon coordination of a given ligand, *e.g.* triethylamine, to a metalloporphyrin it should be beneficial to use porphyrins in which sterical interaction of the coordinated ligand with the porphyrin substituents leads to a distortion of the porphyrin core and thus the chromophoric π -system.

Following this concept, we present novel $\alpha\alpha$ - and $\alpha\beta$ meso A_2B_2 -zinc(II) tetraarylporphyrins bearing mesityl moieties as A groups and sterically demanding rigid ortho-phenylalkynyl substituents as meso-aryl groups B. The interaction of these rigid arms with coordinated amines like triethylamine should lead to a sizeable distortion of the porphyrin core and thereby to an enhanced optical response of this sensor upon amine exposure.

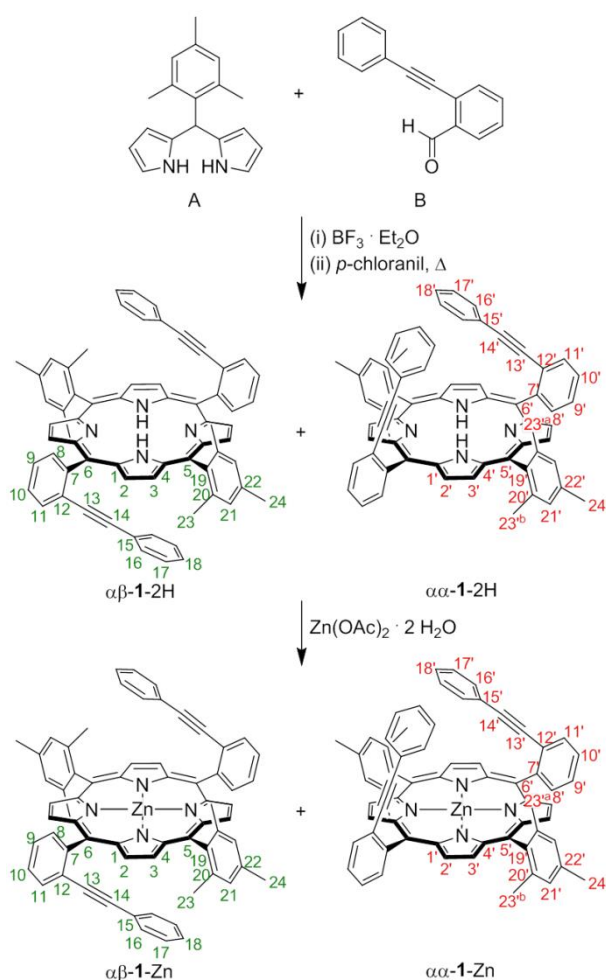
Furthermore, by disturbing the predominant intermolecular π - π -interactions between the porphyrin cores, these two phenylalkynyl arms should lead to an enhanced solubility of these porphyrins, which is important for further processing of molecular sensors to amine sensing materials.

Results and discussion

A. Synthesis of porphyrins and zinc(II) complexes

Rational syntheses of *trans*- A_2B_2 porphyrins have been developed by Lindsey *et al.* for various combinations of A and B substituents by condensation of suitably substituted

dipyrrromethanes with the respective aldehydes.^{24, 25} The synthesis of the novel regioisomerically pure porphyrins $\alpha\alpha$ -1-Zn and $\alpha\beta$ -1-Zn, which bear two *ortho*-phenylalkynyl arms shielding the coordination site, is based on the condensation of *meso*-(mesityl) dipyrrromethane **A**²⁴ and 2-(phenylethynyl) benzaldehyde **B**²⁶ under Lewis acid catalysis followed by oxidation with *p*-chloranil (Scheme 1). Due to the *ortho*-substituted *meso*-aryl groups, this condensation gives rise to two atropisomers $\alpha\alpha$ -1-2H and $\alpha\beta$ -1-2H (Scheme 1). The two isomers were obtained in a statistical ratio (1:1) in a total yield of 28 % and could be separated from a minor impurity (≈ 1 %) of the A₃B-porphyrin bearing three mesityl and one phenylalkynyl arm via repeated column chromatography. No procedure could be established separating the two atropisomers $\alpha\alpha$ -1-2H and $\alpha\beta$ -1-2H at this stage.



Scheme 1 Synthesis of $\alpha\alpha$ -1-Zn and $\alpha\beta$ -1-Zn. Atom numbering as used for NMR assignments.

Metalation of the mixture of the free-base porphyrins $\alpha\alpha$ -1-2H and $\alpha\beta$ -1-2H with zinc(II) ions was performed under standard conditions using zinc(II) acetate dihydrate in dichloromethane. The two atropisomers $\alpha\alpha$ -1-Zn and $\alpha\beta$ -1-Zn were isolated in an overall yield of 89 %. After crude purification on a silica column the atropisomers could

be separated by reversed-phase HPLC using methanol/acetone 1:1 as eluent (see experimental section for details).

B. Composition and structures of free-base porphyrins and zinc(II) complexes

All compounds were characterized by high-resolution mass spectrometry, UV/vis absorption and fluorescence spectroscopy as well as NMR spectroscopy (^1H , $^{13}\text{C}\{^1\text{H}\}$, 2D-NMR). Furthermore, molecular structures of $\alpha\alpha$ -1-Zn and $\alpha\beta$ -1-Zn were confirmed by partial single crystal X-ray diffraction studies. The ^1H NMR spectrum of the isomer mixture of $\alpha\alpha$ -1-2H and $\alpha\beta$ -1-2H in CD_2Cl_2 features two signals in the characteristic region for free-base porphyrin $\text{NH}_{\text{pyrrole}}$ protons at $\delta = -2.56$ and $\delta = -2.52$ ppm, which unambiguously show the presence of two different porphyrins in a 1:1 ratio. Except for the resonances of the *ortho*-methyl groups of the mesityl moiety and the protons $\text{H}^{17}/\text{H}^{17'}$ and $\text{H}^{18}/\text{H}^{18'}$ of the shielding phenyl group, all other resonances in the ^1H NMR spectrum are superimposed and therefore a straightforward assignment to one of the two isomers is impossible. Due to its C_{2h} symmetry $\alpha\beta$ -1-2H shows one resonance for both *ortho*-methyl groups H^{23} at $\delta = 1.83$ ppm while the C_{2v} symmetric $\alpha\alpha$ -1-2H displays two resonances for $\text{H}^{23'}$ ($\text{H}^{23'a}$ and $\text{H}^{23'b}$) at $\delta = 1.81$ and $\delta = 1.84$ ppm, respectively. Thanks to contacts of $\text{H}^{23'a}$ to $\text{H}^{17'}$ in the NOESY spectrum an unambiguous assignment of $\text{H}^{23'a}$ and $\text{H}^{23'b}$ is possible (see Figure 1) with $\text{H}^{23'a}$ pointing to the proximal site.

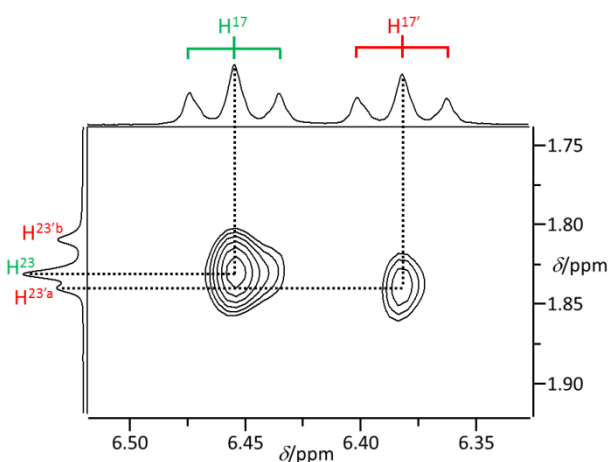
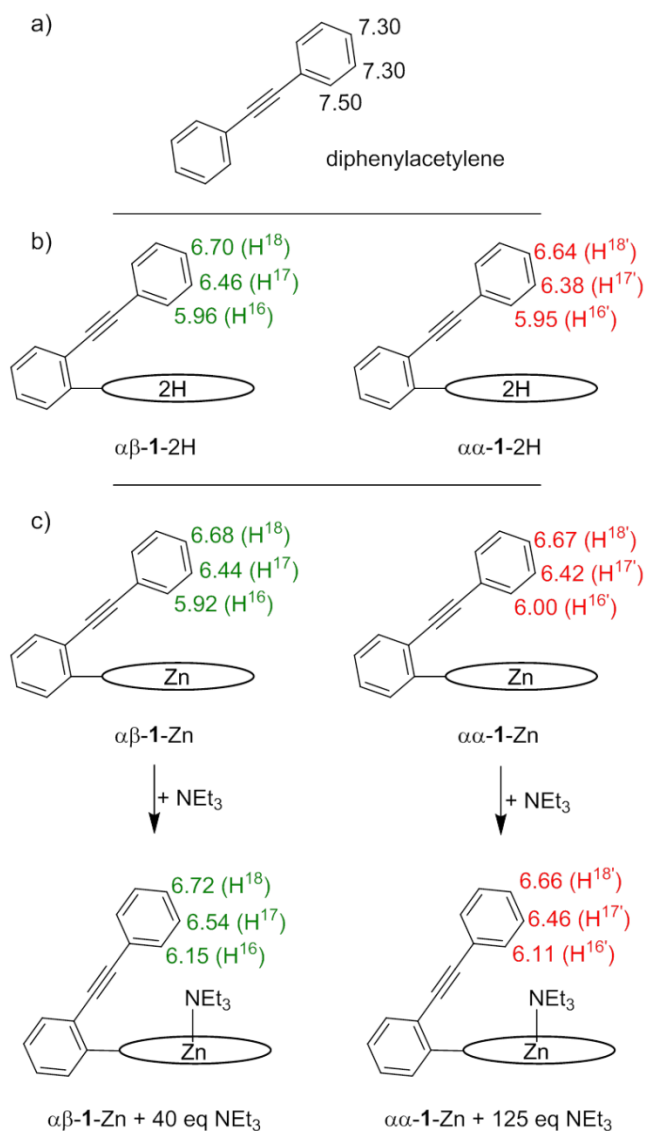


Fig. 1 Partial NOESY NMR spectrum of $\alpha\alpha$ - and $\alpha\beta$ -1-2H isomer mixture in CD_2Cl_2 (atom numbering according to Scheme 1).

Variable temperature ^1H NMR experiments were carried out between 298 K and 353 K in DMSO-d_6 (see Supporting Information). The rotation barrier ΔG_{353}^\ddagger of the mesityl group around the σ -bond to the porphyrin macrocycle of $\alpha\alpha$ -1-2H could be estimated as 74 kJ mol^{-1} from the coalescence temperature ($T_c \approx 353 \text{ K}$) of the $\text{H}^{23'a}$ and $\text{H}^{23'b}$ methyl resonances.[‡]

[‡] The rotation barrier ΔG_{353}^\ddagger was calculated by $\Delta G^\ddagger = \ln\left(\frac{2.22 \Delta \nu h}{k_b T_c}\right) RT_c$, with the frequency difference of the respective proton resonances at 298 K $\Delta \nu = 41.6 \text{ Hz}$, Planck's constant h , Boltzmann's constant k_b , coalescence temperature T_c and gas constant R .

No coalescence could be found for the proton resonances $H^{16}/H^{16'}$ and $H^{17}/H^{17'}$ of the phenylethynyl arms. Obviously, rotation of the phenylethynyl arm with respect to the porphyrin plane is hindered at $T < 353$ K and thus interconversion of the two atropisomers $\alpha\alpha$ -1-2H and $\alpha\beta$ -1-2H is impossible due to the rigid phenylalkynyl arms at the *ortho*-position of the *meso*-aryl groups. In contrast, porphyrins with small *ortho*-substituents, *e.g.* OH, at all four *meso*-aryl groups or $\alpha\alpha$ - and $\alpha\beta$ -isomers with more flexible groups at the *ortho*-position, *e.g.* porphyrins with dendric substituents synthesized by Hirsch *et al*, show rapid atropisomerisation.^{27, 28}



Scheme 2 ^1H chemical shifts in CD_2Cl_2 of (a) reference diphenylacetylene, (b) $\alpha\alpha$ -1-2H and $\alpha\beta$ -1-2H and (c) $\alpha\alpha$ -1-Zn and $\alpha\beta$ -1-Zn before and after addition of excess triethylamine (atom numbering according to Scheme 1).

The proton resonances of the phenyl groups H^{16} , H^{17} , H^{18} and $H^{16'}$, $H^{17'}$, $H^{18'}$, respectively, are considerably shifted to higher field when compared to the reference compound diphenylacetylene (see Scheme 2 a) and b)).²⁹ This can be attributed to the

fact, that the phenyl ring is located above the porphyrin π -system ring current, which shifts the phenyl proton resonances to higher field. The strongest effect is seen for the $H^{16}/H^{16'}$ resonances, as these protons directly point onto the porphyrin π -system. The more remote $H^{18}/H^{18'}$ nuclei are less affected.

As expected, for the zinc porphyrins $\alpha\alpha$ -1-Zn and $\alpha\beta$ -1-Zn obtained after HPLC the resonances around $\delta = -2.5$ ppm are absent. All other 1H as well as ^{13}C resonances can unambiguously be assigned with the help of $^1H, ^1H$ -COSY, NOESY, HMBC and HSQC 2D-NMR experiments (see Supporting Information for details). Analogous to the free-base porphyrins the H^{16} , H^{17} , H^{18} , $H^{16'}$, $H^{17'}$, $H^{18'}$ resonances of the phenylethynyl arms of the Zn(II) porphyrins experience the ring current of the porphyrin macrocycle (see Scheme 2 c)).

Further proof of the correct assignment of both the $\alpha\alpha$ - and $\alpha\beta$ -isomers was provided by (partial) single crystal X-ray diffraction studies of $\alpha\alpha$ -1-Zn and $\alpha\beta$ -1-Zn (see Figure 2).

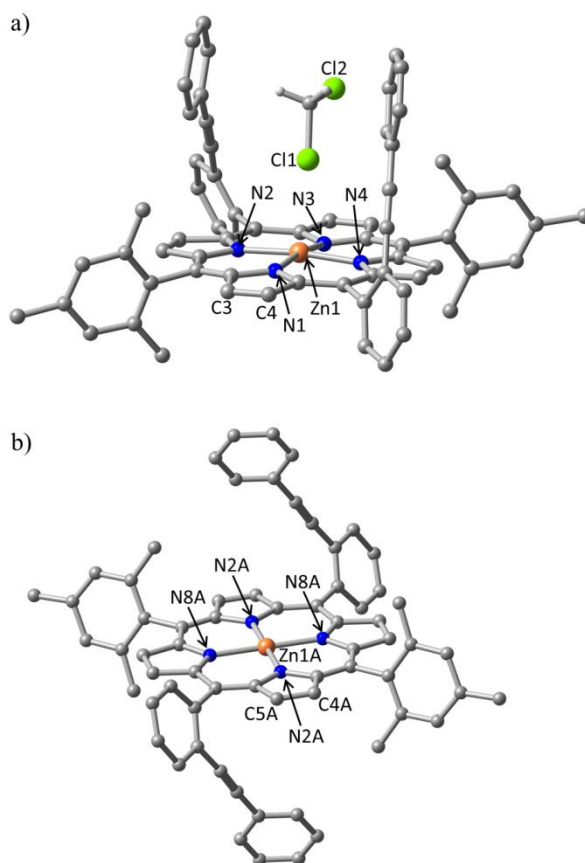


Fig. 2 Molecular structures of (a) $\alpha\alpha$ -1-Zn and (b) $\alpha\beta$ -1-Zn in the solid state as derived from partial single crystal X-ray diffraction studies. For $\alpha\beta$ -1-Zn the molecule positioned at the ab -plane ($1/2, 1/2, 0$; $\alpha\beta$ -1-Zn(C)) is shown. Porphyrin protons are omitted for clarity.

The asymmetric unit of the $\alpha\beta$ -1-Zn isomer contains three independent centrosymmetric molecules whose zinc centers are located on the origin of the cell (0, 0, 0; $\alpha\beta$ -1-Zn(A)), the center of the cell ($\frac{1}{2}, \frac{1}{2}, \frac{1}{2}$; $\alpha\beta$ -1-Zn(B)), and the center of the ab-plane ($\frac{1}{2}, \frac{1}{2}, 0$; $\alpha\beta$ -1-Zn(C)) of the triclinic unit cell, respectively. No solvent molecules are co-crystallized and therefore all zinc(II) ions are coordinated in a square planar manner by the four porphyrin nitrogen atoms. The three different molecules are connected via π - π -interactions between the porphyrin core of one molecule and a phenyl group of another porphyrin. An offset-face-to-face interaction between the porphyrin core of $\alpha\beta$ -1-Zn(A) and the *meso*-phenyl ring of $\alpha\beta$ -1-Zn(B) as well as between the porphyrin core of $\alpha\beta$ -1-Zn(C) and the phenylethynyl group of $\alpha\beta$ -1-Zn(A) is observed. Furthermore, there is an edge-to-face interaction between the *ortho*-methyl group of $\alpha\beta$ -1-Zn(C) and the porphyrin core of $\alpha\beta$ -1-Zn(B). The observed π - π -interactions are in good agreement with typical examples for aromatic π - π -interactions found in the literature.³⁰ As in other tetraaryl porphyrins all *meso*-aryl groups are non-co-planar with the porphyrin plane.³¹

The asymmetric unit of the $\alpha\alpha$ -1-Zn isomer contains a single porphyrin molecule. Two disordered dichloromethane molecules are co-crystallized within the crystal. In contrast to the $\alpha\beta$ -1-Zn isomer, π - π -interactions between the individual porphyrins are entirely absent. In addition to the fourfold coordination by the porphyrin nitrogen atoms, the zinc(II) ion shows an interaction with one chlorine atom of a dichloromethane encapsulated by the phenylethynyl substituents at the proximal site and the zinc(II) ion is displaced from the porphyrin mean plane towards the chlorine atom.

Typically, a multitude of intermolecular π - π -interactions between simple *meso*-tetraphenyl porphyrin macrocycles, *e.g.* in zinc(II)tetraphenylporphyrin (Zn(TPP)), leads to their poor solubility, especially in non-polar solvents. As shown above, these interactions are reduced in $\alpha\beta$ -1-Zn and absent in $\alpha\alpha$ -1-Zn and therefore the solubility of $\alpha\alpha$ -1-Zn and $\alpha\beta$ -1-Zn should be enhanced as compared to Zn(TPP). The solubility has been probed in the non-polar solvent hexamethyldisiloxane (HMDSO), as solubility therein is a crucial point for possible application of the porphyrins in sensor fabrication.¹⁷ The solubility of $\alpha\beta$ -1-Zn ($4.6 \times 10^{-6} \text{ mol L}^{-1}$, 4.4 mg L^{-1}) is five times higher as compared to Zn(TPP) ($8.4 \times 10^{-7} \text{ mol L}^{-1}$, 0.6 mg L^{-1}) while the solubility of $\alpha\alpha$ -1-Zn ($1.0 \times 10^{-4} \text{ mol L}^{-1}$, 96.0 mg L^{-1}) is even enhanced by more than two orders of magnitude. The remarkable difference between $\alpha\alpha$ -1-Zn and $\alpha\beta$ -1-Zn can be attributed to the complete absence of intermolecular π - π -interactions in the solid state of $\alpha\alpha$ -1-Zn.

C. Optical and redox properties of zinc(II)porphyrins

Absorption and emission spectra of the free-base porphyrin mixture $\alpha\alpha$ -1-2H / $\alpha\beta$ -1-2H and the isomerically pure zinc porphyrins $\alpha\alpha$ -1-Zn and $\alpha\beta$ -1-Zn were

Table 1 Absorption properties of $\alpha\alpha$ -1-Zn, $\alpha\alpha$ -1-Zn(NEt₃), $\alpha\beta$ -1-Zn, $\alpha\beta$ -1-Zn(NEt₃), Zn(TPP) and Zn(TPP)(NEt₃)^a

		<i>n</i> -Hexane			HMDSO			Dichloromethane			Acetonitrile			Chloroform		
		Pure	+ NEt ₃ ^b	Δ	Pure	+ NEt ₃ ^b	Δ	Pure	+ NEt ₃ ^b	Δ	Pure	+ NEt ₃ ^b	Δ	Pure	+ NEt ₃ ^b	Δ
$\alpha\alpha$ -1-Zn	Soret	420	433	13	420	431	11	423	433	10	426	428	2	428	429	1
	Q(1,0)	548	566	18	548	564	16	551	564	13	560	561	1	557	558	1
	Q(0,0)	582	607	25	595	604	9	587	605	18	599	600	1	597	599	2
	A[Q(0,0)/Q(0,1)]	0.04	0.27		0.08	0.27		0.11	0.28		0.28	0.31		0.18	0.20	
$\alpha\beta$ -1-Zn	Soret	419	432	13	419	431	12	423	433	10	426	430	4	427	430	3
	Q(1,0)	548	565	17	548	563	15	550	564	14	559	562	3	555	558	3
	Q(0,0)	580	606	26	590	603	13	587	605	18	599	602	3	595	602	7
	A[Q(0,0)/Q(0,1)]	0.08	0.28		0.07	0.26		0.09	0.40		0.35	0.32		0.16	0.21	
Zn(TPP)	Soret	414	425	11												
	Q(1,0)	544	558	14												
	Q(0,0)	583	598	15												
	A[Q(0,0)/Q(0,1)]	0.08	0.35													

^a λ_{max} in nm. ^b Measured with excess triethylamine.

measured in dichloromethane at room temperature. The porphyrins show a small bathochromic shift of the Soret-band upon zinc(II) complexation and the number of Q-bands is reduced due to the higher local symmetry of the complex. The absorption spectra of $\alpha\alpha$ -1-Zn and $\alpha\beta$ -1-Zn are almost superimposable and their Soret absorption bands are shifted bathochromically as compared to Zn(TPP). The photophysical data of the new compounds are compiled in Table 1. Additionally, solvatochromic effects of the zinc porphyrins were investigated in *n*-hexane, HMDSO, acetonitrile and chloroform. As shown in Figure 3, the Soret-band of $\alpha\alpha$ -1-Zn is observed at $\lambda_{\text{Soret}} = 420$ nm in *n*-hexane and HMDSO and displays a bathochromic shift going from dichloromethane ($\lambda_{\text{Soret}} = 423$ nm) over acetonitrile ($\lambda_{\text{Soret}} = 426$ nm) to chloroform ($\lambda_{\text{Soret}} = 428$ nm), which is in good agreement with the solvatochromism described for other porphyrins in the literature.¹⁹

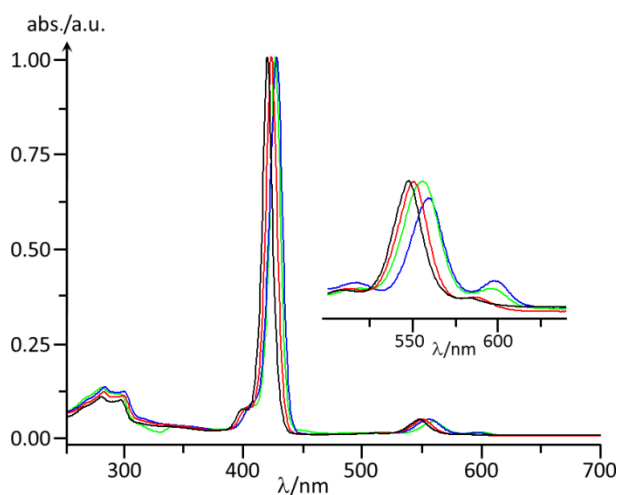


Fig. 3 Normalized (to Soret-band) absorption spectra of $\alpha\alpha$ -1-Zn in *n*-hexane (—), dichloromethane (—), acetonitrile (—) and chloroform (—). Inset shows magnification of Q-band region.

The Q-bands are shifted bathochromically in the order *n*-hexane < HMDSO < dichloromethane < chloroform < acetonitrile with the absorbance ratio

A[Q(0,0)]:A[Q(1,0)] increasing in the same order. Spectra of $\alpha\beta$ -1-Zn in these solvents are very similar to those of $\alpha\alpha$ -1-Zn with only marginal differences and the same general trends can be observed (see Table 1 and Supporting Information).

Four reversible redox processes are observed for $\alpha\alpha$ -1-Zn as expected for Zn(II) porphyrins while only three are detected for $\alpha\beta$ -1-Zn under our conditions (see Table 2). As all redox processes are ligand-centered the reductions lead to the π -anion radical and the porphyrin dianion whereas the oxidations lead to the π -cation radical and the porphyrin dication. Both isomers are more difficult to oxidise and to reduce as compared to Zn(TPP) under the same conditions (see Table 2). Comparing the two isomers, the $\alpha\beta$ -1-Zn isomer has lower potentials $E_{1/2}(\text{ox1})$ and $E_{1/2}(\text{red1})$ as compared to $\alpha\alpha$ -1-Zn, which indicates that the porphyrin macrocycle is slightly more electron rich. Nevertheless, the HOMO-LUMO gap as estimated from $E_{1/2}(\text{ox1})-E_{1/2}(\text{red1})$ is essentially the same for both isomers and larger as compared to Zn(TPP), which is in good agreement with their identical absorption properties described above. Furthermore, the HOMO-LUMO gaps calculated by DFT methods correctly reproduce the experimental trends (Table 2).

Table 2 Redox potentials of $\alpha\alpha$ -1-Zn and $\alpha\beta$ -1-Zn in $n\text{Bu}_4\text{NPF}_6/\text{CH}_2\text{Cl}_2$ at 298 K vs. FcH/FcH⁺ and calculated frontier orbital energies

	$E_{1/2}(\text{red2})/\text{V}$	$E_{1/2}(\text{red1})/\text{V}$	$E_{1/2}(\text{ox1})/\text{V}$	$E_{1/2}(\text{ox2})/\text{V}$	$\Delta E(E_{1/2}(\text{ox1}) - E_{1/2}(\text{red1}))/\text{eV}$	$\Delta(\Delta E(E_{1/2}(\text{ox1}) - E_{1/2}(\text{red1})))/\text{eV}$	$\Delta E(\text{HOMO-LUMO})/\text{eV}^a$	$\Delta(\Delta E(\text{HOMO-LUMO}))/\text{eV}^a$
$\alpha\alpha$ -1-Zn	-2.43	-1.86	0.40	0.82	2.260	0.070 ^b	2.794	0.051 ^b
$\alpha\beta$ -1-Zn		-1.90	0.37	0.73	2.270	0.080 ^c	2.807	0.065 ^c
Zn(TPP)	-2.21	-1.85	0.34	0.66	2.190	—	2.742	—

^a Calculated by DFT (B3LYP, LanL2DZ). ^b $\Delta E(\alpha\alpha$ -1-Zn) - $\Delta E(\text{Zn}(\text{TPP}))$. ^c $\Delta E(\alpha\beta$ -1-Zn) - $\Delta E(\text{Zn}(\text{TPP}))$.

D. Determination of the NEt_3 coordination site by NMR and DFT

Proton NMR spectra of the two zinc porphyrins $\alpha\beta$ -1-Zn and $\alpha\alpha$ -1-Zn were measured in CD_2Cl_2 at room temperature before and after addition of several equivalents triethylamine. In both cases, coordination of the amine leads to significant shifts of the proton NMR resonances. As ligand exchange is fast under these conditions, no individual resonances of NEt_3 coordinated and four-coordinate zinc porphyrins are detected.³⁴

For $\alpha\beta$ -1-Zn the pyrrole (H^2 , H^3) and *meso*-phenyl (H^8 , H^9 , H^{10}) resonances are shifted to higher field and resonances of the shielding phenyl group (H^{16} , H^{17} , H^{18}) are shifted to lower field, while triethylamine coordination has negligible effects on the *meso*-mesityl protons H^{21} (see Figure 4, bottom). The observed upfield shifts can be attributed to the fact that the zinc(II) ion is displaced from the porphyrin plane upon amine coordination which leads to a weaker interaction with the porphyrin nitrogen atoms and therefore the Lewis acidic effect of zinc(II) on the porphyrin is reduced.^{34, 35} This effect is further enhanced by electron donation from triethylamine to zinc which is reflected in shielding of the pyrrole ($\text{H}^2/\text{H}^{2'}$, $\text{H}^3/\text{H}^{3'}$) and *meso*-phenyl protons ($\text{H}^8/\text{H}^{8'}$,

$H^9/H^{9'}$, $H^{10}/H^{10'}$). The resonance shift of the arm phenyl protons (H^{16} , H^{17} , H^{18}) is likely connected to changes in the porphyrin topology due to interaction of the arm with the coordinating amine.

As described above, the protons of the shielding phenyl group of $\alpha\beta$ -1-Zn are considerably shifted to higher field compared to resonances of the reference compound diphenylacetylene (see Scheme 2). The extent of the shift can be correlated to the proximity of the respective proton to the porphyrin core with H^{16} being shifted most as it directly points to the core. Upon triethylamine coordination to the zinc(II) center the arm is deflected from its position above the ring center due to steric interactions with the amine. Therefore, the influence of the ring current is diminished and the proton resonances are shifted to lower field with a major effect on the *ortho* H^{16} and a minor one on the *para* H^{18} (see Figure 4).

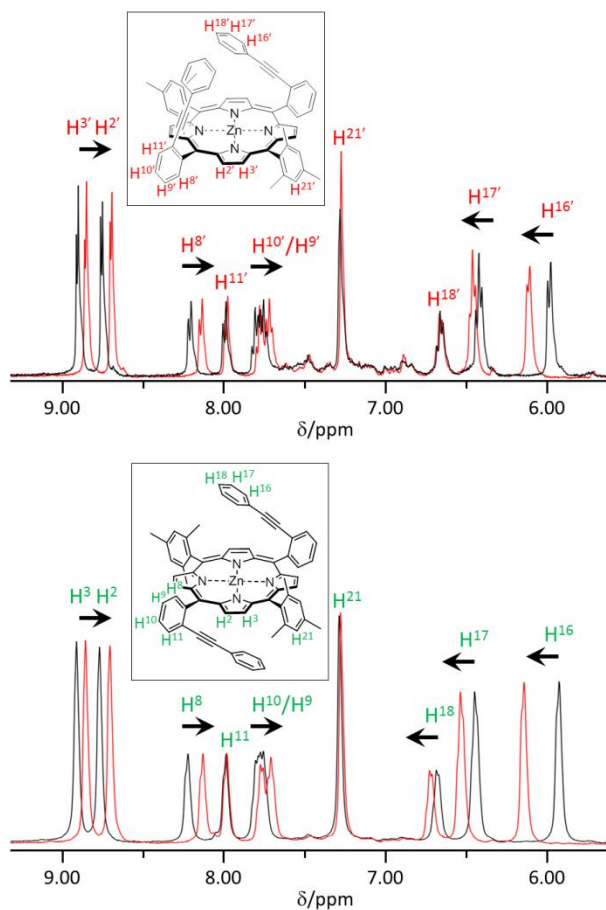


Fig. 4 Partial ^1H NMR spectrum of $\alpha\alpha$ -1-Zn (top) and $\alpha\beta$ -1-Zn (bottom) before (black) and after (red) addition of excess triethylamine in CD_2Cl_2 .

To elucidate the effects described above, DFT calculations (B3LYP, LanL2DZ) were carried out to compare the deformations of the porphyrin geometry before and after triethylamine coordination. As can be seen from the optimized structures of $\alpha\beta$ -1-Zn and $\alpha\beta$ -1-Zn(NEt_3) in Figure 5, coordination of the amine leads to the expected

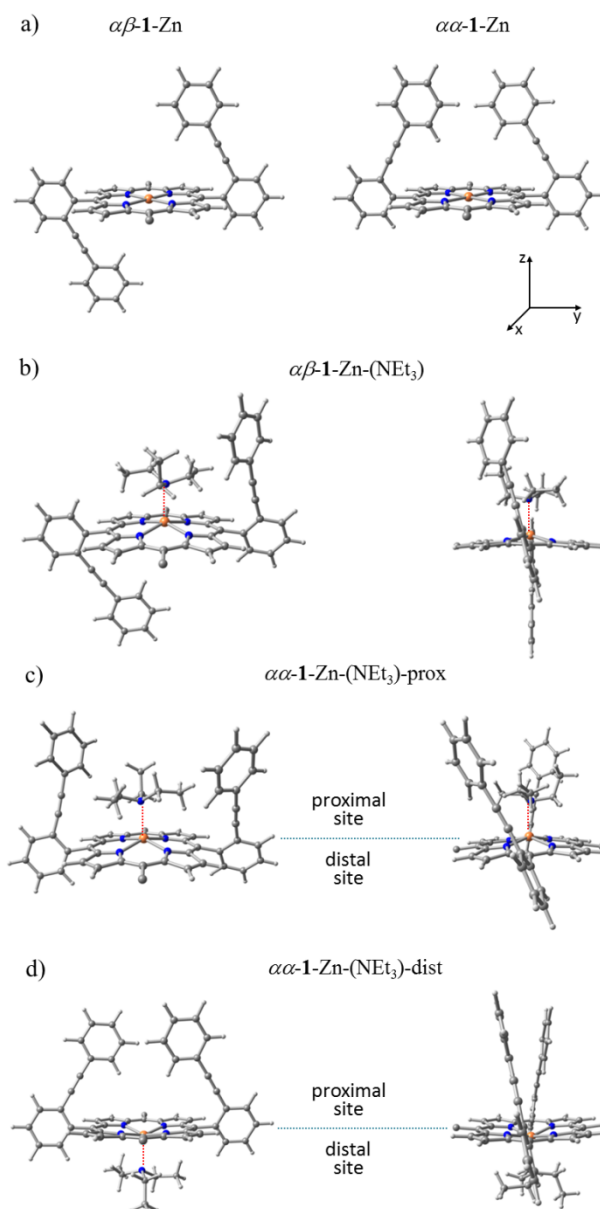


Fig 5 Geometry optimized structures (B3LYP, LanL2DZ) of (a) $\alpha\beta$ -1-Zn and $\alpha\alpha$ -1-Zn, (b) $\alpha\beta$ -1-Zn-NEt₃, (c) $\alpha\alpha$ -1-Zn-NEt₃-prox, (d) $\alpha\alpha$ -1-Zn-NEt₃-dist; in (b), (c) and (d) views along x-axis (left) and views along y-axis (right) are shown. Mesityl groups are omitted for clarity.

displacement (0.57 Å) of the zinc(II) ion from the porphyrin plane towards the amine and a doming (A_{2u} symmetrical) dominated deformation of the porphyrin core (see Table 3). Even though the arm position is likely to be flexible in solution to some extent, the structural parameters derived from the static geometry optimized structures represent general trends upon triethylamine coordination. The interaction of the phenylethynyl arm with triethylamine on the one hand is expressed by the torsion angle of the proximal *meso*-aryl group bearing the arm relative to the porphyrin core. This angle is decreased from almost orthogonal (88.8°) without amine to 74.4°

with amine coordination whereas the respective angle of the distal phenylethynyl arm is not affected (89.4°, see Table 3). To quantify the displacement of the arms upon interaction with the amine, the distances of the phenyl group centroids to the centroid of the porphyrin 24 atom least square plane are calculated. This distance increases from 6.87 Å to 7.90 Å for the proximal arm interacting with the amine and slightly decreases to 6.27 Å for the distal arm (Table 3). The larger distance to the porphyrin center is in good agreement with the decreasing influence of the porphyrin ring current on this group as revealed by NMR (Scheme 2).

Table 3 NSD analysis^a and selected angles (°) and distances (Å) of $\alpha\alpha$ -1-Zn, $\alpha\beta$ -1-Zn, Zn(TPP) and their NEt₃ complexes derived from DFT calculations

	B_{2u} (sad) ^b	B_{1u} (ruf) ^c	A_{2u} (dom) ^d	$E_g(x)$ (wav-x) ^e	$E_g(y)$ (wav-y) ^e	A_{1u} (pro) ^f	D_{oop} ^g	$\Delta(D_{oop})$ ^h	Angle porphyrin core to <i>meso</i> -aryl groups ⁱ		Distance shielding arm to porphyrin core ^j	
$\alpha\alpha$ -1-Zn	0.071	0.048	0.006	0.001	0.001	0.002	0.086		80.7		6.78	
$\alpha\alpha$ -1-Zn(NEt ₃)-prox	0.157	0.028	0.456	0.053	0.047	0.007	0.488	0.402	65.5	79.7	8.19	8.06
$\alpha\alpha$ -1-Zn(NEt ₃)-dist	0.064	0.060	0.367	0.004	0.035	0.004	0.379	0.293		80.8		6.65
$\alpha\beta$ -1-Zn	0.001	0.001	0.001	0.007	0.001	0.001	0.009			88.8		6.87
$\alpha\beta$ -1-Zn(NEt ₃)	0.046	0.036	0.412	0.025	0.042	0.006	0.419	0.410	74.4	89.4	7.90	6.27
Zn(TPP)	0.002	0.000	0.000	0.120	0.001	0.001	0.120					
Zn(TPP)(NEt ₃)	0.123	0.035	0.352	0.010	0.132	0.005	0.398	0.278				

^a Normal coordinate structural decomposition³² using NSD software from ref. 33. ^b Saddling. ^c Ruffling. ^d Doming. ^e Waving. ^f Propellering. ^g Total out-of-plane distortion. ^h Differences of D_{oop} compared to amine free species. ⁱ Angles were calculated between the 24 atoms least square plane of the porphyrin core and the least square plane of *meso*-aryl groups bearing the phenylethynyl arm. ^j Distances were calculated between the centroid of the porphyrin core 24 atoms and the centroid of the respective shielding phenyl group.

The same general trends of the proton resonances are seen for $\alpha\alpha$ -1-Zn after addition of triethylamine (see Scheme 2 and Figure 4). To relate these chemical shifts to topological changes of the $\alpha\alpha$ -porphyrin the site of triethylamine coordination has to be considered. Therefore, DFT calculations (B3LYP, LanL2DZ) have been performed with triethylamine either coordinated to the proximal ($\alpha\alpha$ -1-Zn(NEt₃)-prox) or to the distal site ($\alpha\alpha$ -1-Zn(NEt₃)-dist). The geometry optimized structures of $\alpha\alpha$ -1-Zn, $\alpha\alpha$ -1-Zn(NEt₃)-prox and $\alpha\alpha$ -1-Zn(NEt₃)-dist are shown in Figure 5 and pertinent structural data are summarized in Table 3. As the $\alpha\alpha$ -1-Zn proton resonances of the phenylethynyl group (H^{16'}, H^{17'}, H^{18'}) are shifted to lower field upon coordination of triethylamine, similar to the $\alpha\beta$ -1-Zn case (H¹⁶, H¹⁷, H¹⁸), the distance of the phenyl group centroids to the porphyrin centroid should be larger as well. Indeed the initial distances in $\alpha\alpha$ -1-Zn (6.78 Å) increase to 8.19 and 8.06 Å, respectively, for the amine coordinating proximal to the arms in $\alpha\alpha$ -1-Zn(NEt₃)-prox while coordination of NEt₃ to the distal site leads to a smaller distance of 6.65 Å in $\alpha\alpha$ -1-Zn(NEt₃)-dist. Thus, based on the downfield shift of the proton resonances H^{16'}, H^{17'} and H^{18'}, coordination of triethylamine at the proximal site is highly probable.

Nuclear Overhauser Spectroscopy (NOESY) is used as a further tool to probe the coordination site of triethylamine to $\alpha\alpha$ -1-Zn. No unambiguous contacts between amine protons and any porphyrin proton can be assigned as the required large excess of amine in the sample leads to an intense trace in the spectrum masking possible cross peaks of NEt₃. Nevertheless, NOESY experiments run before and after addition of

excess triethylamine give information about the coordination site of NEt_3 by estimating the distance of $\text{H}^{16'}$ to $\text{H}^{23'a}$ from the NOE between these protons. Using the cross peak intensity between $\text{H}^{24'}$ and $\text{H}^{21'}$ within the mesityl moiety, which should be unchanged upon amine coordination, as internal standard, the distance change between $\text{H}^{16'}$ and $\text{H}^{23'}$ can be estimated by comparing the normalized cross peak intensities before and after exposing the sample to excess triethylamine.

Indeed, the cross peak intensity decreases by a factor of 1.3 upon amine coordination to $\alpha\alpha\text{-1-Zn}$ which is attributed to an increased distance between $\text{H}^{16'}$ and $\text{H}^{23'}$.[§] DFT calculations show that the distance between $\text{H}^{16'}$ and the protons $\text{H}^{23'a}$ increases for $\alpha\alpha\text{-1-Zn}(\text{NEt}_3)\text{-prox}$ by about 0.6 Å on average for both arms but decreases for $\alpha\alpha\text{-1-Zn}(\text{NEt}_3)\text{-dist}$ by about 0.4 Å.

In contrast to the distal coordination of nitrogen bases for example to picket-fence iron(II) porphyrins^{36, 37}, we infer from the experimental NMR data in conjunction with the insights from DFT calculations as discussed above that triethylamine binds to the proximal-site of $\alpha\alpha\text{-1-Zn}$ within the pocket spanned by the phenyl rings. This argumentation is further corroborated by the fact that dichloromethane coordinates to the proximal site of $\alpha\alpha\text{-1-Zn}$ as observed in the solid state structure of $\alpha\alpha\text{-1-Zn}$ described above (Figure 2).

§ The intensity of NOESY cross peaks is proportional to r^{-6} with r being the distance between the two nuclei undergoing cross-relaxation. As this relation to NOE peak areas is only valid for short mixing times (<200 ms), explicit distances are not calculated, because mixing times of 2 s had to be used in these experiments.

E. Photophysical effects caused by NEt_3 coordination

The UV/vis titration of $\alpha\beta\text{-1-Zn}$ with triethylamine in dichloromethane is depicted in Figure 6a. As expected for zinc porphyrins, the Soret as well as the Q-bands are considerably shifted bathochromically.¹⁹ For $\alpha\alpha\text{-1-Zn}$ and $\alpha\beta\text{-1-Zn}$ this leads to a visible colour change from red to yellow (insets in Figure 6a and 6b), while for $\text{Zn}(\text{TPP})$ a barely visible change from pink to pale purple is observed (inset Figure 6c). In the spectra of $\alpha\alpha\text{-1-Zn}$ and $\alpha\beta\text{-1-Zn}$ two isosbestic points at 428 and 558 nm reveal the involvement of two distinct species in this process, which is in good agreement with the favoured formation of 1:1 complexes for zinc(II) porphyrins and amines in solution.³⁴ Further experiments in *n*-hexane, hexamethyldisiloxane, acetonitrile and chloroform show that absorption shifts are more pronounced in the weakly coordinating solvents *n*-hexane, hexamethyldisiloxane and dichloromethane with shifts of the Soret-band of about $\Delta\lambda_{\text{Soret}} = 10 - 13$ nm, respectively, but are smaller for the more competitive solvents acetonitrile and chloroform ($\Delta\lambda_{\text{Soret}} = 3 - 4$ nm). All absorption changes in the Soret as well as in the Q-band region are summarized in Table 1 showing essentially the same shifts for $\alpha\beta\text{-1-Zn}$ and for $\alpha\alpha\text{-1-Zn}$. The

absorption changes of $\alpha\alpha$ -1-Zn and $\alpha\beta$ -1-Zn are larger than those of Zn(TPP) by 2 nm (Soret-band) and 11 nm (Q-bands).

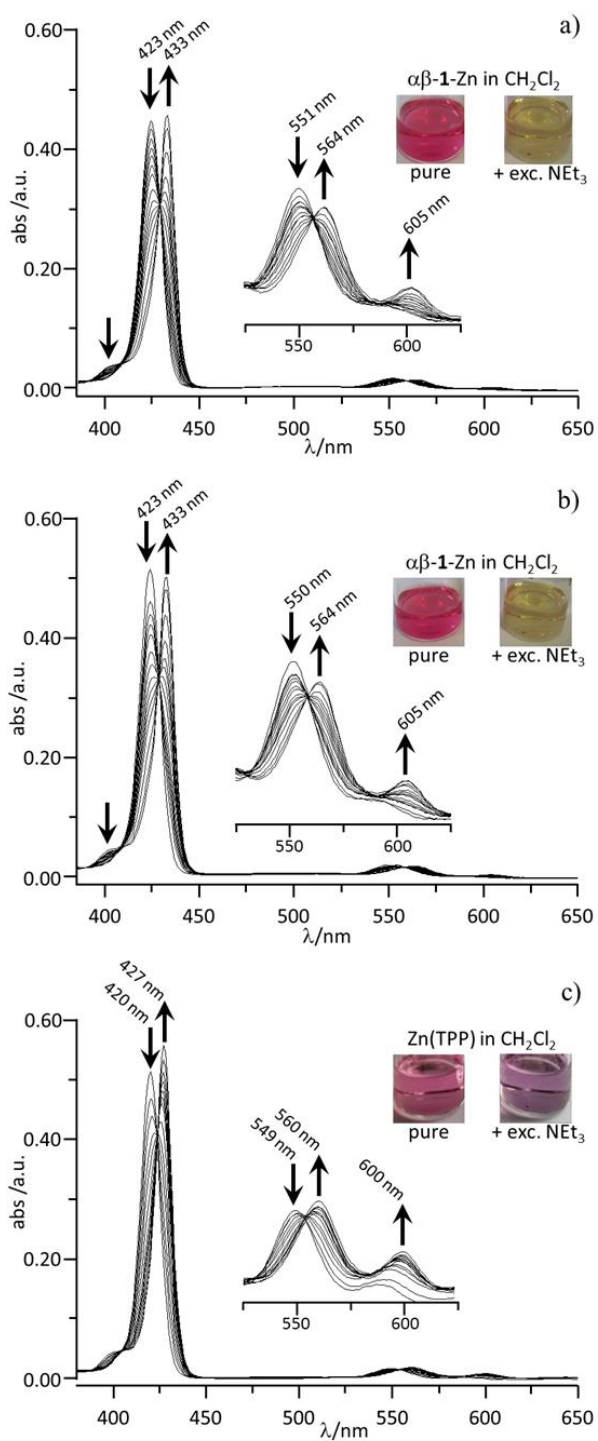


Fig. 6 UV/vis titration of (a) $\alpha\alpha$ -1-Zn, (b) $\alpha\beta$ -1-Zn and (c) Zn(TPP) with NEt_3 in dichloromethane using 1.0×10^4 to 1.0×10^6 equivalents. Insets show magnifications of the Q-band region and a photograph of the solution before and after addition of excess NEt_3 .

The emission bands of the two zinc(II) porphyrins in dichloromethane also undergo a bathochromic shift upon amine coordination, which leads to three isosbestic points at 605, 627 and 662 nm in the emission spectra when titrated with triethylamine and excited at 428 nm, the isosbestic point in the absorption spectrum (see Figure 7). The Q(0,0) emission is shifted by 11 nm to 612 nm and the Q(0,1) emission by 13 nm to 662 nm for both isomers (see Table 6). Due to symmetry changes the intensity ratio $E[Q(0,0):Q(0,1)]$ of the Q-band is essentially inverted from [0.63:1] for $\alpha\alpha$ -1-Zn to [1:0.73] for $\alpha\alpha$ -1-Zn(NEt₃) and from [0.58:1] for $\alpha\beta$ -1-Zn to [1:0.74] for $\alpha\beta$ -1-Zn(NEt₃). The quantum yield is nearly unaffected by NEt₃ coordination with a slight decrease from $\Phi(\alpha\alpha$ -1-Zn) = 0.07 to $\Phi(\alpha\alpha$ -1-Zn(NEt₃)) = 0.06 and from $\Phi(\alpha\beta$ -1-Zn) = 0.08 to $\Phi(\alpha\beta$ -1-Zn(NEt₃)) = 0.07, respectively.

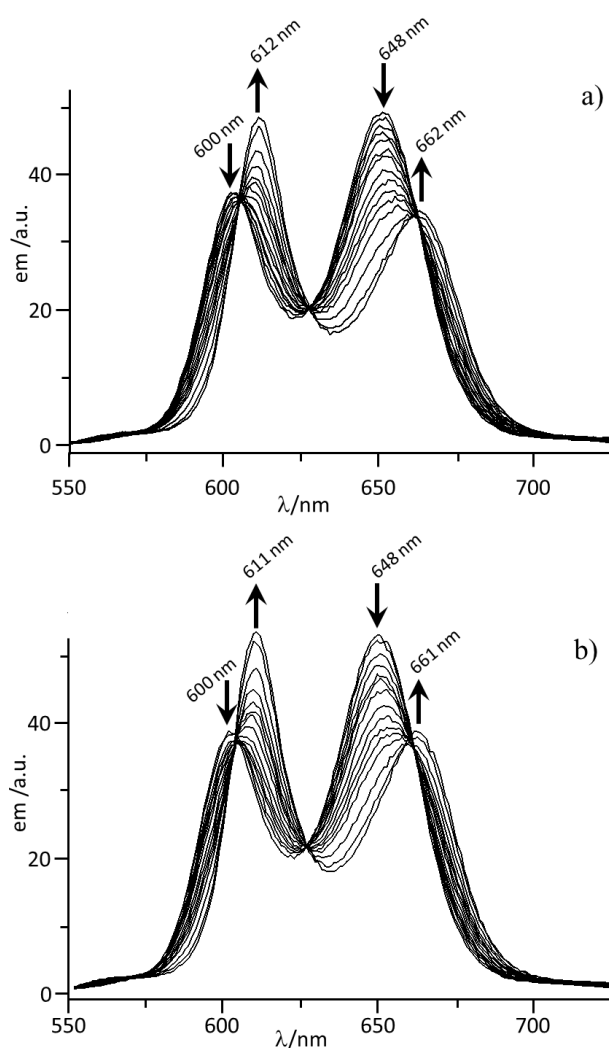


Fig. 7 Fluorescence changes of $\alpha\alpha$ -1-Zn (a) and $\alpha\beta$ -1-Zn (b) with NEt₃ in dichloromethane using 1.0×10^4 to 1.0×10^6 equivalents.

The more pronounced colour shifts of $\alpha\alpha$ -1-Zn and $\alpha\beta$ -1-Zn with triethylamine compared to Zn(TPP) is related to the distinct deformations of the porphyrin cores upon complex formation, as suggested in the literature.²³ Therefore, the DFT calculated

geometry optimized structures described above were analyzed with respect to deformations of the porphyrin core before and after triethylamine binding and compared to calculated structures of Zn(TPP). Table 3 summarizes the normal structural decomposition (NSD)³³ analyses of these structures. The total out-of-plane distortions (D_{oop}) of the triethylamine complexes $\alpha\alpha\text{-1-Zn(NEt}_3\text{)-prox}$ and $\alpha\beta\text{-1-Zn(NEt}_3\text{)}$ is more pronounced than that of Zn(TPP)(NEt₃), the distortion of the unfavoured distal isomer $\alpha\alpha\text{-1-Zn(NEt}_3\text{)-dist}$ being slightly smaller. The difference in distortion before and after coordination of triethylamine (ΔD_{oop}) of the $\alpha\alpha\text{-1-Zn}$ and $\alpha\beta\text{-1-Zn}$ isomers exceeds that of Zn(TPP), being increased by a factor of 1.5 for $\alpha\alpha\text{-1-Zn(NEt}_3\text{)-prox}$ and $\alpha\beta\text{-1-Zn(NEt}_3\text{)}$, respectively. Furthermore, the absolute change of the D_{oop} for $\alpha\alpha\text{-1-Zn(NEt}_3\text{)-prox}$ ($\Delta D_{\text{oop}} = 0.40$) and $\alpha\beta\text{-1-Zn(NEt}_3\text{)}$ ($\Delta D_{\text{oop}} = 0.41$) is practically identical which is in good agreement with their similar colour changes after amine coordination. In addition to the conclusions drawn from the NMR experiments described above, this is a further evidence for the $\alpha\alpha\text{-1-Zn(NEt}_3\text{)-prox}$ coordination mode, as the deformation change of the $\alpha\alpha\text{-1-Zn(NEt}_3\text{)-dist}$ ($\Delta D_{\text{oop}} = 0.29$) is significantly smaller and more similar to that of Zn(TPP) ($\Delta D_{\text{oop}} = 0.28$, see Table 3).

Analysis of the normal modes which contribute to the D_{oop} reveals that the interaction of the shielding phenylethynyl arms with the coordinating triethylamine does not lead to a distinctly different deformation pattern as compared to Zn(TPP). In all cases, the doming normal coordinate *dom* contributes most to D_{oop} , as significant doming is induced by the displacement of the zinc(II) ion from the mean plane due to coordination by triethylamine. Nevertheless, doming is significantly enhanced by the arm-amine interaction. Interaction of the phenylethynyl arms with the coordinating triethylamine can best be seen from the torsion angle of the *meso*-aryl group bearing the arm around its σ -bond to the porphyrin core (see Figure 5 and Table 3).

F. Amine affinity

From the UV/vis titration data depicted in Figure 6 the binding constants K of triethylamine to the two isomers at $T = 298$ K in dichloromethane were calculated using a form of the Benesi-Hildebrand equation^{5,38}. The linear double reciprocal plots derived from the absorption changes of $\alpha\alpha\text{-1-Zn}$ and $\alpha\beta\text{-1-Zn}$ at 433 nm are shown in Figure 8 and the binding constants derived thereof are calculated as $K(\alpha\alpha\text{-1-Zn}) = (3.56 \pm 0.32) \text{ L mol}^{-1}$ and $K(\alpha\beta\text{-1-Zn}) = (4.58 \pm 0.38) \text{ L mol}^{-1}$, respectively.

§ Benesi-Hildebrand equation:

$$\frac{1}{\Delta A} = \frac{1}{K \Delta A_{\text{max}} [\text{NEt}_3]} + \frac{1}{\Delta A_{\text{max}}}$$

with absorbance change $\Delta A = A - A_0$, the equilibrium constant K , the maximal absorbance change $\Delta A_{\text{max}} = A_{\infty} - A_0$ with fully amine coordinated porphyrin and the total amine concentration $[\text{NEt}_3]$.

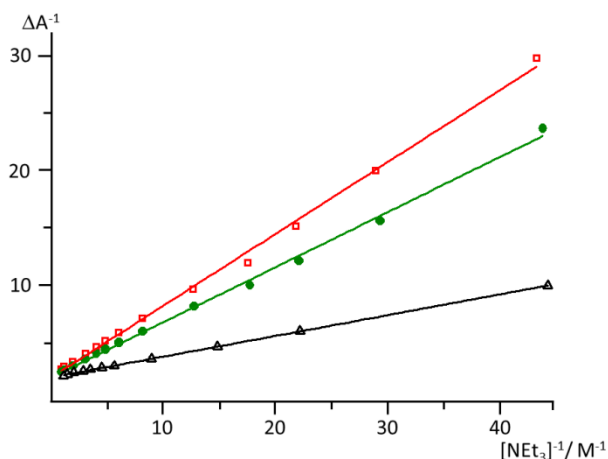


Fig. 8 Benesi-Hildebrand plots of the absorption changes with NEt_3 in dichloromethane for $\alpha\alpha$ -1-Zn (\square) and $\alpha\beta$ -1-Zn (\bullet) at 433 nm and for Zn(TPP) (\blacktriangle) at 427 nm.

The binding affinity of $\alpha\alpha$ -1-Zn and $\alpha\beta$ -1-Zn towards NEt_3 is identical within 3σ , however the affinity is slightly reduced by a factor of 2 – 3 as compared to the affinity $K(\text{Zn(TPP)}) = (13.1 \pm 1.2) \text{ L mol}^{-1}$ of Zn(TTP) to NEt_3 in dichloromethane. Nevertheless, the relative amine affinity of $\alpha\alpha$ -1-Zn and $\alpha\beta$ -1-Zn as compared to Zn(TPP) is still high, as for sterically more demanding bis-pocket porphyrins synthesized by Suslick *et al.* the amine affinity towards different amines is reduced by factors of 10 to 10^7 compared to Zn(TPP).³⁹

Conclusions

In this study the synthesis and separation of $\alpha\alpha$ - and $\alpha\beta$ -*meso*- A_2B_2 -Zn(II)-tetraarylporphyrin atropisomers with A = mesityl and B = *ortho*-alkenylphenyl-phenyl with hindered rotation of the arm has been reported. Both isomers show large optical response upon coordination of NEt_3 . Detailed structural, spectroscopic and photophysical characterizations were performed and the pronounced spectral changes have been correlated to deformations of the porphyrin macrocycle imposed by steric interactions with the coordinating amine. Nevertheless, the amine affinity is still high. Results were compared to simple Zn(TTP) and rationalized by DFT calculations.

Solubility in non-polar hexamethyldisiloxane is about five times higher for the $\alpha\beta$ - and about two orders of magnitude higher for the $\alpha\alpha$ -isomer as compared to Zn(TTP), which has been related to impeded intermolecular π - π -interactions and is of special interest for further processing of the porphyrins, *e.g.* as amine sensor materials.

Work using high affinity metal centers and incorporation of the metalloporphyrins into polymeric thin films and onto solid supports for real world applications is currently in progress and will be reported in due course.

Experimental section

General methods

5-(Mesityl) dipyrromethane **A** was prepared according to reported methods.²⁴ 2-(Phenylethynyl) benzaldehyde **B** was prepared by Sonogashira coupling of *ortho*-bromobenzaldehyde with phenyl acetylene.²⁶ Spectral properties of **A** and **B** conform with literature data. Solvents were dried by standard methods. Other reagents were used as received from commercial suppliers (Acros, Sigma-Aldrich, ABCR). NMR spectra were recorded on a Bruker Avance DRX 400 spectrometer at 400.31 MHz (¹H) and 100.05 MHz (¹³C{¹H}). Resonances are reported in ppm versus the solvent signal as internal standard CD₂Cl₂ (¹H: δ = 5.32 ppm, ¹³C: δ = 53.84 ppm) and DMSO-d₆ (¹H: δ = 2.50 ppm). (s) = singlet, (d) = doublet, (t) = triplet, (pt) = pseudo triplet (unresolved doublet of doublets), (m) = multiplet. Electrochemical experiments were carried out on a BioLogic SP-50 voltammetric analyzer using a glassy carbon working electrode, a platinum wire as counter electrode and a 0.01 m Ag/AgNO₃ electrode as reference electrode. The measurements were carried out at a scan rate of 100 mV s⁻¹ for cyclic voltammetry experiments and for square wave voltammetry experiments using 0.1 M (*n*Bu₄N)(PF₆) as supporting electrolyte in CH₂Cl₂. Potentials are given relative to the ferrocene/ferrocenium couple. UV/Vis/NIR spectra were recorded on a Varian Cary 5000 spectrometer using 1.0 cm cells (Hellma, suprasil). Emission spectra were recorded on a Varian Cary Eclipse spectrometer. Quantum yields were determined by comparing the areas under the emission spectra on an energy scale [cm⁻¹] recorded for optically matched solutions of the samples and the reference { ϕ ([H₂TPP]) = 0.11 in dichloromethane}⁴⁰; experimental uncertainty 15%. FD mass spectra were recorded on a FD Finnigan MAT90 spectrometer. ESI mass spectra were recorded on a Micromass Q-TOF-Ultima spectrometer. HPLC separations were performed on a JASCO semipreparative HPLC system with a Reprosil C₁₈ column (5 μ m) using acetone/MeOH (1:1, v/v) as eluent (17 ml min⁻¹) and UV/Vis detection at 420 nm.

Crystal structure determination

Intensity data were collected with a Bruker AXS Smart1000 CCD diffractometer using Mo-K α radiation (λ = 0.71073 Å) for $\alpha\alpha$ -**1**-Zn and with a STOE IPDS-2T diffractometer using Cu-K α radiation (λ = 1.54178 Å) for $\alpha\beta$ -**1**-Zn and were corrected for absorption and other effects. The diffraction frames were integrated using the Bruker SAINT or STOE X-RED package and most were corrected for absorption with MULABS or SADABS.^{41, 42} The structures were solved by direct methods and refined by the full-matrix method based on F^2 using the SHELXTL software package.^{43, 44} All non-hydrogen atoms were refined anisotropically while the positions of all hydrogen atoms were generated with appropriate geometric constraints and allowed to ride on their respective parent carbon atoms with fixed isotropic thermal parameters.

Crystal data of $\alpha\alpha$ -1-Zn: $C_{67.5}H_{51}Cl_3N_4Zn$ (1089.92); $T = 173(2)$ K; purple plate; $0.13 \times 0.12 \times 0.02$ mm; monoclinic; $C2/c$; $a = 16.910(4)$ Å; $b = 20.344(4)$ Å; $c = 31.623(7)$ Å; $V = 108664(4)$ Å³. Due to the small weakly diffracting crystal and the disordered co-crystallized dichloromethane molecules only a partial structure solution and refinement was possible. However, there is no ambiguity concerning the orientation of the rigid arms in the molecules present in the crystal.

Crystal data of $\alpha\beta$ -1-Zn: $C_{33}H_{24}N_2Zn_{0.5}$ (476.26); $T = 193(2)$ K; purple plate; $0.06 \times 0.05 \times 0.01$ mm; triclinic; $P-1$; $a = 14.415(3)$; $b = 17.893(4)$ Å; $c = 18.148(4)$ Å; $V = 3804.5(17)$ Å³. Due to the small weakly diffracting crystal and the presence of three independent (centrosymmetric) molecules in the asymmetric unit only a partial structure solution and refinement was possible. However, there is no ambiguity concerning the orientation of the rigid arms in the molecules present in the crystal.

Computational method

Density functional calculations were carried out with the Gaussian09/DFT series of programs.⁴⁵ The B3LYP formulation of density functional theory was used employing the LANL2DZ basis set. No symmetry constraints were imposed on the molecules. The presence of energy minima of the ground states was checked by analytical frequency calculations ($N_{\text{imag}} = 0$).

Preparations

Synthesis of $\alpha\alpha$ -1-2H and $\alpha\beta$ -1-2H: 5-(Mesityl) dipyrromethane (2.58 mmol, 0.68 g) and 2-(phenylethynyl) benzaldehyde (2.58 mmol, 0.53 mg) were dissolved in dry CH_2Cl_2 (340 mL) under an inert atmosphere and purged with argon for 20 min. $BF_3 \cdot OEt_2$ (0.86 mmol, 0.11 mL) were added and the reaction mixture was stirred at room temperature for 100 min in the dark. After addition of *p*-chloranil (3.66 mmol, 0.90 g) and heating the solution to reflux for 12 h the solvent was removed under reduced pressure. Crude purification was performed by flash column chromatography (silica gel, petroleum ether (40/60) : CH_2Cl_2 , 1:1, v/v). After further flash column chromatography (silica gel, petroleum ether (40/60) : CH_2Cl_2 : ethyl acetate : NEt_3 , 15:4:1:0.5, v/v) $\alpha\alpha$ -1-2H and $\alpha\beta$ -1-2H could be isolated as a purple solid as a (1:1) isomer mixture (0.33 g, 0.37 mmol, 28%).

To isolate isomerically pure $\alpha\alpha$ -1-2H and $\alpha\beta$ -1-2H, isomerically pure $\alpha\alpha$ -1-Zn or $\alpha\beta$ -1-Zn was treated with conc. HCl_{aq} in dichloromethane. After neutralization with $NaHCO_3$ the resulting free-base porphyrin was purified by flash column chromatography (silica gel, petroleum ether (40/60) : CH_2Cl_2 , 1:1, v/v).

$\alpha\alpha$ -1-2H: ¹H NMR (CD_2Cl_2 , $T = 298$ K, 400 MHz): $\delta = -2.52$ (s, 2H, NH), 1.82 (s, 12H, $H^{23'b}$), 1.85 (s, 12H, $H^{23'a}$), 2.61 (s, 6H, $H^{24'}$), 5.97 (dd, $^3J_{H,H} = 7.78$ Hz, $^4J_{H,H} = 1.03$ Hz, 4H, $H^{16'}$), 6.36 – 6.42 (m, 4H, $H^{17'}$), 6.62 – 6.67 (m, 2H, $H^{18'}$), 7.29 (s, 2H, $H^{21'b}$), 7.30 (s, 2H,

H^{21'a}), 7.74 – 7.80 (m, 2H, H^{9'}), 7.78 – 7.83 (m, 2H, H^{10'}), 7.98 – 8.02 (m, 2H, H^{11'}), 8.20 – 8.23 (m, 2H, H^{8'}), 8.69 (d, ³J_{H,H} = 4.66 Hz, 4H, H^{2'}), 8.84 (d, ³J_{H,H} = 4.66 Hz, 4H, H^{3'}) ppm. ¹³C{¹H} NMR (CD₂Cl₂, T = 298 K, 100 MHz): δ = 21.6 (s, C^{24'}), 21.7 (s, C^{23'b}), 21.9 (s, C^{23'a}), 118.2 (s, C^{6'}), 118.6 (s, C^{5'}), 122.5 (s, C^{15'}), 127.3 (s, C^{9'}), 127.5 (s, C^{12'}), 127.8 (s, C^{17'}), 127.9 (s, C^{18'}), 128.1 (s, C^{21'a}/C^{21'b}), 128.6 (s, C^{10'}), 130.8 (s, C^{16'}), 131.7 (s, C^{11'}), 135.5 (s, C^{8'}), 138.2 (s, C^{22'}), 138.7 (s, C^{19'}), 139.6 (s, C^{20'a}), 139.7 (s, C^{20'b}), 144.4 (s, C^{7'}). C¹, C², C³, C⁴, C¹³, C¹⁴ resonances were not observed. HR-MS (ESI⁺): m/z = 899.4122 (calcd for C₆₆H₅₁N₄: 899.4114).

αβ-1-2H: ¹H NMR (CD₂Cl₂, T = 298 K, 400 MHz): δ = -2.56 (s, 2H, NH), 1.84 (s, 12H, H²³), 2.60 (s, 6H, H²⁴), 5.96 (dd, ³J_{H,H} = 7.58 Hz, ⁴J_{H,H} = 1.12 Hz, 4H, H¹⁶), 6.42 – 6.50 (m, 4H, H¹⁷), 6.67 – 6.73 (m, 2H, H¹⁸), 7.28 (s, 4H, H²¹), 7.73 – 7.78 (m, 2H, H⁹), 7.78 – 7.83 (m, 2H, H¹⁰), 7.98 – 8.02 (m, 2H, H¹¹), 8.19 – 8.23 (m, 2H, H⁸), 8.69 (d, ³J_{H,H} = 4.65 Hz, 4H, H²), 8.84 (d, ³J_{H,H} = 4.65 Hz, 4H, H³) ppm. ¹³C{¹H} NMR (CD₂Cl₂, T = 298 K, 100 MHz): δ = 21.6 (s, C²⁴), 21.8 (s, C²³), 90.1 (s, C¹³), 94.0 (s, C¹⁴), 118.2 (s, C⁶), 118.6 (s, C⁵), 122.6 (s, C¹⁵), 127.3 (s, C⁹), 127.5 (s, C¹²), 127.8 (s, C¹⁷), 127.9 (s, C¹⁸), 128.1 (s, C²¹), 128.6 (s, C¹⁰), 130.9 (s, C¹⁶), 131.7 (s, C¹¹), 135.4 (s, C⁸), 138.2 (s, C²²), 138.7 (s, C¹⁹), 139.7 (s, C²⁰), 145.5 (s, C⁷). C¹, C², C³, C⁴ resonances were not observed. HR-MS (ESI⁺): m/z = 899.4122 (calcd for C₆₆H₅₁N₄: 899.4114).

Synthesis of *αα*-1-Zn and *αβ*-1-Zn: A 1:1 mixture of *αα*-1-2H and *αβ*-1-2H (0.25 mmol, 0.22 g) was dissolved in CH₂Cl₂ (150 mL) together with zinc acetate dihydrate (1.47 mmol, 0.32 g) and stirred at room temperature for 16 h. The solvent was removed under reduced pressure and the crude product was purified by flash column chromatography (silica gel, petroleum ether (40/60) : CH₂Cl₂ 3:1) to give a 1:1 mixture of *αα*-1-Zn and *αβ*-1-Zn (0.23 mmol, 0.22 g, 93%) as a purple solid. Separation of the isomers was achieved via reversed phase HPLC (Reprosil C₁₈ column (5 μm), methanol : acetone 1:1) to give isomerically pure *αα*-1-Zn (0.11 mmol, 0.11 g, 46%) and *αβ*-1-Zn (0.11 mmol, 0.10 g, 43%).

αα-1-Zn: ¹H NMR (CH₂Cl₂, T = 298 K, 400 MHz): δ = 1.81 (s, 6H, H^{23'b}), 1.86 (s, 6H, H^{23'a}), 2.61 (s, 6H, H^{24'}), 6.03–5.95 (m, 4H, H^{16'}), 6.47 – 6.37 (m, 4H, H^{17'}), 6.70 – 6.63 (m, 4H, H^{18'}), 7.28 (s, 2H, H^{21'b}), 7.29 (s, 2H, H^{21'a}), 7.78 – 7.72 (m, 2H, H^{9'}), 7.83 – 7.78 (m, 2H, H^{10'}), 8.03 – 7.97 (m, 2H, H^{11'}), 8.25 – 8.19 (m, 2H, H^{8'}), 8.76 (d, ³J_{HH} = 4.60 Hz, 2H, H^{3'}), 8.91 (d, ³J_{HH} = 4.60 Hz, 2H, H^{2'}). ¹³C{¹H} NMR (CD₂Cl₂, T = 298 K, 100 MHz): δ = 21.6 (s, C^{24'}), 21.7 (s, C^{23'b}), 22.0 (s, C^{23'a}), 90.5 (s, C^{13'}), 93.6 (s, C^{14'}), 119.0 (s, C^{6'}), 119.4 (s, C^{5'}), 122.7 (s, C^{15'}), 127.1 (s, C^{9'}), 127.4 (s, C^{12'}), 127.8 (s, C^{17'}), 127.8 (s, C^{18'}), 127.9 (s, C^{21'a}), 128.0 (s, C^{21'b}), 128.3 (s, C^{10'}), 130.9 (s, C^{16'}), 131.0 (s, C^{3'}), 131.6 (s, C^{11'}), 132.6 (s, C^{2'}), 135.5 (s, C^{8'}), 137.9 (s, C^{22'}), 139.4 (s, C^{20'a}), 139.5 (s, C^{19'}), 139.6 (s, C^{20'b}), 145.4 (s, C^{7'}), 150.3 (s, C^{4'}), 150.5 (s, C^{1'}). UV/Vis (CH₂Cl₂): λ_{max} (ε) = 282 (5.04 × 10⁴ M⁻¹ cm⁻¹), 299 (4.83 × 10⁴), 403 (sh, 3.51 × 10⁴), 423 (46.6 × 10⁴), 551 (2.01 × 10⁴), 585 (0.21 × 10⁴) nm. Fluorescence (CH₂Cl₂): λ = 600 (0.63), 648 (1.00) nm; Φ = 0.07. CV (CH₂Cl₂,

(*n*Bu₄N)(PF₆): $E_{1/2} = -2.43, -1.86, 0.40, 0.82$ V vs. FcH/FcH⁺. HR-MS (ESI⁺): $m/z = 960.3146$ (calcd for C₆₆H₄₈N₄Zn: 960.3170).

$\alpha\beta$ -1-Zn: ¹H NMR (CH₂Cl₂, $T = 298$ K, 400 MHz): $\delta = 1.84$ (s, 12H, H²³), 2.61 (s, 6H, H²⁴), 5.92 (dd, ³ $J_{HH} = 8.15$ Hz, ⁴ $J_{HH} = 1.03$ Hz, 4H, H¹⁶), 6.44 (dd, ³ $J_{HH} = 8.15$ Hz, ³ $J_{HH} = 7.85$ Hz, 4H, H¹⁷), 6.68 (tt, ³ $J_{HH} = 7.85$, ⁴ $J_{HH} = 1.03$, 2H, H¹⁸), 7.28 (s, 4H, H²¹), 7.73 – 7.78 (m, 2H, H⁹), 7.78 – 7.84 (m, 2H, H¹⁰), 7.96 – 8.02 (m, 2H, H¹¹), 8.19 – 8.25 (m, 2H, H⁸), 8.76 (d, ³ $J_{HH} = 4.63$ Hz, 4H, H²), 8.90 (d, ³ $J_{HH} = 4.63$ Hz, 4H, H³). ¹³C{¹H} NMR (CD₂Cl₂, $T = 298$ K, 100 MHz): $\delta = 21.6$ (s, C²⁴), 21.9 (s, C²³), 90.4 (s, C¹³), 93.7 (s, C¹⁴), 119.0 (s, C⁶), 119.5 (s, C⁵), 122.6 (s, C¹⁵), 127.1 (s, C⁹), 127.4 (s, C¹²), 127.8 (s, C¹⁷), 127.9 (s, C¹⁸), 128.0 (s, C²¹), 128.4 (s, C¹⁰), 130.9 (s, C¹⁶), 131.0 (s, C³), 131.5 (s, C¹¹), 132.6 (s, C²), 135.3 (s, C⁸), 138.0 (s, C²²), 139.4 (s, C¹⁹), 139.5 (s, C²⁰), 145.4 (s, C⁷), 150.4 (s, C⁴), 150.5 (s, C¹). UV/Vis (CH₂Cl₂): $\lambda_{max} (\epsilon) = 281 (5.40 \times 10^4 \text{ M}^{-1} \text{ cm}^{-1}), 298 (4.99 \times 10^4), 403 (\text{sh}, 3.54 \times 10^4), 423 (47.0 \times 10^4), 550 (2.00 \times 10^4), 585 (0.19 \times 10^4)$ nm. Fluorescence (CH₂Cl₂): $\lambda_{max} = 600 (0.58), 648 (1.00)$ nm; $\Phi = 0.08$. CV (CH₂Cl₂, (*n*Bu₄N)(PF₆)): $E_{1/2} = -1.90, 0.37, 0.73$ V vs. FcH/FcH⁺. HR-MS (ESI⁺): $m/z = 960.3146$ (calcd for C₆₆H₄₈N₄Zn: 960.3170).

Acknowledgements: We thank the Fonds National de la Recherche Luxembourg (FNR) for financial support through the “SurfAmine” project.

Notes and references

- 1 A. Pacquit, J. Frisby, D. Diamond, K. T. Lau, A. Farrell, B. Quilty and D. Diamond, *Food Chem.*, 2007, **102**, 466-470.
- 2 F. Özogul, K. D. A. Taylor, P. Quantick and Y. Özogul, *J. Food Sci.*, 2002, **67**, 2497-2501.
- 3 C.-Y. Yeh, S.-J. Lin and D.-F. Hwang, *J. Food Drug Anal.*, 2004, **12**, 128-132.
- 4 K. I. Oberg, R. Hodyss and J. L. Beauchamp, *Sens. and Actuators B*, 2006, **115**, 79-85.
- 5 N. T. Greene and K. D. Shimizu, *J. Am. Chem. Soc.*, 2005, **127**, 5695-5700.
- 6 G. J. Mohr, N. Tirelli, C. Lohse and U. E. Spichiger-Keller, *Adv. Mater.*, 1998, **10**, 1353-1357.
- 7 G. J. Mohr, *Anal Bioanal Chem*, 2006, **386**, 1201-1214.
- 8 C. Patze, K. Broedner, F. Rominger, O. Trapp and U. H. Bunz, *Chem. Eur. J.*, 2011, **17**, 13720-13725.
- 9 S. Körsten and G. J. Mohr, *Chem. Eur. J.*, 2011, **17**, 969-975.
- 10 S. M. A. Pinto, M. A. O. Lourenço, M. J. F. Calvete, A. R. Abreu, M. T. S. Rosado, H. D. Burrows and M. M. Pereira, *Inorg. Chem.*, 2011, **50**, 7916-7918.
- 11 T. Carofiglio, E. Lubian, I. Menegazzo, G. Saielli and A. Varotto, *J. Org. Chem.*, 2009, **74**, 9034-9043.
- 12 L. Elisa, F. Baldini, A. Giannetti, C. Trono and T. Carofiglio, *Chem. Comm.*, 2010, **46**, 3678-3680.
- 13 K. S. Suslick, N. A. Rakow and A. Sen, *Tetrahedron*, 2004, **60**, 11133-11138.
- 14 N. A. Rakow, A. Sen, M. C. Janzen, J. B. Ponder and K. S. Suslick, *Angew. Chem.*, 2005, **44**, 4528-4532.
- 15 A. Alimelli, G. Pennazza, M. Santonico, R. Paolesse, D. Filippini, A. D’Amico, I. Lundström and C. Di Natale, *Anal. Chim. Acta*, 2007, **582**, 320-328.

- 16 N. D. Boscher, P. Choquet, D. Duday, N. Kerbellec, J.-C. Lambrechts and R. Maurau, *J. Mater. Chem.*, 2011, **21**, 18959-18961.
- 17 N. D. Boscher, D. Duday, P. Heier, K. Heinze, F. Hilt and P. Choquet, *Sens. Actuators B*, submitted.
- 18 O. Kolling, *Inorg. Chem.*, 1979, **18**, 1175-1176.
- 19 M. Nappa and J. S. Valentine, *J. Am. Chem. Soc.*, 1978, **100**, 5075-5080.
- 20 J. A. Shelnutt, X.-Z. Song, J.-G. Ma, S.-L. Jia, W. Jentzen, C. J. Medforth and C. J. Medforth, *Chem. Soc. Rev.*, 1998, **27**, 31-42.
- 21 R. E. Haddad, S. Gazeau, J. Pécaut, J.-C. Marchon, C. J. Medforth and J. A. Shelnutt, *J. Am. Chem. Soc.*, 2003, **125**, 1253-1268.
- 22 Z. Zhou, C. Cao, Q. Liu and R. Jiang, *Org. Lett.*, 2010, **12**, 1780-1783.
- 23 R. Harada, Y. Matsuda, H. Ōkawa, R. Miyamoto, S. Yamauchi and T. Kojima, *Inorg. Chim. Acta*, 2005, **358**, 2489-2500.
- 24 C.-H. Lee and J. S. Lindsey, *Tetrahedron*, 1994, **50**, 11427-11440.
- 25 J. S. Lindsey, *Acc. Chem. Res.*, 2010, **43**, 300-311.
- 26 A. Malkov, M. Westwater, A. Gutnov, P. Ramirezlopez, F. Friscourt, A. Kadlcikova, J. Hodacova, Z. Rankovic, M. Kotora and P. Kocovsky, *Tetrahedron*, 2008, **64**, 11335-11348.
- 27 L. K. Gottwald and E. F. Ullman, *Tetrahedron Lett.*, 1969, **10**, 3071-3074.
- 28 M. Ruppert, W. Bauer and A. Hirsch, *Chem. Eur. J.*, 2011, **17**, 8714-8725.
- 29 H. Meyer, M. Hesse, B. Zeeh, *Spektroskopische Methoden in der organischen Chemie*; Georg Thieme Verlag, Stuttgart, New York, **1995**.
- 30 C. Janiak, *J. Chem. Soc., Dalton Trans.*, 2000, 3885-3896.
- 31 W. R. Scheidt, J. U. Mondal, C. W. Eigenbrot, A. Adler, L. J. Radonovich and J. L. Hoard, *Inorg. Chem.*, 1986, **25**, 795-799.
- 32 W. Jentzen, J.-G. Ma and J. A. Shelnutt, *Biophys. J.*, 1998, **74**, 753-763.
- 33 <http://jasheln.unm.edu/jasheln/>.
- 34 J. K. M. Sanders, N. Bampos, Z. Clyde-Watson, S. L. Darling, J. C. Hawley, H.-J. Kim, C. C. Mak, S. J. Webb, in *The Porphyrin Handbook*; ed. M. Kadish, K. M. Smith, R. Guilard; Academic Press, New York, **2000**; Vol. 3, pp. 1-48.
- 35 T. Kojima, T. Nakanishi, T. Honda, R. Harada, M. Shiro and S. Fukuzumi, *Eur. J. Inorg. Chem.*, 2009, **2009**, 727-734.
- 36 J. P. Collman, R. R. Gagne, T. R. Halbert, J. C. Marchon and C. A. Reed, *J. Am. Chem. Soc.*, 1973, **95**, 7868-7870.
- 37 J. P. Collman, R. R. Gagne, C. Reed, T. R. Halbert, G. Lang and W. T. Robinson, *J. Am. Chem. Soc.*, 1975, **97**, 1427-1439.
- 38 J. R. Miller and G. D. Dorough, *J. Am. Chem. Soc.*, 1952, **74**, 3977-3981.
- 39 A. Sen and K. S. Suslick, *J. Am. Chem. Soc.*, 2000, **122**, 11565-11566.
- 40 C.-Y. Huang and Y. O. Su, *Dalton Trans.*, 2010, **39**, 8306-8312.
- 41 SMART Data Collection and SAINT-Plus Data Processing Software for the SMART System (various versions); Bruker Analytical X-Ray Instruments, Inc.: Madison, WI, **2000**.
- 42 a) SADABS Area-Detector Absorption Correction; Siemens Industrial Automation, Inc.: Madison, WI, **1996**; b) MULABS: R. H. Blessing, *Acta Cryst.* 1995, **A51**, 33-38.
- 43 G. M. Sheldrick, SHELXTL, Version 5.1; Bruker AXS: Madison, WI, **1998**.
- 44 G. M. Sheldrick, SHELXL-97; University of Göttingen, Göttingen, Germany, **1997**.
- 45 Gaussian 09, Revision A.02, M. J. Frisch, G. W. Trucks, H. B. Schlegel, G. E. Scuseria, M. A. Robb, J. R. Cheeseman, G. Scalmani, V. Barone, B. Mennucci, G. A. Petersson, H. Nakatsuji, M. Caricato, X. Li, H. P. Hratchian, A. F. Izmaylov, J. Bloino, G. Zheng, J. L. Sonnenberg, M. Hada, M. Ehara, K. Toyota, R.

Fukuda, J. Hasegawa, M. Ishida, T. Nakajima, Y. Honda, O. Kitao, H. Nakai, T. Vreven, J. A. Montgomery, Jr., J. E. Peralta, F. Ogliaro, M. Bearpark, J. J. Heyd, E. Brothers, K. N. Kudin, V. N. Staroverov, R. Kobayashi, J. Normand, K. Raghavachari, A. Rendell, J. C. Burant, S. S. Iyengar, J. Tomasi, M. Cossi, N. Rega, J. M. Millam, M. Klene, J. E. Knox, J. B. Cross, V. Bakken, C. Adamo, J. Jaramillo, R. Gomperts, R. E. Stratmann, O. Yazyev, A. J. Austin, R. Cammi, C. Pomelli, J. W. Ochterski, R. L. Martin, K. Morokuma, V. G. Zakrzewski, G. A. Voth, P. Salvador, J. J. Dannenberg, S. Dapprich, A. D. Daniels, O. Farkas, J. B. Foresman, J. V. Ortiz, J. Cioslowski, D. J. Fox, Gaussian, Inc., Wallingford CT, **2009**.

3.5

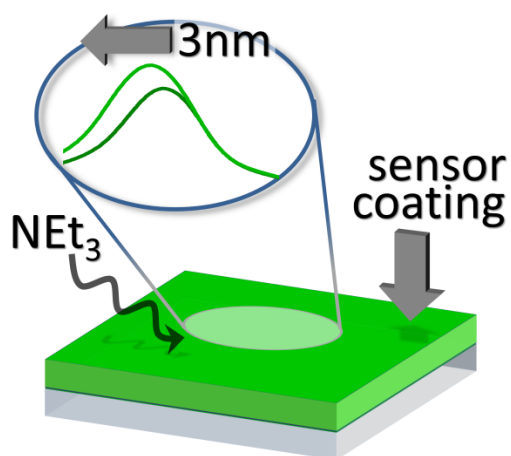
New class of Zn^{II} and Cr^{III} porphyrins incorporated into mesoporous polymer matrixes via an atmospheric pressure plasma enhanced CVD to form gas sensing layers

P. Heier, N. Boscher, T. Bohn, K. Heinze, P. Choquet


Journal of Materials Chemistry A **2014**, *2*, 1560 - 1570

Abstract

Designed Zn^{II} and Cr^{III} porphyrins (Zn^{II}P, Cr^{III}P(Cl)(H₂O)) and conventional Zn^{II}TPP and Cr^{III}TPP(Cl)(H₂O) are immobilized into porous polysiloxane films *via* chemical vapor deposition enhanced by an atmospheric pressure dielectric barrier discharge. UV/vis spectroscopy and mass spectrometry prove the integrity of the chromophores after the plasma treatment. The optical amine sensing capabilities of the films are investigated spectroscopically on exposure to triethylamine vapors. A series of coatings with different porphyrin loadings indicate the influences of the deposition conditions on the growth of the sensing films and hence the device performance. Additionally, the synthesis and characterization of the novel porphyrin complex Cr^{III}P(Cl)(H₂O) is reported.



Reproduced by permission of The Royal Society of Chemistry

Supplementary Information can be found at pp. 199 – 204 

Introduction

Porphyrin based and porphyrin containing coatings are widely investigated for dye-sensitized solar cells¹⁻⁵, photonic and electronic devices⁶⁻¹⁰ and sensing applications.¹¹⁻²⁸ Porphyrins are of special interest for the design of colorimetric sensors as they exhibit intense absorptions within the visible part of the electromagnetic spectrum. Their absorption characteristics can be changed by interaction of different analytes with the porphyrin macrocycle and especially with the metal center of metallo porphyrins.

Applications of porphyrin based colorimetric sensing surfaces range from the detection of explosives^{11,12} and NO₂¹³⁻¹⁵ over volatile organic compounds (VOC) in general¹⁶⁻²⁰ to alcohol vapors²¹⁻²³ and volatile amines in particular.²⁴⁻²⁸ The detection of volatile amines is of special interest as they can be used as freshness indicators for several food categories.²⁹⁻³¹ Therefore, their detection by smart food packages using colorimetric sensor surfaces may lead to simple yet powerful devices for food quality control used by customers and manufacturers.³²

Preparation of porphyrin based sensing layers has been achieved by different techniques including spin-coating,^{22,13} vacuum evaporation,^{13,22} glow-discharge induced sublimation^{21,13} and Langmuir-Blodgett^{33,34} as well as Langmuir-Schaefer³⁵ techniques. An important approach to improve the overall performance of gas sensing devices is to incorporate the sensing molecules into a suitable stable and adherent matrix. The sensing molecules should be well dispersed within the matrix to prevent agglomeration and tightly trapped to enhance the mechanical stability of the device. On the other hand, the matrix needs to be porous to allow diffusion of analytes towards the sensing sites. Porphyrins have been incorporated into different matrices to form composite sensing layers typically by immobilization in polymers and plasticizers^{25,27,36} or sol-gel deposited silica films.^{12,24,20}

A new arising technology for the preparation of smart composite coatings is chemical vapor deposition (CVD) enhanced by an atmospheric pressure dielectric barrier discharge (AP-DBD). It is a versatile method to deposit thin films from a broad range of precursors and on several substrates.^{37,38} Even heat sensitive polymers can be treated as AP-DBD creates cold plasmas.³⁹ During the process only minor amounts of waste or by-products are produced and inexpensive process gases such as nitrogen⁴⁰ or even air⁴¹ can be used. In contrast to the limitations of industrial implementations of low-pressure plasmas and sol-gel methods, AP-DBD based processes can be easily integrated into roll-to-roll production lines and are indeed already used in industry for thin film deposition, surface cleaning, sterilizing as well as wettability and adhesion enhancement.⁴²

Deposition of lanthanide-containing polymer particles along with siloxane precursors by an AP-DBD method lead to luminescent composite coatings⁴³ while the

incorporation of AlCeO₃ nanoparticles in a similar matrix gave rise to anti-corrosive layers.⁴⁴ Bio-active coatings could be achieved by immobilizing enzymes in AP-DBD polymerized acetylene and pyrrole matrices.⁴⁵ The enzymes are reported to be protected from plasma alteration by a surrounding water shell, yet helium has to be used as process gas.

Recently, the successful incorporation of metallo *meso*-tetraphenyl porphyrins (M = Zn^{II}, Cr^{III}) into plasma polymerized siloxane matrices has been achieved.^{46,47} The porosity of the matrices could be controlled by tuning the deposition parameters and first demonstrations of amine sensing properties of these composite coatings have been shown.^{46,48} In this context, novel porphyrins have been developed to improve the optical response upon interaction with amines and to enhance their solubility in the matrix precursor in order to achieve highly colored coatings.⁴⁹ Based on these developments, we herein report the co-deposition of these sophisticated metallo porphyrins Zn^{II}P and Cr^{III}P(H₂O)(Cl) along with siloxane precursors in an AP-DBD enhanced chemical vapor deposition onto aluminum and polyethylene terephthalate (PET) substrates. The integrity of the porphyrin based sensor molecules in the siloxane matrix is investigated by UV/vis spectroscopy as well as by mass spectrometry, while the chemical composition of the hybrid coatings is analyzed by IR and XPS spectroscopy. The gas sensing capabilities of the novel layers are spectroscopically investigated by exposing them to NEt₃ vapors. To rationalize the performances of these coatings, comparable layers containing the *meso*-tetraphenyl porphyrins Zn^{II}TPP and Cr^{III}TPP(Cl)(H₂O) were deposited under similar conditions. The amine sensing performance of the devices is correlated to the porphyrin loading of the foils.

Experimental Section

General Materials

The porphyrins Zn^{II}P⁴⁹ and Cr^{III}TPP(Cl)(H₂O)⁵⁰ have been synthesized according to literature procedures and their physical properties conform to reported data. Zinc 5,10,15,20-tetraphenylporphyrin (Zn^{II}TPP), hexamethyldisiloxane (HMDSO, 98.5 %), vinyltrimethoxysilane (VTMOS, 98 %), dichloromethane (DCM, 99.8 %) and triethylamine (NEt₃, 99 %) have been obtained from Sigma-Aldrich (St. Louis, MO) and were used without further purification. Nitrogen (99.999 %, Air Liquide, Pétange, Luxembourg) was moisturized by bubbling through 18 MΩ water (Millipore, Billerica, MA). Polyethylene terephthalate foil (50 μm thick) has been received from Goodfellow (Huntington, UK) and cold-rolled aluminum foil (200 μm thick, 8011 series) from Eurofoil (Belvaux, Luxembourg).

Synthesis of Cr^{III}P(Cl)(H₂O)

A mixture of αα/αβ-H₂P metal-free porphyrins (see **Figure S1**) has been synthesized according to literature procedures.⁴⁹ Under inert atmosphere a 1:1 mixture of αα/αβ-

H₂P isomers (300 mg, 0.33 mmol, 1.0 eq) and Cr(CO)₆ (1.47 g, 6.67 mmol, 20 eq) have been dissolved in dry and degassed toluene (175 mL) and the mixture was heated to reflux for 24 h. The Cr(CO)₆, which has sublimated on the top of the flask during this time, was transferred back into the solution several times. The reaction mixture was cooled to room temperature (RT) and 0.5 mL of concentrated aqueous HCl was added. After stirring at RT under air for 2 h, the solvents have been removed via distillation and residual Cr(CO)₆ via sublimation. The obtained dark solid was dissolved in CHCl₃ (75 mL) and filtered. The filtrate was purified via column chromatography on Al₂O₃ (Brockmann activity IV, CHCl₃). The first fraction containing metal free $\alpha\alpha/\alpha\beta$ -H₂P has been discarded while the second collected fraction contained the purified product. After removing the solvent under reduced pressure, 231 mg (0.23 mmol, 70%) of Cr^{III}P(Cl)(H₂O) was isolated as a purple solid.

UV/vis (CH₂Cl₂): λ_{\max} (ϵ) = 282 (7.2×10^4), 290 (6.7×10^4), 300 (6.6×10^4), 322 (3.6×10^4), 337 (3.2×10^4), 363 (2.8×10^4), 398 (4.17×10^4), 452 (26.4×10^4), 565 (1.16×10^4), 602 ($0.63 \times 10^4 \text{ M}^{-1} \text{ cm}^{-1}$) nm. MS (ESI⁺): m/z = 948.33 [M – Cl – H₂O]⁺, 966.34 [M – Cl]⁺, 989.33 [M – Cl + Na]⁺, 1005.30 [M – Cl + K]⁺. HR-MS (ESI⁺): m/z = 948.3282 (calcd for C₆₆H₄₈CrN₄: 948.3284).

Plasma Deposition

The general procedure employed to create the composite coatings via an AP-DBD enhanced CVD has been described before, including the schematic setup of the prototype.^{43,47} The coatings described here vary in the type of the porphyrin and the porphyrin concentration within the precursor solutions, while all other deposition parameters were kept constant.

With help of an ultrasonic atomizing nozzle (Sono-Tek Corporation, Milton, NY) operating at 48 kHz and fed by a syringe driver delivering 0.25 mL min⁻¹ the precursor solution was sprayed onto the respective substrate (PET foil, 50 μm thick; aluminum foil, 200 μm thick), which was placed on the aluminum moving stage of the AP-DBD reactor. The moving stage speed, set up to 6 m min⁻¹, allowed prompt exposition of the formed liquid layer to the plasma discharge in order to polymerize the siloxane precursor. Delay time between the liquid layer deposition and the plasma treatment was one second. The AP-DBD reactor consisted of two flat parallel high voltage electrodes (0.7 \times 13 cm²) covered with alumina and the moving stage as the grounded electrode. The discharge gap between the high voltage electrode and the substrate placed on the grounded electrode was maintained at 1 mm. The AP-DBD reactor was fed by a 20 L min⁻¹ nitrogen flow containing 200 ppm HMDSO vapor. The plasma discharge was ignited by means of a 10 kHz sinusoidal signal, chopped by a 1667 Hz rectangular signal. The operating discharge power density was maintained at 0.5 W cm⁻². 100 passes were performed, corresponding to 14 s effective deposition time.

Coatings on PET foils were used for UV/vis studies, amine sensing experiments, XPS analysis and top view SEM. Coatings on aluminum foils were used for IR measurements.

Characterization of Deposited Layers

Scanning electron microscopy (SEM) was performed on a Hitachi SU-70 FE-SEM. Prior to SEM observations the non-conductive samples were sputter coated with a thin layer of platinum to prevent charging. FT-IR analysis was performed on a Bruker Hyperion 2000 spectrometer equipped with a Ge-ATR-crystal. XPS analyses were realized with a Kratos Axis-Ultra DLD instrument using a monochromatic Al K_{α} X-ray source ($h\nu = 1486.6$ eV) at a pass energy of 20 eV. Extracts of the deposited layers were obtained by rinsing the foils repetitively with 10 mL of ethanol. The collected extracts were concentrated prior to analysis. The HPLC-MS analysis of the Zn-1 extracts were performed on a Dionex Ultimate 3000 HPLC system coupled with an AB/Sciex API 3200 triple-quadrupole tandem MS. The analytical column was an Agilent Zorbay Bonus-RP (150 mm \times 4.6 mm \times 5 μ m). The eluents were H₂O and acetonitrile, both containing 0.1% formic acid. The gradient profile started with 50% acetonitrile during 2 min, then the acetonitrile fraction was increased to 100% over 3 min and then kept at 100% for 7 min. The flow rate was kept constant at 1 mL min⁻¹ and the column temperature was 40°C. The mass spectrometer was operated in positive electrospray ionization mode and detection was done in full-scan mode. The high-resolution mass spectra of the Cr-1 extracts were collected using a LTQ-Orbitrap Elite hybrid mass spectrometer (ThermoFisher Scientific) equipped with an electrospray ionization source (ESI). The liquid samples were injected by loop injection in a constant flow of methanol. No separation step by liquid chromatography was performed before analysis. The averaged mass spectra were collected in full scan mode at high resolution, allowing a relative error of the measured m/z ratio below 2 ppm.

Amine Sensing Experiments

The gas sensing properties of the deposited coatings were tested at 20°C by a DU800 Beckman Coulter UV/vis spectrometer with a home-build gas flow setup, which has been described in detail elsewhere.⁴⁸ The foils were placed in 3 mL septum capped quartz cuvettes through which a constant gas flow of 250 mL min⁻¹ was passed. Prior to amine exposure, the cuvette was purged with the carrier gas, nitrogen with 50% RH, to monitor the baseline response of the sensing foils and after 10 min the carrier gas was enriched with 1 vol% NEt₃. The change of the absorption was monitored over 120 min in intervals of 10 s at the specific wavelength at which the foils show the largest change before and after exposure to the amine. These monitoring wavelengths are 434 nm for Zn-1, 428 nm for ZnTPP-1, 446 nm for Cr-1, Cr-2, Cr-3 and 441 nm for CrTPP-1, CrTPP-2 and CrTPP-3. Baseline absorbance was monitored at 500 nm for every data

point. Additionally, absorption spectra of the Soret region have been measured before and after exposure to NEt_3 .

Plasma Deposition of Sensor Coatings

Four different metallo porphyrins were incorporated into porous siloxane matrices via AP-DBD enhanced CVD to form colored, transparent and adherent sensing films. The porphyrin complexes $\text{Zn}^{\text{II}}\text{P}$ and $\text{Cr}^{\text{III}}\text{P}(\text{Cl})(\text{H}_2\text{O})$ shown in **Figure 1a** have been tailored for colorimetric amine sensing by introduction of two phenylalkynyl arms shielding the coordination site.⁴⁹ Both metallo porphyrins were used as a 1:1 mixture of $\alpha\alpha$ - and $\alpha\beta$ -isomers. For comparison, the corresponding 5,10,15,20-tetraphenylporphyrins $\text{Zn}^{\text{II}}\text{TPP}$ and $\text{Cr}^{\text{III}}\text{TPP}(\text{Cl})(\text{H}_2\text{O})$ (**Figure 1b**) were deposited by the same technique and similar process parameters. **Table 1** summarizes the compositions of the precursor solutions, which differ in the type and concentration of the porphyrins. All solutions were based on 20 vol% dichloromethane (DCM) and 80 vol% vinyltrimethoxysilane (VTMOS), as siloxane precursor, and contained 0.08 to 3.0 g L^{-1} of the respective porphyrin. The plasma process gas was enriched with hexamethyldisiloxane (HMDSO) vapors, which also contribute to the growth of the porous siloxane matrix in which the porphyrins are incorporated. The general deposition parameters were adapted from the successful process conditions that allowed the deposition of the reference foil CrTPP-1, which has been proven to show the best amine sensing properties within a series of $\text{Cr}^{\text{III}}\text{TPP}(\text{Cl})(\text{H}_2\text{O})$ containing layers prepared by the same method (for details see experimental section).⁴⁸

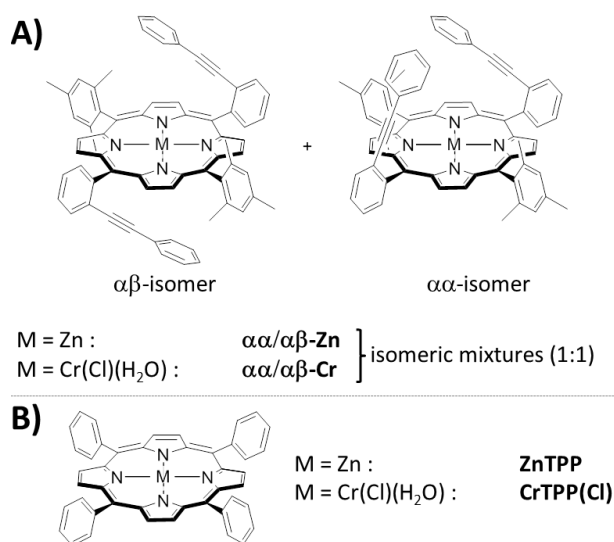


Figure 1 a) Molecular structures of the deposited porphyrin complexes $\text{Zn}^{\text{II}}\text{P}$ and $\text{Cr}^{\text{III}}\text{P}(\text{Cl})(\text{H}_2\text{O})$ and b) molecular structures of the deposited reference compounds $\text{Zn}^{\text{II}}\text{TPP}$ and $\text{Cr}^{\text{III}}\text{TPP}(\text{Cl})(\text{H}_2\text{O})$.

Table 1 Composition of precursor solutions.

Porphyrin	Concentration ^a [g L ⁻¹]	Foil sample
Zn ^{II} P	0.75	Zn-1
Zn ^{II} TPP	0.75	ZnTPP-1
Cr ^{III} P(Cl)(H ₂ O)	0.75	Cr-1
	1.50	Cr-2
	3.00	Cr-3
Cr ^{III} TPP(Cl)(H ₂ O)	0.75	CrTPP-1 ^b
	0.32	CrTPP-2
	0.08	CrTPP-3

^a In 80 vol.% VTMOs and 20 vol.% DCM. ^b Has been described in ref. 48.

Deposition of Zn^{II} Porphyrin Containing Coatings

For the Zn^{II}P based coating Zn-1 a solution of 0.75 g L⁻¹ of the respective porphyrin in VTMOs/DCM has been used as the precursor solution (**Table 1**). The solution was sprayed onto the PET substrate by an ultrasonic atomizing nozzle and the sample was subsequently exposed to the AP-DBD. To form the final layer, the substrate passed 100 times through the precursor mist and the atmospheric plasma (see experimental section for details). The Zn^{II}TPP containing reference ZnTPP-1 has been prepared using 0.75 g L⁻¹ Zn^{II}TPP in the precursor solution employing the same general deposition process.

Both coatings are adherent to the PET substrate foils and are stable towards water. Neither visually noticeable cracks nor particles were observed on the surface by eye. They show similar FT-IR spectra with the characteristic absorptions of plasma-polymerized organosiloxanes (see **Figure 2**). The strong and broad band observed at 1087 cm⁻¹ is assigned to a Si-O-Si network vibration while the absorptions at 806 cm⁻¹ (ν (Si-CH₃)), 847 cm⁻¹ (ν (Si-C) and ρ (CH₃)), 1261 cm⁻¹ (δ^s (Si-CH₃)), 1409 cm⁻¹ (ν^a (CH₃)), 2915 and 2960 cm⁻¹ (ν (CH₃)) prove the high retention of the methyl groups from the siloxane monomer.⁵¹ The peak observed at 1675 cm⁻¹ is commonly observed for nitrogen plasma-polymerized organosiloxanes and is attributed to C=N vibrations, as nitrogen is partially incorporated from the plasma gas.⁴⁰ No distinct vibrations from the incorporated porphyrin macrocycles can be observed as they are hidden by the intense matrix vibrations. XPS analysis show an elemental composition as expected for carbon rich plasma-polymerized organosiloxanes due to high methyl group retention. Zn-1 is composed of 16 at-% silicon, 25at-% oxygen, 55at-% carbon and 4at-% nitrogen, while for ZnTPP-1 16at-% silicon, 26at-% oxygen, 54at-% carbon and 4at-% nitrogen are observed. This is in good agreement with literature values.^{46,47} As the zinc content of the incorporated porphyrins is rather low (0.84 at-% in Zn^{II}P and 1.3 at-% in Zn^{II}TPP) only traces of zinc could be detected by XPS in the foil. The deposited matrix Zn-1

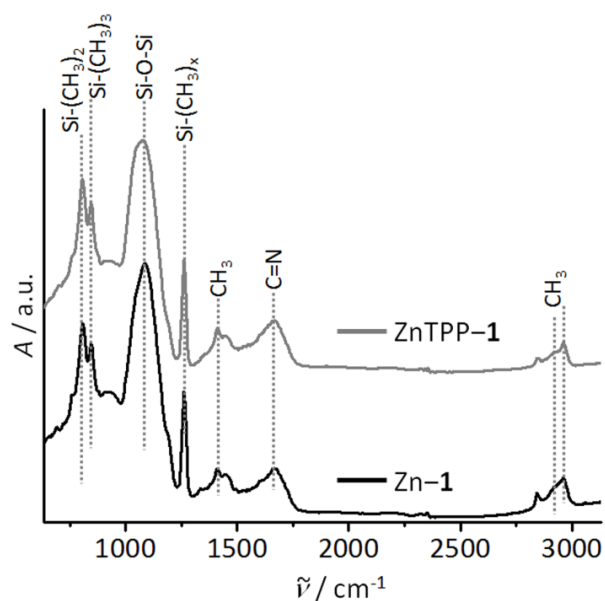


Figure 2 FT-IR absorption spectra of Zn-1 on aluminium (bottom, black) and ZnTPP-1 on aluminium (top, grey).

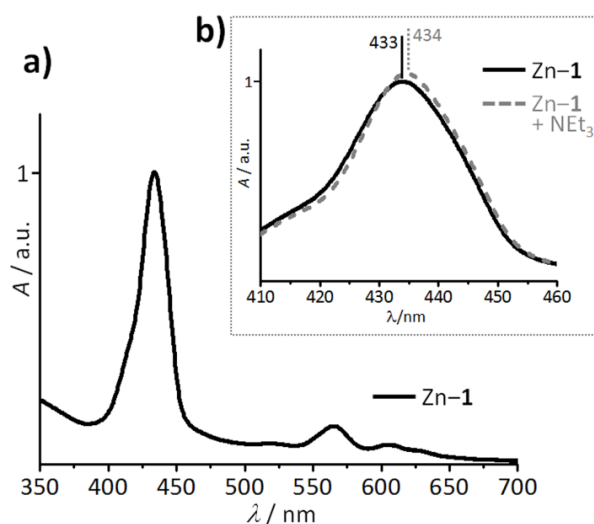


Figure 3 a) Normalized UV/vis absorption spectrum of Zn-1 with the Soret band absorption at 433 nm and Q-band absorptions at 565 and 603 nm; b) Magnification of the Soret band region before (black, solid) and after (grey, dotted) 2h exposure to 1% NEt_3 vapor.

contains (0.2 ± 0.1) at-% zinc and ZnTPP-1 (0.3 ± 0.1) at-%, which represents a relatively high porphyrin loading of the matrix of about $(22 \pm 8)\%$ in both cases.

Both foils show uniform transparent pale orange-green coloration and exhibit the characteristic UV/vis absorption spectra of the incorporated intact metallo porphyrin macrocycle. The foils show Soret band absorptions at 433 nm for Zn-1 (**Figure 3a**) and at 428 nm for ZnTPP-1 (**Figure 4a**). These absorptions are shifted bathochromically by 14 nm as compared to the spectra observed for $\text{Zn}^{\text{II}}\text{P}$ and $\text{Zn}^{\text{II}}\text{TPP}$ in *n*-hexane solutions.

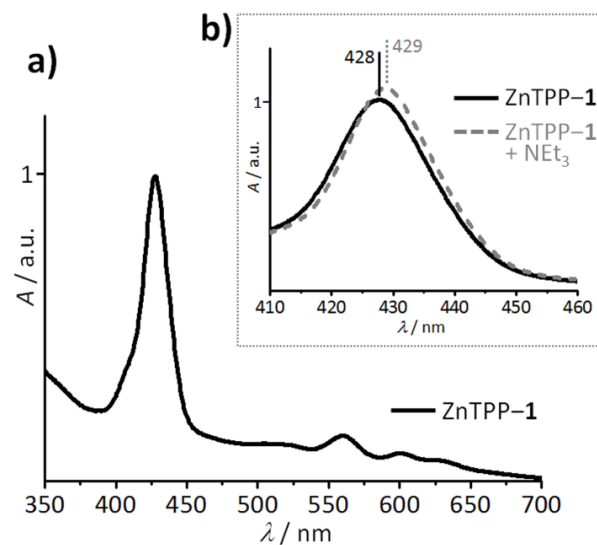


Figure 4 a) Normalized UV/vis absorption spectrum of ZnTPP-1 with the Soret band absorption at 428 nm and Q-band absorptions at 560 and 600 nm; b) Magnification of the Soret band region before (black, solid) and after (grey, dotted) 2h exposure to 1% NEt₃ vapor.

Q-band absorptions are found at 565 and 603 nm and at 560 and 600 nm for Zn-1 and ZnTPP-1, respectively. UV/vis spectra of porphyrins are known to be affected by their environment as emphasized by solvatochromic series. In solution their absorption is known to be red-shifted in polar solvents.⁴⁹ A similar effect may be responsible for the bathochromic shift within the polysiloxane matrix, as it contains several polar groups. The rigidity of the matrix can additionally lead to a slight distortion of the entrapped porphyrin macrocycles which is also known to induce bathochromic shifts. The red-shift of the porphyrins' absorption within the matrix may therefore be attributed to a general solvatochromic effect. The UV/vis spectra strongly indicate that the macrocycle is unaltered by the plasma deposition process. As FWHM values of the Soret band are similar to values observed in solution, stacking and aggregation of the porphyrins is obviously suppressed by their thorough and stable dispersion within the matrix.

The integrity of the relatively simple Zn^{II}TPP sensor molecule after the described plasma treatment has already been successfully proven by mass spectrometry of ethanol extracts from the layer.⁴⁷ To prove the preservation of the more complex Zn^{II}P structure after the plasma deposition, ethanol extracts of Zn-1 have been analyzed by HPLC-MS. The only prominent peaks seen in the HPLC chromatogram in **Figure 5** can be clearly assigned to the αβ-isomer of Zn^{II}P at 8.1 min and to the αα-isomer at 11.9 min based on the mass spectral analysis as well as by comparison with literature retention data.⁴⁹ Hence, the entire molecular structure of the sensor molecules, including the shielding phenylalkynyl arms and the labile bound Zn^{II}, is preserved. Moreover, the initial isomeric ratio of 1:1 (αα:αβ) is unaltered, showing that both isomers are incorporated in the matrix.

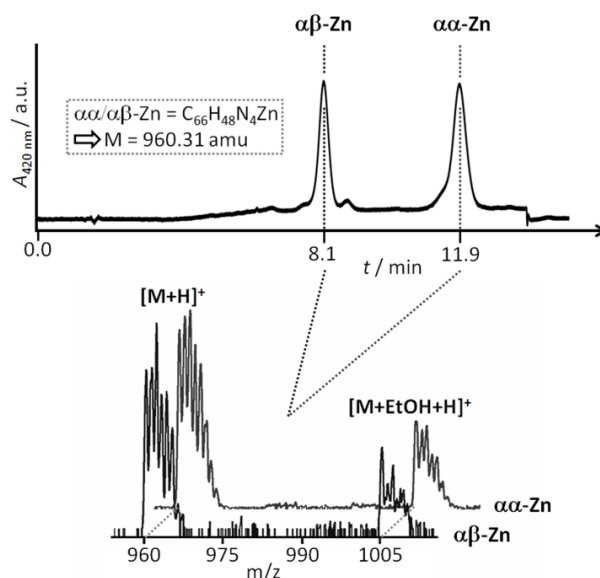


Figure 5 Top: chromatogram of the HPLC-MS analysis of extracts from Zn-1; bottom: ESI-MS analysis of the respective peaks at 8.1 min (front) and 11.9 min (back).

Deposition of Cr^{III} Porphyrin Containing Coatings

Cr^{III} porphyrin complexes are known to have high affinity towards nitrogen containing axial ligands (e.g. amines) and they show large spectral changes upon interaction with amines in solution. Therefore, they are good candidates for the preparation of amine sensing devices. We have recently reported the formation of Cr^{III}TPP(Cl)(H₂O) containing layers by AP-DBD which are capable of colorimetric amine sensing.⁴⁸ In this context, we have developed the novel porphyrin complex Cr^{III}P(Cl)(H₂O). Its synthesis is described in the experimental section. In contrast to the trends observed for zinc porphyrin complexes,⁴⁹ Cr^{III}P(Cl)(H₂O) does not outclass its simple tetraphenyl porphyrin equivalent Cr^{III}TPP(Cl)(H₂O) with respect to spectral shifts upon interaction with NEt₃ in solution. In DCM, both Cr^{III} porphyrin complexes show a large hypsochromic shift upon NEt₃ exposure of about 17 nm of the Soret band. For Cr^{III}P(Cl)(H₂O) a shift from 452 to 435 nm is observed in DCM (see **Figure S2**), while Cr^{III}TPP(Cl)(H₂O) shows a shift from 448 to 431 nm. The benefit of the Cr^{III}P(Cl)(H₂O) complexes is their strikingly higher solubility in the precursor solution as compared to Cr^{III}TPP(Cl)(H₂O). The solubility of Cr^{III}TPP(Cl)(H₂O) in VTMS:DCM 80:20 is 7.8 mmol · L⁻¹ while 39.3 mmol · L⁻¹ of Cr^{III}P(Cl)(H₂O) can be dissolved in the precursor solution. The increased solubility of the Cr^{III}P(Cl)(H₂O) complexes is attributed to their molecular structure with the two arms above one or both sites of the porphyrin macrocycle, which suppresses π - π stacking of the porphyrins.⁴⁹ Therefore, significantly higher complex concentrations in the precursor solutions can be used during the deposition process leading to sensing foils with a more intense coloration as compared to the intensities achievable with Cr^{III}TPP(Cl)(H₂O). This is a crucial step towards simple devices for the inspection of food freshness whose response should be visible by the human eye instead of spectrometers.

As indicated in **Table 1**, $\text{Cr}^{\text{III}}\text{P}(\text{Cl})(\text{H}_2\text{O})$ based coatings were deposited from three different precursor solutions containing 0.75 g L^{-1} (Cr-1), 1.50 g L^{-1} (Cr-2) and 3.00 g L^{-1} (Cr-3). The deposition parameters in all cases were equivalent to the ones used for the reference foil CrTPP-1 (see experimental section for details).⁴⁸ All three Cr^{III} porphyrin containing coatings are adherent to the PET substrate foils and are stable towards water. Neither visually noticeably cracks nor particles were observed on the surface by eye. As the FT-IR spectra are dominated by the absorptions of the plasma-polymerized organosiloxane matrix rather than by the different incorporated porphyrins, the FT-IR spectra of all foils are similar among each other and also to the one shown in **Figure 2** for Zn-1. Therefore, no signs of the incorporated Cr^{III} porphyrins are detected in the FT-IR spectra of Cr-1, Cr-2 and Cr-3 (**Figure S3**). The chromium percentage of Cr-1 is expected to be around the 0.2at-% as that observed for zinc in Zn-1, as deposition parameters and solution concentrations are equal for Zn^{II} and Cr^{III} containing coatings. But in contrast to zinc, chromium contents could not be quantified in foils Cr-1, Cr-2 and Cr-3 reliably down to this range by XPS, as the signals are hardly above the noise level. This is probably because the Relative Sensitivity Factor (RSF) of the Cr 2p is smaller compared to Zn 2p ($\text{RSF}_{\text{Cr}2\text{p}}=2.4$; $\text{RSF}_{\text{Zn}2\text{p}}=5.59$). The elemental composition estimated by XPS regarding silicon, oxygen, carbon and nitrogen is similar to the one measured for the zinc porphyrins containing coating Zn-1 and ZnTPP-1.

The coloration of the three $\text{Cr}^{\text{III}}\text{P}(\text{Cl})(\text{H}_2\text{O})$ containing foils varies from slightly green for Cr-1 to intense green for Cr-3 (see insets in **Figure 6**). Their UV/vis absorption spectra show the characteristic absorptions of intact Cr^{III} porphyrin complexes at the same energy for each foil. The absorptions of Cr-1 to Cr-3 only grow in intensity (**Figure 6**). Hence even though the different porphyrin loadings within the coatings could not be estimated by XPS, the absorption spectra corroborate that the porphyrin content is

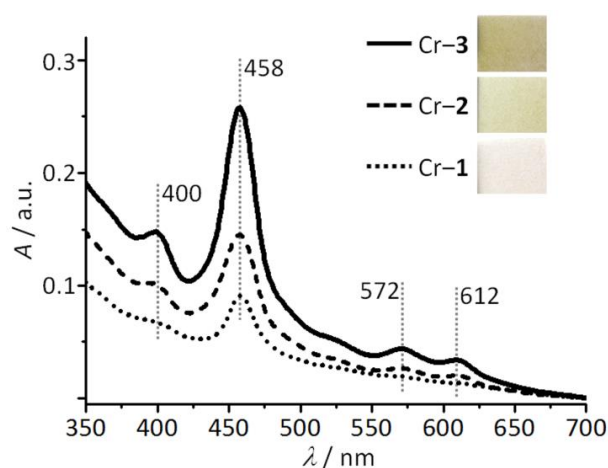


Figure 6 UV/vis absorption spectra of Cr-1 (dotted), Cr-2 (dashed) and Cr-3 (straight) with a charge transfer absorption at 400 nm, the Soret band absorption at 458 nm and Q-band absorptions at 572 and 612 nm; insets show photographs of the respective foils.

proportional to their concentration within the initial precursor solutions. The intense Soret band absorption is seen at 458 nm and the weaker Q-band absorptions at 572 and 612 nm. The weak absorption at 400 nm is characteristic for Cr^{III} porphyrin complexes with anionic axial ligands and is attributed to a $\pi(a_{2u}, a_{1u}) \rightarrow d(e_g)$ charge transfer absorption from the porphyrin to the metal center.⁵² The presence of these UV/vis absorptions is a strong indicator that neither the molecular structure of the porphyrin macrocycle nor the oxidation state of the chromium central metal is changed during the plasma deposition process.

To further substantiate the integrity of the molecular structure during the deposition, ethanol extracts of the coatings were studied by mass spectrometry (for details see experimental section). As no method could be developed to separate the Cr^{III}P(Cl)(H₂O) isomers via HPLC, as was successful for Zn^{II}P,⁴⁹ the samples were analyzed via high resolution ESI mass spectrometry. **Figure 7a** shows a representative mass spectrum of the Cr-1 extracts in the front (black) and the reference mass spectrum of molecular Cr^{III}P(Cl)(H₂O) before plasma deposition in the back (grey). The spectra clearly demonstrate the integrity of the porphyrin macrocycle, the retention of the shielding

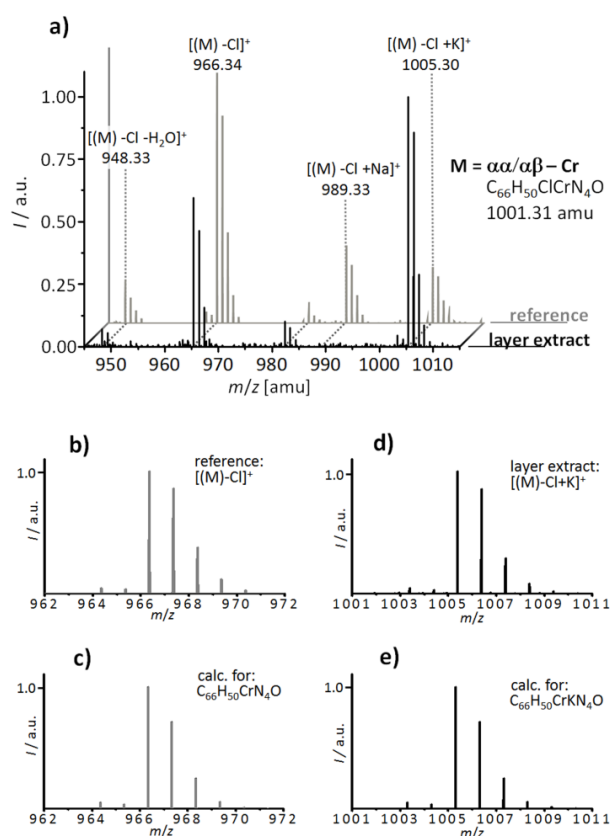


Figure 7 a) ESI mass spectrum of extracts from Cr-1 (black, front) and reference ESI mass spectrum of Cr^{III}P(Cl)(H₂O) before plasma deposition (grey, back); each spectrum is normalized to the most intense peak; b) and d) Magnification of the most intense peak of the reference spectrum and the layer extract analysis, respectively; c) and e) calculated isotopic pattern for $[(M)-Cl]^+$ and $[(M)-Cl+K]^+$, respectively.

phenylalkynyl arms and the presence of the metal in the porphyrin. Experimental isotopic patterns shown in **Figure 7b** and **7d** match with calculated patterns (**Figure 7c** and **7e**, respectively) revealing the correct assignments of the fragmentation peaks.

Amine Sensing Experiments

To probe the colorimetric amine sensing ability of the deposited coatings, foil samples were placed in a 3 mL flow cuvette and exposed to a constant flow of 1 vol% NEt_3 vapor in the carrier gas (N_2 with 50% relative humidity) over 2 h (for details see Experimental Section). The initial absorption of the Zn^{II} and Cr^{III} containing foils does not change under humid conditions as compared to inert atmosphere. The amine sensing performance of zinc porphyrin containing foils is also not affected by change of the relative humidity (RH) in the carrier gas (see **Figure S4**). In contrast, the performance of the chromium porphyrin based matrices is greatly enhanced under humid conditions (see **Figure S5**). For real-life applications like e.g. food packaging the compatibility with humid conditions is rather beneficial than detrimental, as the ubiquitous humidity gives no false response with the sensor system but enhances its performance. The detailed mechanism of the interaction of Cr^{III} porphyrins with NEt_3 either in solution or in polymer matrices under different humid conditions is currently under investigation in our laboratories and mechanistic results will be published in due course.

Amine Sensing with Zn^{II} Porphyrins

The Soret band absorptions of Zn-1 and ZnTPP-1 before (solid line) and after (dotted line) 2 h of exposure to 1 vol% NEt_3 in the carrier gas are shown in **Figure 3b** and **Figure 4b**, respectively. Zn-1 shows a small 1 nm bathochromic shift of the Soret band from 433 to 434 nm upon interaction with NEt_3 and a slight increase in intensity along with a decrease of the FWHM of the signal. Similar minor changes are observed for ZnTPP-1 with a Soret band shift from 428 to 429 nm. The colorimetric responses of the sensing foils are not as large as the ones reported for the respective porphyrin complexes exposed to NEt_3 in *n*-hexane solutions. Under homogenous conditions the Soret band of Zn^{II} TPP in *n*-hexane is shifted by 11 nm from 414 to 425 nm and the one of Zn^{II} P by even 13 nm from 419 to 432 nm upon amine coordination.⁴⁹ As intact molecular sensors are embedded within the matrix (see previous section), the observed discrepancy between the sensor's performance in *n*-hexane solution and in the matrix must be attributed to other reasons. One possibility may be a poor accessibility of the chromophores within the matrix. Another issue could be an environmental matrix effect. It has been shown in serial trials with different solvents that the absorption shifts upon NEt_3 coordination decrease as the initial Soret absorption is shifted bathochromically.⁴⁹ For instance in chloroform solutions the bathochromic shift upon interaction with NEt_3 also amounts only to 1 nm from 428 to 429 nm. Therefore, we propose that the diminished absorbance shifts of the sensor molecules entrapped in the matrix is rather ascribed to sensor-matrix interactions,

comparable to the solvatochromic effect observed in solution, than indicating a low porosity of the matrix.

Amine Sensing with Cr^{III} Porphyrins

The foils Cr-1, Cr-2 and Cr-3 were placed in flow cuvettes and exposed to a constant flow of nitrogen (50% RH) enriched with 1 vol% of NEt₃. The responses of the foils were monitored by changes of the Soret band absorption by UV/vis spectroscopy (see experimental section for details). **Figure 8** shows the Soret band absorptions of the foils before (solid line) and after (dotted line) two hours exposure to a nitrogen flow containing NEt₃. The absorptions are shifted hypsochromically between 2 and 3 nm along with a slight increase in intensity and a broadening of the band (see **Table 2**). The changes are similar to that of the reference foil CrTPP-1 under identical conditions. The difference spectra of Cr-1, Cr-2 and Cr-3, calculated by subtraction of the spectra before interaction with NEt₃ from the spectra after NEt₃ treatment, are shown in **Figure 9**. As already indicated by the different absorptions shown in **Figure 8**, the foil with the highest porphyrin loading, Cr-3, gives the largest absolute response upon amine exposure. For all foils the maximum change in absorption is observed at 446 nm.

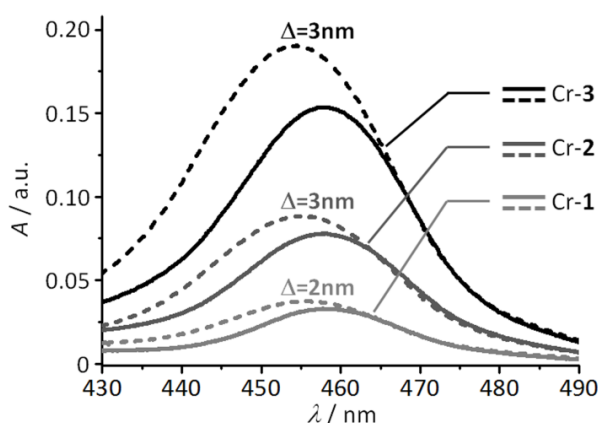


Figure 8 Soret band UV/vis absorption before (solid lines) and after (dashed lines) 2h exposure to a constant nitrogen flow containing 1 vol% NEt₃ for Cr-1, Cr-2 and Cr-3; hypsochromic shifts upon interaction with NEt₃ are indicated above the respective curves.

To measure the dynamic responses of the foils towards amine exposure the changes of the absorptions at 446 nm were monitored referenced to the absorption at 500 nm (baseline) every ten seconds while exposed to a constant flow of 1 vol% NEt₃ in the carrier gas (N₂ with 50% RH). As the foils have different initial absorption intensities, the recorded responses were normalized to their respective initial Soret band absorption intensity. These normalized absorption changes are depicted in **Figure 10a**. During the first 10 min, the foils were exposed to a constant flow of nitrogen with 50% RH without any amine to record the baseline response. The evanescent signals for all foils show that there is no interaction with humidity. After 110 min exposure to a

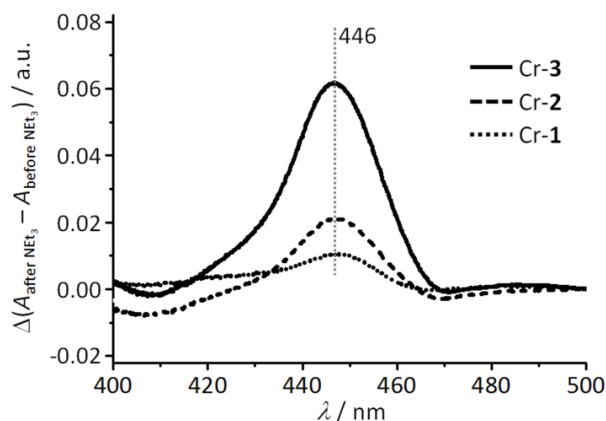


Figure 9 Difference spectra of Cr-1 (dotted), Cr-2 (dashed) and Cr-3 (solid) calculated by subtraction of the UV/vis spectra before exposure to NEt_3 from the respective spectra after 2h exposure.

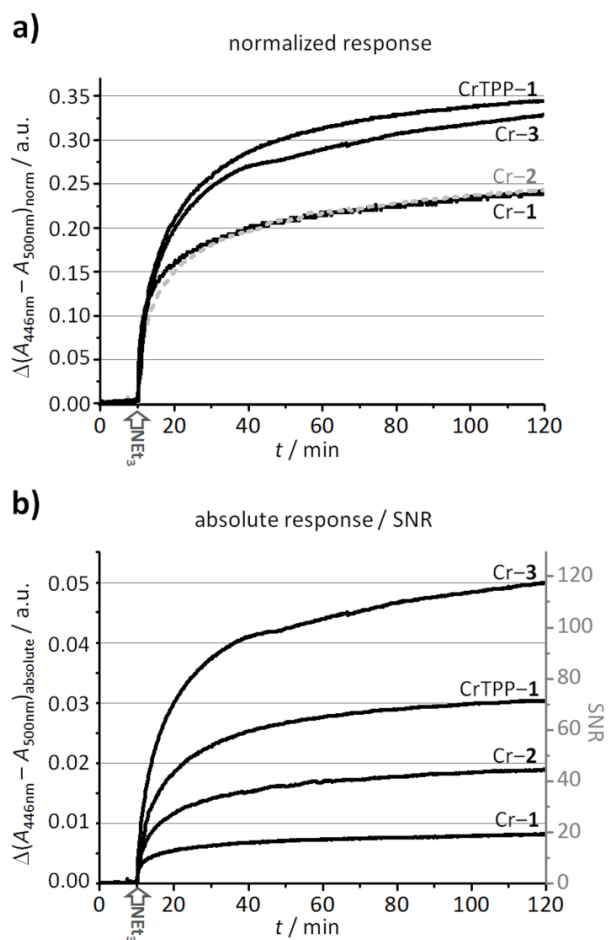


Figure 10 Time traces of the absorption change at 446 nm relative to the absorption at 500 nm upon exposure to a constant flow of 1 vol% NEt_3 ; data points measured every 10 s; exposure starts at 10 min; a) Values normalized to the initial Soret band intensity; b) Absolute values as measured by the spectrometer (left scale) and converted to the respective signal-to-noise ratio (SNR, right scale).

1 vol% NEt_3 flow, Cr-1 shows a normalized response of about 0.25 a.u.. This is about one third smaller than that observed with the reference CrTPP-1, which is prepared from the corresponding $\text{Cr}^{\text{III}}\text{TPP}(\text{Cl})(\text{H}_2\text{O})$ containing precursor solution under the same deposition conditions. As the responses are normalized to the initial absorption intensities, this is a sign of less sensor molecules interacting with the analyte in Cr-1 than within CrTPP-1. This difference is also expressed by the absolute responses of the foils and depicted in **Figure 10b**. Even though the initial Soret band intensity of the two foils is similar, a significantly smaller signal change is observed for Cr-1 as compared to CrTPP-1.

When the amount of $\text{Cr}^{\text{III}}\text{P}(\text{Cl})(\text{H}_2\text{O})$ is doubled within the sensing layers, the absolute response of the foils towards amine exposure proportionally increases, as can be seen from a comparison of the responses of Cr-1 (0.009 a.u.) and Cr-2 (0.018 a.u.) in **Figure 10b**. The normalized responses of Cr-1 and Cr-2, however, are superimposable. The identical normalized response of Cr-1 and Cr-2 shows that the same fraction of sensor molecules interacts with the amines. The similar time profile of the two foils additionally proves that diffusion of the analyte through the matrix is similar. We ascribe this to a similar porosity and similar incorporation of the chromophores accomplished during the deposition process. This indicates that the growth of the matrix and thereby the matrix properties are not significantly affected by doubling the porphyrin concentration within the precursor solution from 0.75 g L^{-1} (Cr-1) to 1.50 g L^{-1} (Cr-2).

This behavior obviously changes when the initial porphyrin concentration is increased to $3.00 \text{ g} \cdot \text{L}^{-1}$ (Cr-3). The normalized response of this foil (see **Figure 10a**) is increased as compared to Cr-1 and Cr-2 and is rather similar to that observed for the reference compound CrTPP-1. And even though the initial Soret band intensity is doubled compared to Cr-2 (see **Table 2**), the absolute response as shown in **Figure 10b** is increased by a factor of three. Both illustrations suggest that in Cr-3 a higher fraction of porphyrin molecules interacts with the amines compared to Cr-1 and Cr-2 with lower porphyrin concentrations. This observation indicates that above a certain threshold of porphyrin concentration within the precursor solution, the mechanism of the matrix growth is changed which enables more chromophores to interact with the amine. As can be seen from the normalized response, the fraction of porphyrin sites interacting with the analyte in Cr-1 is comparable to that in CrTPP-1. On the other hand the absolute number of porphyrins within the matrix is higher, which leads to a stronger absolute response of Cr-1. After 110 min exposure to NEt_3 an absolute response of 0.049 a.u is observed for Cr-1, which represents a 1.6 fold increase as compared to the 0.030 a.u. of CrTPP-1.

To compare the sensors' performance with results from other sensing systems, the foils' responses towards NEt_3 exposure were converted into the respective signal-to-noise ratio (SNR) parameter (see **Figure 10b**). This dimensionless value is defined by

the observed signal change divided by the signal noise of the chosen analytical method. For a positive detection event, a $\text{SNR} \geq 3$ has been defined.^{12,28} The superior performance of Cr-3 compared to the reference compound CrTPP-1 is also expressed by their SNR values of 117.6 and 70.6, respectively. This has been achieved by the increased solubility of the novel porphyrin chromophores and hence the higher loading of the foil.

Table 2 Compiled UV/vis data for Cr-1, Cr-2 and Cr-3 before and after exposure to NEt_3 .

Foil sample	As deposited			After NEt_3 exposure ^a		
	Position [nm]	Height [a.u.]	FWHM ^b [nm]	Position [nm]	Height [a.u.]	FWHM ^b [nm]
Cr-1	458	0.03	23.8	456	0.04	27.8
Cr-2	458	0.07	27.5	455	0.09	29.2
Cr-3	458	0.15	28.1	455	0.19	30.6

^a 110 min exposure to 1% NEt_3 . ^b Full width at half maximum.

Influence of Cr^{III} Porphyrin Concentration on the Sensor Properties

As shown in the previous part for Cr-1, Cr-2 and Cr-3, the performance of the deposited layers with respect to colorimetric amine sensing is associated with the porphyrin concentration within the precursor solutions. The normalized responses of the foils as depicted in **Figure 10a** show a disproportional dependence on the solution concentrations, with a sudden increase upon a certain threshold. The solubility of the porphyrins in the precursor solution seems to be decisive for this behavior. If the solutions are nearly saturated before deposition, like for Cr-3, small aggregates may be formed upon solvent evaporation during the spray process which may influence the later sensor performance in two ways.

On the one hand, the formed aggregates may act as seeds for the matrix growth leading to a more porous material and therefore enable more chromophores to interact with the amine. Unfortunately, no direct experimental evidence could so far be obtained for this assumption as SEM analyses of the three foils show a similar surface morphology (see **Figure S6**). Cr-1, Cr-2 and Cr-3 do all show smooth surfaces with potential small porosities covered by the platinum layer which has been sputtered onto the samples to avoid charging effects. Attempts to obtain SEM pictures with less or no platinum coating were unsuccessful due to the insulating properties of both the substrate and the layer. On the other hand formation of aggregates during the deposition from nearly saturated solutions may more often lead to spatially close incorporation of the chromophores within a matrix pore. If more than one chromophore is involved in the actual sensing event with NEt_3 , this could explain the remarkably higher response of Cr-3.

Even though there is no direct experimental proof for these assumptions, the general dependence of the sensor foils' performances on the initial chromophore concentration in solution becomes obvious by further comparison of the $\text{Cr}^{\text{III}}\text{P}(\text{Cl})(\text{H}_2\text{O})$ and $\text{Cr}^{\text{III}}\text{TPP}(\text{Cl})(\text{H}_2\text{O})$ systems. As Cr-3 and CrTPP-1 show a similar normalized response towards NEt_3 vapors (**Figure 10a**), which reflects a similar fraction of porphyrin molecules interacting with NEt_3 , a similar constitution of both matrices can be assumed. To achieve these properties, an initial porphyrin concentration of 3.00 g L^{-1} within the precursor solution was necessary for Cr-3, while for CrTPP-1 0.75 g L^{-1} $\text{Cr}^{\text{III}}\text{TPP}(\text{Cl})(\text{H}_2\text{O})$ has been used. Both concentrations represent almost saturated solutions for the respective porphyrin, as the solubility of $\text{Cr}^{\text{III}}\text{P}(\text{Cl})(\text{H}_2\text{O})$ in the precursor solution is approximately 5 times higher than the solubility of $\text{Cr}^{\text{III}}\text{TPP}(\text{Cl})(\text{H}_2\text{O})$. From diluted solutions as used for the preparation of Cr-1 (0.75 g L^{-1}) and Cr-2 (1.50 g L^{-1}), sensors with lower performance have been obtained. This is seen by their superimposable, but lower, normalized response towards NEt_3 as depicted in **Figure 10a**. Accordingly, layers have been deposited from diluted $\text{Cr}^{\text{III}}\text{TPP}(\text{Cl})(\text{H}_2\text{O})$ precursor solutions containing 0.32 g L^{-1} and 0.08 g L^{-1} porphyrin to form CrTPP-2 and CrTPP-3, respectively. As shown in **Figure 11**, their optical response towards NEt_3 exposure is also significantly lowered by 52% as compared to CrTPP-1 and is comparable to that observed for Cr-2 and Cr-3. This shows that also in $\text{Cr}^{\text{III}}\text{TPP}(\text{Cl})(\text{H}_2\text{O})$ based coatings only a smaller fraction of chromophores interact with the analyte if they are deposited from diluted solutions.

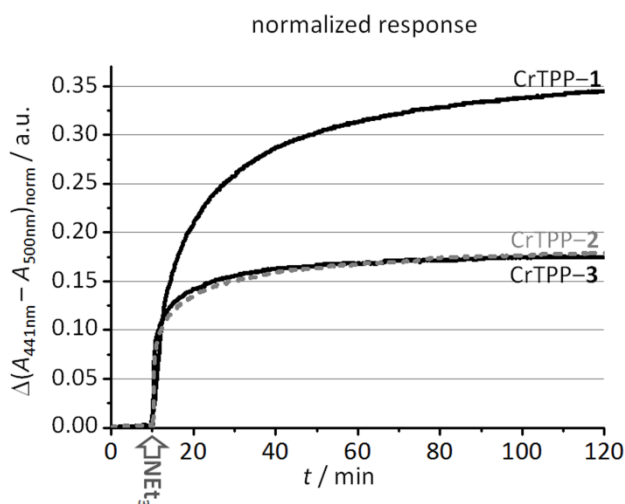


Figure 11 Time traces for CrTPP-1, CrTPP-2 and CrTPP-3 of the absorption change at 441 nm relative to the absorption at 500 nm upon exposure to a constant gas flow of 1 vol% NEt_3 ; Data points measured every 10 s; exposure starts at 10 min; response normalized to the initial Soret band intensity.

The similar dependence of the sensor responses on the respective initial concentration of $\text{Cr}^{\text{III}}\text{P}(\text{Cl})(\text{H}_2\text{O})$ or $\text{Cr}^{\text{III}}\text{TPP}(\text{Cl})(\text{H}_2\text{O})$ in the precursor solutions reveals a common influence on the matrix growth mechanism. If the precursor solution's concentration is increased above a certain threshold value, approaching the saturation limit, a

matrix/chromophore constitution is achieved which facilitates the interaction of a higher fraction of chromophores with the analyte leading to a remarkably better sensor performance. The detailed mechanism, however, is so far unclear and is under current investigation in our laboratories.

Conclusions

Four different metallo porphyrins, Zn^{II}P, Cr^{III}P(Cl)(H₂O), Zn^{II}TPP and Cr^{III}TPP(Cl)(H₂O) were successfully incorporated into porous polysiloxane matrices via an atmospheric pressure plasma enhanced chemical vapor deposition. The structure of the metallo porphyrin complexes was entirely stable during the plasma treatment, even the complex molecular structure of Zn^{II}P and Cr^{III}P(Cl)(H₂O) with two phenylalkynyl substituents is fully retained.

Due to the porous nature of the matrix and the amine sensing properties of the incorporated porphyrins, the deposited layers can be used for the colorimetric detection of volatile amines as exemplified by exposure to NEt₃. The layers based on zinc porphyrins show a 1 nm bathochromic shift of the Soret band absorption along with a slight increase of intensity upon interaction with NEt₃. The remarkable color changes observed in *n*-hexane solutions, especially of Zn^{II}P, could not completely be transferred to the deposited thin coatings. This behavior is attributed to a solvatochromic effect of the matrix on the porphyrins' absorption properties, as a similar effect is also observed e.g. in chloroform solutions.

The Cr^{III} porphyrin containing layers show a larger spectral shift and exhibit a stronger sensor response signal upon interaction with NEt₃. Layers based on the novel metallo porphyrin Cr^{III}P(Cl)(H₂O) show a 3 nm hypsochromic shift when exposed to NEt₃, which is comparable to responses observed for coatings containing Cr^{III}TPP(Cl)(H₂O). Due to the significantly higher solubility of Cr^{III}P(Cl)(H₂O) as compared to Cr^{III}TPP(Cl)(H₂O), coatings with higher chromophore loading could be produced. This leads to a visible intense coloration of the foils and a stronger response upon NEt₃ exposure. The signal-to-noise ratio is greatly enhanced up to 117.6 which is beneficial for the production of amine sensing devices.

Higher porphyrin loadings not only proportionally increase the coloration and the sensitivity of the sensor, but also a certain non-linear effect is noted. Above a certain threshold concentration the constitution of the deposited matrices is changed in such a way that a higher fraction of chromophores interacts with the analyte. This leads to an improvement of the normalized sensor response of 140% for Cr^{III}P(Cl)(H₂O) based coatings and 200% for Cr^{III}TPP(Cl)(H₂O) based ones.

As for the first time functionalized porphyrins have been deposited unaltered via an atmospheric pressure plasma enhanced CVD, new possibilities to improve the sensing layer properties open up. The possibility to use further optimized porphyrins or other chromophore classes may finally lead to colorimetric sensing foils which i) show a

visible color change and ii) have been produced by this environmentally friendly and easy to scale up process. The potential demonstrated here may be inspiring for researchers working in the fields of hybrid functional materials and immobilization of organic compounds in general.

Acknowledgements The authors thank the Luxembourgish “Fonds National de la Recherche” (FNR) for financial support through the SurfAmine CORE project. Skillful characterizations of and valuable discussions with Dr. C. Guignard, Dr. G. Frache and J. Didierjean from the CRP-Gabriel Lippmann are gratefully acknowledged.

Notes and References

1. L.-L. Li and E. W.-G. Diau, *Chem. Soc. Rev.*, 2013, **42**, 291.
2. A. Yella, H.-W. Lee, H. N. Tsao, C. Yi, A. K. Chandiran, M. K. Nazeeruddin, E. W.-G. Diau, C.-Y. Yeh, S. M. Zakeeruddin, and M. Grätzel, *Science*, 2011, **334**, 629.
3. H. Imahori, S. Kang, H. Hayashi, M. Haruta, H. Kurata, S. Isoda, S. E. Canton, Y. Infahsaeng, A. Kathiravan, T. Pascher, P. Chábera, A. P. Yartsev, and V. Sundström, *J. Phys. Chem. A*, 2011, **115**, 3679.
4. A. Huijser, T. J. Savenije, A. Kotlewski, S. J. Picken, and L. D. A. Siebbeles, *Adv. Mater.*, 2006, **18**, 2234.
5. C.-L. Wang, W.-B. Zhang, R. M. Van Horn, Y. Tu, X. Gong, S. Z. D. Cheng, Y. Sun, M. Tong, J. Seo, B. B. Y. Hsu, and A. J. Heeger, *Adv. Mater.*, 2011, **23**, 2951.
6. Z. Liu, A. a Yasser, J. S. Lindsey, and D. F. Bocian, *Science*, 2003, **302**, 1543.
7. M. O. Senge, M. Fazezas, E. G. A. Notaras, W. J. Blau, M. Zawadzka, O. B. Locos, and E. M. Ni Mhuircheartaigh, *Adv. Mater.*, 2007, **19**, 2737.
8. M. H. Hoang, Y. Kim, M. Kim, K. H. Kim, T. W. Lee, D. N. Nguyen, S.-J. Kim, K. Lee, S. J. Lee, and D. H. Choi, *Adv. Mater.*, 2012, **24**, 5363.
9. S.-J. Choi, Y.-C. Lee, M.-L. Seol, J.-H. Ahn, S. Kim, D.-I. Moon, J.-W. Han, S. Mann, J.-W. Yang, and Y.-K. Choi, *Adv. Mater.*, 2011, **23**, 3979.
10. A. Huijser, B. M. J. M. Suijkerbuijk, R. J. M. Klein Gebbink, T. J. Savenije, and L. D. A. Siebbeles, *J. Am. Chem. Soc.*, 2008, **130**, 2485.
11. B. Johnson-White, M. Zeinali, K. M. Shaffer, C. H. Patterson Jr, P. T. Charles, and M. A. Markowitz, *Biosens. Bioelectron.*, 2007, **22**, 1154.
12. S. Tao, G. Li, and H. Zhu, *J. Mater. Chem.*, 2006, **16**, 4521.
13. M. Tonezzer, G. Maggioni, and E. Dalcanale, *J. Mater. Chem.*, 2012, **22**, 5647.
14. T. H. Richardson, R. A. Brook, F. Davis, and C. A. Hunter, *Colloids Surf., A*, 2006, **284-285**, 320.
15. O. Worsfold, C. M. Dooling, T. H. Richardson, M. O. Vysotsky, R. Tregonning, C. A. Hunter, and C. Malins, *Colloids Surf., A*, 2002, **200**, 859.
16. N. A. Rakow and K. S. Suslick, *Nature*, 2000, **406**, 710.
17. A. D. F. Dunbar, S. Brittle, T. H. Richardson, J. Hutchinson, C. A. Hunter, D. Building, B. Hill, and S. Sheffield, *J. Phys. Chem. B*, 2010, 11697.
18. S. a. Brittle, T. H. Richardson, A. D. F. Dunbar, S. M. Turega, and C. a. Hunter, *J. Mater. Chem.*, 2011, **21**, 4882.
19. C. Di Natale, D. Salimbeni, R. Paolesse, A. Macagnano, and A. D’Amico, *Sens. Actuators, B*, 2000, **65**, 220.
20. S. H. Lim, L. Feng, J. W. Kemling, C. J. Musto, and K. S. Suslick, *Nat. Chem.*, 2009, **1**, 562.
21. M. Tonezzer, G. Maggioni, A. Quaranta, S. Carturan, and G. Della Mea, *Sens. Actuators, B*, 2009, **136**, 290.

22. M. Tonezzer, A. Quaranta, G. Maggioni, S. Carturan, and G. Della Mea, *Sens. Actuators, B*, 2007, **122**, 620.
23. S. Kladsomboon and T. Kerdcharoen, *Anal. Chim. Acta*, 2012, **757**, 75.
24. D. Delmarre and C. Bied-Charreton, *Sens. Actuators, B*, 2000, **62**, 136.
25. W. Qin, P. Parzuchowski, W. Zhang, and M. E. Meyerhoff, *Anal. Chem.*, 2003, **75**, 332.
26. J. Spadavecchia, R. Rella, P. Siciliano, M. G. Manera, and A. Alimelli, *Sens. Actuators, B*, 2006, **115**, 12.
27. F. A. Nwachukwu and M. G. Baron, *Sens. Actuators, B*, 2003, **90**, 276.
28. N. A. Rakow, A. Sen, M. C. Janzen, J. B. Ponder, and K. S. Suslick, *Angew. Chem., Int. Ed.*, 2005, **44**, 4528.
29. M. T. Veciana-Nogués, A. Mariné-Font, and M. C. Vidal-Carou, *J. Agric. Food Chem.*, 1997, **45**, 2036.
30. C. Balamatsia, A. Patsias, M. Kontominas, and I. Savvaidis, *Food Chem.*, 2007, **104**, 1622.
31. Y. Xu, W. Xia, and J. M. Kim, *Int. J. Food Sci. Technol.*, 2009, **44**, 1547.
32. J. P. Kerry, M. N. O'Grady, and S. A. Hogan, *Meat Sci.*, 2006, **74**, 113.
33. T. H. Richardson, C. M. Dooling, L. T. Jones, and R. A. Brook, *Adv. Colloid Interface Sci.*, 2005, **116**, 81.
34. C. M. Dooling, O. Worsfold, T. H. Richardson, R. Tregonning, M. O. Vysotsky, C. A. Hunter, K. Kato, K. Shinbo, and F. Kaneko, *J. Mater. Chem.*, 2001, **11**, 392.
35. A. D. F. Dunbar, T. H. Richardson, J. Hutchinson, and C. A. Hunter, *Sens. Actuators, B*, 2008, **128**, 468.
36. A. A. Vaughan, M. G. Baronb, and R. Narayanaswamy, *Anal. Commun.*, 1996, **33**, 393.
37. P. Heyse, R. Dams, S. Paulussen, K. Houthoofd, K. Janssen, P. a. Jacobs, and B. F. Sels, *Plasma Processes Polym.*, 2007, **4**, 145.
38. C. Tendero, C. Tixier, P. Tristant, J. Desmaison, and P. Leprince, *Spectrochim. Acta B*, 2006, **61**, 2.
39. R. Prat, Y. . Koh, Y. Babukutty, M. Kogoma, S. Okazaki, and M. Kodama, *Polymer*, 2000, **41**, 7355.
40. N. D. Boscher, P. Choquet, D. Duday, and S. Verdier, *Plasma Processes Polym.*, 2010, **7**, 163.
41. N. D. Boscher, P. Choquet, D. Duday, and S. Verdier, *Surf. Coat. Technol.*, 2011, **205**, 5350.
42. U. Kogelschatz, *Plasma Chem. Plasma Process.*, 2003, **23**, 1.
43. N. D. Boscher, P. Choquet, D. Duday, N. Kerbellec, J.-C. Lambrechts, and R. R. Maurau, *J. Mater. Chem.*, 2011, **21**, 18959.
44. J. Bardon, J. Bour, D. Del Frari, C. Arnoult, and D. Ruch, *Plasma Processes Polym.*, 2009, **6**, S655.
45. P. Heyse, A. Van Hoeck, M. B. J. Roeffaers, J.-P. Raffin, A. Steinbüchel, T. Stöveken, J. Lammertyn, P. Verboven, P. A. Jacobs, J. Hofkens, S. Paulussen, and B. F. Sels, *Plasma Processes Polym.*, 2011, **8**, 965.
46. N. D. Boscher, D. Duday, P. Heier, K. Heinze, F. Hilt, and P. Choquet, *Surf. Coat. Technol.*, 2013, **234**, 48.
47. N. D. Boscher, D. Duday, P. Heier, K. Heinze, F. Hilt, and P. Choquet, *Plasma Processes Polym.*, 2013, **10**, 336.
48. N. D. Boscher, T. Bohn, P. Heier, F. Moisy, B. Untereiner, K. Heinze, and P. Choquet, *Sens. Actuators, B*, 2014, **191**, 553..
49. P. Heier, C. Förster, D. Schollmeyer, N. Boscher, P. Choquet, and K. Heinze, *Dalton Trans.*, 2013, **42**, 906.
50. D. A. Summerville, R. D. Jones, B. M. Hoffmann, and F. Basolo, *J. Am. Chem. Soc.*, 1977, **99**, 8195.
51. N. D. Boscher, P. Choquet, D. Duday, and S. Verdier, *Surf. Coat. Technol.*, 2010, **205**, 2438.
52. M. Gouterman, L. K. Hanson, G.-E. Khalil, W. R. Leenstra, and J. W. Buchler, *J. Chem. Phys.*, 1975, **62**, 2343.

3.6

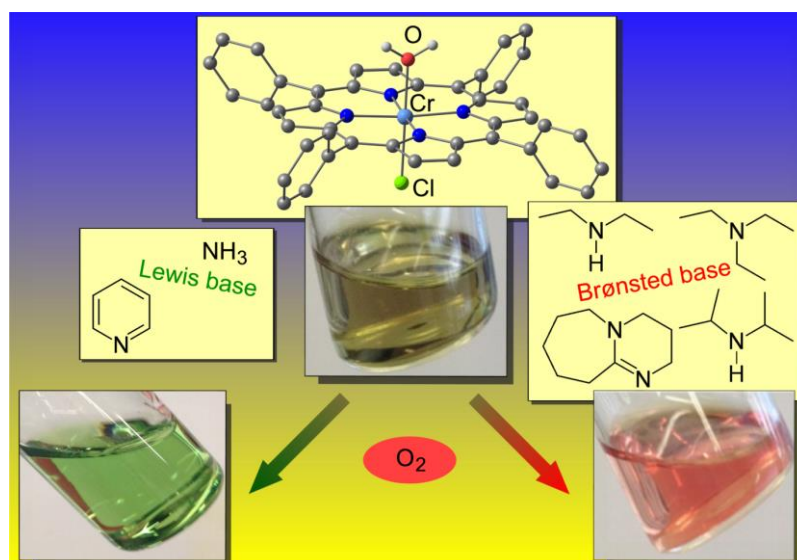
Dual Application of (Aqua)(Chlorido)(Porphyrinato)Chromium(III) as Hypersensitive Amine-Triggered ON Switch and for Dioxygen Activation


P. Heier, N. Boscher, K. Heinze, P. Choquet

submitted

Abstract

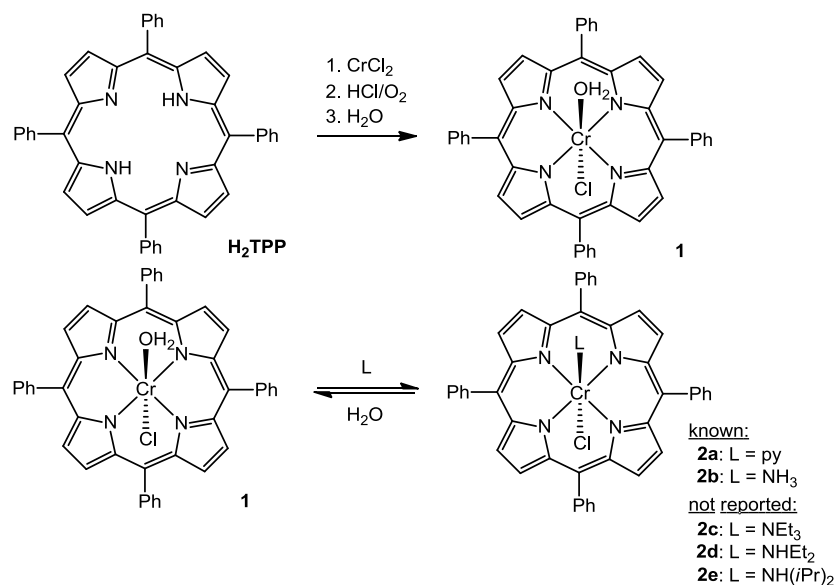
Although synthesis and substitution reactions of chlorido chromium(III) porphyrins $\text{Cr}^{\text{III}}(\text{TPP})(\text{Cl})(\text{L})$ (H_2TPP = 5,10,15,20-tetraphenyl porphyrin, L = pyridine, H_2O , ROH , ...) are well established in coordination chemistry for decades an unexpected dichotomous reactivity of $\text{Cr}^{\text{III}}(\text{TPP})(\text{Cl})(\text{H}_2\text{O})$ (**1**) towards amines is disclosed here. This reactivity leads to the application of **1** as highly sensitive substoichiometric and irreversible ON switch for amine detection by an autocatalytic pathway. The concomitant activation of O_2 by the **1**/amine system is furthermore exploited in an electrochemically driven epoxidation of norbornene using O_2 as initial oxidant.



Supplementary Information can be found at pp. 205 – 213 

Introduction

Chromium porphyrins were introduced in 1966 by Tsutsui and co-workers with the synthesis of chromium(II) and chromium(III) mesoporphyrin IX dimethyl ester.^{1,2} Shortly after, the preparation of chromium *meso*-tetraphenyl porphyrins from H₂TPP and CrCl₂ in DMF was reported by Adler *et al.* (Scheme 1)³ and an optimized aqueous purification procedure was subsequently developed by Summerville *et al.* in 1977.⁴



Scheme 1 Synthesis and reactivity of **1**.

The initially formed chromium(III) porphyrin complex is considered to be the five-coordinate Cr^{III}(TPP)(Cl) complex which readily coordinates a sixth ligand L to form the respective stable six-coordinate octahedral Cr^{III}(TPP)(Cl)(L) complexes **2**. Generally, the Cr^{III} ion cannot be easily removed from the porphyrin macrocycle except upon exposure to strong mineral acids.⁵ Members of the Cr^{III}(TPP)(Cl)(L) family have been thoroughly analyzed by cyclic voltametry,^{6–8} EPR,^{4,9} emission^{10,11} and UV/vis spectroscopy.^{4,11,12} All complexes show characteristic porphyrin absorptions with the intense Soret band around 445 – 460 nm and the weaker Q bands around 500 – 610 nm. Chromium(III) porphyrins show additional absorptions in the near-UV as well as in the near-IR region and have been classified as d-type hyper porphyrins.^{11,13} The exact energy of the porphyrins' absorption bands strongly depends on the nature of the sixth ligand L.

As has been shown in 1995, the commonly employed synthetic procedure described by Summerville,⁴ which includes an aqueous work-up, yields the aqua complex Cr^{III}(TPP)(Cl)(H₂O) (**1**).¹⁴ The axial water ligand can easily be substituted by other ligands L such as pyridine or ammonia (Scheme 1, **2a** or **2b**) as axial ligand exchange in chromium(III) porphyrins is reported to be up to 10⁴ times faster compared to other chromium(III) complexes.^{15,16} Substitution by several pyridine derivatives occurs in a dissociative manner via the five-coordinate intermediate Cr^{III}(TPP)(Cl).¹⁷ This

intermediate is also generated photochemically by laser-photolysis which has advanced further kinetic studies.^{14,18,19} Even though a direct comparison of all available studies dealing with thermal or photo-initiated ligand exchange is difficult, a general trend for the affinity of Cr^{III}(TPP)(Cl) towards different donor atoms has been extracted by Hoffman and Basolo which follows the order N >> P > O ≈ S.^{4,5} In the absence of steric restrictions, the affinity of chromium(III) porphyrins towards nitrogen donor ligands increases as the p*K*_b of the ligand decreases.¹² For example, the binding constant of Cr^{III}(TPP)(Cl) for pyridine (p*K*_b = 8.73) in dichloromethane is reported to be $K = 1.9 \times 10^5 \text{ M}^{-1}$ while *sec*-butylamine (p*K*_b = 3.44) binds 3.5 times stronger ($K = 6.6 \times 10^5 \text{ M}^{-1}$).¹² The properties of Cr^{III}(TPP)(Cl)(L) porphyrins **1** and **2** suggest their application as colorimetric amine sensors for the following reasons: a) the complexes show intense absorptions in the visible spectral region which are strongly dependent on the coordinated sixth ligand L; b) they display a very high affinity for nitrogen containing ligands and discriminate them from phosphorous, oxygen and sulfur based ones, and c) in contrast to zinc(II) porphyrins often employed in amine sensing,^{20–24} the Cr^{III}(porphyrinato) core is exceptionally stable towards acidic and basic conditions. Hence, we had developed sensing devices²⁵ for volatile amines based on Cr^{III}(porphyrinato) complexes applicable to the control of food freshness in easy-to-use packaging foils.^{26–28} Interestingly, the employed (aqua)(chlorido)(porphyrinato) chromium(III) complexes feature an unexpected pronounced hypsochromic shift of the Soret and Q bands in the reaction with NEt₃ as a prototypical volatile amine. Furthermore, the reaction with NEt₃ is irreversible, a rather unusual finding for a simple O donor to N donor ligand substitution.^{4,12}

Here we disclose the puzzling reactivity and unusual color change of **1** treated with triethylamine and other *N*-donor ligands in solution. The distinct mechanism, which opens a novel “green” pathway to oxido chromium(IV) porphyrins, is clarified and applications in the fields of amine sensing and aerobic alkene epoxidation²⁹ are discussed.

Results and Discussion

The aqua complex **1** has been prepared according to the literature from CrCl₂ and H₂TPP giving intermediate Cr(TPP) (**3**) and its subsequent aeral oxidation to **1**.^{4,14,19} Its correct formation is corroborated by FD and ESI mass spectrometry ($m/z = 682.18$ [M–Cl]⁺; $m/z = 699.14$ [M–H₂O]⁺; Figure S1). The UV/vis absorption spectrum of **1** in CH₂Cl₂ shown in Figure 1a (black curve) fully conforms to literature data.⁴ The olive-green colored solution exhibits a strong Soret band at 448 nm, Q band absorptions at 563 and 603 nm and a quite prominent ligand-to-metal charge transfer band at 396 nm (Figure 1, inset a). Exposure of this solution to excess pyridine (py) leads to the expected formation of Cr^{III}(TPP)(Cl)(py) (**2a**) and a rather unremarkable color change to grass-green (Figure 1, inset b). This is caused by the expected bathochromic shift of the absorption bands to 458 nm (Soret band) and to 572/610 nm (Q bands), respectively

(Figure 1, dashed green curve). As bathochromic shifts are typically observed for substitutions of oxygen donor ligands by nitrogen donors at chromium(III) porphyrins^{4,12} this observation corresponds well to values reported in the literature for the aqua to pyridine ligand substitution in toluene⁴ or in CH₂Cl₂.¹²

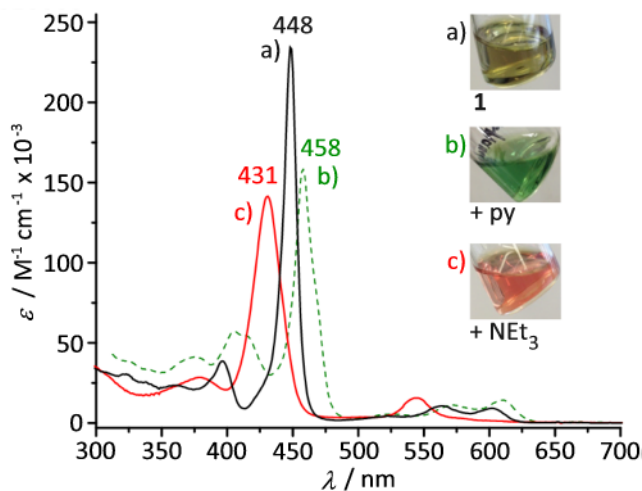
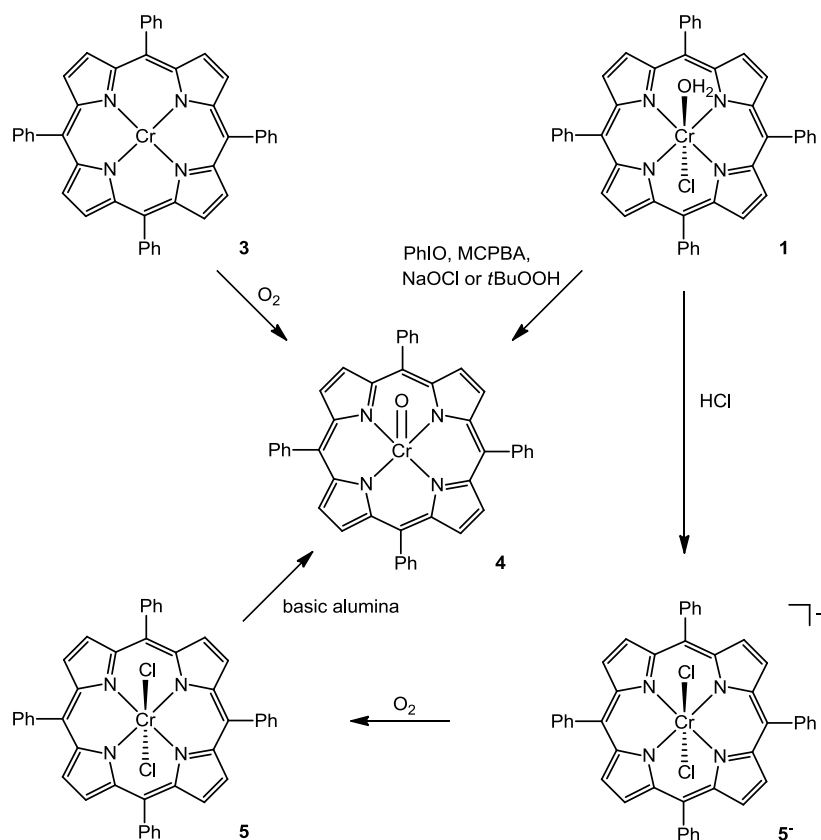


Figure 1 UV/vis absorption spectra in CH₂Cl₂ of a) **1** (black), b) **1** with excess pyridine (dashed green) and c) **1** with excess NEt₃ (red); insets show photographs the respective solutions.

Fully unexpected, a solution of **1** in CH₂Cl₂ turns bright red in the presence of triethylamine. Hypsochromic shifts are observed with the Soret band at 431 nm, the Q band at 544 nm and the LMCT band around 380 nm (Figure 1c). This observation suggests that a different complex is formed instead of the expected substitution product Cr^{III}(TPP)(Cl)(NEt₃) (**2c**) (Scheme 1).

UV/Vis, IR, and ¹H NMR analysis of the resulting red solution clearly suggest that the diamagnetic oxido chromium(IV) complex Cr^{IV}(TPP)(O) (**4**) has been formed quantitatively (Scheme 2; Figures S2 and S3).³⁰⁻³³ The oxido complex **4** has been previously prepared by aerobic oxidation of the chromium(II) complex **3**^{30,32}, by oxygenation of **1** with strong oxygen atom transfer reagents (iodosylbenzene^{31,34,35}, *meta*-chloroperoxybenzoic acid (MCPBA)³⁵, sodium hypochlorite³⁶, *tert*-butyl hydroperoxide³⁴, *p*-cyano-*N,N*-dimethylaniline *N*-oxide/photoexcitation³⁷) and via aerobic oxidation under acidic conditions (HCl) and subsequent basic workup possibly via a dichlorido intermediate **5**⁻ and its porphyrin radical cation complex **5**³⁰ (Scheme 2). To the best of our knowledge, formation of the oxido chromium(IV) complex **4** by amines under ambient conditions (humid air) has not yet been reported. Interestingly, Cr^V(corrolato)(O) complexes have been directly obtained from free-base corrole, Cr(CO)₆ and O₂ showing that corroles stabilize high metal oxidation states.³⁸ The only feasible oxidant in the present reaction scheme **1**/NEt₃ is dioxygen as well. However, as the chromium(III) complex **1** itself is completely inert towards dioxygen the amine obviously activates **1** prior to the oxidation by O₂. As the reaction with O₂



Scheme 2 Known routes to Cr^{IV} complex **4**.

also occurs in the absence of light a photochemical pathway such as found for an (octakis(*p*-*tert*-butylphenyl)-corrolazinato)manganese(III) complex³⁹ is excluded.

A possible first route requires an initial reduction of Cr^{III} to Cr^{II} (**3**) by the amine and further reaction of the Cr^{II} complex **3** with O₂ corresponding to a reductive activation by electron transfer. A second possible pathway occurs via a hydroxido complex [Cr^{III}(TPP)(OH)(Cl)]⁻ (**6**⁻) obtained by proton transfer. In order to observe the initially formed active species in this complex reaction scheme **1** → **4** we first investigated the reaction of **1** with NEt₃ in the absence of dioxygen.

Reaction of **1** with NEt₃ in the absence of dioxygen.

Chromium(III) porphyrin **1** is treated with 0.5 eq, 1.0 eq or excess NEt₃ in CH₂Cl₂ under exclusion of O₂ and the respective UV/vis spectra are depicted in Figure 2.

The absorption bands of **1** are replaced by new bands at higher energies, their intensities being proportional to the amount of added NEt₃ with a quantitative conversion accomplished with one equivalent NEt₃. Excess NEt₃ does not further change the spectrum. The charge transfer band around 396 nm is diminished, the Soret band is shifted from 448 to 435 nm and the Q bands are shifted from 563 to 557 nm and from 603 to 596 nm, respectively. These spectral data differ from that of **4** and pyridine complex **2a** suggesting neither oxidation of **1**, nor substitution of the H₂O

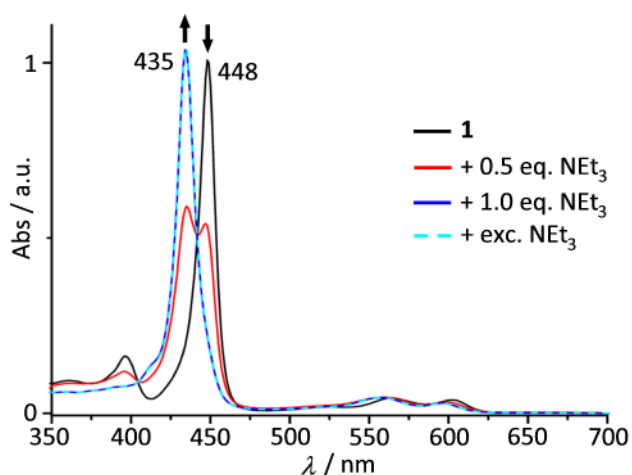


Figure 2 UV/vis absorption spectra of **1** in CH₂Cl₂ under Ar atmosphere; a) **1** (black, solid) and after the addition of b) 0.5 eq NEt₃ (red, solid), c) 1.0 eq NEt₃ (dark blue, solid) and d) exc. NEt₃ (light blue, dashed).

ligand by NEt₃. Isosbestic points at 404, 442 and 562 nm indicate a clean reaction without observable intermediates. A similar spectral behavior of chromium(III) porphyrins has been described in the literature for the substitution of a chlorido ligand by an alkoxido ligand.⁴⁰ In the present case this either indicates deprotonation of the aqua ligand by NEt₃ giving [Cr^{III}(TPP)(OH)(Cl)]⁻ (**6**⁻) and subsequent substitution of the chlorido ligand by H₂O to form Cr^{III}(TPP)(OH)(H₂O) (**7**)⁴¹ or direct substitution of the chlorido ligand of **1** by hydroxide (**7**). The latter reaction might be less favorable as the aqua ligand in **1** is only weakly *trans*-activating. The formation of hydroxido complexes (**6**⁻, **7**) is further supported by the reaction of **1** with LiOH. Treatment of **1** with a deoxygenated solution of LiOH in CH₂Cl₂ results in exactly the same absorption spectrum as the addition of NEt₃ does (Figure 3). Subsequent exposure of both solutions to air results in the slow formation of **4**.

No Cr^{II}(TPP) intermediate **3** with its characteristic Soret band at 420 nm^{42,43} is observed by UV/Vis spectroscopy after addition of NEt₃ or OH⁻ to **1**. Attempts to chemically reduce the aqua complex **1** to **3** by one equivalent of decamethylcobaltocene CoCp^{*}₂ ($E_{1/2} = -1.94$ V in CH₂Cl₂ vs. ferrocene/ferrocenium)⁴⁴ only resulted in the formation of **6**⁻/**7** instead of Cr^{II}(TPP) as seen from the absorption spectrum in Figure 3 (dotted green curve; minor differences in the near UV part region result from [CoCp^{*}₂]⁺ absorptions). We ascribe this observation to proton reduction by CoCp^{*}₂⁴⁵ resulting in a net deprotonation of **1** as observed for the reactions of **1** with NEt₃ or with OH⁻. Hence, a reductively initiated pathway via **3** seems unlikely. Furthermore, the redox potential of NEt₃ ($E_{1/2} = 0.47$ V in CH₃CN vs. ferrocene/ferrocenium)⁴⁴ is insufficient to reduce **1** ($E_p = -1.33$ V; irrev.; Cr^{III} → Cr^{II}). In fact, the cyclic and square wave voltammetric data confirm that the Cr^{III} → Cr^{II} reduction is even more difficult in the presence of LiOH ($E_p = -1.54$ V; irrev.; Cr^{III} → Cr^{II}) (Figure S4). This is in good agreement with the proposed formation of hydroxido complexes **6**⁻ and/or **7**. The assignment is

furthermore consistent with results published for $\text{Cr}^{\text{III}}(\text{OEP})(\text{Cl})$ complexes (OEP = octaethylporphyrin) showing a 0.26 V shift by chlorido to hydroxido substitution in DMSO.^{6,34} First and second reversible oxidations to the porphyrin radical cation and the porphyrin dication are slightly affected by the presence of LiOH (Figure S4). The first wave shifts from 0.44 V to 0.41 V and the second one from 0.93 to 0.91 V. A weak wave around 0.17 V is assigned to the oxidation of chloride ($E_{1/2} = 0.18$ V in CH_3CN vs. ferrocene/ferrocenium)⁴⁴. In summary all spectroscopic evidence point to the presence of hydroxido complexes **6**⁻ and/or **7** in the presence of NEt_3 or LiOH under anaerobic conditions.

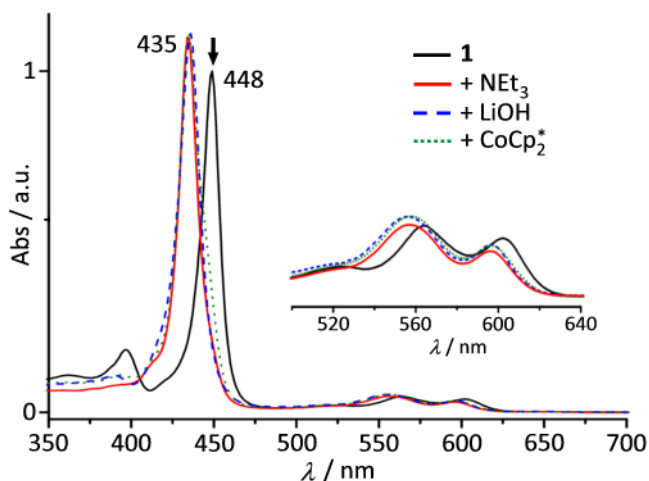


Figure 3 UV/vis absorption spectra in CH_2Cl_2 under Ar atmosphere of a) **1** (solid black curve), b) **1** with 1 eq NEt_3 (solid red curve), c) **1** with exc. LiOH (dashed blue curve) and d) **1** with 1 eq. CoCp_2^* (dotted green curve). The inset shows magnifications of the Q band region.

DFT studies on the reaction of **1** with NEt_3 .

The conceivable reaction products of **1** with NEt_3 have been studied by density functional calculations (B3LYP, LANL2DZ, iefpcm model for CH_2Cl_2 ; Figure 4)⁴⁷ and selected metrical data are summarized in Table 1. Substitution of the aqua ligand by NEt_3 to give **2c** is calculated to be thermodynamically disfavored by 74 kJ mol^{-1} (Figure 4, Table 1). The normal coordinate analysis of the porphyrin deformation (NSD)⁴⁸ and the derived total out-of-plane distortion D_{oop} of the porphyrin clearly reveal a rather strong distortion of the porphyrin due to the NEt_3 coordination. This is also reflected in the out-of-plane displacement of the chromium towards the amine (Table 1). All these distortions imposed by the steric bulk might account for the low stability of the NEt_3 complex **2c**.

On the other hand, attack of NEt_3 at the aqua ligand of **1** gives the hydroxido complex **6**⁻ with an asymmetric hydrogen bond to the ammonium ion, hence a hydrogen-bonded contact ion pair $[\text{HNEt}_3^+][\text{6}^-]$ is formed (Figure 4). This proton transfer is thermodynamically favorable by 6 kJ mol^{-1} . Almost isoenergetic to hydrogen-bonded **6**⁻

is the neutral (aqua)(hydroxido)chromium(III) complex **7** and triethylammonium chloride (Figure 4). Complex **7** might be easily formed from **6⁻** due to the stronger *trans*-influence of OH⁻ (**6⁻**: Cr-Cl 2.47 Å) as compared to H₂O (**1**: Cr-Cl 2.39 Å) labilizing the Cr-Cl bond. Hence, both complexes **6⁻** and **7** should be in equilibrium in alkaline solution. Especially the anionic complex **6⁻** might be susceptible towards oxidation by O₂ similar to the reactivity of the proposed dichlorido intermediate **5⁻**.³⁰ Formation of electron-rich anionic Cr^{III} complexes is thus likely the key factor for the oxidation of **1** with dioxygen as no reaction **1** with O₂ is observed in the absence of OH⁻ or Cl⁻.

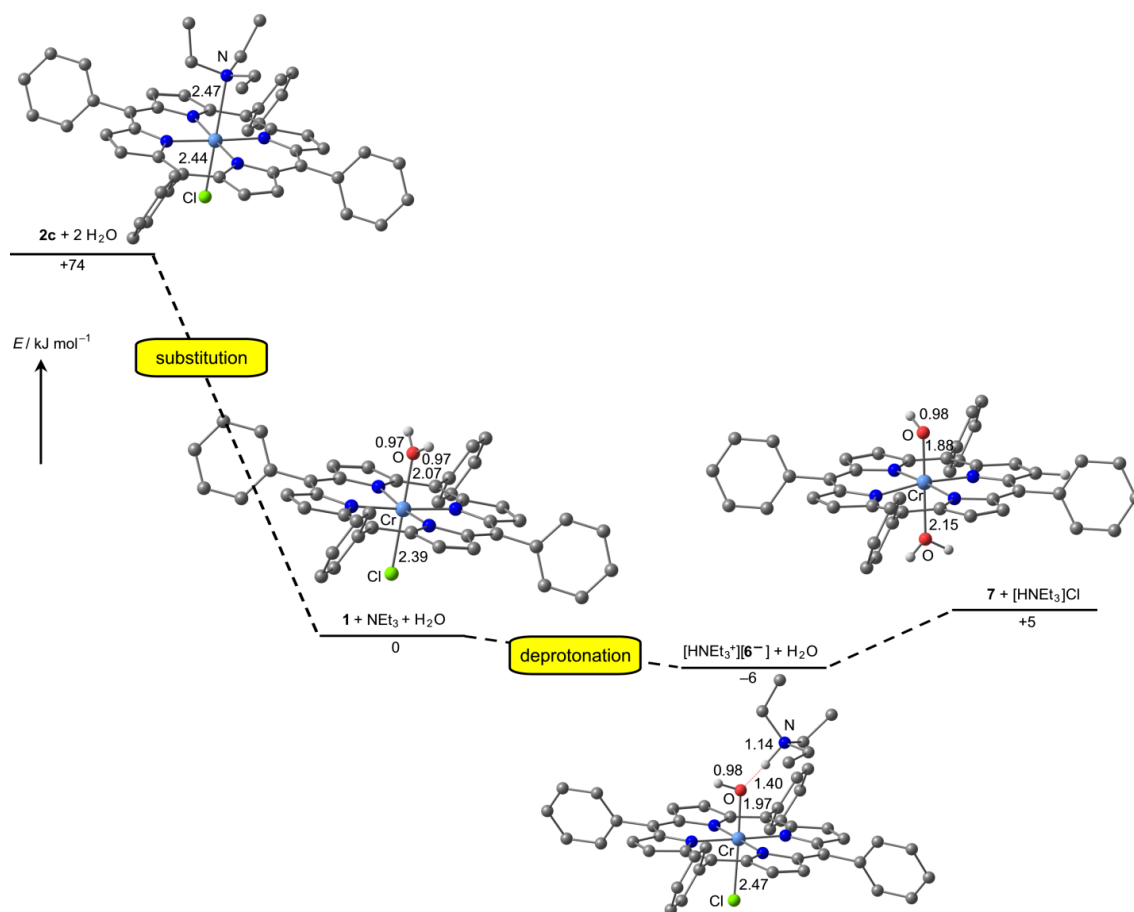


Figure 4 DFT (B3LYP, LANL2DZ, iefpcm model for CH₂Cl₂) optimized structures and relative thermal energies of **1**+NEt₃+H₂O; **2c**+2H₂O, [HNEt₃⁺][**6⁻**]+H₂O, and **7**+HNEt₃Cl. CH hydrogen atoms are omitted for clarity. Distances are given in Å; energies in kJ mol⁻¹.

Table 1 Selected bond lengths [Å] and angles [deg] of **1** in the solid state¹⁴ and as derived from DFT calculations (B3LYP, LANL2DZ, iefpcm model for CH₂Cl₂) for **1**+NEt₃+H₂O, [HNEt₃][6⁻]+H₂O, **7**+[HNEt₃]Cl and **2c**+2H₂O.

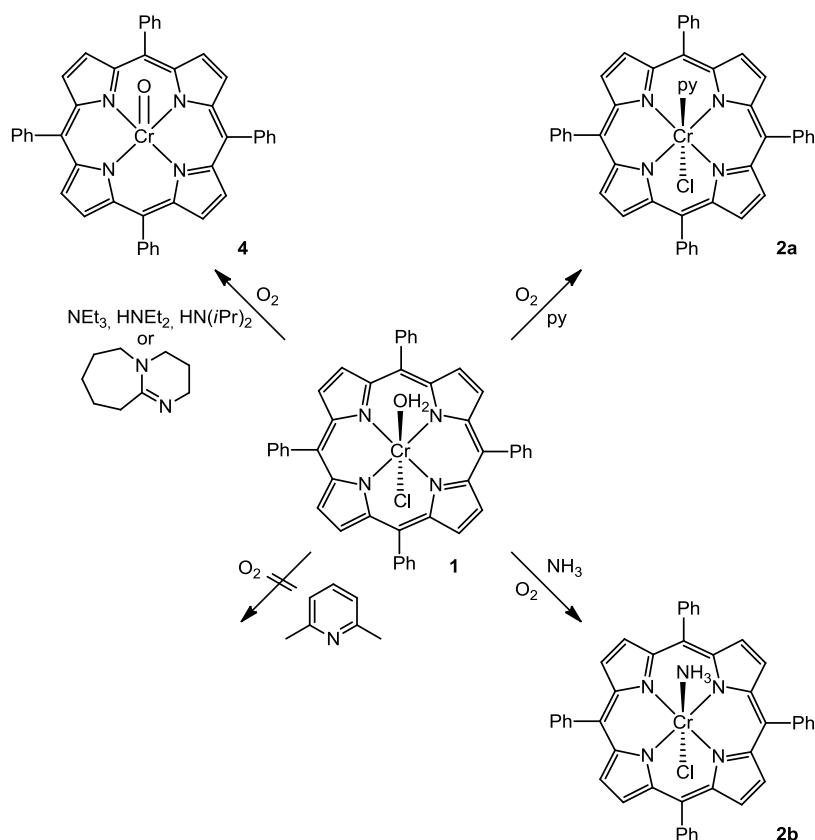
	1 (XRD)	1 (DFT)	[HNEt ₃][6 ⁻] ^b	7	2c
	X = Cl	X = Cl	X = Cl	X = OH	X = Cl
	L = H ₂ O	L = H ₂ O	L = HO...H	L = H ₂ O	L = NEt ₃
Cr-X	2.242(3)	2.388	2.474	1.883	2.436
Cr-L	2.239(3)	2.066	1.967	2.148	2.471
Cr-N(porph)	2.031(2)	2.051	2.057	2.060	2.049
O-H		0.974/0.974	0.978/1.396	0.981	
H-N			1.144		
X-Cr-L	180.0	179.9	178.1	179.3	178.1
X-Cr-N(porph) ^b	89.0(1)	92.3	90.0	93.2	89.0
L-Cr-N(porph) ^b	91.0(1)	87.7	90.0	86.8	91.0
out-of-plane distance Cr-porph	0.035 to X	0.073 to X	0.018 to L	0.109 to X	0.119 to L
<i>D</i> _{oop} ^c		0.1316	0.1608	0.1504	0.4638
<i>E</i> / kJ mol ⁻¹		0	-6	+5	+74

^a From ref. 14; ^b values averaged for the four nitrogen atoms of the porphyrin; ^c total out-of-plane distortions as obtained from normal structural decomposition (NSD)⁴⁸ analysis.

Reaction of **1** with other nitrogenous bases.

As the results presented so far indicate that H₂O ligand substitution does not occur at **1** with NEt₃ but that NEt₃ acts as a Brønsted base instead, different nitrogen-based ligands of different basicity and steric demand were investigated. The results are compiled in Scheme 3.

The weak base pyridine ($pK_b = 8.7^{49a}$) substitutes the aqua ligand to give the pyridine complex **2a**.¹² Similarly, ammonia ($pK_b = 4.8^{49b}$) yields the respective green ammine complex **2b** by ligand substitution (Figure S5). The stronger bases NEt₃ ($pK_b = 3.2^{50}$), HNEt₂ ($pK_b = 3.0^{50}$) and HN(*i*Pr)₂ ($pK_b = 2.9^{50}$) finally yield the red oxido chromium(IV) complex **4**. The same observation holds for the weakly coordinating but strong base DBU (1,8-diazabicyclo[5.4.0]undec-7-ene, $pK_b = 2.0^{50}$). On the other hand sterically demanding 2,6-lutidine ($pK_b = 7.2^{49a}$) is neither competent to substitute nor to deprotonate the aqua ligand. As *sec*-butylamine ($pK_b = 3.44$) has been reported to coordinate to Cr^{III}¹² a clear reactivity borderline between ligand deprotonation (Brønsted acid/base reaction; $pK_b \leq 3.2$) and ligand substitution is obvious (Lewis acid/base reaction; $pK_b \geq 3.4$).



Scheme 3 Dichotomous reactivity of **1** with potential N ligands under ambient conditions (py = pyridine).

Reactions of $\text{Cr}^{\text{III}}(\text{TPP})(\text{Cl})(\text{THF})$ (**8**).

To strengthen the conclusion that deprotonation of the aqua ligand in **1** is the key step in the conversion of **1** to **4** initiated by NEt_3 water-free $\text{Cr}^{\text{III}}(\text{TPP})(\text{Cl})(\text{THF})$ (**8**) was treated with NEt_3 . The THF complex **8** has been prepared by dissolving **1** in THF and drying the solution with CaCl_2 . The spectral data of **8** are in full accordance with literature values (Figure S6).⁴ Treating **8** with excess NEt_3 in THF under exclusion of dioxygen and water does not give any spectral changes (Figure S6). Obviously NEt_3 is unable to replace thf in **8** to give **2c** in the presence of excess THF and even in anhydrous CH_2Cl_2 . Dissolving **8** in CH_2Cl_2 under humid air and addition of NEt_3 forms **4** albeit much slower than in the reaction starting from **1**. Likely, the aqua complex **1** or the hydroxido complexes **6**⁻/**7** have to be formed first from **8**.

Reaction of **1** with sub-stoichiometric amounts of NEt_3 .

All results described above have been achieved using an excess of strong bases. This leads to a rapid conversion of **1** to **4** within minutes with a stable (irreversible) absorption shift. The distinct absorption changes, which are clearly visible to the naked eye (Figure 1) had suggested the use of **1** incorporated in a porous matrix²⁶⁻²⁸ as a colorimetric sensor for basic volatile amines^{21-24,50} for the control of food freshness⁵¹⁻⁵³.

In order to determine the detection limit **1** was treated with stoichiometric and sub-stoichiometric amounts of NEt_3 .

Figure 5a shows the temporal evolution of the UV/vis spectra of a solution of **1** in CH_2Cl_2 after addition of one equivalent NEt_3 . Under these conditions quantitative conversion of **1** to **4** is achieved in 60 – 90 min (red line). No isosbestic points are found indicating the accumulation of intermediates. This is in good agreement with the deprotonation/oxidation pathway described above. **1** is initially deprotonated by NEt_3 to form intermediate hydroxido complexes **6**⁻ / **7** ($\lambda_{\text{Soret}} = 435 \text{ nm}$) which are subsequently oxidized by O_2 to the final product **4** ($\lambda_{\text{Soret}} = 431 \text{ nm}$). Unexpectedly, addition of 0.1 equivalents of NEt_3 also lead to a quantitative conversion to **4** as shown in Figure 5b although this reaction is only completed after 14 hours. For ease of comparison, the 90 min spectrum of this reaction still showing the presence of residual starting material is also plotted in Figure 5b (red curve).

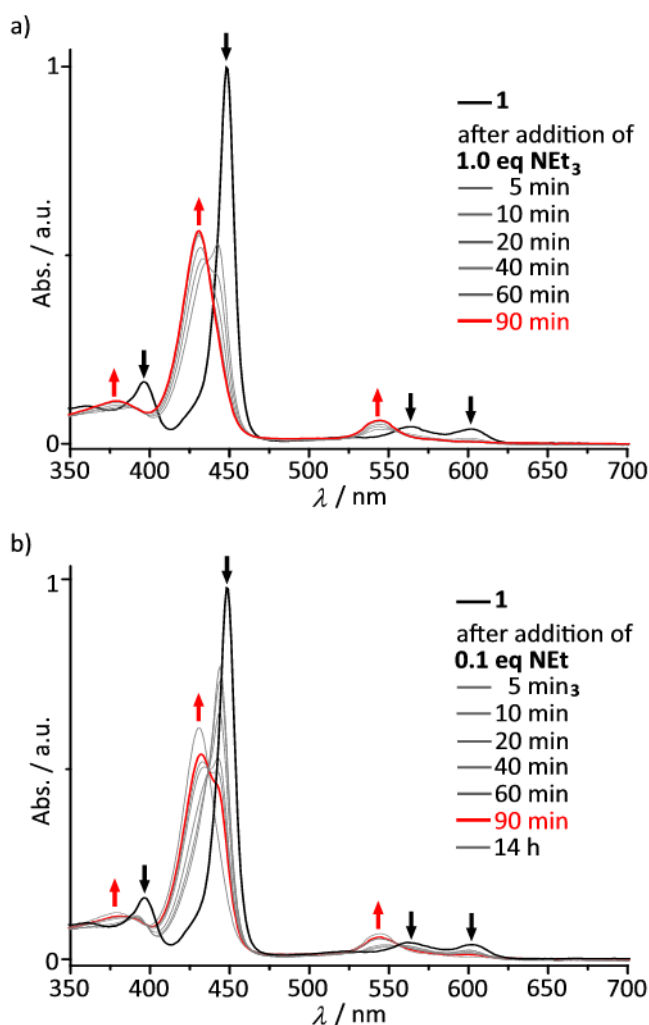


Figure 5 Temporal evolution of UV/vis absorption spectra of **1** in CH_2Cl_2 after addition of a) 1.0 eq. NEt_3 and b) 0.1 eq. NEt_3 . Red curves represent spectra after 90 min.

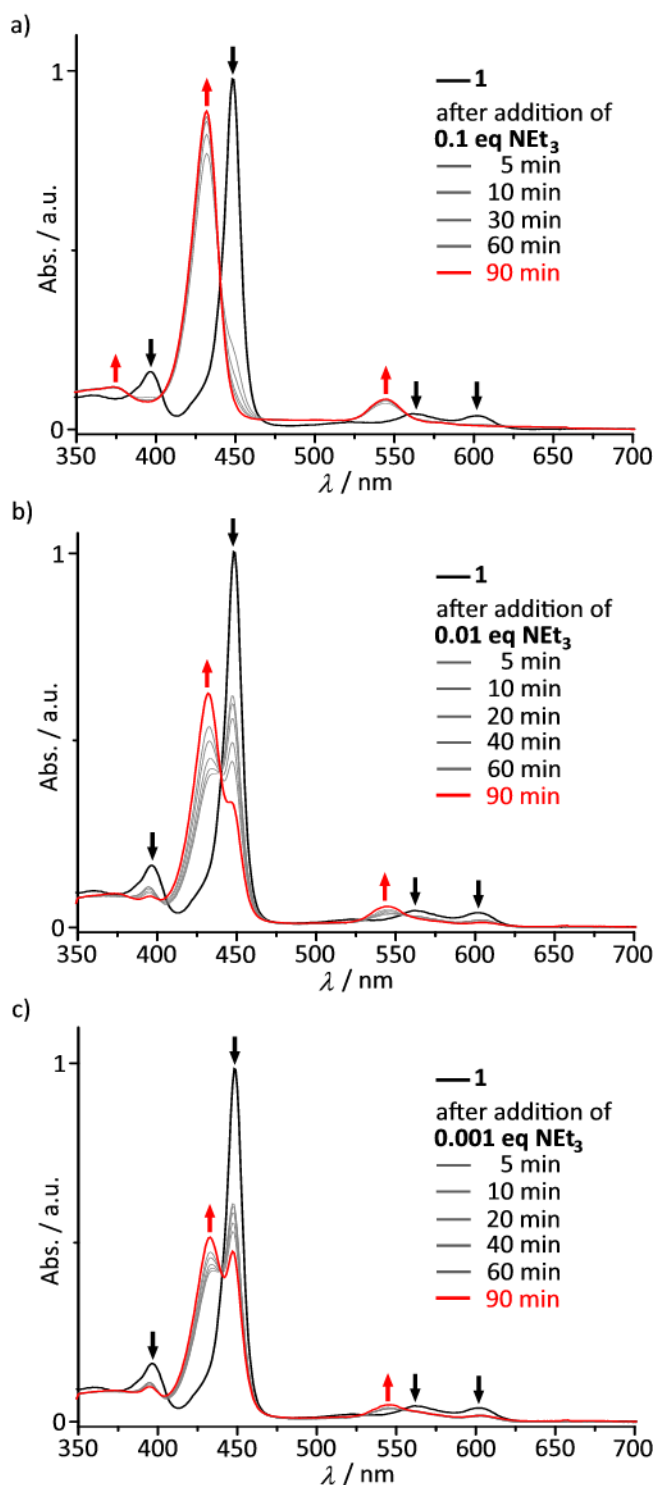


Figure 6 Temporal evolution of UV/vis absorption spectra of **1** in toluene after addition of a) 0.1 eq. NEt_3 , b) 0.01 eq. NEt_3 and c) 0.001 eq. NEt_3 . Red curves represent spectra after 90 min.

The rate of the conversion of **1** to **4** depends on the solvent used. Reactions in non-polar toluene (Figure 6a) are much faster as compared to reactions in more polar CH_2Cl_2 solutions (Figure 5b). As O_2 solubility is similar in both solvents⁵⁴ a simple

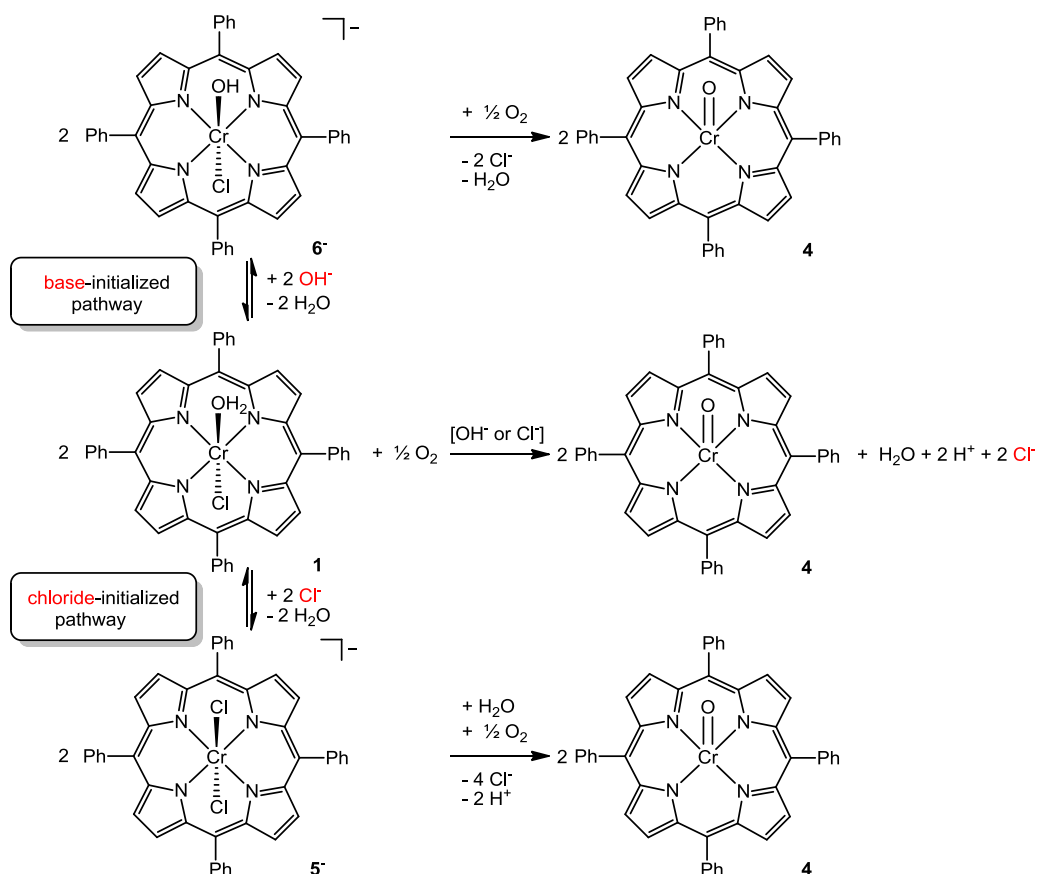
concentration effect is not responsible. In toluene the reaction of **1** with 0.1 equivalents of NEt_3 is already completed within 90 min instead of the 14 h required in CH_2Cl_2 . Clean isosbestic points are observed in the UV/Vis spectra for the reaction in toluene at 440 and 556 nm (Figure 6a). This indicates that the intermediate (presumably $\mathbf{6}^- / \mathbf{7}$) does not accumulate in toluene but is rapidly oxidized by O_2 .

As the reaction of **1** with 0.1 equivalents of NEt_3 in toluene is quantitative within a reasonable amount of time studies with even less amounts of NEt_3 have been performed in toluene solution. Addition of 0.01 and 0.001 eq. of NEt_3 also lead to a distinct absorption change after 90 min as depicted in Figures 6b and 6c. In both cases conversion to **4** is not yet quantitative after 90 min, but obviously significantly larger than 1% or 0.1%, respectively, as would be expected for a stoichiometric reaction of **1** with NEt_3 to give **4**. From the spectra depicted in Figure 6b and 6c conversions of 79% and 63% (based on **1**) after 90 min are determined for the reaction of **1** with 0.01 and 0.001 equivalents of NEt_3 , respectively.

To interpret this observation we take a closer look at the net reaction of **1** to **4** (Scheme 4, center). The initial step is the deprotonation of **1** to the intermediate $\mathbf{6}^-$ (Scheme 4, base-initialized pathway) which is subsequently oxidized to **4** by O_2 . In the net reaction one chloride ion and one proton per chromium(III) porphyrin **1** is released apart from H_2O formation (Scheme 4, center). From the literature it is known that HCl can induce the autooxidation of **1** to **4** presumably via the dichlorido complex $\mathbf{5}^-$ (Scheme 4, chloride-initiated pathway).³⁰ Hence, only a small amount of base (either strong nitrogenous bases or LiOH) is initially required as one of the products, namely the chloride ion, also induces the transformation. This amplification by a product is a typical autocatalytic process.

To confirm the proposed chloride effect, a solution of **1** in CH_2Cl_2 was treated with excess LiCl. Analysis of the resulting UV/vis spectra over time shows, that **1** is indeed slowly converted to **4** under these conditions indicating the formation of the dichlorido complex $\mathbf{5}^-$ which is subsequently oxidized to **4** (Figure S7). This result confirms the chloride-initiated pathway from **1** to **4** depicted in the lower part of Scheme 4. Combination of both pathways explains the hyper-stoichiometric conversion observed with respect to NEt_3 . The initially inert chromium(III) complex **1** is deprotonated by the amine generating the reactive intermediate $\mathbf{6}^-$ which is oxidized by dioxygen to give **4** and chloride. During that reaction the base is consumed but chloride accumulates stoichiometrically opening a second activation pathway of **1** via the formation of $\mathbf{5}^-$. This autocatalytic reaction finally results in a slow, yet full conversion of **1** to **4**.

The kinetic traces suggest that the base-initialized pathway via $\mathbf{6}^-$ (early stages) proceeds faster than the chloride-initialized pathway via $\mathbf{5}^-$ (later stages, Figure 7). The slower reaction via intermediate $\mathbf{5}^-$ can either be ascribed to a less favorable activation of **1** to form of $\mathbf{5}^-$ or a slower reaction of $\mathbf{5}^-$ with O_2 .



Scheme 4 Reaction pathways of inert **1** to **4** via anionic intermediate **5⁻** or **6⁻**.

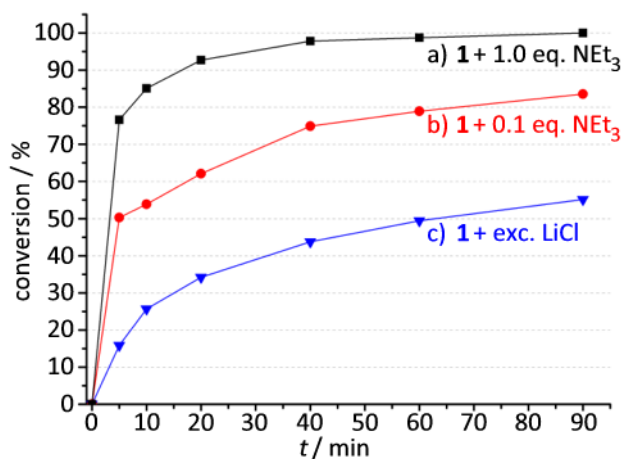


Figure 7 Kinetic traces of a) **1** and 1 eq. NEt₃ in CH₂Cl₂ (black), b) **1** and 0.1 eq. NEt₃ in CH₂Cl₂ (red) and c) **1** and exc. LiCl in CH₂Cl₂ (blue) under ambient conditions.

Colorimetric amine sensing with **1**.

As **1** switches the color from green to red (Figure 1) upon exposure to nitrogenous bases with $\text{p}K_b \leq 3.2$ or hydroxide complex **1** can be used as a simple colorimetric base indicator. Yet it shows distinct features distinguishing **1** from conventional colorimetric pH-indicators. On the one hand the color change is irreversible. The initially reversibly

formed species $6^- / 7$ are subsequently oxidized irreversibly to form **4** which is responsible for the observed red color. On the other hand even sub-stoichiometric amounts of bases are detected with a full color change of the sensor, as the reaction is autocatalytically driven to completion by the released chloride (although slower). Sensor systems based on **1** can therefore be advantageously used for sensing applications which require a highly sensitive (amplified) ON response towards an analyte rather than quantification of the analyte via reversible binding.⁵⁵ Possible applications are the detection of toxic amine release into the environment or amine detection for the control of food freshness.⁵¹⁻⁵³ Because the detection event is easily visible to the human eye with its irreversible color change from green to red (Figure 1), the use of **1** or its derivatives leads to simple but powerful sensing devices.²⁶⁻²⁸ As the chromium porphyrin chromophores can be successfully embedded in a suitable matrix²⁶⁻²⁸ for gas sensing devices, false positive signals resulting from adventitious Cl^- or OH^- are avoided and only strong volatile amines will trigger the sensor to the ON state.

Dioxygen activation with **1** / base.

As epoxides are extremely valuable building blocks in synthetic organic chemistry a variety of protocols have been developed for the production of epoxides from olefins.²⁹ Essentially all protocols use oxidants such as hydroperoxides, peracids, hypochlorite or iodosylbenzene.²⁹ Notable exceptions are the industrial aerobic epoxidation of ethane to ethylene oxide by an Al_2O_3 supported silver catalyst⁵⁶ and the aerobic epoxidation of olefins by $Ru^{VI}(\text{porphyrinato})(O)_2$ ^{57a,57b}, $Ru(\text{salen})(O)_n$ complexes^{57c} and a $Ru^{IV}(6,6'-(\text{SePh})-2,2'\text{-bpy})_2(O)_2$ complex⁵⁸ as well as a recently reported MOF based on $Mn(\text{salen})$ complexes.⁵⁹

Epoxidation of olefins starting from **1** and MCPBA or iodosylbenzene/pentafluoro iodosylbenzene^{34,60} as well as an electrochemically driven epoxidation using **4**^{61,62} have been described before. In all cases reactive high-valent $[Cr^V(\text{TPP})(O)]^+$ species (**4**⁺) are believed to be involved, although epoxidations with oxido chromium(V) complexes (in the gas-phase) are shown to be formally spin-forbidden due to the different spin states of $d^1\text{-Cr}^V$ (doublet) and $d^3\text{-Cr}^{III}$ (quartet).⁶³

We now have a clean pathway from **1** to **4** at hand by activation of **1** with bases and oxidation with O_2 instead of strong oxidants such as iodosylbenzene. Hence, the oxido chromium(IV) complex **4** prepared from **1**/LiOH/ O_2 was employed in an electrochemical epoxidation of norbornene via single-electron oxidation of **4** to the reactive oxido chromium(V) porphyrin **4**⁺. Indeed, (spectro)electrochemical oxidation of **4** to **4**⁺ yields the Cr^V oxido complex which is characterized by its Soret band at 411 nm with half of the original Soret band intensity as expected for **4**⁺ (Figure 8a).^{31,64} An X-band EPR spectrum of this solution showed resonances at $g < 2.0$ expected for a $d^1\text{-Cr}^V$ complex ($g_1 = 1.9865$, $g_2 = 1.9780$; 77 K; CH_2Cl_2 ; Figure S8).⁶⁴ Addition of

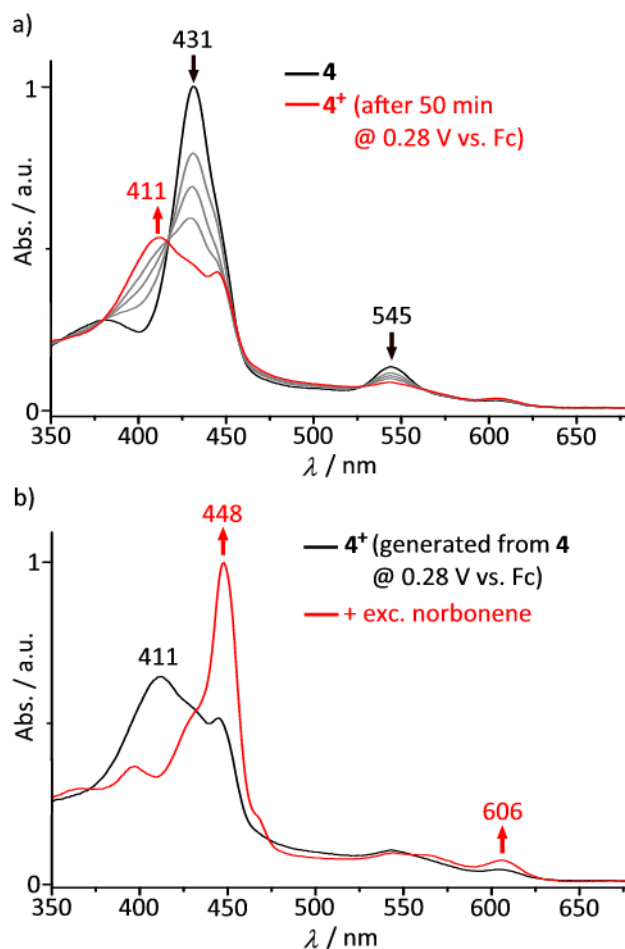


Figure 8 a) Spectroelectrochemical oxidation of **4** in $\text{CH}_2\text{Cl}_2/0.1 \text{ m } (n\text{Bu}_4\text{N})(\text{PF}_6)$ and b) UV/Vis spectrum after subsequent addition of norbonene to 4^+ .

norbonene caused the Soret band of 4^+ to disappear with concomitant appearance of the absorption bands of **1** similar to the reported electrochemical studies (Figure 8b).^{61,62} Finally, GC analysis of the solution from a bulk electrolysis of **4** in the presence of norbornene revealed the formation of *exo*-norbornene oxide during the course of the reaction by comparison with an authentic sample (see Figures S9 and S10) similar to results reported in [61,62] starting from **4** prepared by conventional oxygenation of **1**. Oxidative electrolysis of **4** in the presence of excess norbonene yields the Cr^{III} complex **1** without accumulation of 4^+ according to spectroelectrochemical studies suggesting that the oxygen atom transfer to norbonene is comparably fast under these conditions (Figure S11). Future studies will be devoted to optimizing the reaction conditions (base, porphyrin substituents⁶⁵, dioxygen pressure, solvent, electrolyte), to exploring the substrate scope and eventually to designing an electrocatalytic cycle using $1/\text{OH}^-$ with O_2 as abundant, low-cost and environmentally benign oxidant.⁶⁶⁻⁶⁸

Conclusion

In this study we disclosed the disjunctive mechanistic pathways of the reaction of different amines with the chromium(III) porphyrinato complex $\text{Cr}^{\text{III}}(\text{TPP})(\text{Cl})(\text{H}_2\text{O})$ (**1**).

Less basic amines **1** with $pK_b \geq 3.4$ act as Lewis bases substituting the aqua ligand to give green $\text{Cr}^{\text{III}}(\text{TPP})(\text{Cl})(\text{L})$ complexes (**2**). However, amines with $pK_b \leq 3.2$ act as Brønsted bases deprotonating the aqua ligand to give the anionic hydroxido complex $[\text{Cr}^{\text{III}}(\text{TPP})(\text{Cl})(\text{OH})]^-$ (**6**⁻). The latter is susceptible towards irreversible oxidation by dioxygen to the bright red oxido chromium(IV) complex $\text{Cr}^{\text{IV}}(\text{TPP})(\text{O})$ (**4**). Hence **1** discriminates weakly and strongly basic amines by a distinct colorimetric green/red response. Furthermore, the activation/oxidation reaction sequence of the **1**/amine/ O_2 system is autocatalytic as **1** is also activated by chloride which is stoichiometrically produced during the reaction. The irreversible formation of red **4** renders **1** a very sensitive amine-triggered ON switch which is highly suitable for applications in food freshness control. The chromogenic signal is not only stable over time but also strongly amplified by the disclosed autocatalytic pathway. Furthermore, the “green” formation of the oxido chromium(IV) complex **4** by dioxygen (instead of hypochlorite, peracids or iodosylbenzene) allows to use this highly desirable oxidant for the (electrochemical) production of value-added products such as epoxides.

Acknowledgments We thank the Fonds National de la Recherche Luxembourg (FNR) for financial support through the “SurfAmine” project. We thank Dominik Schmitt, Michael Mirion, Sebastian Herold and Prof. Siegfried R. Waldvogel for assistance with the bulk electrolysis and the GC measurements.

References

- (1) Tsutsui, M.; Mitsuo, I.; Vohwinkel, F.; Keinosuke, S. *J. Am. Chem. Soc.* **1966**, *569*, 854-855.
- (2) Tsutsui, M.; Velapoldi, R. A.; Suzuki, K.; Vohwinkel, F.; Ichikawa, M.; Koyano, T. *J. Am. Chem. Soc.* **1969**, *91*, 6262-6266.
- (3) Adler, A. D.; Longo, F. R.; Kampas, F.; Kim, J. *J. Inorg. Nucl. Chem.* **1970**, *32*, 2443-2445.
- (4) Summerville, D. A.; Jones, R. D.; Hoffmann, B. M.; Basolo, F. *J. Am. Chem. Soc.* **1977**, *99*, 8195-8202.
- (5) Sanders, J. K. M.; Bampos, N.; Clyde-Watson, Z.; Darling, S. L.; Hawley, J. C.; Kim, H.-J.; Mak, C. C.; Webb, S. J. in *The Porphyrin Handbook*; Kadish, M.; Smith, K. M.; Guillard, R., Eds.; Academic Press: New York, 2000; Vol. 3, pp. 1-48.
- (6) Guldi, D. M.; Hambright, P.; Lexa, D.; Neta, P.; Savéant, J.-M. *J. Phys. Chem.* **1992**, *96*, 4459-4466.
- (7) Bottomley, L. A.; Kadish, K. M. *Inorg. Chem.* **1983**, *22*, 342-349.
- (8) Bottomley, L. A.; Kadish, K. M. *J. Chem. Soc., Chem. Commun.* **1981**, 1212-1214.
- (9) More, K. M.; Eaton, G. R.; Eaton, S. S.; Hideg, K. *Inorg. Chem.* **1986**, *25*, 3865-3869.
- (10) Harriman, A. *J. Chem. Soc., Faraday Trans. I* **1982**, *78*, 2727-2734.
- (11) Gouterman, M.; Hanson, L. K.; Khalil, G.-E.; Leenstra, W. R.; Buchler, J. W. *J. Chem. Phys.* **1975**, *62*, 2343-2353.
- (12) Ozawa, T.; Hanaki, A. *Inorg. Chim. Acta* **1985**, *102*, 169-171.
- (13) Suslick, K. S.; Watson, R. A. *New J. Chem.* **1992**, *16*, 633-642.
- (14) Inamo, M.; Hoshino, M.; Nakajima, K.; Aizawa, S.; Funahashi, S. *Bull. Chem. Soc. Jpn.* **1995**, *68*, 2293-2303.
- (15) Fleischer, E. B.; Krishnamurthy, M. *J. Am. Chem. Soc.* **1971**, *93*, 3784-3786.

- (16) O'Brien, P.; Sweigart, D. A. *Inorg. Chem.* **1982**, *21*, 2094-2095.
- (17) Inamo, M.; Sugiura, S.; Fukuyama, H.; Funahashi, S. *Bull. Chem. Soc. Jpn.* **1994**, *67*, 1848-1854.
- (18) Inamo, M.; Hoshino, M. *Photochem. Photobiol.* **1999**, *70*, 596-601.
- (19) Inamo, M.; Nakaba, H.; Nakajima, K.; Hoshino, M. *Inorg. Chem.* **2000**, *39*, 4417-4423.
- (20) Heier, P.; Förster, C.; Schollmeyer, D.; Boscher, N.; Choquet, P.; Heinze, K. *Dalton Trans.* **2013**, *42*, 906-917.
- (21) Pinto, S. M. A.; Lourenço, M. A. O.; Calvete, M. J. F.; Abreu, A. R.; Rosado, M. T. S.; Burrows, H. D.; Pereira, M. M. *Inorg. Chem.* **2011**, *50*, 7916-7918.
- (22) Rakow, N. A.; Sen, A.; Janzen, M. C.; Ponder, J. B.; Suslick, K. S. *Angew. Chem.* **2005**, *117*, 4604-4608; *Angew. Chem. Int. Ed.* **2005**, *44*, 4528-4532.
- (23) a) Suslick, K. S.; Rakow, N. A.; Sen, A. *Tetrahedron* **2004**, *60*, 11133-11138; b) Rakow, N. A. Suslick, K. S. *Nature* **2000**, *406*, 710-713.
- (24) Elisa, L.; Baldini, F.; Giannetti, A.; Trono, C.; Carofiglio, T. *Chem. Commun.* **2010**, *46*, 3678-3680.
- (25) Anslyn, E. V., *J. Am. Chem. Soc.* **2010**, *132*, 15833-15835.
- (26) Boscher, N. D.; Duday, D.; Heier, P.; Heinze, K.; Hilt, F.; Choquet, P. *Surf. Coat. Technol.* **2013**, *234*, 48-52.
- (27) Boscher, N. D.; Bohn, T.; Heier, P.; Moisy, F.; Untereiner, B.; Heinze, K.; Choquet, P. *Sens. Actuators B* **2014**, *191*, 553-560.
- (28) Heier, P.; Bohn, T.; Choquet, P.; Boscher, N. D.; Heinze, K. *Adv. Funct. Mater.* **2014**, *2*, 1560-1570.
- (29) Oyama, S. T. (Ed.) *Mechanisms of homogeneous and heterogeneous epoxidation catalysis*; Elsevier B.V., **2008**.
- (30) Liston, D. J.; West, B. O. *Inorg. Chem.* **1985**, *24*, 1568-1576.
- (31) Groves, J. T.; Kruper, W. J.; Haushalter, R. C.; Butler, W. M. *Inorg. Chem.* **1982**, *21*, 1363-1368.
- (32) Budge, J. R.; Gatehouse, B. M. K.; Nesbit, M. C.; West, B. O. *J. Chem. Soc., Chem. Commun.* **1981**, 370-371.
- (33) Woo, L. K.; Hays, J. A.; Goll, J. G. *Inorg. Chem.* **1990**, *29*, 3916-3917.
- (34) Groves, J. T.; Kruper Jr., W. J. *J. Am. Chem. Soc.* **1979**, *101*, 7613-7615.
- (35) Yuan, L. C.; Bruice, T. C. *J. Am. Chem. Soc.* **1985**, *107*, 512-513.
- (36) Buchler, J. W.; Lay, K. L.; Ullrich, V. *Inorg. Chem.* **1982**, *21*, 842-844.
- (37) Yuan, L.-C.; Calderwood, T. S.; Bruice, T. C. *J. Am. Chem. Soc.* **1985**, *107*, 8273-8274.
- (38) (a) Meier-Callahan, A. E.; Gray, H. B.; Gross, Z. *Inorg. Chem.* **2000**, *39*, 3605-3607. (b) Meier-Callahan, A. E.; Di Bilio, A. J.; Simkhovich, L.; Mahammed, A.; Goldberg, I.; Gray, H. B.; Gross, Z. *Inorg. Chem.* **2001**, *40*, 6788-6793. (c) Mahammed, A.; Gray, H. B.; Meier-Callahan, A. E.; Gross, Z. *J. Am. Chem. Soc.* **2003**, *125*, 1162-1163. (d) Egorova, O. A.; Tsay, O. G.; Khatua, S.; Huh, J. O.; Churchill, D. G. *Inorg. Chem.* **2009**, *48*, 4634-4636. (e) Egorova, O. A.; Tsay, O. G.; Khatua, S.; Meka, B.; Maiti, N.; Kim, M. K.; Kwon, S. J.; Huh, J. O.; Bucella, D.; Kang, S. O.; Kwak, J.; Churchill, D. G. *Inorg. Chem.* **2010**, *49*, 502-512.
- (39) Prokop, K. A.; Goldberg, D. P. *J. Am. Chem. Soc.* **2012**, *134*, 8014-8017.
- (40) Fleischer, E. B.; Srivastava, T. S. *Inorg. Chim. Acta* **1971**, *5*, 151-154.
- (41) Buchler, J. W.; Dreher, C.; Lay, K.-L.; Raap, A.; Gersonde, K. *Inorg. Chem.* **1983**, *22*, 879-884.
- (42) Reed, C. A.; Kouba, J. A. Y. K.; Grimes, C. J.; Cheung, S. K. *Inorg. Chem.* **1978**, *17*, 2666-2670.
- (43) Cheung, S. K.; Grimes, C. J.; Wong, J.; Reed, C. A. *J. Am. Chem. Soc.* **1976**, *98*, 5028-5030.
- (44) Connelly, N. G.; Geiger, W. E. *Chem. Rev.* **1996**, *96*, 877-910.
- (45) Koelle, U.; Infelta, P. P.; Grätzel, M. *Inorg. Chem.* **1988**, *27*, 879-883.
- (46) Fuhrhop, J. H.; Kadish, K. M.; Davis, D. G. *J. Am. Chem. Soc.* **1973**, *95*, 5140-5147.

- (47) Frisch, M. J.; Trucks, G. W.; Schlegel, H. B.; Scuseria, G. E.; Robb, M. A.; Cheeseman, J. R.; Scalmani, G.; Barone, V.; Mennucci, B.; Petersson, G. A.; Nakatsuji, H.; Caricato, M.; Li, X.; Hratchian, H. P.; Izmaylov, A. F.; Bloino, J.; Zheng, G.; Sonnenberg, J. L.; Hada, M.; Ehara, M.; Toyota, K.; Fukuda, R.; Hasegawa, J.; Ishida, M.; Nakajima, T.; Honda, Y.; Kitao, O.; Nakai, H.; Vreven, T.; Montgomery, Jr., J. A.; Peralta, J. E.; Ogliaro, F.; Bearpark, M.; Heyd, J. J.; Brothers, E.; Kudin, K. N.; Staroverov, V. N.; Kobayashi, R.; Normand, J.; Raghavachari, K.; Rendell, A.; Burant, J. C.; Iyengar, S. S.; Tomasi, J.; Cossi, M.; Rega, N.; Millam, J. M.; Klene, M.; Knox, J. E.; Cross, J. B.; Bakken, V.; Adamo, C.; Jaramillo, J.; Gomperts, R.; Stratmann, R. E.; Yazyev, O.; Austin, A. J.; Cammi, R.; Pomelli, C.; Ochterski, J. W.; Martin, R. L.; Morokuma, K.; Zakrzewski, V. G.; Voth, G. A.; Salvador, P.; Dannenberg, J. J.; Dapprich, S.; Daniels, A. D.; Farkas, Ö.; Foresman, J. B.; Ortiz, J. V.; Cioslowski, J.; Fox, D. J. *Gaussian 09*, **2009**, Revision A.02; Gaussian, Inc., Wallingford, CT.
- (48) a) Jentzen, W.; Ma, J.-G.; Shelnut, J. A. *Biophys. J.* **1998**, *74*, 753–763; b) <http://jasheln.unm.edu/jasheln/>.
- (49) a) Chrystiuk, E.; Williams, A. *J. Am. Chem. Soc.* **1987**, *109*, 3040-3046; b) Hall, H. K. *J. Am. Chem. Soc.* **1957**, *79*, 5441-5444.
- (50) McGrier, P. L.; Solntsev, K. M.; Miao, S.; Tolbert, L. M.; Miranda, O. R.; Rotello, V. M.; Bunz, U. H. F. *Chem. – Eur. J.* **2008**, *14*, 4503-4510.
- (51) Xu, Y.; Xia, W.; Kim, J. M. *Int. J. Food Sci. Technol.* **2009**, *44*, 1547-1552.
- (52) Balamatsia, C.; Patsias, A.; Kontominas, M.; Savvaidis, I. *Food Chem.* **2007**, *104*, 1622-1628.
- (53) Veciana-Nogués, M. T.; Mariné-Font, A.; Vidal-Carou, M. C. *J. Agric. Food Chem.* **1997**, *45*, 2036-2041.
- (54) Golovanov, I. B.; Zhenodarova, S.M. *Russ. J. Gen. Chem.* **2005**, *75*, 1795-1797.
- (55) a) Kumpf, J.; Bunz, U. H. F. *Chem. – Eur. J.* **2012**, *18*, 8921-8924; b) Körsten, S.; Mohr, G. J. *Chem. – Eur. J.* **2011**, *17*, 969-975; c) Lee, B.; Scopelliti, R.; Sverin, K. *Chem. Commun.* **2011**, *47*, 9639-9641; d) Patze, C.; Broedner, K.; Rominger, F.; Trapp, O.; Bunz, U. H. F. *Chem. – Eur. J.* **2011**, *17*, 13720-13725; e) Steiner, M.-S.; Meier, R. J.; Duerkop, A.; Wolfbeis, O. S. *Anal. Chem.* **2010**, *82*, 8402-8405; f) Mohr, G. J. *Anal. Bioanal. Chem.* **2006**, *386*, 1201-1214; g) Mohr, G. J.; Klimant, I.; Spichiger-Keller, U. E.; Wolfbeis, O. S. *Anal. Chem.* **2001**, *73*, 1053-1056; h) Mohr, G. J.; Tirelli, N.; Lohse, C.; Spichiger-Keller, U. E. *Adv. Mater.* **1998**, *10*, 1353-1357.
- (56) Kilty, P. A.; Sachtler, W. M. *Catal. Rev. – Sci. Eng.* **1974**, *10*, 1-16.
- (57) a) Groves, J. T.; Quinn, R. *J. Am. Chem. Soc.* **1985**, *107*, 5790-5792; b) Lai, T.-S.; Zhang, R.; Cheung, K.-K.; Kwong, H.-L.; Che, C.-M. *Chem. Commun.* **1998**, 1583-1584; c) Koya, S.; Nishioka, Y.; Mizoguchi, H.; Uchida, T.; Katsuki, T. *Angew. Chem.* **2012**, *124*, 8368-8371; *Angew. Chem. Int. Ed.* **2012**, *51*, 8243-8246.
- (58) Laskavy, A.; Shimon, L. J. W.; Konstantinovski, L.; Iron, M. A.; Neumann, R. *J. Am. Chem. Soc.* **2010**, *132*, 517-523.
- (59) Bhunia, A.; Gotthardt, M. A.; Yadav, M.; Gamer, M. T.; Eichhöfer, A.; Kleist, W.; Roesky, P. W. *Chem. Eur. J.* **2013**, *19*, 1986-1995.
- (60) Traylor, T. G.; Miksztal, A. R. *J. Am. Chem. Soc.* **1989**, *111*, 7443-7448.
- (61) Creager, S. E.; Murray, R. W. *Inorg. Chem.* **1985**, *24*, 3824-3828.
- (62) Garrison, J. M.; Bruice, T. C. *J. Am. Chem. Soc.* **1989**, *111*, 191-198.
- (63) Crestoni, M. E.; Fornarini, S.; Lanucara, F.; Warren, J. J.; Mayer, J. M. *J. Am. Chem. Soc.* **2010**, *132*, 4336-4343.
- (64) Groves, J. T.; Haushalter, R. C. *J. Chem. Soc., Chem. Commun.* **1981**, 1165-1166.
- (65) a) Melomedov, J.; Wünsche von Leupoldt, A.; Meister, M.; Laquai, F.; Heinze, K. *Dalton. Trans.* **2013**, *42*, 9727-9739; b) Melomedov, J.; Ochsmann, J. R.; Meister, M.; Laquai, F.; Heinze, K. *Eur. J. Inorg. Chem.* **2014**, 1984-2001; c) Melomedov, J.; Ochsmann, J. R.; Meister, M.; Laquai, F.; Heinze, K. *Eur. J. Inorg. Chem.* **2014**, 2902-2915.

- (66) Punniyamurthy, T.; Velusamy, S.; Iqbal, J. *Chem. Rev.* **2005**, *105*, 2329-2363.
- (67) Meunier, B. *Chem. Rev.* **1992**, *92*, 1411-1456.
- (68) Tabushi, I. *Coord. Chem. Rev.* **1988**, *86*, 1-42.

4. Summary

In this work, the successful incorporation of porphyrin chromophores into polysiloxane matrices deposited by a dielectric barrier discharge enhanced chemical vapour deposition has been presented. The sensing layers formed with $\text{Cr}^{\text{III}}\text{TPP}(\text{Cl})(\text{H}_2\text{O})$ have been used for the colourimetric detection of NEt_3 vapours down to concentrations of 10 ppm. Coatings based on the novel porphyrin $\text{Cr}^{\text{III}}\text{P}(\text{Cl})(\text{H}_2\text{O})$ introduced in this work (see section 3.5) already indicated even superior sensing properties in first experiments. However, their exact detection limit has not yet been identified, as the required low amine concentrations could hardly be controlled reliably.

The possible application of the formed sensing foils in smart packaging solutions for the control of food freshness has been shown by the detection of prominent metabolites of microbiological activity (HNMe_2 , NMe_3) and first food storage experiments.

These results have been made possible by the substantial contributions of this work to the fields of DBD enhanced CVD and the design of porphyrin based colourimetric amine sensors.

The presented DBD setup with a grounded moving table passing two flat parallel high voltage electrodes facilitates the deposition of smart hybrid coatings on large surface areas. Its versatility could be shown by the coating of silicon wafers as well as aluminium and PET foils. During the process only minor amounts of waste and by-products are produced and nitrogen could be used as a cheap and abundant process gas.

The DBD enhanced CVD described here yielded highly coloured, transparent and adherent porphyrin containing polysiloxane layers. The integrity of the different used porphyrins after the plasma treatment could be shown by UV/vis spectroscopy as well as mass spectrometry. Their tight incorporation within the matrix prevents them from

agglomeration and their homogeneous lateral distribution along the layer has been shown by SIMS analysis. Optimisation of the process parameters moreover enabled the deposition of stable porous sensing matrices which facilitates the analytes diffusion to and interaction with the chromophores within.

In addition, a novel design concept for porphyrin based chromophores for colourimetric sensing applications has been introduced. The attachment of two rigid arms shielding the coordination site of the porphyrin strongly amplifies the absorption change of zinc porphyrins upon the interaction with NEt_3 . In solution the novel porphyrins show a clearly discernible colour change from red to yellow in contrast to the slight change from violet to pink observed for simple ZnTPP. The responsible pronounced distortion of the novel porphyrin's macrocycle upon NEt_3 coordination and its steric interaction with the porphyrins periphery has been investigated by UV/vis and NMR spectroscopy along with supporting DFT calculations.

Chromium porphyrins, which have been reported to have high affinities towards nitrogen containing ligands in previous works, have also been employed for amine detection in this work. However, it could be shown that the colour change from green to red as observed upon the exposure of $\text{Cr}^{\text{III}}\text{TPP}(\text{Cl})(\text{H}_2\text{O})$ to NEt_3 is rather connected to the formation of $\text{Cr}^{\text{IV}}\text{TPP}(\text{O})$ than the previously expected substitution of the water ligand by NEt_3 . As steric interactions play a minor role in chromium(IV) oxido porphyrins, the introduction of the two rigid arms similar to the zinc porphyrins did not lead to a stronger absorption change of the chromium(III) porphyrins with NEt_3 . However, the associated higher solubility of the novel porphyrin derivatives facilitated their further processing in the CVD process resulting in sensing layers with superior properties.

The mechanistic studies on the interaction of different amines with $\text{Cr}^{\text{III}}\text{TPP}(\text{Cl})(\text{H}_2\text{O})$ moreover revealed a novel pathway to $\text{Cr}^{\text{IV}}\text{TPP}(\text{O})$ with dioxygen as the terminal oxidant. Therefore, preliminary electrochemical epoxidation reactions using $\text{Cr}^{\text{IV}}\text{TPP}(\text{O})$ could be performed without the need for strong oxidants like *e.g.* iodosylbenzene as described for such reactions in the literature.

5. Outlook

Although the sensing of volatile amines has been successful spectroscopically, it has to be noted that the sensor foils' response upon exposure to volatile amines cannot yet be seen by the human eye – in contrast to the clearly discernible colour changes chromium porphyrins as well as the novel zinc porphyrins show in solution. But the mechanistic studies performed in this work already indicate strategies to overcome this discrepancy.

It could be shown, that the colour changes observed for the zinc porphyrins upon exposure to NEt_3 are strongly dependent on the solvent used. The more bathochromically shifted the Soret band in the neat solvent the less distinct the absorbance change upon exposure to NEt_3 . This is *e.g.* exemplified by a Soret band shift of the novel zinc porphyrins from 420 to 433 in *n*-hexane but only from 428 to 429 in chloroform. Within the deposited sensing foils, the Soret band of the porphyrins is already bathochromically shifted to 433 nm – and following the trends observed in solution, the bathochromic shift with NEt_3 vapours amounts only to 1 nm. The strategy to enhance the foils absorbance change upon exposure to NEt_3 would thus be to diminish the “solvatochromic” effect of the matrix on the embedded porphyrin chromophores. This may be achieved by changing the nature of the matrix by the use of different precursors or further improvement of the plasma conditions.

Similar approaches may be employed for the improvement of sensing foils containing chromium(III) porphyrins. It has been shown that the reaction responsible for the colour change of these porphyrins upon exposure to basic amines, namely the formation of a Cr^{IV} oxido species, is also dependent on the solvent: the reaction is much faster in toluene than in dichloromethane. Therefore, improvements of the matrices' “solvent” properties may also facilitate this oxidation reaction and in consequence the visible colour change of the sensing foils.

As different metalloporphyrins have been incorporated unaltered into polysiloxane matrices on different substrates, the use of the reported DBD enhanced CVD method may also be extended to the deposition of other hybrid coatings. For instance, established colourimetric sensors for amines, but also other analytes like *e.g.* toxic gases or explosives (see sections 1.2.2 and 1.4.1) may be incorporated into appropriate membranes. Furthermore, as porous matrices can be deposited by the described method, molecular catalysts may be immobilised to form catalytic active surfaces in contact with gaseous or liquid phases.

In addition, the revealed novel pathway for the formation of Cr^{IV}TPP(O) opens up the possibility for “green” electrochemical epoxidation reactions with dioxygen as the terminal oxidant. The process parameters (solvent, temperature, oxygen pressure) and the porphyrin’s properties may be optimised to establish a catalytic epoxidation process with the formal use of oxygen as abundant, low-cost and environmentally friendly oxidant. Furthermore, by tailoring the porphyrin’s substituents, enantioselective epoxidations of prochiral alkenes can be possible.

6. Supporting Information

Supporting Information to

Section 3.4 pp. 183 – 198

Section 3.5 pp. 199 – 204

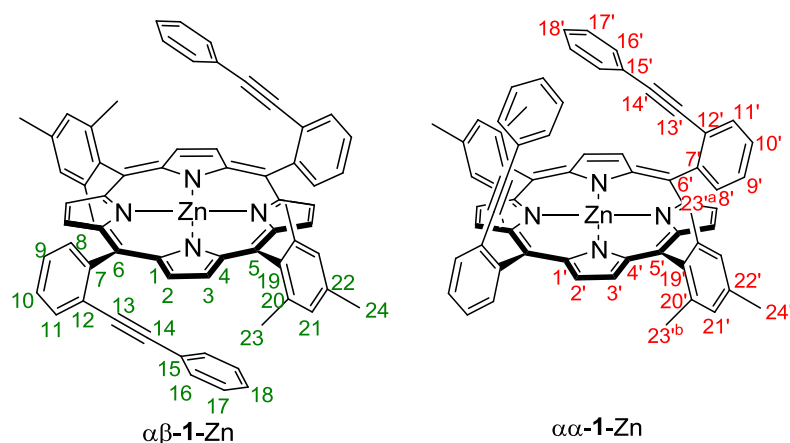
Section 3.6 pp. 205 – 213

***αα*- and *αβ*-Zinc-meso-A₂B₂-Tetraarylporphyrins with large optical response to volatile amines**

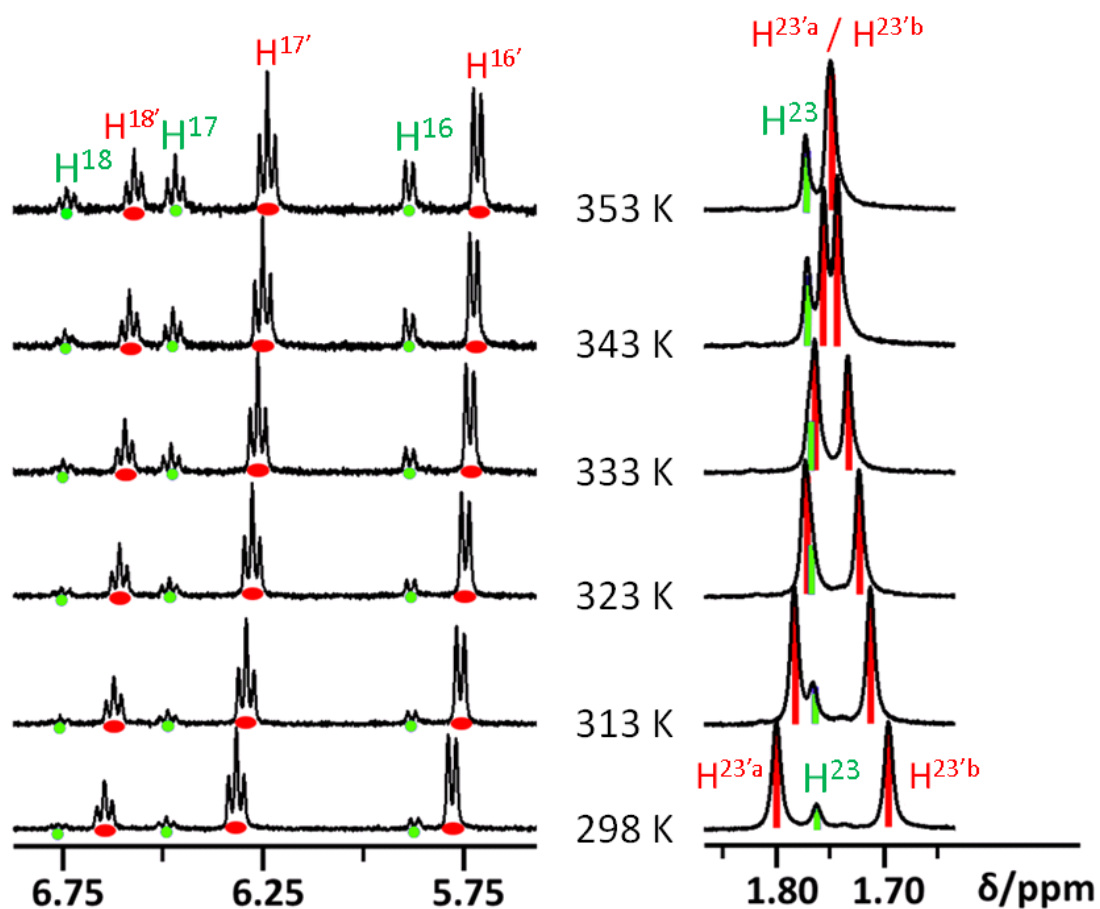
Philip Heier,^{a,b} Christoph Förster,^a Dieter Schollmeyer,^a Nicolas Boscher,^b
Patrick Choquet^b and Katja Heinze^{*a}

Supplementary Information

- **Figure S1** Atom numbering as used for NMR assignments
- NOESY (CD₂Cl₂, 298 K, 400 MHz) of *αα*-**1**-2H and *αβ*-**1**-2H
- Temperature dependent NMR ($T = 278 - 353$ K) of *αα*- and *αβ*-**1**-Zn in DMSO-d₆
- ¹³C{¹H}-NMR (CD₂Cl₂, 298 K, 100 MHz) of *αα*-**1**-Zn
- HMBC (CD₂Cl₂, 298 K) of *αα*-**1**-Zn
- HMBC (CD₂Cl₂, 298 K) of *αα*-**1**-Zn (aromatic region)
- HSQC (CD₂Cl₂, 298 K) of *αα*-**1**-Zn
- HSQC (CD₂Cl₂, 298 K) of *αα*-**1**-Zn (aromatic region)
- NOESY (CD₂Cl₂, 298 K, 400 MHz) of *αα*-**1**-Zn
- ¹³C{¹H}-NMR (CD₂Cl₂, 298 K, 100 MHz) of *αβ*-**1**-Zn
- HMBC (CD₂Cl₂, 298 K) of *αβ*-**1**-Zn
- HMBC (CD₂Cl₂, 298 K) of *αβ*-**1**-Zn (aromatic region)
- HSQC (CD₂Cl₂, 298 K) of *αβ*-**1**-Zn
- HSQC (CD₂Cl₂, 298 K) of *αβ*-**1**-Zn (aromatic region)
- Normalized (to Soret band) absorption spectra of *αβ*-**1**-Zn
- Cartesian Coordinates of DFT optimised of *αα*-**1**-Zn, *αα*-**1**-Zn(NEt₃)-dist, *αα*-**1**-Zn(NEt₃)-prox, *αβ*-**1**-Zn and *αβ*-**1**-Zn(NEt₃)

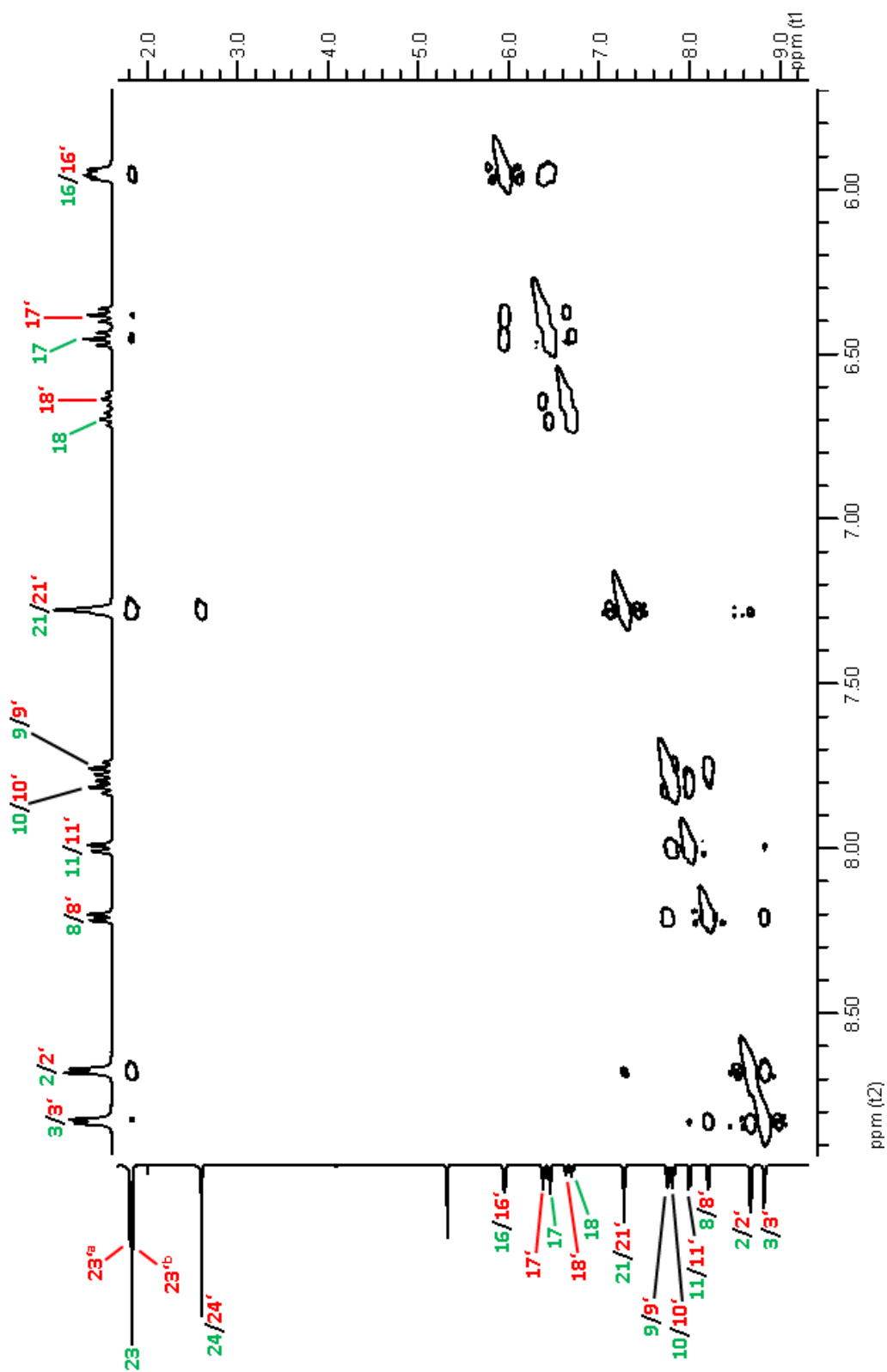
Figure S1 Atom numbering as used for NMR assignments**Temperature dependent NMR ($T = 278 - 353$ K) of $\alpha\alpha$ - and $\alpha\beta$ -1-Zn in DMSO- d_6**

Partial NMR spectra of $\alpha\alpha$ -1-Zn (red) and $\alpha\beta$ -1-Zn (green) mixture in DMSO- d_6 at different temperatures. Increasing signal intensity for $\alpha\beta$ -1-Zn is due to increasing solubility at higher temperatures.



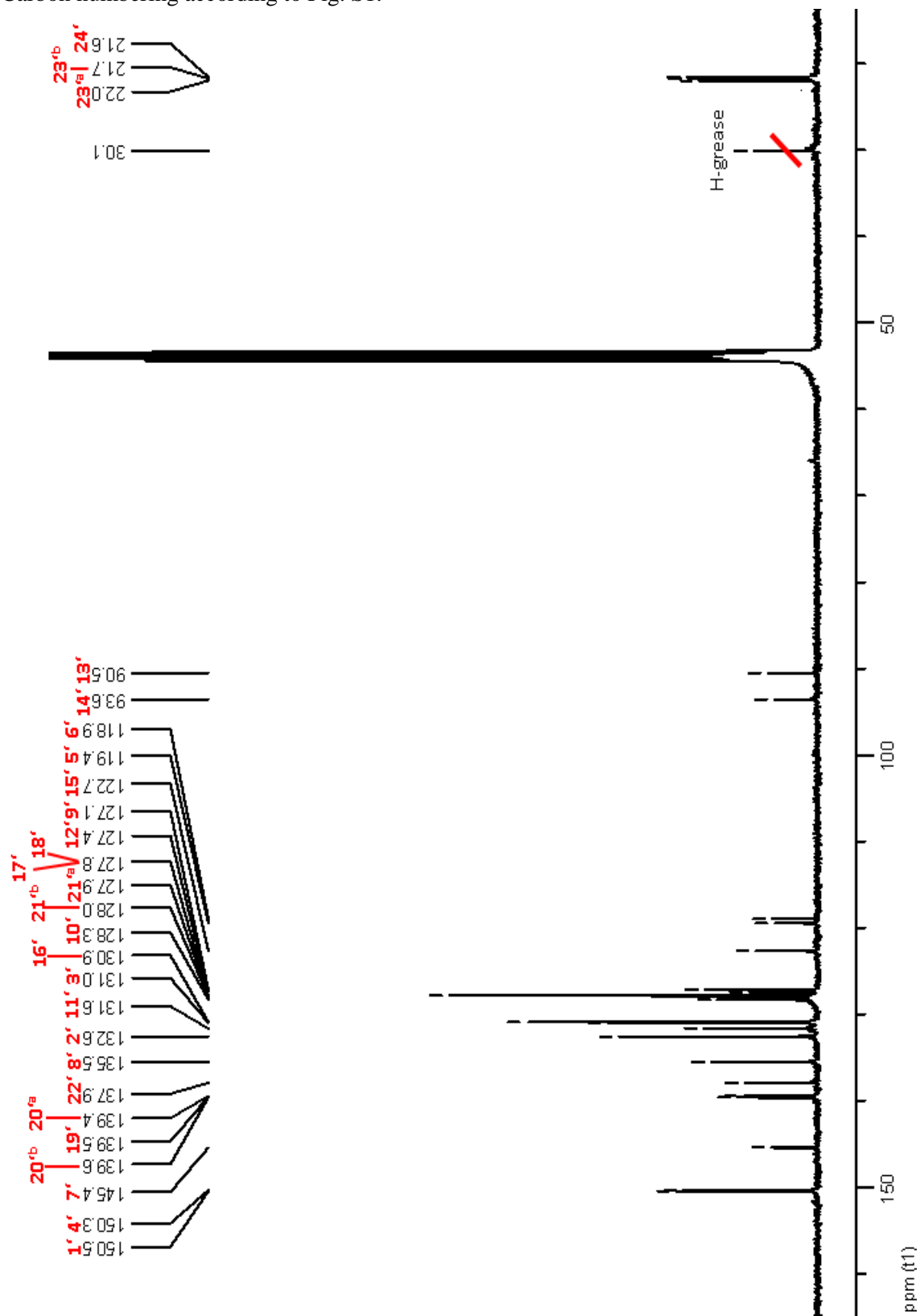
NOESY (CD₂Cl₂, 298 K, 400 MHz) of $\alpha\alpha$ -1-2H and $\alpha\beta$ -1-2H

Proton numbering according to Fig. S1.



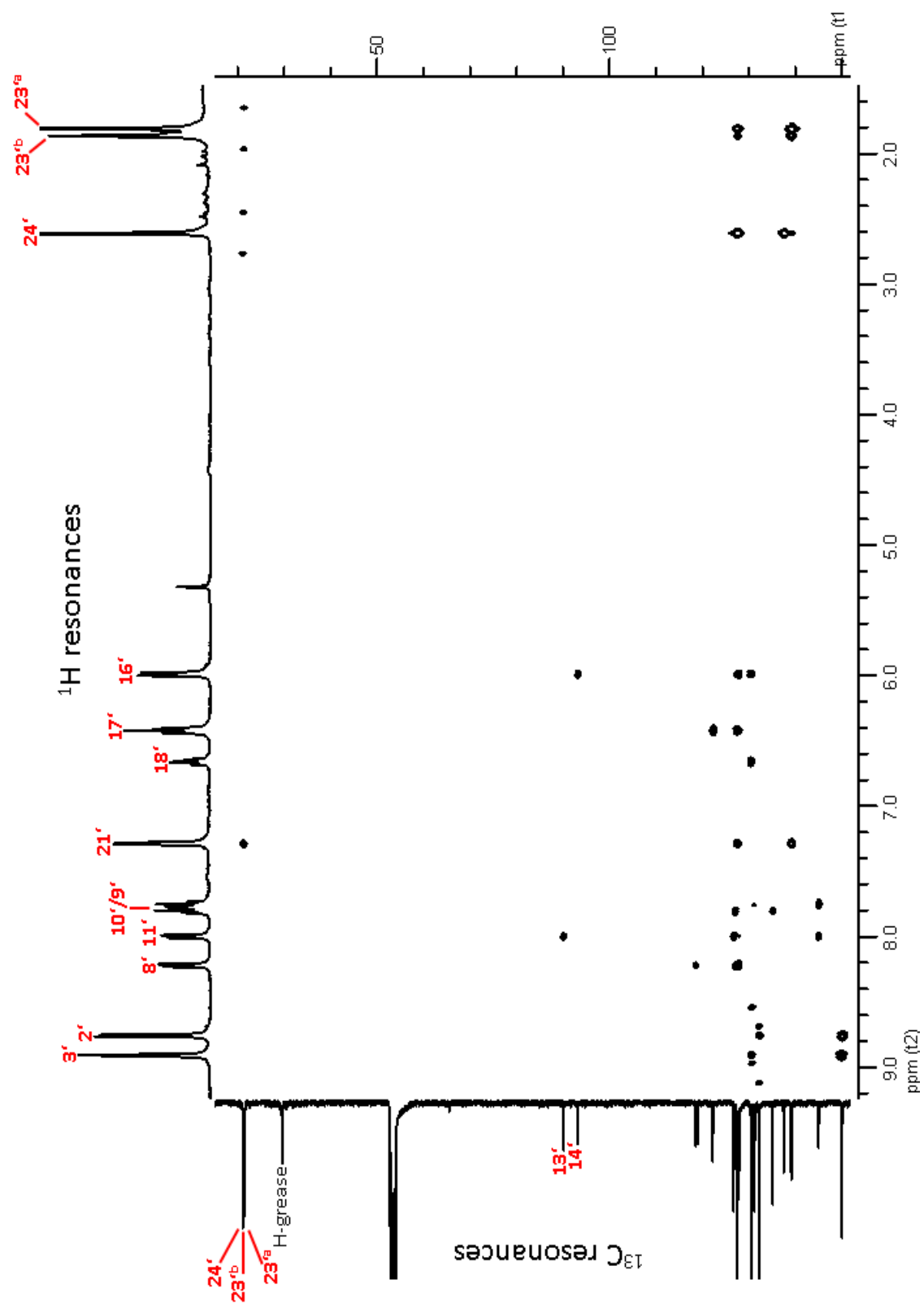
$^{13}\text{C}\{^1\text{H}\}$ -NMR (CD_2Cl_2 , 298 K, 100 MHz) of $\alpha\alpha$ -1-Zn

Carbon numbering according to Fig. S1.



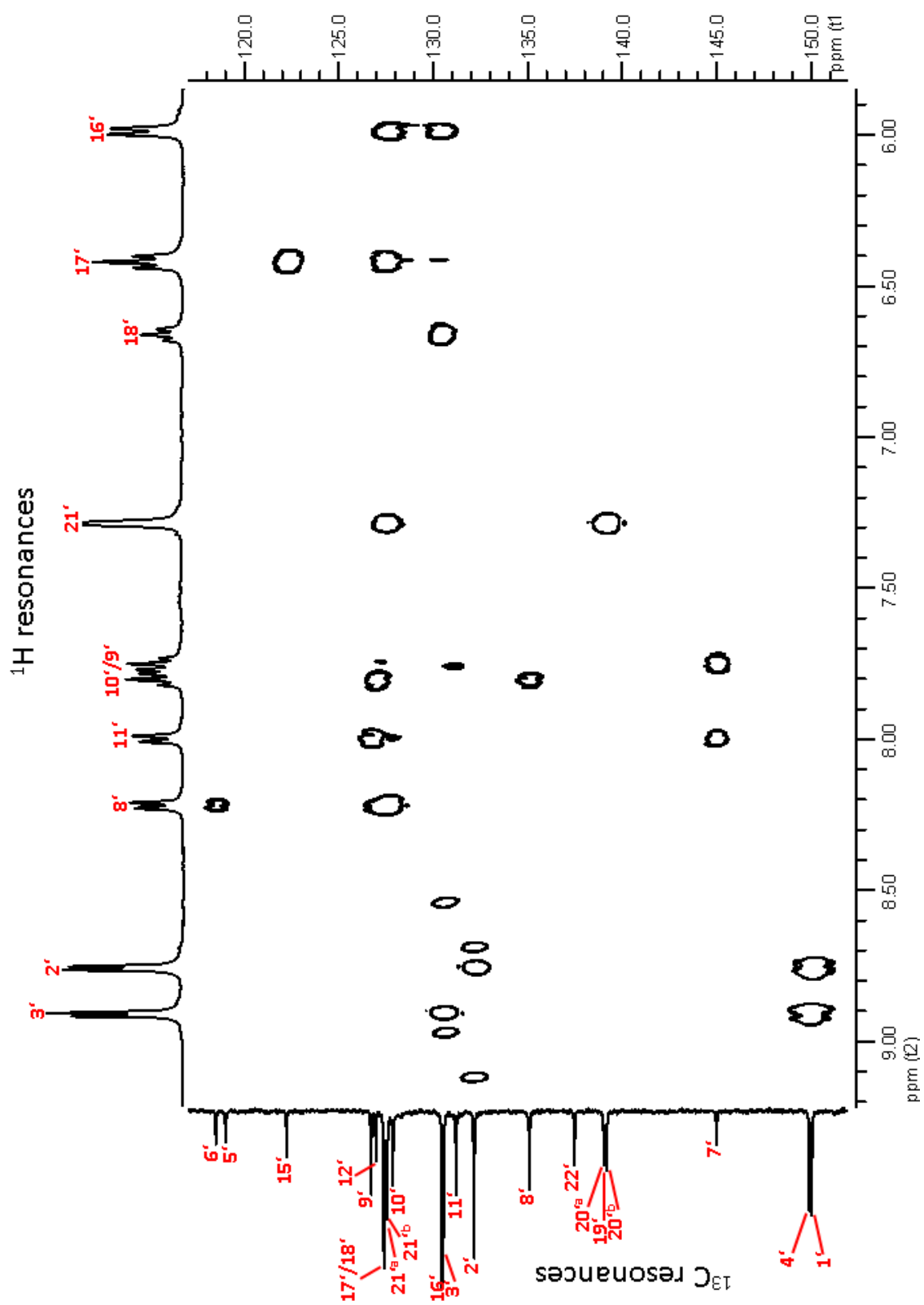
HMBC (CD_2Cl_2 , 298 K) of $\alpha\alpha$ -1-Zn

Atom numbering according to Fig. S1.



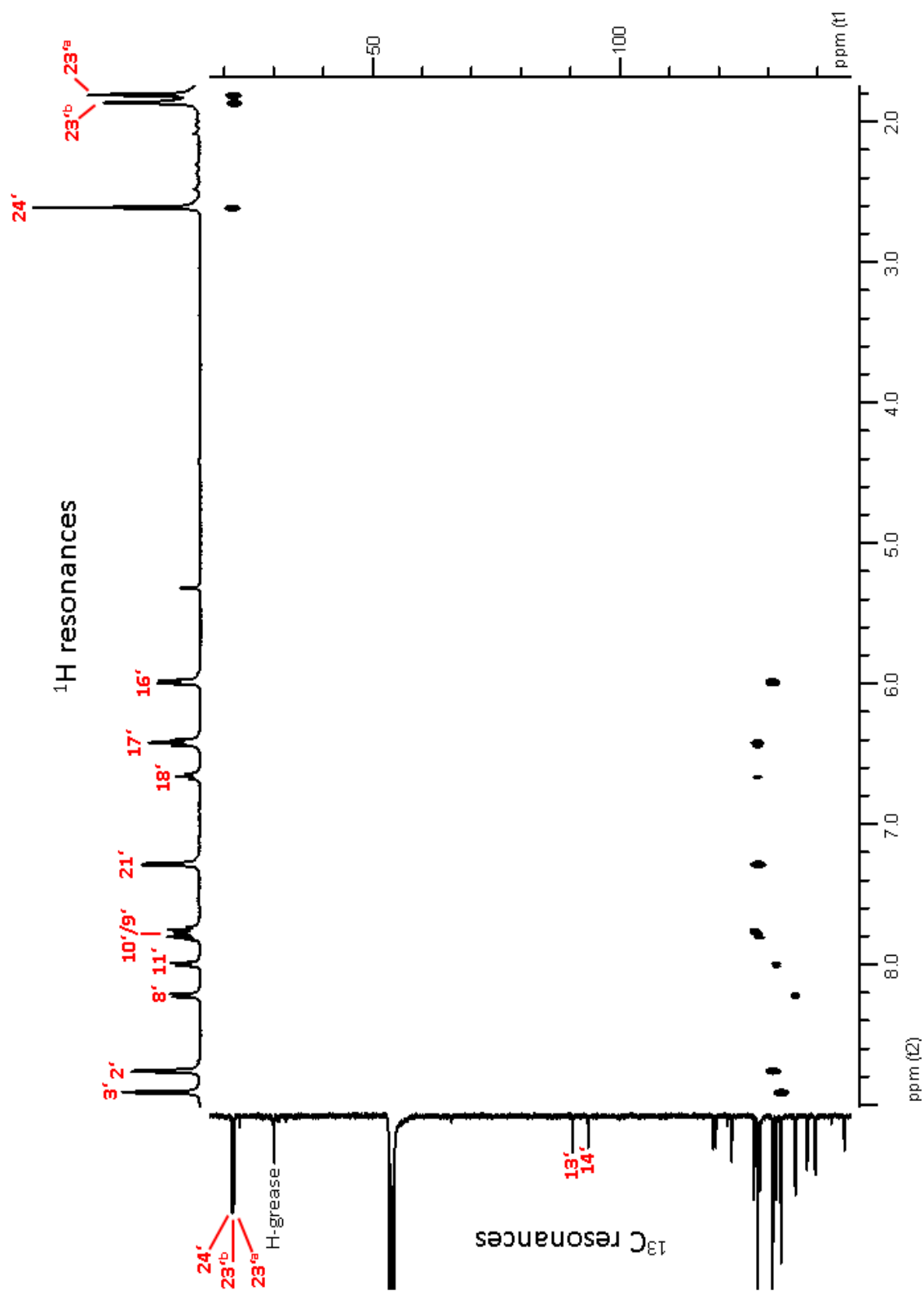
HMBC (CD_2Cl_2 , 298 K) of $\alpha\alpha$ -1-Zn (aromatic region)

Atom numbering according to Fig. S1.



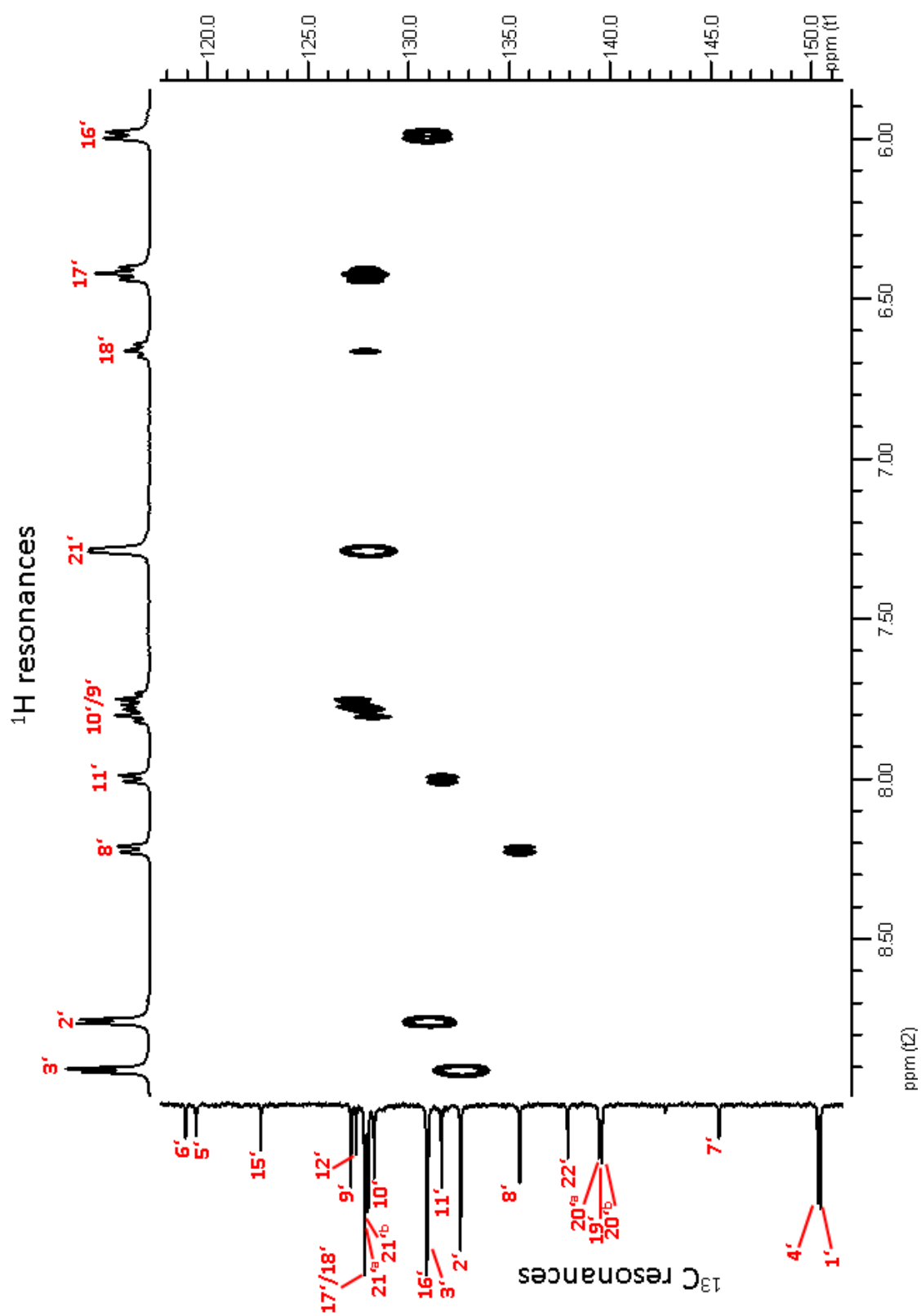
HSQC (CD_2Cl_2 , 298 K) of $\alpha\alpha$ -1-Zn

Atom numbering according to Fig. S1



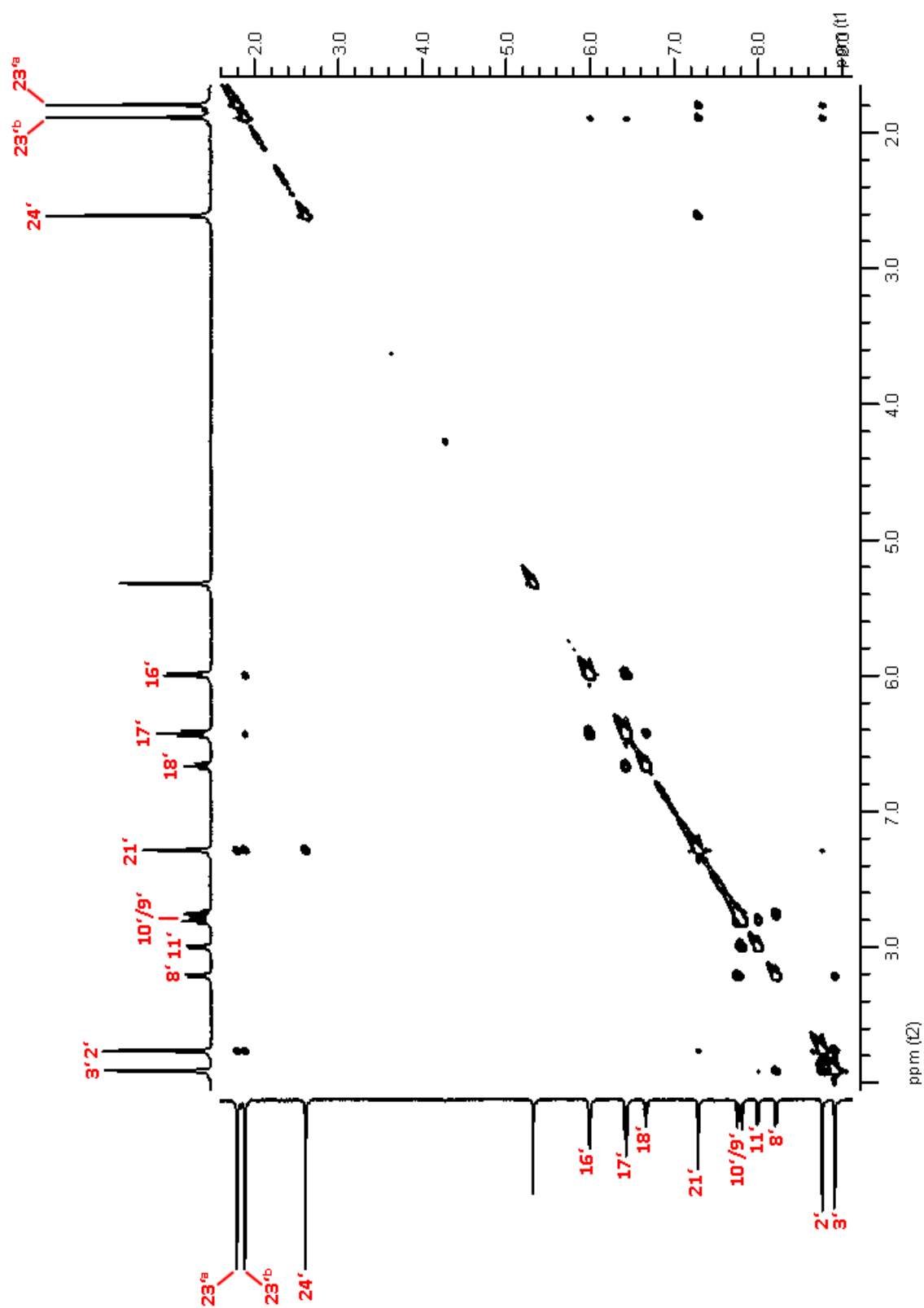
HSQC (CD_2Cl_2 , 298 K) of $\alpha\alpha$ -1-Zn (aromatic region)

Atom numbering according to Fig. S1



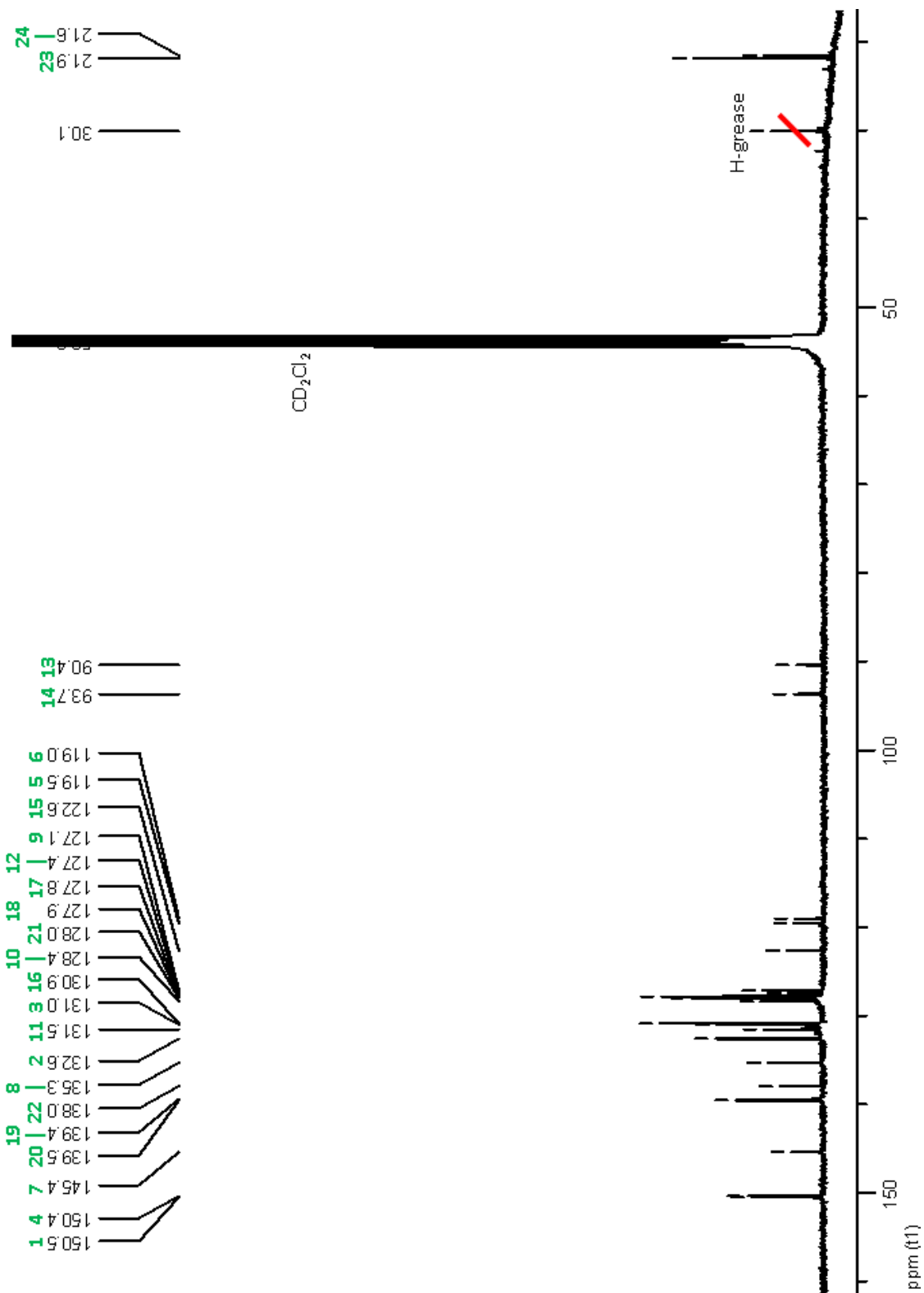
NOESY (CD₂Cl₂, 298 K, 400 MHz) of $\alpha\alpha$ -1-Zn

Proton numbering according to Fig. S1.



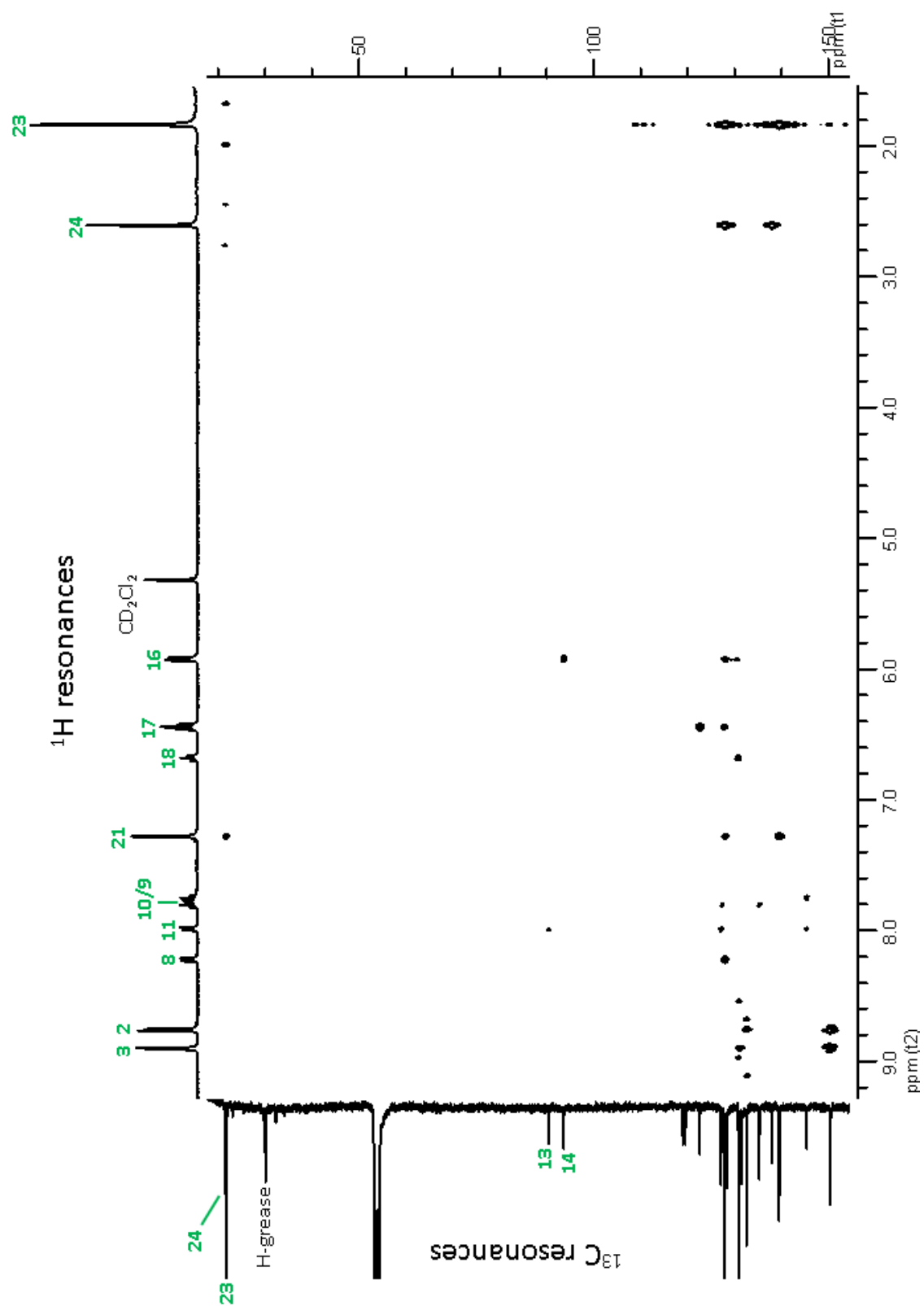
$^{13}\text{C}\{^1\text{H}\}$ -NMR (CD_2Cl_2 , 298 K, 100 MHz) of $\alpha\beta$ -1-Zn

Carbon numbering according to Fig. S1.



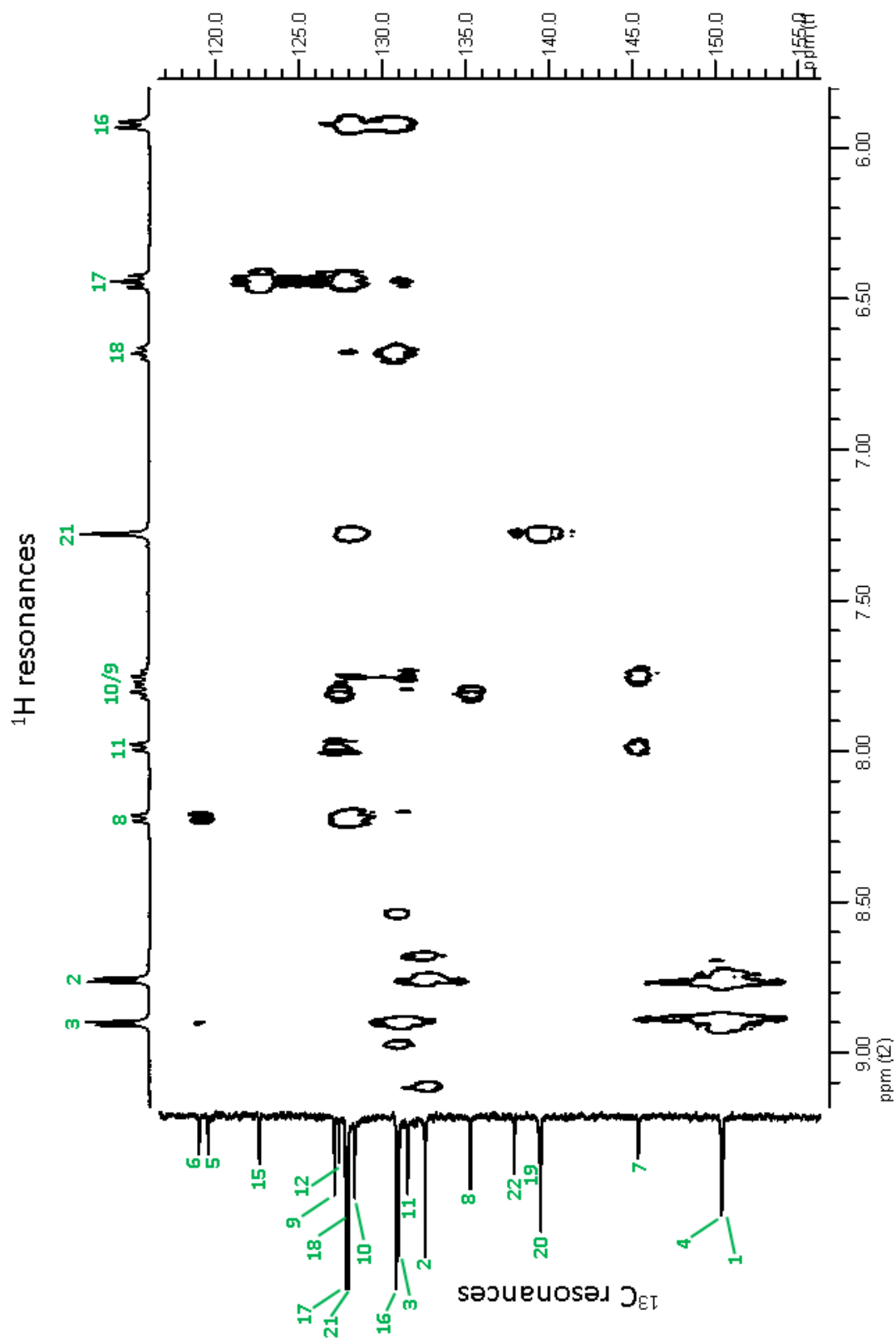
HMBC (CD_2Cl_2 , 298 K) of $\alpha\beta$ -1-Zn

Atom numbering according to Fig. S1.



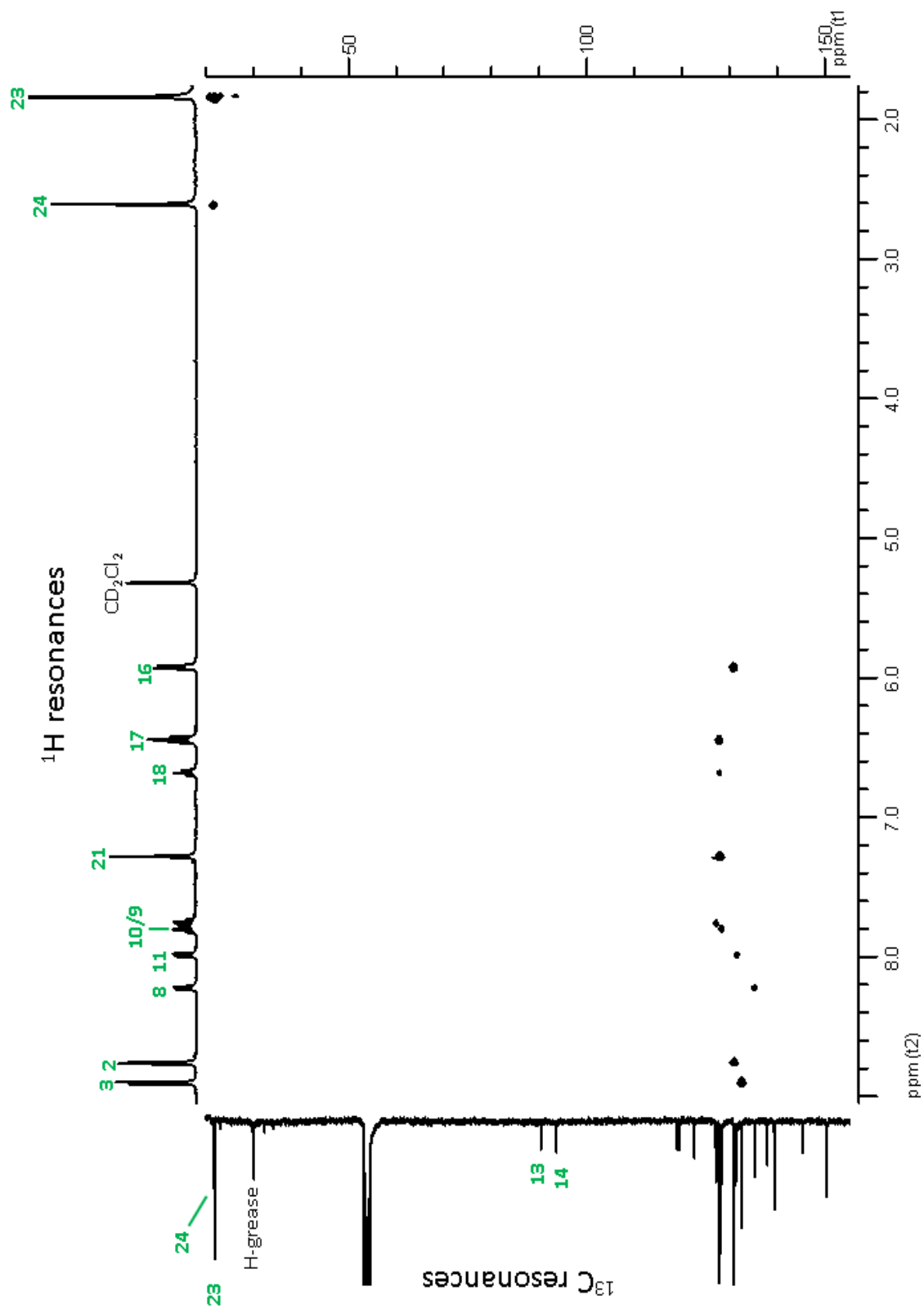
HMBC (CD_2Cl_2 , 298 K) of $\alpha\beta$ -1-Zn (aromatic region)

Atom numbering according to Fig. S1.



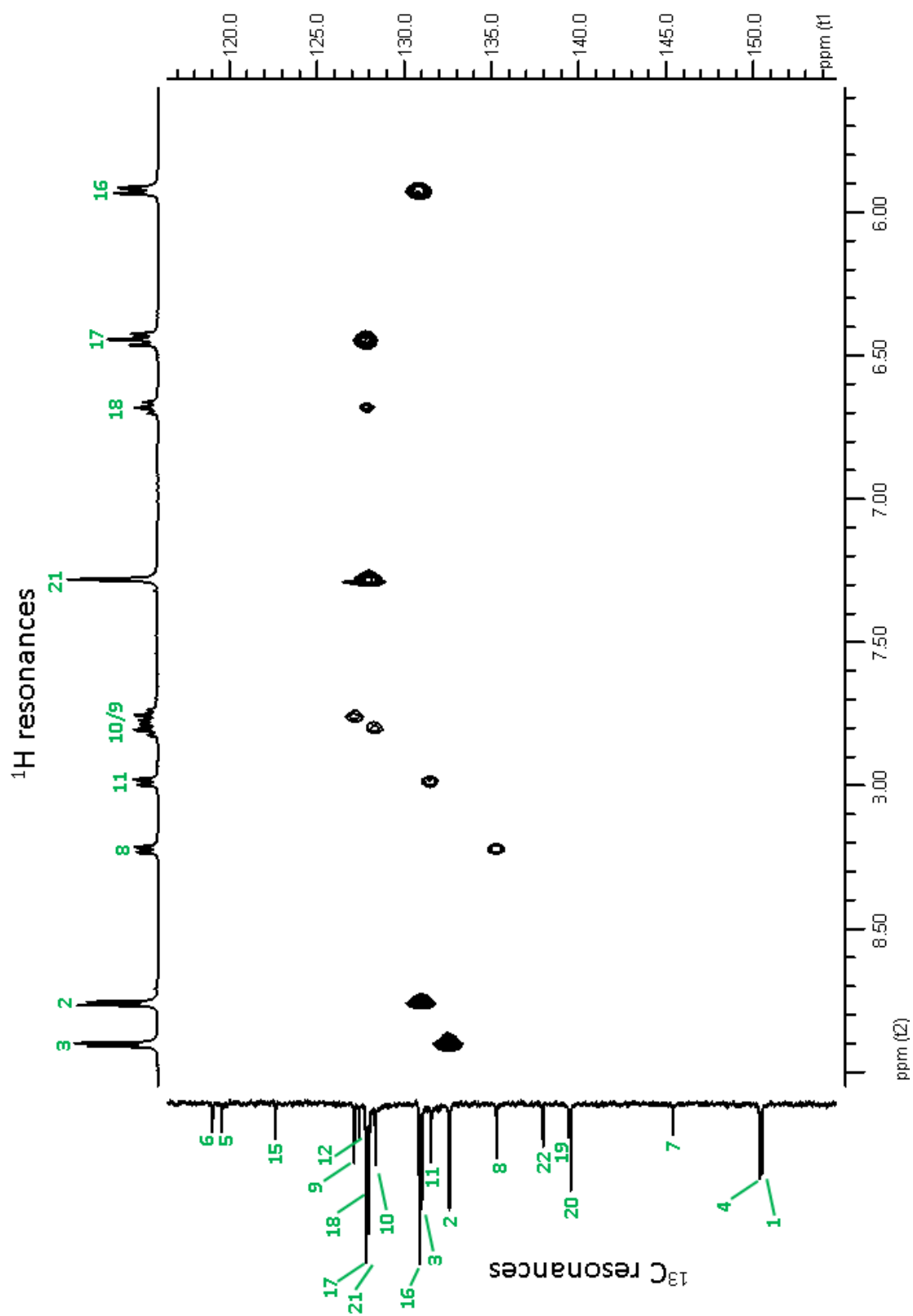
HSQC (CD_2Cl_2 , 298 K) of $\alpha\beta$ -1-Zn

Atom numbering according to Fig. S1



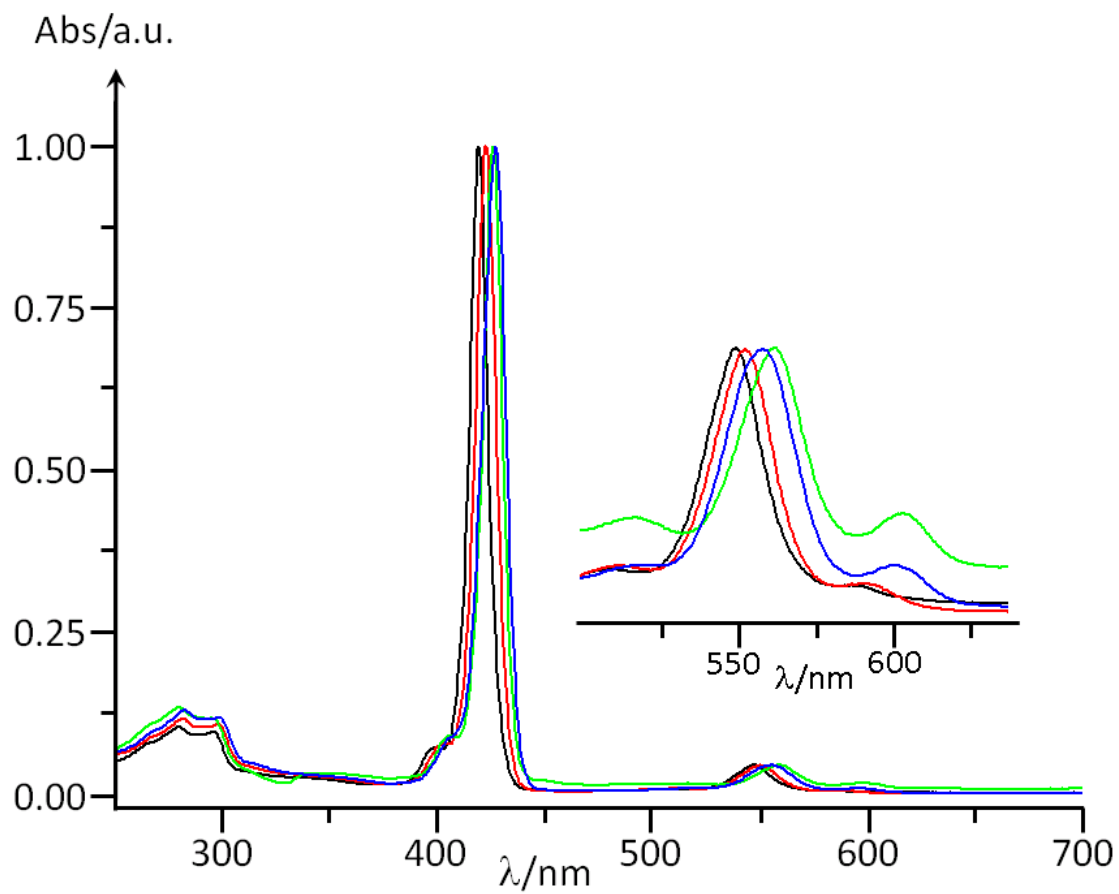
HSQC (CD_2Cl_2 , 298 K) of $\alpha\beta$ -1-Zn (aromatic region)

Atom numbering according to Fig. S1



Normalized (to Soret band) absorption spectra of $\alpha\beta$ -1-Zn

in *n*-hexane (—), dichloromethane (—), acetonitrile (—) and chloroform (—). Inset shows magnification of Q-band region.



New class of Zn(II) and Cr(III) porphyrins incorporated into porous polymer matrices via an atmospheric pressure plasma enhanced CVD to form gas sensing layers

Philip Heier, Nicolas D. Boscher,* Torsten Bohn, Katja Heinze,* Patrick Choquet

Supplementary Information

Figure S1 molecular structure of $\alpha\alpha$ - and $\alpha\beta$ -H₂P

Figure S2 UV/vis spectra of Cr^{III}P(Cl)(H₂O) in CH₂Cl₂ pure and with NEt₃

Figure S3 IR spectra of Cr-1, Cr-2 and Cr-3

Figure S4 UV/vis spectra of Zn-1 under dry and humid conditions with and without NEt₃

Figure S5 UV/vis spectra of Cr-3 under dry and humid conditions with and without NEt₃

Figure S6 SEM pictures of Cr-1, Cr-2 and Cr-3

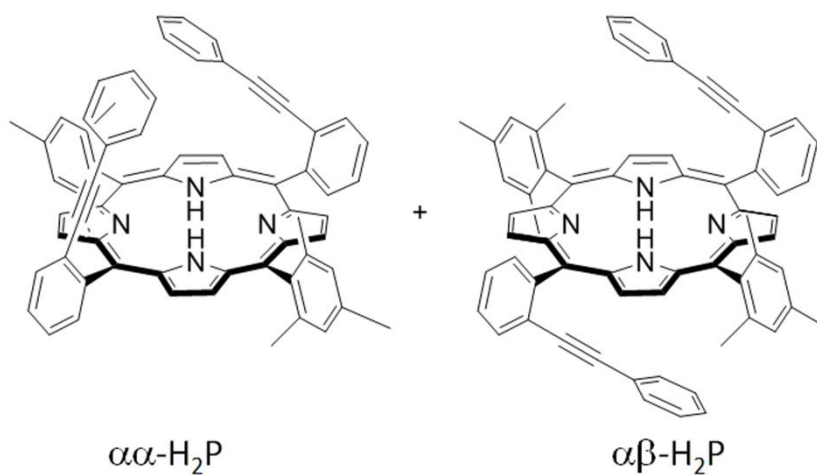


Figure S1 Structure of the metal-free porphyrins $\alpha\alpha\text{-}$ and $\alpha\beta\text{-H}_2\text{P}$ as synthesized according to Ref. 49

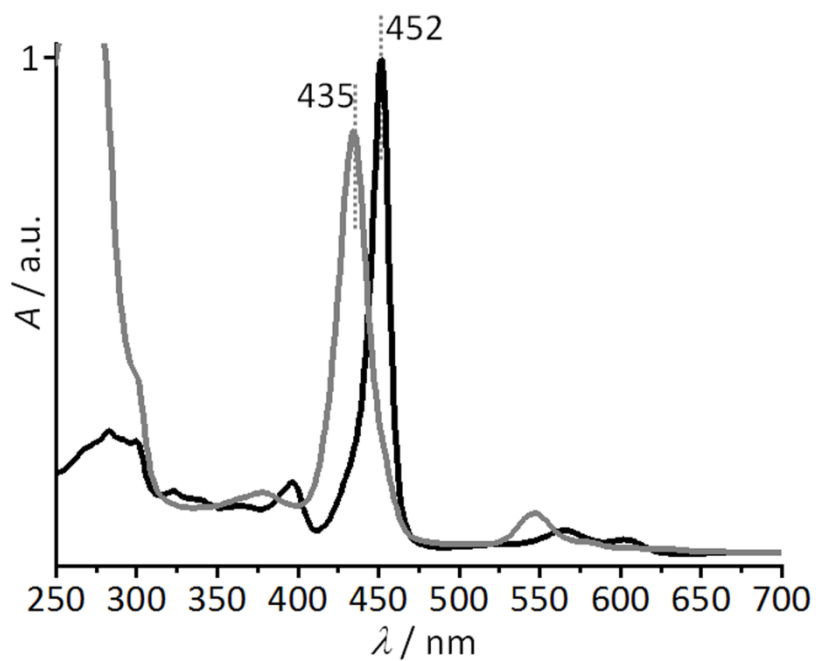


Figure S2 UV/vis absorption spectra of $\text{Cr}^{\text{III}}\text{P}(\text{Cl})(\text{H}_2\text{O})$ in pure CH_2Cl_2 (black) and after addition of excess NEt_3 (grey); the strong absorption arising around 300 nm with NEt_3 is attributed to absorptions of NEt_3 .

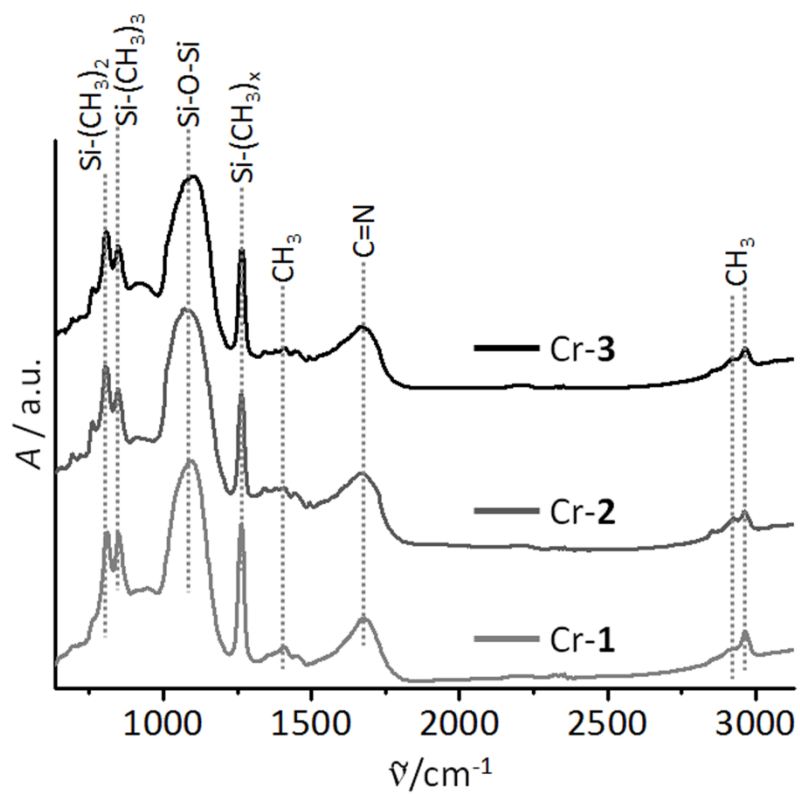


Figure S3 FT-IR absorption spectra of Cr-1 (bottom), Cr-2 (middle) and Cr-3 (top) on aluminum.

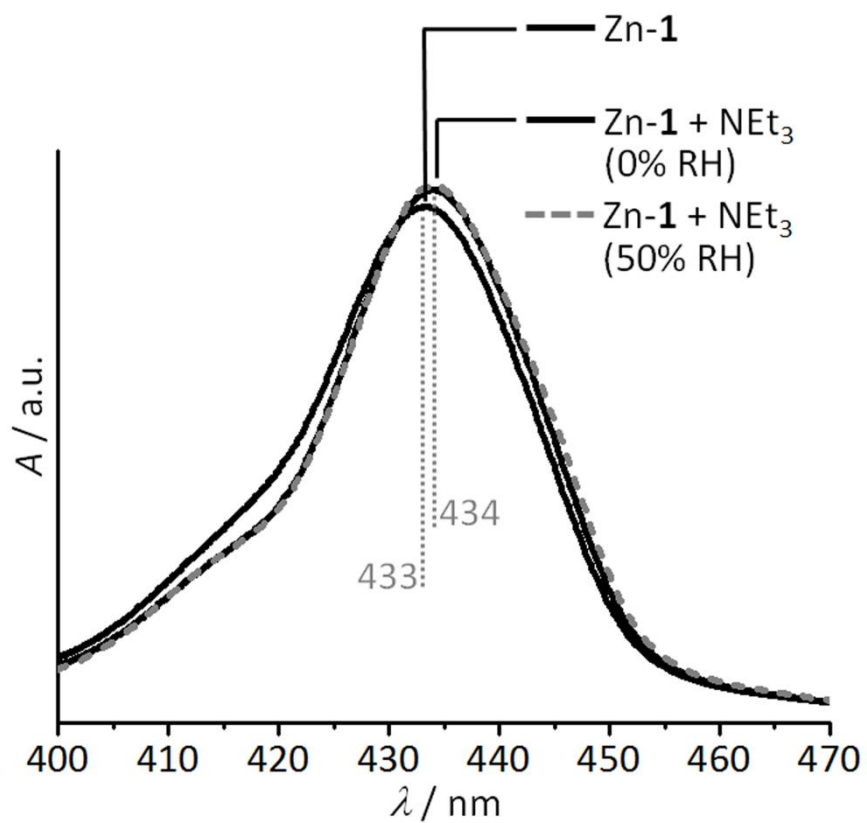


Figure S4 Absorption change of Zn-1 upon exposure to NEt₃ under different RH conditions: Zn-1 before amine exposure, after 2 h with 1% NEt₃ in dry nitrogen and with 50% RH (dashed, grey).

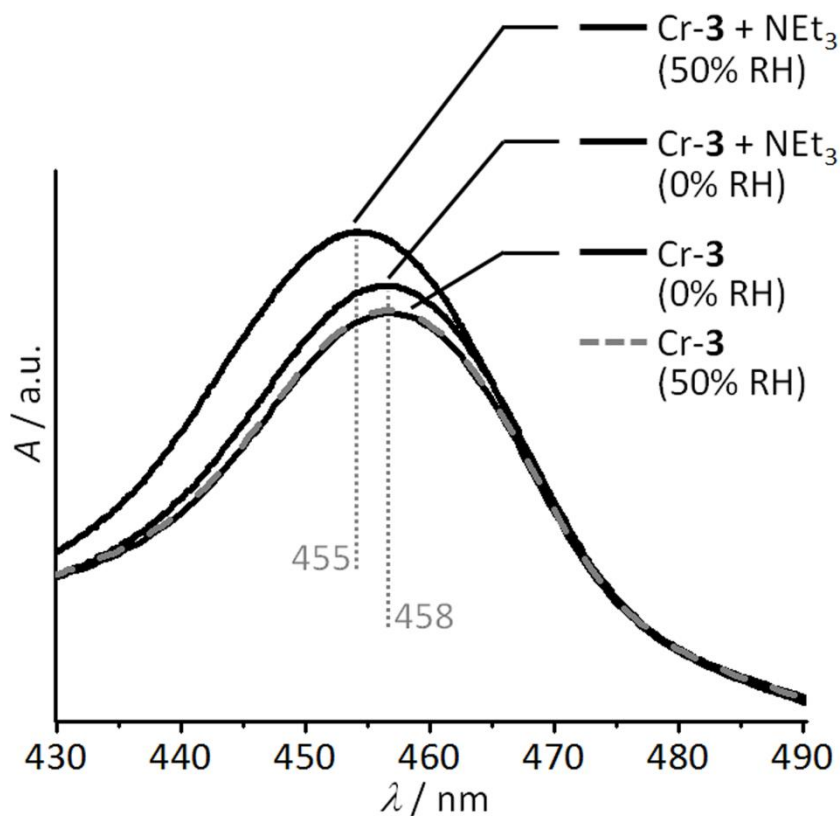


Figure S5 UV/vis absorption of Cr-3 under different relative humidity conditions before and after NEt₃ exposure: Cr-3 in a dry nitrogen atmosphere, in a nitrogen atmosphere with 50% relative humidity (dashed, grey), after NEt₃ exposure in dry nitrogen atmosphere and after NEt₃ exposure with 50% RH.

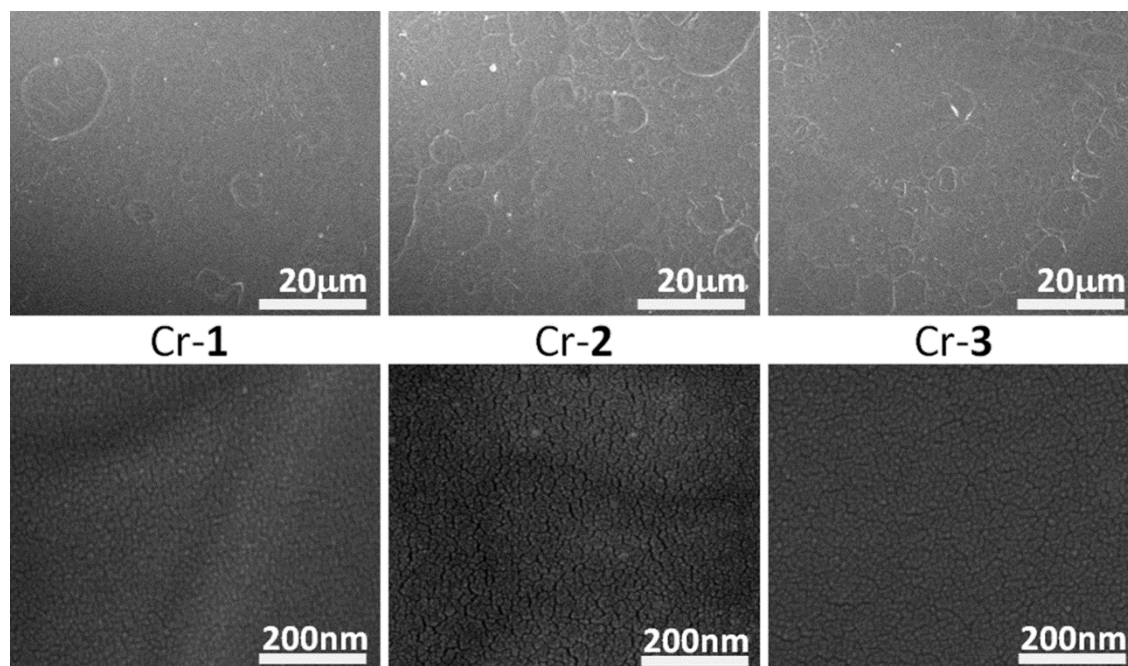


Figure S6 Top-view SEM images of Cr-1, Cr-2 and Cr-3;
upper row: 1k magnification; lower row: 100k magnification

**Dual Application of
(Aqua)(Chlorido)(Porphyrinato)Chromium(III) as
Hypersensitive Amine-Triggered ON Switch and
for Dioxygen Activation**

Philip Heier, Nicolas D. Boscher, Patrick Choquet, Katja Heinze*

Supplementary Information

Experimental Section

General procedures. **1** was prepared according to reported methods and analytical properties conform with literature data.¹ Solvents and triethylamine for measurements under inert atmosphere were dried by standard methods and degassed by three pump-thaw-cycles using argon. Other reagents were used as received from commercial suppliers (Sigma Aldrich). UV/vis spectra were recorded on a Varian Cary 5000 spectrometer using 1.0 cm cells (Hellma, suprasil). Samples for measurements under inert atmosphere have been prepared in a glove-box and were measured in 1.0 cm quartz cells equipped with a Young valve. The NMR spectrum was recorded on a Bruker Avance DRX 400 spectrometer at 400.31 MHz (¹H). Resonances are reported in ppm *versus* the solvent signal as internal standard CHCl₃ (¹H: δ = 7.26 ppm). Samples for mass spectrometry were dissolved in acetonitrile. FD mass spectra were recorded on a FD Finnigan MAT95 spectrometer. ESI mass spectra were recorded on a Micromass Q-TOF-Ultima spectrometer. Electrochemical experiments were carried out on a BioLogic SP-50 voltammetric analyzer using a glassy carbon working electrode, a platinum wire as a counter electrode and a 0.01 m Ag/AgNO₃ electrode as a reference electrode. The measurements were carried out at a scan rate of 200 mV s⁻¹ for cyclic voltammetry experiments and for square wave voltammetry experiments at negative potentials and of 100 mV s⁻¹ for positive potentials. 0.1 m (*n*Bu₄N)(PF₆) was used as a supporting electrolyte in CH₂Cl₂. Potentials are given relative to the ferrocene/ferrocenium redox couple ($E_{1/2}$ = 265 ± 5 mV under the experimental conditions). Spectroelectrochemical experiments were performed using a thin layer quartz glass (path length 1 mm) cell kit (GAMEC Analysentechnik, Illingen, Germany) equipped with a Pt gauze working electrode, a Pt counter electrode and a Ag/AgNO₃ reference electrode (10⁻⁵ m solutions in CH₂Cl₂ containing 0.1 m (*n*Bu₄N)(PF₆)). CW EPR spectra (X-band; ca. 9.4 GHz; ca. 20 mm) were measured on a Miniscope MS 300 at 298 K (Magnettech GmbH, Berlin, Germany). Settings were as follows: center field: 2499.01 G; modulation amplitude: 3000 mG; receiver gain: 5.0; microwave attenuation: 3 dB; sweep time: 120 s. *g*-values are referenced to external Mn²⁺ in ZnS (g = 2.118, 2.066, 2.027, 1.986, 1.946, 1.906). Simulations of EPR spectra were performed with EasySpin (v 4.0.0)² for MatLab (R2007b). Bulk electrolysis of CH₂Cl₂ solutions containing **4** (4.6 10⁻⁴ m) and 100 eq. *exo*-norbornene has been performed in an electrochemical cell with two separated magnetically stirred compartments. The anode chamber has been connected to the cathode chamber by a P2 glass filter membrane. A platinum mesh has been used as anode and a platinum wire as cathode. The Ag/AgNO₃ reference electrode has been placed in the anode chamber. 0.5 m (*n*Bu₄N)(ClO₄) has been used as the supporting electrolyte. The voltage has been set to 0.48 V (vs. Fc/Fc⁺) for a period of 2 h. GC measurements were performed on a GC-2010 gas chromatograph (Shimadzu, Japan) equipped with a HP-5 silica capillary column (Agilent Technologies, USA; length 30 m, inner diameter: 0.25 mm, layer thickness of stationary phase: 0.5 μm) and a flame ionization detector. Carrier gas: hydrogen gas; temperature of injector: 250°C;

temperature of detector: 310°C; column inlet pressure 64 kPa. Program: start temperature for 5 min: 30°C; heating rate: 5°C min⁻¹, end temperature: 100°C.

Density functional calculations were carried out with the Gaussian09/DFT series³ of programs. The B3LYP formulation of density functional theory was used employing the LANL2DZ basis set. No symmetry constraints were imposed on the molecules. The presence of energy minima of the ground states was checked by analytical frequency calculations. Solvent modeling was done employing the integral equation formalism polarizable continuum model (IEFPCM, dichloromethane). The approximate free energies at 298 K were obtained through thermochemical analysis of the frequency calculation, using the thermal correction to Gibbs free energy as reported by Gaussian09.

UV/vis experiments using 1. For all measurements 10⁻⁶ m solutions of **1** in CH₂Cl₂ or toluene were employed. 3 mL of this solution were transferred to a UV/vis cuvette to measure the initial UV/Vis spectrum. For reactions with excess amines 10 μL of the respective neat amines were added. Excess LiCl was added in form of 100 μL of a saturated solution in CH₂Cl₂. For experiments using 1.0, 0.1, 0.01 or 0.001 equivalents solutions of NEt₃, LiOH or CoCp*₂ were prepared separately in the respective solvent with 100 μL containing the given equivalents. All cuvettes were shaken vigorously to ensure complete mixture before the measurements. Spectra recorded were numerically corrected for the respective concentration change by dilution.

UV/vis experiments using 8. A 10⁻⁶ m solution of **1** was prepared in dry THF and stirred with dry solid CaCl₂ under inert atmosphere for 30 min. An aliquot of this solution was transferred to a cuvette with a Young valve via a syringe equipped with a syringe filter. The UV/vis spectrum of this solution matches the literature data for **8**.¹ Another filtered aliquot was treated with excess dry NEt₃. The UV/vis spectrum of this solution remained unchanged. After 3 h the volatiles of this solution were removed under reduced pressure. The remaining solid was re-dissolved in CH₂Cl₂ under humid air and excess NEt₃ was added. UV/vis spectra indicated the slow formation of **4**.

Characterization of 4. ¹H NMR: A sample of **1** in CDCl₃ was treated with exc. NEt₃ under air. The formation of **4** was monitored by UV/vis spectroscopy.^{4,5} The solution was concentrated to give a concentration suitable for ¹H NMR spectroscopic analysis. ¹H NMR (400 MHz, T = 298 K): δ = 9.08 (s, 8H, CH^{pyrrole}), 8.28 (br. s, 4 H, CH^{ortho}), 8.16 (br. s, 4 H, CH^{ortho}), 7.78 (br. s, 12 H, CH^{meta,para}).⁵ For IR measurements a sample of **1** in CH₂Cl₂ was treated with LiOH/air and the complete formation of **4** has been checked by UV/Vis spectroscopy prior to recording the IR spectrum of **4** in CH₂Cl₂. IR(CH₂Cl₂): $\tilde{\nu}$ = 1021 (m, CrO), 998 (s) cm⁻¹.⁵

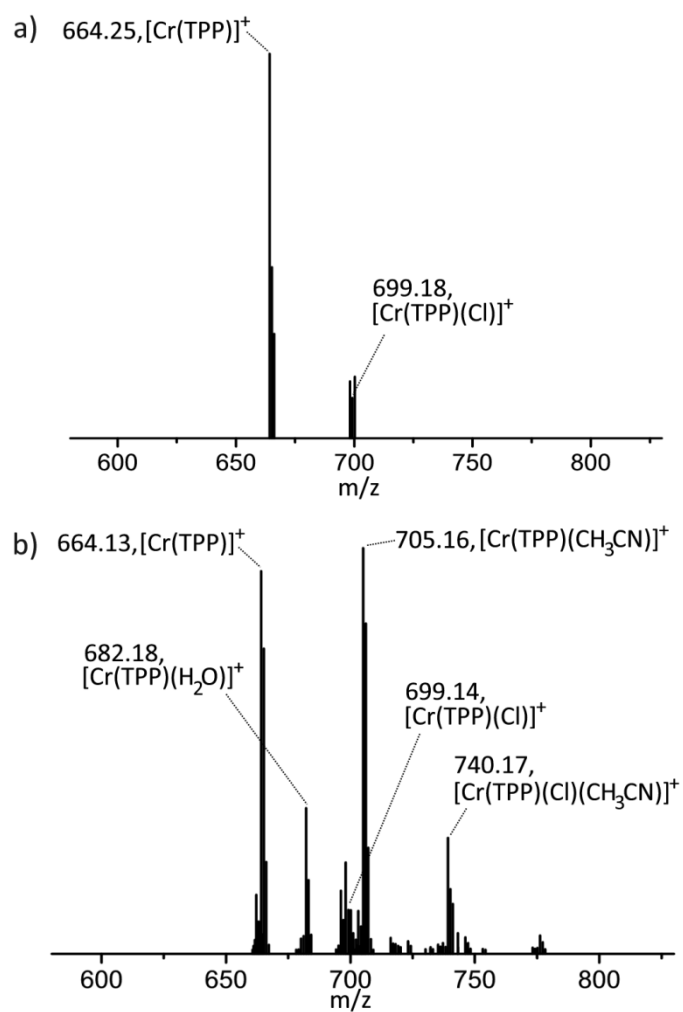


Figure S1 a) FD mass spectrum of **1**; b) ESI mass spectrum of **1**; samples were prepared in acetonitrile (CH₃CN).

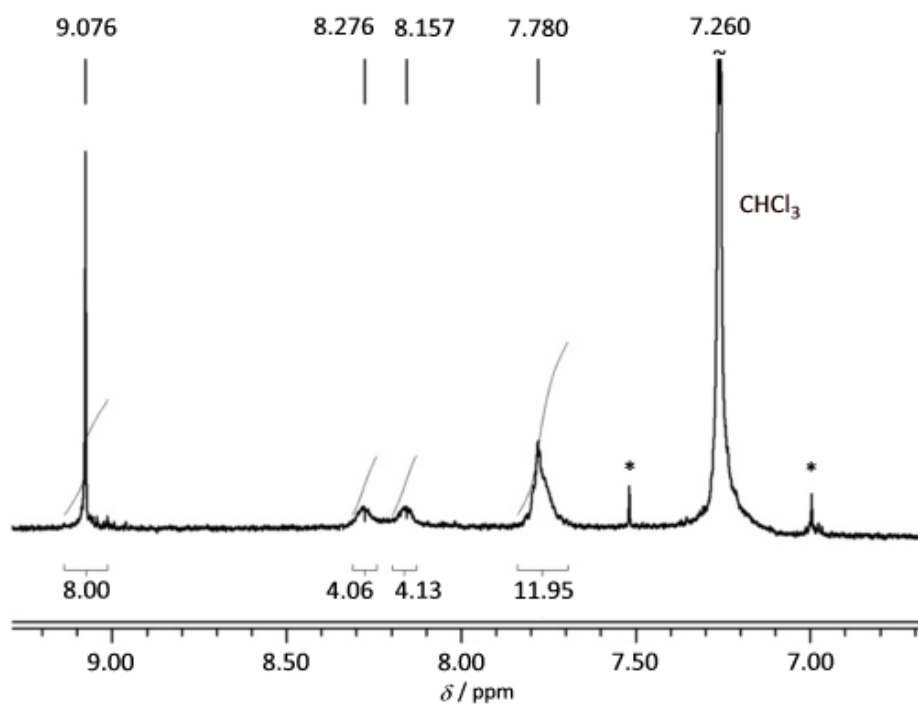


Figure S2 ^1H NMR spectrum of **4** in CDCl_3 ; sample was prepared by exposing a solution of **1** in CDCl_3 to exc. NEt_3 and air; * marks ^{13}C satellites of the solvent signal; resonances agree with literature values.⁵

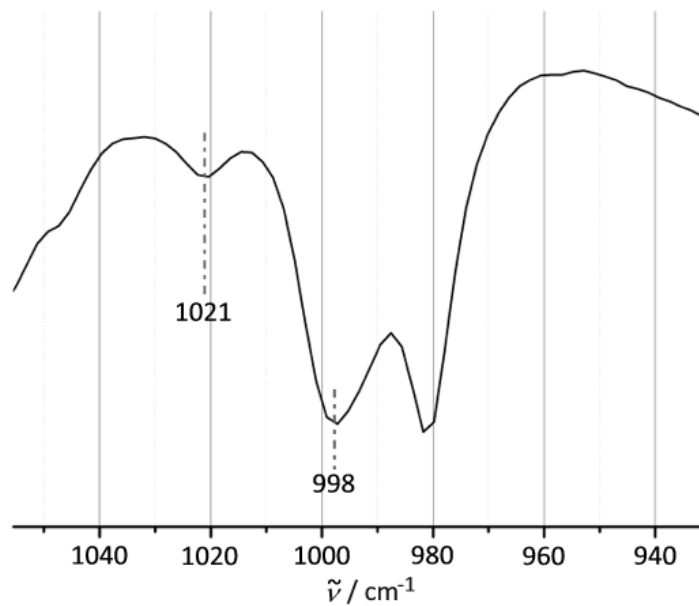


Figure S3 IR spectrum of **4** in CH_2Cl_2 ; sample was prepared by exposing a solution of **1** in CH_2Cl_2 to exc. LiOH and air; absorptions agree with literature values.⁵

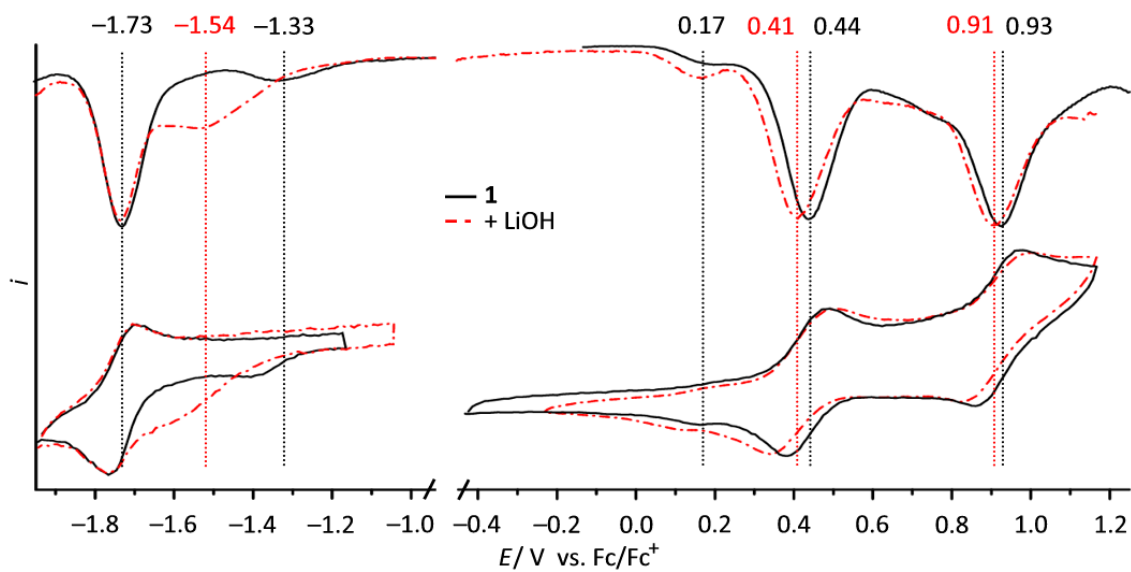


Figure S4 Square-wave voltammograms (top) and cyclic voltammograms (bottom) of **1** in CH_2Cl_2 in the absence (solid black curves) and in the presence of exc. LiOH (dashed red curves) under inert conditions.

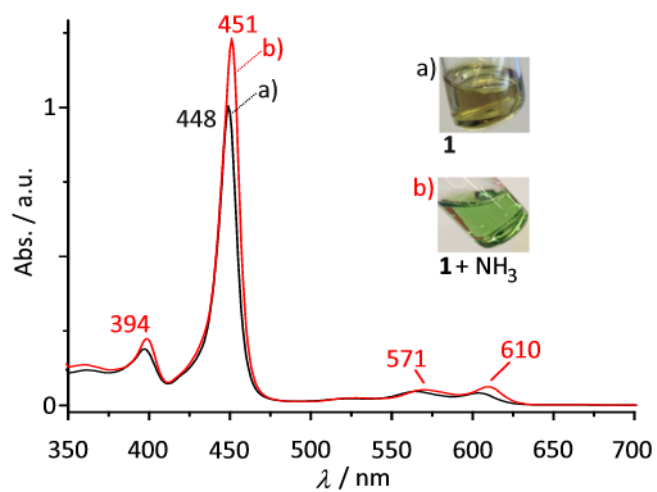


Figure S5 UV/vis absorption spectra in CH_2Cl_2 of a) **1** (black) and b) **1** with exc. NH_3 (red); insets show photographs the respective solutions.

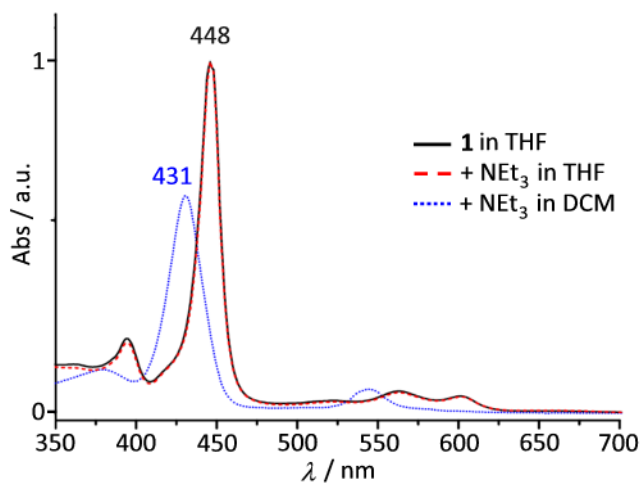


Figure S6 UV/vis spectra of a) **8** in THF (solid black curve), b) **8** in THF with exc. NEt_3 (dashed red curve) and c) **8** in CH_2Cl_2 with exc. NEt_3 exposed to moist air (dotted blue curve).

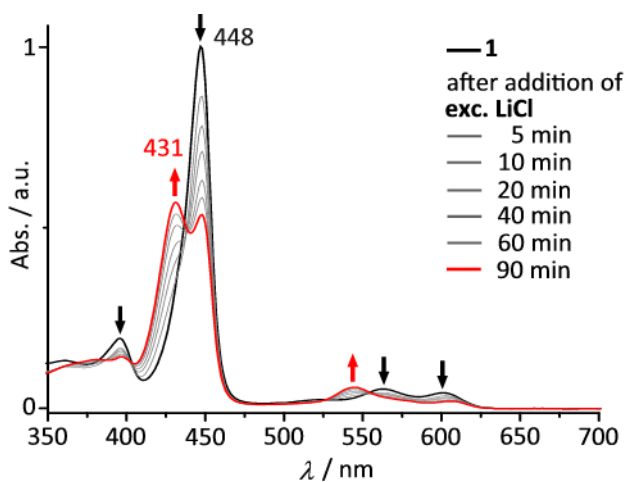


Figure S7 Temporal evolution of UV/vis absorption spectra of **1** in CH_2Cl_2 after addition of exc. LiCl ; red curve represents spectrum after 90 min.

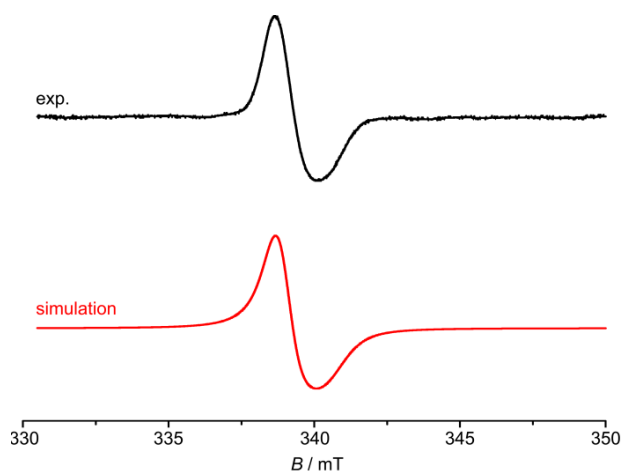


Figure S8 X-band EPR spectrum of **4**⁺ prepared electrochemically from **4** in $\text{CH}_2\text{Cl}_2/0.1 \text{ M } (n\text{Bu}_4\text{N})(\text{PF}_6)$ and frozen to 77 K and simulation ($g_1 = 1.9865$, $g_2 = 1.9780$).

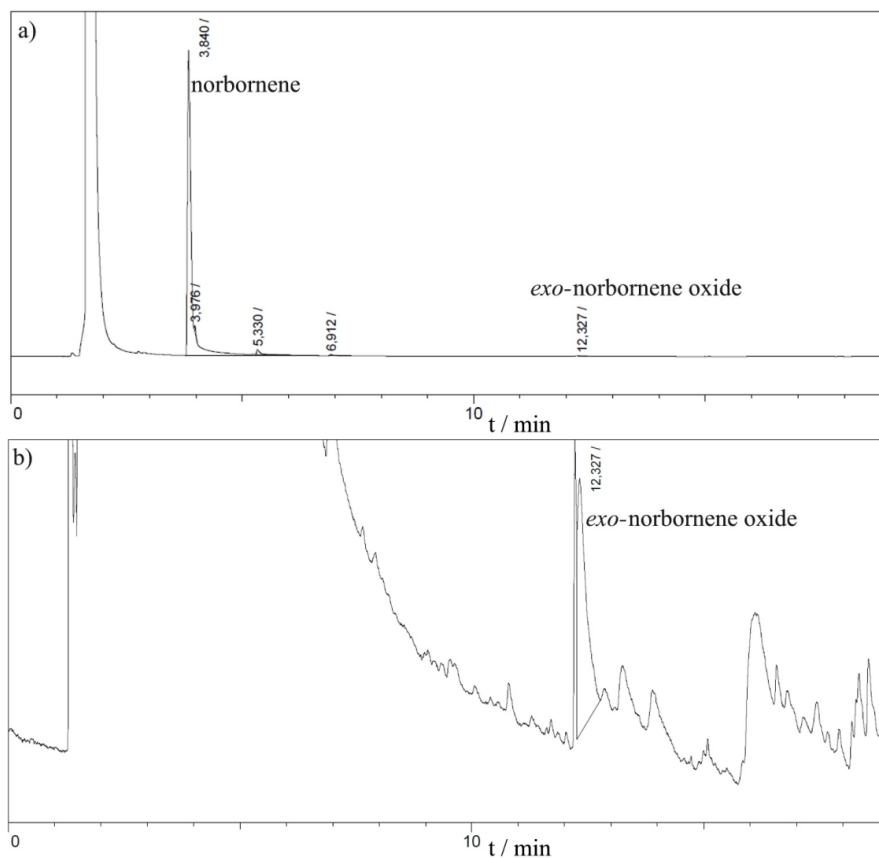


Figure S9 a) Full gas chromatogram of the electrolysis solution of **4** and 100 eq norbornene; b) magnification.

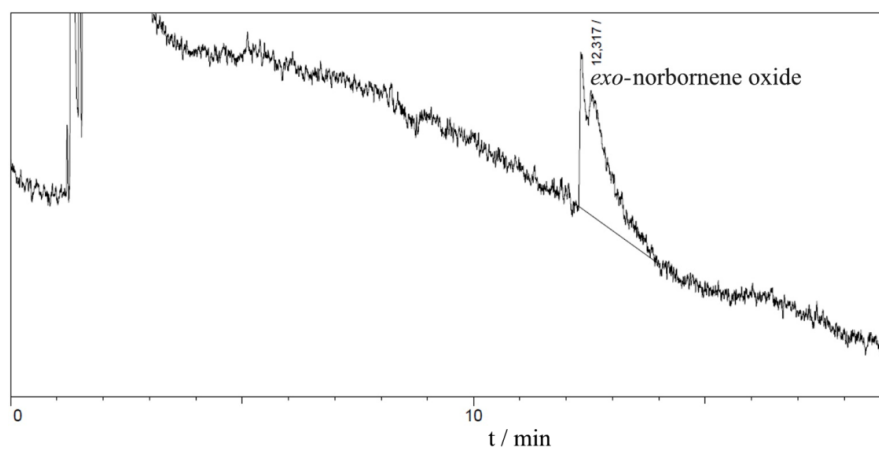


Figure S10 Gas chromatogram of an authentic sample of *exo*-norbornene oxide as received from Sigma-Aldrich at approximately the same concentration as in Figure S9 ($c = 1.8 \cdot 10^{-4} \text{ mol L}^{-1}$).

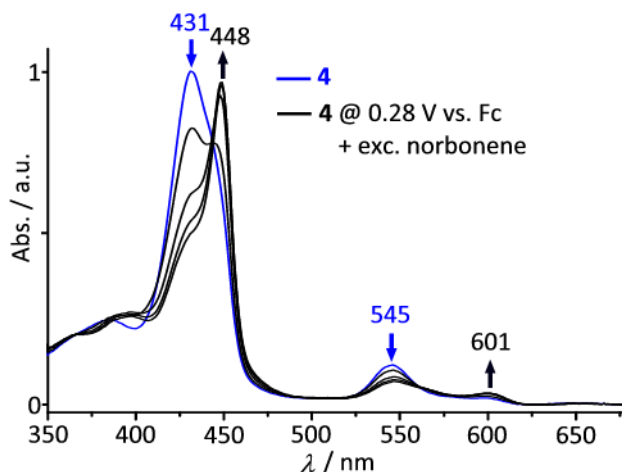


Figure S11 Spectroelectrochemical oxidation of **4** in $\text{CH}_2\text{Cl}_2/0.1 \text{ M } (n\text{Bu}_4\text{N})(\text{PF}_6)$ in the presence of norbornene.

REFERENCES

- (1) Tsutsui, M.; Mitsuo, I.; Vohwinkel, F.; Keinosuke, S. *J. Am. Chem. Soc.* **1966**, *569*, 854–855.
- (2) Stoll, S.; Schweiger, A. *J. Magn. Reson.* **2006**, *178*, 42–55.
- (3) Frisch, M. J.; Trucks, G. W.; Schlegel, H. B.; Scuseria, G. E.; Robb, M. A.; Cheeseman, J. R.; Scalmani, G.; Barone, V.; Mennucci, B.; Petersson, G. A.; Nakatsuji, H.; Caricato, M.; Li, X.; Hratchian, H. P.; Izmaylov, A. F.; Bloino, J.; Zheng, G.; Sonnenberg, J. L.; Hada, M.; Ehara, M.; Toyota, K.; Fukuda, R.; Hasegawa, J.; Ishida, M.; Nakajima, T.; Honda, Y.; Kitao, O.; Nakai, H.; Vreven, T.; Montgomery, Jr., J. A.; Peralta, J. E.; Ogliaro, F.; Bearpark, M.; Heyd, J. J.; Brothers, E.; Kudin, K. N.; Staroverov, V. N.; Kobayashi, R.; Normand, J.; Raghavachari, K.; Rendell, A.; Burant, J. C.; Iyengar, S. S.; Tomasi, J.; Cossi, M.; Rega, N.; Millam, J. M.; Klene, M.; Knox, J. E.; Cross, J. B.; Bakken, V.; Adamo, C.; Jaramillo, J.; Gomperts, R.; Stratmann, R. E.; Yazyev, O.; Austin, A. J.; Cammi, R.; Pomelli, C.; Ochterski, J. W.; Martin, R. L.; Morokuma, K.; Zakrzewski, V. G.; Voth, G. A.; Salvador, P.; Dannenberg, J. J.; Dapprich, S.; Daniels, A. D.; Farkas, Ö.; Foresman, J. B.; Ortiz, J. V.; Cioslowski, J.; Fox, D. J. *Gaussian 09*, **2009**, Revision A.02; Gaussian, Inc., Wallingford, CT.
- (4) Liston, D. J.; West, B. O. *Inorg. Chem.* **1985**, *1*, 1568–1576.
- (5) Groves, J. T.; Kruper, W. J.; Haushalter, R. C.; Butler, W. M. *Inorg. Chem.* **1982**, *21*, 1363–1368.

7. Acknowledgments

[Redacted text block]

[Redacted text block]

[Redacted text block]

[Redacted text block]

[Redacted text block]

[Redacted text block]

[REDACTED]

The Luxembourgish Fonds National de la Recherche is thanked for financial support through the SurfAmine project.



Philip Christoph Heier

Date of Birth: 24. 02. 1984

Place of Birth: Oldenburg

Nationality: German

8. Curriculum Vitae

PhD Thesis

10/2010 – 08/2014 *“Novel metallo-porphyrin based colorimetric amine sensors and their processing via plasma enhanced chemical vapour deposition at atmospheric pressure – synthesis, characterisation and mechanistic studies”*

At the Institute of Inorganic and Analytical Chemistry, Johannes Gutenberg-University, Mainz, Germany;
and the Centre de Recherche Public – Gabriel Lippmann, Belvaux, Luxembourg;
under the supervision of [REDACTED]

Overall grade: *summa cum laude*

Education

10/2004 – 03/2010 Studies of Chemistry (Diplom Chemie)
Georg-August-University Göttingen, Germany

03/2010 **Diploma in Chemistry**
“Synthesis of novel iron fluorescence sensors based on 3-hydroxypyridin-4-ones for potential surface coupling”
under the supervision of [REDACTED] at
the Georg-August-University Göttingen, Germany

10/2006 Intermediate Diploma in Chemistry (Vordiplom)
Georg-August-University Göttingen, Germany

09/1996 – 07/2003 **General Qualification for University Entrance**
(Allgemeine Hochschulreife)
Gymnasium an der Willmstraße, Delmenhorst, Germany

Teaching activities

since 10/2013 Teaching assistant at the Institute for Inorganic and Analytical
Chemistry, Johannes Gutenberg-University, Mainz, Germany

06/2011 – 07/2011 Teaching assistant at the Institute for Inorganic and Analytical
Chemistry, Johannes Gutenberg-University, Mainz, Germany

01/2009 – 09/2009 Teaching assistant at the Institute for Inorganic Chemistry at the
Georg-August-University, Göttingen, Germany

8.1 List of Publications

2013

N. Boscher, D. Duday, **P. Heier**, K. Heinze, F. Hilt, P. Choquet

“Plasma Polymer Membranes for Immobilising Metalloporphyrins”

Plasma Process. Polym. **2013**, *10*, 336 – 344.

N. Boscher, D. Duday, **P. Heier**, K. Heinze, F. Hilt, P. Choquet

“Atmospheric pressure plasma polymerization of metalloporphyrin containing mesoporous membranes for gas sensing applications”

Surf. Coat. Technol. **2013**, *234*, 48 – 52.

P. Heier, C. Förster, D. Schollmeyer, N. Boscher, P. Choquet, K. Heinze

“ $\alpha\alpha$ - and $\alpha\beta$ -zinc-meso- A_2B_2 -tetraarylporphyrins with large optical response to volatile amines”

Dalton Trans. **2013**, *42*, 906 – 917; **cover article**.

2014

N. Boscher, T. Bohn, **P. Heier**, F. Moisy, B. Untereiner, K. Heinze, P. Choquet

“Optical Sensing Responses for $Cr^{III}(Cl)(TPP)(H_2O)$ -Based Coatings Obtained by an Atmospheric Pressure Plasma Method – Application to the Detection of Volatile Amines”

Sens. Actuators B **2014**, *191*, 553 – 560.

P. Heier, T. Bohn, P. Choquet, N. Boscher, K. Heinze

“New Class of Zn(II) and Cr(III) Porphyrins Incorporated into Porous Polymer Matrices via an Atmospheric Pressure Plasma Enhanced CVD to Form Gas Sensing Layers.”

J. Mater. Chem. A **2014**, *2*, 1560 – 1570.

P. Heier, N. Boscher, P. Choquet, K. Heinze

“Dual Application of (Aqua)(Chloro)(Porphyrinato)Chromium(III) as Hypersensitive Amine-Triggered ON Switch and for Dioxygen Activation”

submitted 2014.

8.2 Conference contributions

- 09/2013 EUROMAT 2013 (European Congress and Exhibition on Advanced Materials and Processes), Sevilla, Spain.
Oral presentation
“Colorimetric Gas Sensing Surfaces – Deposition of Porphyrin Containing Composite Films via AP-DBD Enhanced CVD”
- 02/2013 9. Koordinationschemie Treffen, Bayreuth, Germany
Oral presentation
“On the road towards smart sensing coatings: New metalloporphyrins with large optical responses to volatile amines”
Best oral presentation award
- 09/2012 13th International Conference on Plasma Surface Engineering, Garmisch-Partenkirchen, Germany
Oral presentation
“Atmospheric Pressure Dielectric Barrier Discharge – Deposition of Porphyrin Containing Colorimetric Gas-Sensing Surfaces”
- 02/2012 8. Koordinationschemie Treffen, Dortmund, Germany
Poster presentation
“On the road towards smart sensing coatings: Novel metalloporphyrins suitable for volatile amine detection and plasma deposition”
Best poster award
- 07/2011 Heidelberg Forum of Molecular Catalysis, Heidelberg, Germany
Poster presentation
“Distorted Metalloporphyrins for Volatile Amine Detection”

